

Pion-Pion Decay Distributions for  
 $\pi^- p \rightarrow \pi^+ \pi^- n$  at 100 and 175 GeV/c

Thesis by  
Stuart Reh Stampke

In Partial Fulfillment of the Requirements  
for the Degree of  
Doctor of Philosophy

California Institute of Technology

Pasadena, California

1982

(Submitted May 4, 1982)

-ii-

To Marian

That voice was damned familiar. "Majistral is going to the John Bull," said the pope. "We can catch up with him later."

V. p. 441, Thomas Pynchon

### **Acknowledgements**

This thesis is rather long. I have also taken too long as a student, a period filled with peaks of interest and joy as well as valleys of difficulty. Before closing it, I want to thank the many colleagues and friends who helped me through it.

For my parents, George and Grace Stampke, my brother Don, my sisters Paula, Sue, and Kathy, their children, and my departed uncle Al, for their love and for their quiet and important support while I pursued a crazy goal, my greatest love and gratitude.

It is a pleasure to thank my advisor, Geoffrey Fox, for his many insights, his comments and encouragement, his help in the completion of this thesis, and especially for allowing me the freedom to deal with a difficult period three years ago. I am grateful to Jerry Pine for being my advisor in my early years here, for letting me work on this experiment, and for refusing to let me quit.

It is difficult to find the words to thank Clara and Ricardo Gomez. My love for them is deep. Ricardo tried to teach me some difficult lessons, both professionally and personally. Some I learned, some not. And finally during a crisis, they opened their home to me.

Geoffrey, Ricardo, and Jerry: for your support, your counseling, your help, your criticisms, the friendship, and for just plain putting up with me, I thank you.

I thank my collaborators on E110 and E260. Together we built a major spectrometer and performed two interesting experiments with it. I credit our successes to them: C. Bromberg, J. Dickey, G. C. Fox, R. Gomez, W. Kropac, C. Malone, and J. Pine from Cal Tech; V. Ashford, H. Haggerty and E. Malamud from Fermilab; R. Abrams, R. Delzenero, H. Goldberg, F. Lopez, S. Margulies, D. Mcleod and J. Solomon from UICC; A. Dzierba, F. Fredericksen, R. Heinz, J. Krider, H. Martin, and D. Petersen from Indiana University; and E. Lorenz, M. Medinnis, and P. Schlein from UCLA.

The list must include Carl Malone. While working at Cal Tech he built much of hardware I was responsible for, and he built well. Carl also spent as much time in the trenches as many in the above list.

For their technical skill in building equipment as well as their friendship I thank Jozef Ungerer, Svend Sondergaard, Hans Grau, Dan Sell, Joe Lyvers and Dean Davey. For contributing precious time and effort in preparation for our winter 1978 run I thank Bob Walker, and Alan Barnes.

Several undergraduates were also essential to this experiment. G. Ray Beau-soleil, W. Danchi, and C. Footman all made significant contributions to our analysis.

I want especially to thank Louise Sartain, Roma Gaines, June Bressler, and Nancy Durland not only for their secretarial skill and dedication, but for their friendship. Student life at Cal Tech would have been unbearable without them, and without an understanding counselor. For me this was Lee Daniels of the Athenaeum.

Special thanks to my "co-conspirators", Rich Delzenero of UICC, Frank Fredericksen of Indiana, and Kar Yung of Cal Tech. We worked closely and productively together. This was especially true of Frank and I, even though half a continent usually separated us.

I thank Bob Blair and George Zweig for many varied and interesting hours of conversation on Physics and other things. For literally opening the door to High Energy Physics for me, I thank Frank Sciulli, Steve Frautschi, and Jerry Pine. For getting me into Physics in the first place, I thank Duane Doty, Ryoichi Seki, and especially Robert Romagnoli of CSUN.

Nine years as a graduate student is a long time. Without the friendship of my colleagues, and friendships both inside and outside Cal Tech, I might have never lasted it. Ruth Hitchcock, Alix Martin, and Jim Lowry in Bloomington Indiana befriended me at a crucial moment. My love for them is undiminished by time or distance.

Lynn Anderson, Rosemary Baltrusaitis, Alan Barnes, Mark Bartelt, Tere Blair, Alena Bobb, Eugene Brooks, Wyatt Brown, Linda Contos, Rajan Gupta, Cindy and Shawn Hennegan, Rosemary Kennet, Jai Sam Kim, Steve Knapp, Bill Kropac, Ken McCue, Frank Merritt, Frank Nagy, Beth Nordholt, John Osborne, Becky Rothenberg, Bonnie Strand, Lon Schlundt, Steve Sherman, Eric Siskind, Claude Stevenson, Cathy Van Ingen, Norman Wilson, and the Siskind Memorial Friday Lunch Bunch are honored and respected for their help and their friendship.

I thank the technicians of the Meson Lab and the Target group at Fermilab for their technical support. The analysis for this thesis used the Fermilab Cyber computers. That system was a joy to use. This thesis was "typed" on the Cal Tech High Energy Physics VAX computer using the word processing and typesetting program "troff" under the UNIX operating system.

Lastly, I want to thank the United States Department of Energy. They paid for all this. I hope the coming years will see the investments in me made by them and by Cal Tech pay off.

**Abstract**

We report measurements of the reaction  $\pi^-p \rightarrow \pi^+\pi^-n$  at 100 and 175 GeV/c using a large wire chamber spectrometer at Fermilab. Production of  $\rho^0$ ,  $f^0$ , and  $g^0$  resonances was observed. Cross sections for  $\pi^-p \rightarrow \pi^+\pi^-n$  in the  $\rho^0$  mass region are given. Decay angle distributions for  $\pi\pi$  masses from .55 to 3.5 GeV/c<sup>2</sup> are presented. Moment analyses of the decay distributions are made as a function of  $\pi\pi$  mass from .55 to 2.4 GeV/c<sup>2</sup>. Contours of  $\pi\pi$  decay distribution dips are given in  $s_{\pi\pi}$  and  $t_{\pi\pi}$ . Comparisons with several lower energy experiments are made. Detailed discussions of the apparatus, trigger, and analysis procedures are given.

**Table of Contents**

	page
Acknowledgements	iv
Abstract	vii
<b>Chapter I. Introduction</b>	<b>1</b>
1.1 Perspective	
1.2 E110	
1.3 Almost Raw Data	
<b>Chapter II. Apparatus</b>	<b>15</b>
2.1 Overview	
2.2 M6 West	
2.2.1 Beam Cerenkov Counters, Beam Composition	
2.3 The MPS	
2.3.1 Beam and Interaction Counters	
2.3.2 Target	
2.3.3 Target House, Forward Photon Detectors	
2.3.4 Magnet	
2.3.5 Spark Chambers	
2.3.6 Proportional Chambers	
2.3.7 Shift Registers	
2.3.8 Cerenkov Counters C1 and C2	
2.4 Triggers	
2.5 Beam Momentum, Resolution	

<b>Chapter III. Event Reconstruction and Scaler Analysis</b>	<b>55</b>
--	-----------

3.1	Introduction
3.2	TEARS
3.3	Event Selection
3.3.1	Run Rejection, Data Set
3.4	Scaler Analysis

<b>Chapter IV. Data Corrections</b>	<b>76</b>
-------------------------------------	-----------

4.1	Weights
4.2	Veto Failure Background
4.3	Neutron Vetos
4.4	BCD Delta Rays
4.5	A-Station Trigger Correction
4.6	Target Region Delta Rays
4.7	Interaction and Decay Losses
4.8	Chamber Efficiency Correction
4.9	Background Rejection by C1 and C2
4.10	Beam Corrections
4.11	Weight Summary

<b>Chapter V. Acceptance, Cross Section, Moments</b>	<b>106</b>
--	------------

5.1	Acceptance
5.1.1	Acceptance Weights
5.2	General Correction Formalism
5.2.1	Moments

5.3	Cross Section Results
5.4	The $\pi\pi$ Mass Spectrum
5.5	Moments <i>versus</i> Mass
5.5.1	A PMA Test
5.6	Moments <i>versus</i> $t_{pn}$
5.7	$\frac{d\sigma}{dt}$ Distributions

**Chapter VI. Decay Distributions**

147

6.1	Scatter Plots
6.2	Resonance Region
6.3	High Mass, Low $t_{pn}$ Fits
6.4	Transformation to $t_{\pi\pi}$
6.4.1	High Mass Exponential Slope
6.5	Dips
6.6	Review

**Appendix A Kinematics, OPE, PMA**

182

A.1	Kinematics
A.1.1	$t_{\pi\pi}$
A.2	One Pion Exchange
A.3	PMA

**Appendix B Trigger Electronics**

193

**Appendix C TEARS**

207

- C.1 Overview
- C.2 Straight Line Fits
- C.3 Matching and Match Cleanups
- C.4 Beam Processing
- C.5 Targtrk
- C.6 Vtrig
- C.7 Kinks

**Appendix D Corrections**

223

- D.1 Introduction
- D.2 Veto House Correction
  - D.2.1 Measurement
  - D.2.2 Background Subtraction
  - D.2.3  $\Delta^0$  Smearing
  - D.2.4 B8 Failure
- D.3 Neutron Vetos
- D.4 BCD Delta Rays
- D.5 Target Region Delta Rays
- D.6 Chamber Efficiency Measurements

**References**

237

## Chapter I

### Introduction

#### 1.1 Perspective

Studies of the reaction



have been an important part of the high energy physics agenda since the first observations [St61, Er61, Pi61] of  $\rho$  mesons were published in 1960 and 1961. These occurred not long after such resonances were predicted [Dr58, Fr59] to explain nucleon electromagnetic form factors.

Interest in reaction (1.1) has largely focused on the creation and decay of the final state  $\pi\pi$  system as a map of the forces between pion pairs, and between pions and nucleons. At beam energies above a few GeV, one can view the reaction as a "quasi two body" reaction, in which either the final state pions are associated with each other, or one of them is associated with the recoiling neutron. If we draw one particle exchange diagrams for reaction (1.1), as in figure 1-1, these interpretations yield 1-1a and 1-1b. Our experiment favors 1-1a over 1-1b mainly by its design, which limits the  $\pi^\pm$  - neutron acceptance to high masses.

The  $\pi\pi$  effective mass spectrum for reaction 1.1 observed in previous experiments, for example [Bo64, Hy68, Ro73, Gr74, Co78, and Wi78], is dominated by the prominent  $\rho^0(770)$  and  $f^0(1270)$  resonances. To a lesser extent, the  $g^0(1700)$  state was also visible. The  $\omega^0(783)$  meson has a small branching fraction to  $\pi^+\pi^-$ , and its presence in reaction (1.1) is felt mainly through electromagnetic interference effects with the dominant  $\rho^0$ . A continuum of effective masses is also present, and fine scale features of the mass spectrum, when coupled with analyses of the  $\pi\pi$  decay angle distribution have revealed evidence for other states not appearing readily in effective mass spectra. Reported states decaying to  $\pi\pi$  include [PDG80]

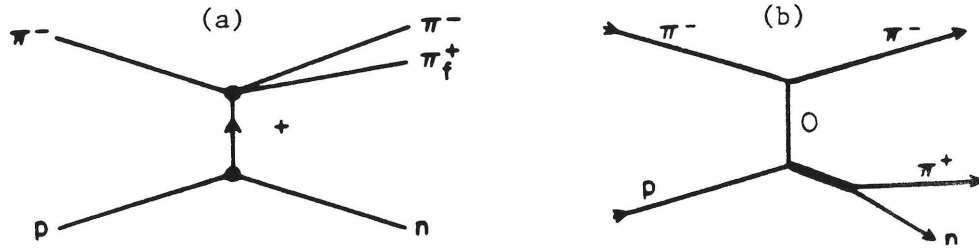


Figure 1-1. One particle exchange diagrams for reaction (1.1) (a)  $\pi\pi$  interaction at the upper vertex, which may or may not be resonant. (b)  $\pi N$  interaction at the lower vertex. Either vertex may or may not be resonant. (a) is kinematically favored by the spectrometer over (b). Resonant interactions at both vertices are backgrounds suppressed by the trigger.

the  $S^*(980)$ ,  $\varepsilon(1300)$ ,  $f'(1515)$ ,  $\rho'(1600)$ , and  $h(2040)$ . Of these, the  $h^0$  comes closest to having a visible effect on simple mass plots. The  $\pi\pi$  decay distribution and the mass spectrum also show non-resonant effects from the  $\pi\pi$  interaction. Sharp drops in mass spectra have been interpreted as caused by zeros in the  $\pi\pi$  interaction amplitude entering into kinematically allowed regions. The first such drop occurs at about 1  $\text{GeV}/c^2$  effective pion mass and the amplitude zero interpretation probably competes with explanations based on the inelastic threshold for  $\pi\pi \rightarrow KK$  and the existence of the  $S^*$ .

The first  $\rho$  meson observations were interpreted as evidence for elastic  $\pi\pi$  scattering, with the "target" pion being a virtual particle emitted by the nucleon. Although no real pion targets exist,  $\pi\pi$  scattering has remained a fairly important and interesting area of strong interaction studies. Data extrapolation procedures beginning with the work of Goebel [Go58] and Chew and Low [Ch59], have allowed reasonable determinations of the  $\pi\pi$  scattering parameters from a number of reactions. The  $\pi\pi$  system found in reaction (1.1) is thus surprisingly complex, and high statistics data are needed to observe all, or most of the above mentioned features.

Reaction (1.1) is representative of a tremendous number of exclusive (all final state particles determined or detected) reactions studied in the last twenty years. Most of these studies were made at beam momenta less than about 20 GeV/c on interactions characterized by relatively low,  $-1 \text{ GeV}/c^2 < t \leq 0$ , momentum transfer between target and recoil systems. A wonderful and varied hadron spectroscopy and the dynamics seen in low  $t$  experiments have both enriched and help to trouble high energy physics. The sheer number and variety of mesons, along with a like proliferation of baryon states, helped show that most observable particles were not, as once hoped, fundamental, while at the same time providing the initial verification of the quark model and unitary symmetry classification schemes.

A "peripheral" reaction [Ja65], (1.1) is characterized by a dominance of small momentum transfers from the proton to the neutron at beam energies above a few GeV. Over half the examples of reaction (1.1) in this experiment were found at  $|t| < .15 \text{ (GeV/c)}^2$ . Such collisions are relatively soft, and can be viewed as resulting from the longest range form of strong interactions. In this, one begins to consider the second main focus in studies of reaction (1.1), the strong interactions between pions and nucleons. At low  $t$ , coupling constants are too large to permit straightforward perturbation analyses of the interactions involved. Quantitative and specific theoretical predictions about the behavior of the strong force (its explicit dependence on observable variables) in this region have come only with concerted effort. Phenomenological analyses, which have blended fairly general principles with reasonable models, have also been fruitful, leading one to believe that many of their results should be derivable from whatever final theory evolves. However, although the successes have been considerable, and important features of the strong force have been quantified, the dynamics of low  $t$  interactions have been difficult to interpret theoretically.

Modern origins of the peripheral model for low  $t$  interactions are found in the work Chew, Low and Goebel, and that of Drell [Dr60]. The simplest peripheral model is just one pion exchange (OPE), in which the exchange of figure 1-1a is a virtual pion. However, although  $\pi$  exchange dominates many reactions, simple OPE is too simple a description for (1.1) and any other reaction allowing  $\pi$  exchange. A number of features of the data are simply inconsistent with OPE and other effects must be present. The simplest models for these are absorbed  $\pi$  exchange models, such as the Williams or "Poor Man's Absorption" (PMA) model [Wi70, Fo71a, Fo71b, Wa73, and Oc73]. In PMA, one has a simple analytic model for the effects of absorption on basic  $\pi$  exchange. PMA appears to be the simplest model that can describe the general features of reaction (1.1) in the low ( $< .15(GeV/c)^2$ )  $t$  region. The agreement with data has been rather good [Oc73, Wi78], and rather detailed studies are needed to see the limitations of the model. Although the significance of its success is still unclear, the model has been surprisingly resilient. Appendix A includes a brief review of OPE and PMA, and defines the kinematic symbols used in this thesis.

PMA generally ignores the effects of other allowed exchanges. A more reasonable approach would be to invoke the principles of Regge theory, in which not virtual particles, but poles in the complex angular momentum plane associated with them represent forces. For reaction (1.1) other exchanges both allowed and found required by low energy data include  $A_1$ ,  $A_2$  Regge poles and cuts associated with the  $\pi$  and  $A$  poles [Ki73, Ki77]. At this level of complexity, Regge models of  $\pi^-p \rightarrow \rho^0 n$  are in excellent agreement with data up to 63 GeV/c [Ki77, Al78].

Despite early difficulties, Regge theory has been found a reasonable, although complicated, framework for describing low and intermediate  $t$  hadronic interactions. This is a regime in which the more fundamental form of strong interactions, the color force of QCD [Fi78], currently runs into computational problems because

of large coupling constants and nonperturbative binding effects. In this context, the many complications needed for a Regge model of relatively "simple" reactions such as  $\rho$  production are not unreasonable.

Although no longer on the frontier of high energy physics, experiments on peripheral interactions, such as reaction (1.1), still have a place. They can add to our spectroscopic knowledge, and continue to map the strong force in an old, but still difficult region. Any allegedly true theory applicable to strong interactions must be able to quantitatively predict the dynamics seen by such an experiment. This report, will hopefully add to the data set for such tests. Our experiment is the highest energy counter experiment to study reaction (1.1).

## 1.2 E110

The experiment described in this report, Fermilab E110A, grew out of three proposals (numbers 35, 51, and 54) submitted to the then National Accelerator Laboratory for peripheral physics experiments with large aperture, spark chamber spectrometers located in hadron beams. The initial E110 proposal [Pi71] projected a systematic physics program covering  $s$  and  $t$  dependences of a series of quasi-two-body peripheral interactions, new resonance searches, and  $\pi\pi$  and  $K\pi$  scattering measurements, all at beam energies up to 80 GeV. At the time it was proposed, 1971, the studies of E110 were of topical interest. There was also a desire for a large, general purpose spectrometer facility at Fermilab.

An amended proposal, 110A [Pi72], was submitted in May 1972, and approved shortly thereafter. Some changes to the proposed spectrometer were made, the physics program was somewhat extended, and beam energies up to 200 GeV were projected. At that time, the E110 collaboration consisted of experimenters from Cal Tech, Fermilab, Indiana University (IU), the University of Illinois Chicago Circle (UICC), and the University of California Los Angeles (UCLA).

In 1973, during the early construction of the E110 spectrometer, a second proposal, E260 [Pi73], was submitted by the E110 collaboration for an investigation of high  $p_t$  phenomena, including the production of hadron jets. E260 would use the E110 spectrometer and take data first since much of the E110 instrumentation would not be needed. Only some large calorimeters, not in the E110 proposal, would have to be added. The group's efforts then centered on E260, which took Beryllium target data in January 1976, and Hydrogen target data during the summer of the same year. The UCLA participation in the collaboration ended with E260, although they refurbished our Cerenkov counters between experiments.

As the data taking for E260 was being completed in September 1976, a few tests were made to evaluate the basic E110 trigger method, which used multiwire proportional chambers as hodoscopes to count charged particles. By this time, E110 represented fairly "old fashioned" physics, and Fermilab requested that the physics goals for E110A be redefined in terms of a limited survey of peripheral interactions and resonance searches at 100 and 200 GeV. The result was a proposal to survey the following reactions simultaneously: high mass  $\pi\pi$  scattering,  $\pi^-p \rightarrow \pi^+\pi^-n$  with emphasis on  $\rho^0$  production,  $\pi^-p \rightarrow \bar{K}^0K^-p$ ,  $K^-p \rightarrow K^0\pi^-p$ ,  $\pi^-p \rightarrow K^0\pi^+\pi^-X$ , and  $\pi^-p \rightarrow K^0\bar{K}^0X$ . A few background reactions would also be recorded. The main data would be taken at 100 and 200 GeV, with some at 17 and 50 GeV. The 17 GeV point was desired for a comparison with results [Gr74] of the Cern Munich collaboration.

Spectrometer modifications, section 2.1, were largely completed by January 1977, and an engineering test run was made in February. Our first major physics run (Run I) took place in May and June of 1977, with most data taken at 100 GeV, and some at 20 and 50 GeV. Twenty, rather than 17 GeV was used after design studies indicated that a fixed spectrometer geometry was preferred for using the lower energies to understand backgrounds expected in  $\pi\pi\pi\pi$  at 100 GeV, and 20 GeV

was the best compromise of resolution and acceptance for our low energy point.

An extremely preliminary analysis of the spring '77 data [St78] indicated overwhelming background and resolution problems for  $\pi\pi n$  at 200 GeV. In response to this, we lowered the beam energy to 175 GeV and additional photon detectors were added at the downstream end of the spectrometer. One of these detectors was a high resolution photon calorimeter originally used for Fermilab E111 [Ba80]. Its installation at the MPS had already been planned as a parasitic test run for a proposal to study  $\omega^0 \rightarrow \pi^+ \pi^- \pi^0$ , P523 [Dz76a]. The other was a "lead wall", backed by scintillator and covering the major part of the forward aperture. Both of these detectors were behind our second Cerenkov counter, C2 (figure 2-2), and both were used, along with repositioned E260 calorimeters, as off line (*not* as part of the trigger) vetos. With these changes, we made a second major run (Run II) in the winter and spring of 1978. Most of the data for this run was taken at 175 GeV, with some at 20, 50, and 100 GeV for calibration purposes. Table 1.1 gives our overall event totals for the two runs excluding alignment and special calibration data.

With the completion of the Run II, analysis of both runs began. Track finding was done at both Fermilab and at Lawrence Berkeley Laboratory by the Indiana and Cal Tech groups. This effort was plagued with several false starts, requiring two repetitions of the tracking analysis on Run I data. This wasn't completed until December 1979 for Run I, and shortly thereafter for Run II, which was held back until the problems in the earlier set were resolved. Although some preliminary studies of our  $\pi\pi n$  data were made during this time, final background and physics work on the  $\pi\pi n$  reaction didn't begin until this stage was completed. Final tracking and physics analyses were made on the Fermilab Cyber 175 computers.

A division of labor was made for the physics analysis of our various triggers. UICC had the  $K^0 \bar{K}^0 X$ , and high mass  $\pi\pi$  scattering triggers. A thesis [De82] has been written on the  $K^0 \bar{K}^0 X$  data. Cal Tech and Indiana shared the "low mass"  $\pi\pi n$

Table 1.1		
Total Events by Run (Thousands)		
$P_{Beam}$	Run I	Run II
20 GeV/c	63	61
50 GeV/c	164	122
100 GeV/c	1058	404
175 GeV/c	0	1680

trigger, called " $\pi\pi m_T$ ". Initial studies of the  $K^0\pi p$  trigger were made at Cal Tech, and Indiana is now pursuing its final analysis. Cal Tech analyzed the  $K^0\pi\pi X$  data, and our E110 publications to date were based the Run I data from this trigger. These were a conference report [Di80] and paper [Br80], on the reactions  $\pi^-p \rightarrow K^0 K^\pm \pi^\mp X$  and  $\pi^-p \rightarrow K^0 K^+ K^- X$  at 100 GeV/c. Observations of the  $D(1265)$  and  $E(1420)$  mesons were reported in  $KK\pi$  channels and possible enhancements were found in the  $KKK$  channel.

The analysis of reaction (1.1) from the  $\pi\pi m_T$  trigger (see section 2.4) involved particularly close collaboration between Cal Tech and Indiana. Two theses, this one and one by Frank Fredericksen of Indiana [Fr82], have resulted. Both reports use 100 and 175 GeV/c data from runs I and II respectively, although the emphasis in the two theses differs. (The 100 GeV/c data from Run II was compromised by a series of problems with the spectrometer.) The data analysis for both energies was, with two important exceptions, essentially identical. These were differences in the forward particle identification with our Cerenkov counters, and the use of the forward photon detectors in the 175 GeV analysis.

This thesis concentrates on decay distributions for reaction (1.1) and attempts a limited  $\pi\pi$  scattering study from the data. Topics in Fredericksen's thesis, and

not here, are effective pion trajectories from the  $\pi\pi n_T$  data and  $\pi^+\pi^-\pi^0$  spectra from the P523 tests. Both theses include spherical harmonic moment distributions at the two energies, and a major goal for both was obtaining the cross section for reaction (1.1) in the  $\rho^0$  mass region. We will make qualitative comparisons between our results and those of several lower energy experiments, [Gr74, Co78, and Al78].

The emphasis in hardware and analysis documentation also differs between the theses. The documentation here, especially numerical correction factors, applies to the Run I spectrometer and analysis. Differences between runs are noted when significant, and the forward photon detection will be briefly described. Fredericksen emphasizes the Run II spectrometer and analysis.

### 1.3 Almost Raw Data

A simple analysis of our data (after particle tracking) reveals its broad outline, and it is perhaps worthwhile to give a quick look at some uncorrected distributions to complete this introduction. The  $\pi\pi n_T$  trigger selected the topology of two charged particles coming from the target and traveling forward through the magnet by counting the number of particles seen in several proportional chambers between the target and downstream face of the magnet. Veto counters surrounding the target and masking off the magnet upstream face suppressed events with extra charged particles, and events with photons coming from the target at large angles. The trigger was not designed to detect the recoil neutron. It was identified in later analysis by missing mass cuts. Also, the trigger didn't select the types of particles involved, either forward or beam. The selection was left to analyses of Cerenkov counters in the beam and spectrometer.

Overall, this experiment recorded about a million events in Run I at 100 GeV. Of these, about 280,000 events were from the  $\pi\pi n_T$  trigger, and roughly 10500 satisfied our requirements to be called  $\pi\pi n$  events. Rough numbers for 175 GeV were 1.7

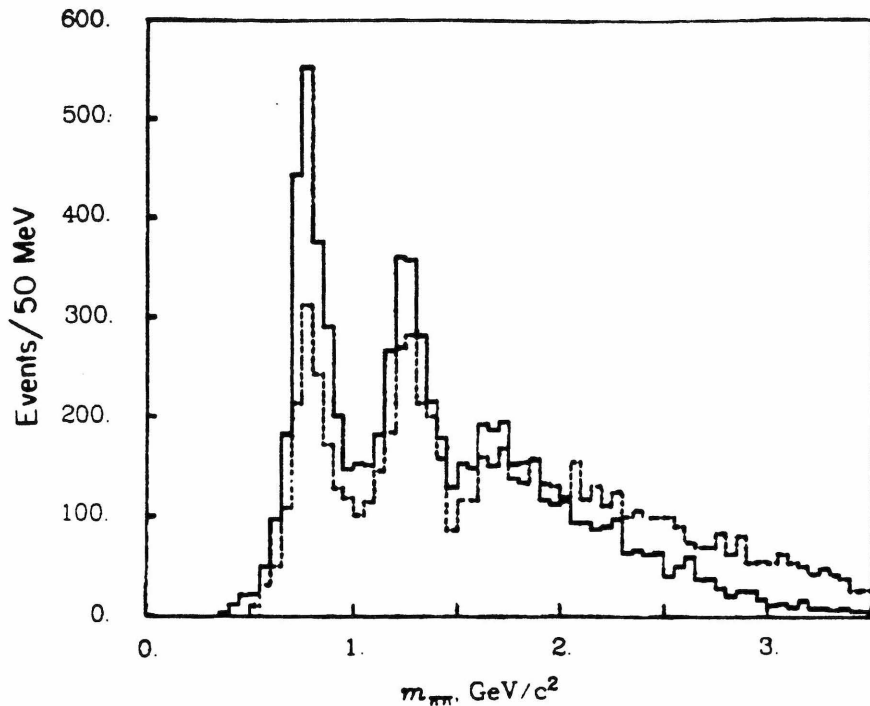


Figure 1-2. Uncorrected  $\pi\pi$  mass spectra at 100 GeV (solid histogram) and 175 GeV (dashed histogram). These are final event samples with  $|t| < .15$   $(\text{GeV}/c)^2$ .

million total triggers, 490000 events from the  $\pi\pi n_T$  trigger, and about 9900  $\pi\pi n$  events. (Both of these final samples include backgrounds of order 10%.) Figure 1-2 shows  $\pi\pi$  mass spectra at 100 and 175 GeV from the final event samples. Peaks for the  $\rho^0$  and  $f^0$  are clear, but not so the  $g^0$ . The  $g^0$  "peak" barely tops a large background at 100 GeV and is even less significant at 175 GeV. The 175 GeV acceptance is better at higher masses relative to the  $\rho^0$  region than the 100 GeV acceptance, and figure 1-2 reflects this. The small final  $\pi\pi n$  event counts will need explanation, and Chapter III gives the details for Run I. One reason was a lack of active forward photon vetos. Most of our data clearly had unvetoed high energy  $\pi^0$ 's, as evidenced by total observed energies much less than the beam energy, figure 1-4.

About half the recorded  $\pi\pi n_T$  data actually had only two forward particles, and figure 1-3 shows the  $\pi\pi$  mass spectrum for those events. In the upper curve we make no missing mass selection, while the lower hatched area includes a rough

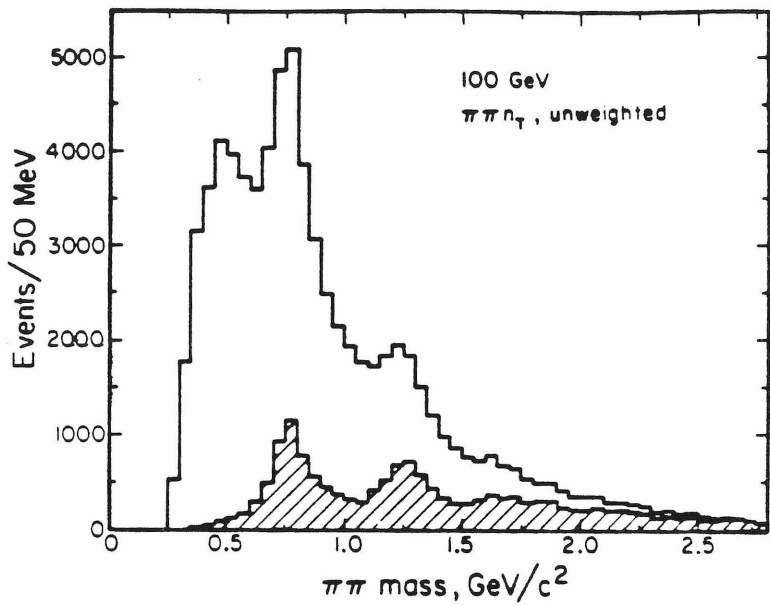


Figure 1-3. Uncorrected  $\pi\pi$  mass spectra without (upper curve) and with (lower curve) a neutron missing mass cut. No Cerenkov cut was made for this figure, all particles were assumed to be pions, and no  $t$  cut was used.

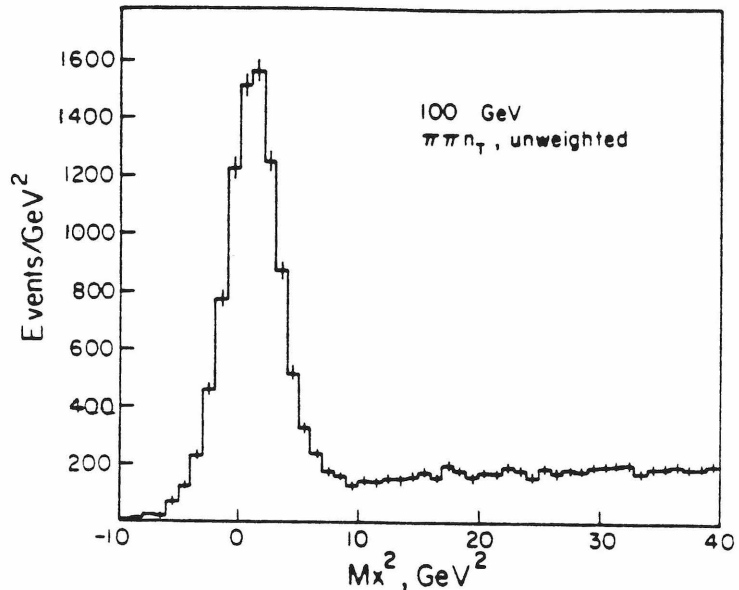


Figure 1-4. Missing mass (squared) spectrum for the  $\pi\pi n_T$  trigger. Large values are roughly twice the missing energy. (See equation A.4b)

neutron missing mass cut. In both curves, prominent peaks at the  $\rho^0$  and  $f^0$  masses are seen. Also present in the upper curve is a bump at about 500 MeV. That bump corresponds to essentially uncorrelated  $\pi^+\pi^-$  pairs and is not a resonant effect. Such pairs can result from particle decays involving one or more undetected and unvetoed  $\pi^0$ , such as the  $\omega^0 \rightarrow \pi^+\pi^-\pi^0$  decay, or from having one charged pion associated with the nucleon system (figure 1-1b). In our spectrometer the former explanation is more likely as the difference between the curves of figure 1-3 represents events with substantial missing energy. This is illustrated by figure 1-4, which is a missing mass (squared) spectrum for reaction (1.1). The large peak in this figure corresponds to neutrons and goes to negative  $Mx^2$  because of our resolution. The continuum in this figure indicates considerable energy lost to neutral particles other than a final state neutron. The most likely candidates for these are one or more  $\pi^0$ 's associated either with the  $\pi^+\pi^-$  system or the recoil nucleon system, or both. The continuum runs to the kinematic limit of about 200 GeV<sup>2</sup> in figure 1-4, and also penetrates under the neutron peak, giving a background of about 10% to the  $\pi\pi n$  signal.

The lack of a 500 MeV bump in figure 1-2 is evidence that the  $\pi\pi$  system we study here corresponds to peripheral  $\pi\pi$  interactions as in figure 1-1a, and not uncorrelated junk or nucleon resonances as in figure 1-1b. Important to this argument is a reasonably poor acceptance for pions coming from low mass  $N^*$  and  $\Delta$  decays, which is zero for pion - neutron masses less than about 2.5 GeV/c<sup>2</sup>. Figure 1-5 illustrates this, showing  $\pi^+ n$  masses plotted against  $\pi\pi$  masses from  $\pi\pi n$  events at 100 GeV. The  $\pi n$  masses were found by forcing the missing mass on successful events to be the neutron mass. The distribution of events within the envelope reflects  $\pi\pi$  decay angle distributions given in chapter VI. What is of interest here is the envelope, which maps the limits of our  $\pi - n$  acceptance. Only  $\pi^+ n$  masses are shown in the figure. Resonances in the  $\pi^- n$  channel require exotic

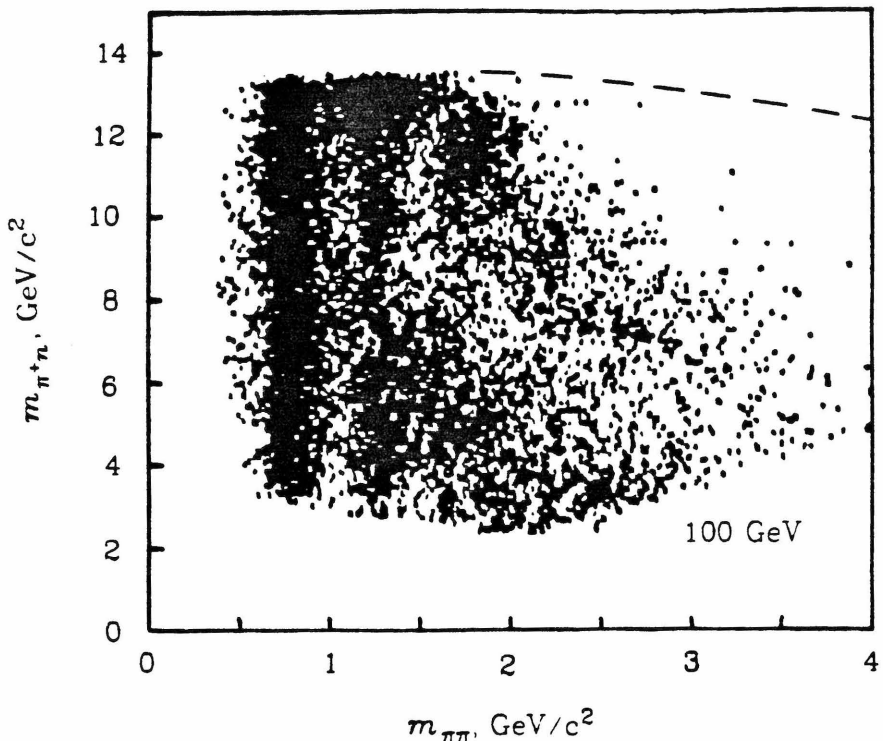


Figure 1-5. Scatter plot of  $\pi^+$  - neutron mass versus  $\pi^+\pi^-$  mass. The dashed line follows the limit seen for  $\pi^-n$  masses.

(charge  $\pm 2$ ) exchanges and none were seen. The  $\pi^-n$  mass limits followed those seen in figure 1-5 for  $\pi^+n$  masses, although the distribution was, naturally, roughly inverted.

Figures 1-6 and 1-7 contain data for our models of the background under the neutron peak in figure 1-4. These figures show the  $\pi\pi$  mass and missing mass squared spectra for data from our  $\pi\pi X$  background trigger. This trigger had the same charged particle topology requirements as did  $\pi\pi n_T$ , but the veto counters surrounding the target were not included in the trigger. In figure 1-7 we also see a prominent peak with low missing masses and a continuum. However, the peak is shifted and distorted from that expected for neutrons. It corresponds to dominant production of  $N^*$  and  $\Delta$  resonant states of various masses.

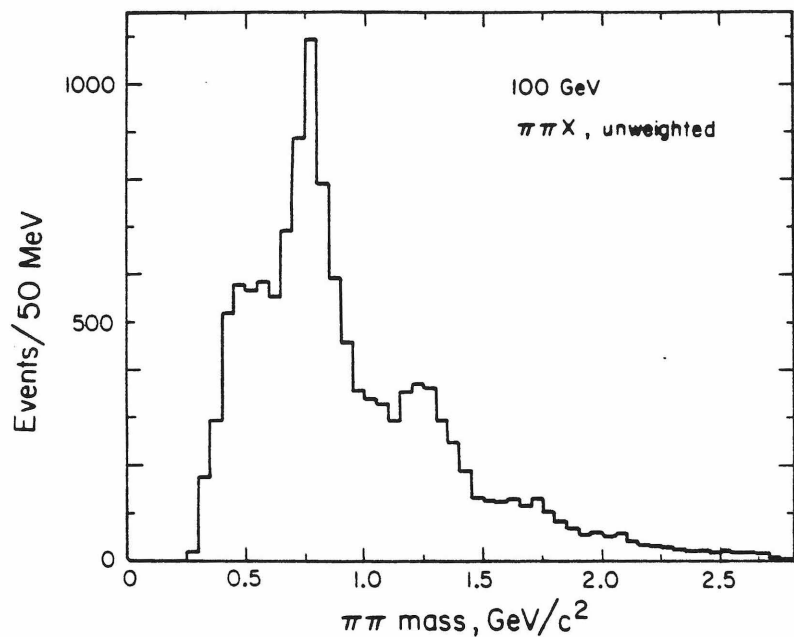


Figure 1-6.  $\pi\pi$  mass spectrum from the  $\pi\pi X$  trigger, no missing mass cut.

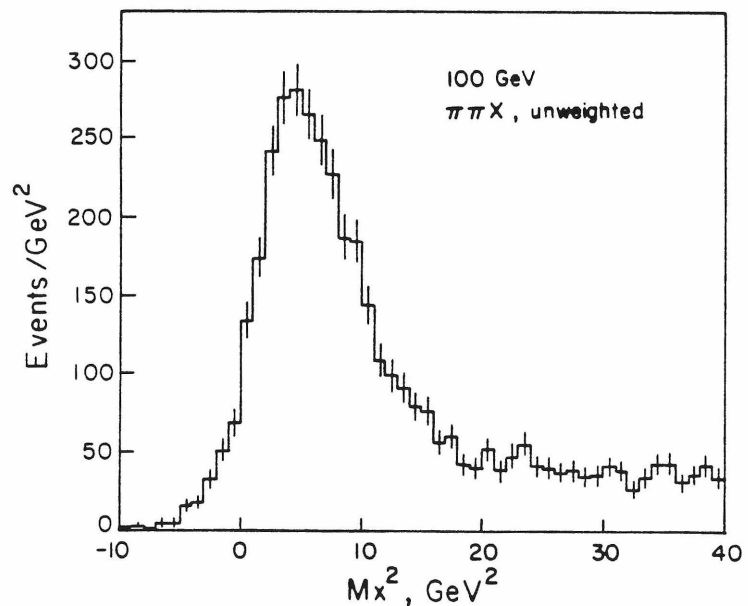


Figure 1-7. Missing mass spectrum for the  $\pi\pi X$  trigger. Compare to figure 1-4.

## Chapter II

### Apparatus

#### 2.1 Overview

The E110 spectrometer, also known as the Fermilab Multiparticle Spectrometer (MPS), was located at the end of the M6 West secondary beam of the Meson Laboratory. The MPS was designed to measure forward going charged particle systems from low to high multiplicities. Descriptions of the beam and spectrometer have been given elsewhere [Br80, Dz77, Me80, Yu80] mainly for our previous experiment, E260. Here, we document the beam and MPS as they existed for the Spring 1977 run of E110. Changes and additions for Run II will be noted. Fredericksen's thesis [Fr82] should be consulted for a complete review of the spectrometer in that run.

Spectrometer modifications for E110 included changing to a trigger based on multiplicity measurements by our proportional chambers and adding a photon veto system upstream of the magnet. We also increased the upstream lever arm (target to MPS magnet) from  $\sim 2.6$  m. in E260 to  $\sim 5$  m. for E110. The geometry downstream of the magnet was largely the same as E260 with only few proportional chambers moved about. The spark chambers and their pulsing system were upgraded to allow longer delays from beam arrival to chamber pulsing, and shorter dead (recovery) time settings. Finally, magnet side lining proportional chambers and a bank of neutron counters were added, neither of which is used in this analysis.

## 2.2 M6 West

One of six independent Meson lab beam lines, M6 [Dz77, Ay77] was a high resolution, medium intensity beam, figure 2-1. It transported particles produced when protons extracted from the main ring of the Fermilab synchrotron struck an 8.00 inch long by .04 inch square beryllium target about 1850 feet upstream of the MPS.

During this experiment, the Fermilab accelerator ran at a maximum (during extraction) energy of 400 GeV, with a cycle time of 10 to 12 seconds. The slow spill used for E110 lasted about 1.1 seconds. The beam had an *r.f.* structure, with  $\sim 1$  ns beam bearing buckets every 18.8 ns. Beam counts at the MPS were typically 500,000 particles per spill. At these intensities, less than 1% of the buckets were populated, and the fraction of those with two or more particles in a bucket was measured at less than 1%. Using timing signals provided by the laboratory, we gated off the extreme ends of a beam pulse to avoid taking data when the beam intensity was unstable on a time scale of order tens of milliseconds. These signals were also used to alert our on line computer to the arrival of the beam. A pile up rejection system (and other features of the trigger electronics, section 2.4 and Appendix B), reduced the effective beam to typically 300,000 particles per pulse.

M6 is shared between three branches, "East," "West," and "Far West," only one of which could run at a time. The part common to all three branches had three stages, each roughly 150 m. long, designed as "point-to-parallel-to-point imaging systems" [Ay77]. The M6-West branch had a fourth stage with final focus near the MPS target.

The first stage of the beam, at a production angle of 3 mr to the primary proton beam provided sign and momentum selection. Fixed collimators near the production target restricted M6 to a solid angle of  $1.34 \mu\text{st}$ . F-stop collimators after septum dipoles provided the main intensity control for the beam, and main bending magnets in the parallel section maximized momentum dispersion. This stage ends

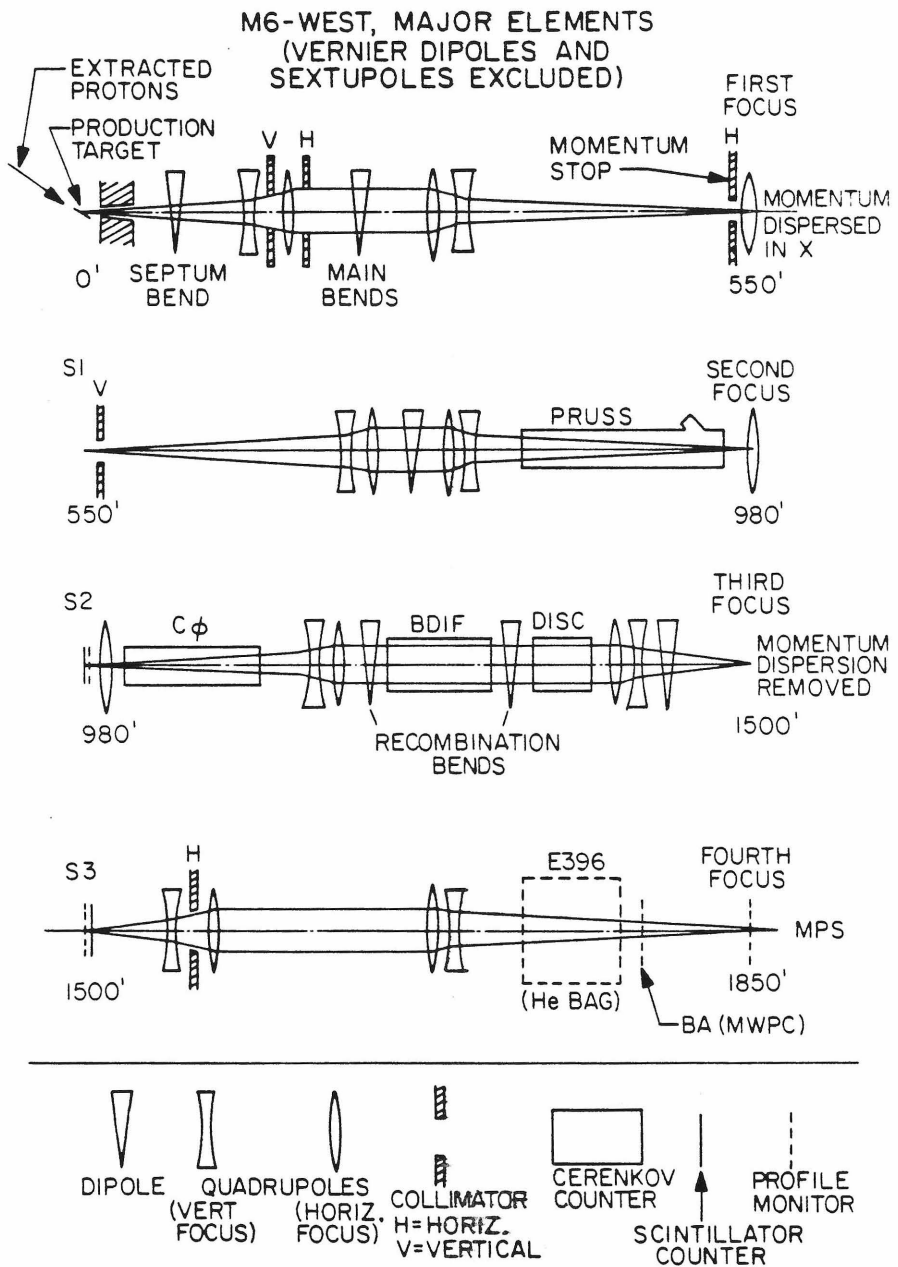


Figure 2-1. M6 West beam. First three stages are common to M6 East and Far West. Beam envelope is schematic. E396 was an experiment, and removed its equipment from the beam when E110 took data.

with a momentum dispersed (in x) focus with dispersion of 2.48 inches/%,  $(\Delta x / (\frac{\Delta p}{p}))$ . Collimators at the first focus set the beam momentum spread. They were set to  $\leq .80$  inches for 50, 100, and 175  $GeV/c$  data and 1.00 inches at 20  $GeV/c$ . Field lenses at the first and second foci constrained trajectories of the momentum dispersed particles, and recombination bends in the third stage removed this dispersion at the third focus.

The second stage included the first of two threshold Cerenkov counters ("PRUSS") and, at the second focus, profile monitors and scintillator counters, a pattern repeated at each focus except the first. The third stage had a long parallel section in which two differential Cerenkov counters, "BDIFF" [An76] and "DISC" [Be72], were located. The second threshold counter, " $C_0$ " [Ay74], was upstream of this parallel section. The fourth stage merely transported the beam to the MPS with the fourth, and final, focus near our target.

Beam magnet settings were computer controlled with a console located in our counting room. The beam was aimed through the target entrance window (figure 2-5) by centering it on a halo anti-counter, Sc, section 2.3.1. Particle transmission from the second focus to the MPS was typically 65%, and of this, about 85% passed through the hole in Sc and was counted as "beam".

### 2.2.1 Beam Cerenkov Counters, Beam Composition

Four gas Cerenkov counters, Table 2.1, tagged beam particle types and measured beam composition. The table also gives the nominal counter settings. PRUSS and  $C_0$  were quite stable counters. DISC (built at CERN for the M6 beam line) was angle sensitive and required constant monitoring and frequent readjustment, especially after long beam down times or retuning the beam for any reason. BDIFF was a little less sensitive, but readjustment after each beam down time was also necessary. To maximize the kaon tagging efficiency, we required only a coincidence of

Table 2.1a  
Beam Cerenkov Counters

Name	Type	Z(*)	Length (ft)	Number & Type of Phototubes	Max. Gas Pressure
PRUSS	Threshold	911	96	2-RCA 31000M	1 atm
$C_0$	Threshold	1079	60	1-RCA 31000M	5 atm
BDIFF	Differential	1245	45	3-Phillips 56 DUVP	15 atm
DISC	Differential	1322	19	8-RCA 31000M	20 atm

\* Distance from production target to counter center

Table 2.1b  
Nominal Settings

	175 GeV	100 GeV	50 GeV	20 GeV
$C_0$	$\pi$	$\pi$	$\pi$	$e^-$
PRUSS	$\pi$	$\pi$	$\pi$	$e^-$
BDIFF	$\bar{p}$	$\bar{p}$	$K^-$	$\pi$
DISC	$K^-$	$K^-$	$\bar{p}$	off

Table 2.2  
100 GeV/c Beam Composition and Counter Efficiencies

	Raw Beam Fraction (%)	Tagged Beam Fraction (%)
$\pi^-$	$92.92 \pm .002$	$91.47 \pm .07$
$K^-$	$3.96 \pm .0013$	$5.19 \pm .05$
$\bar{p}$	$3.12 \pm .0011$	$3.34 \pm .04$

	Efficiencies (%)		
	$C_0$	PRUSS	BDIFF
$\pi^-$	$98.44 \pm .01$	$86.41 \pm .01$	$.17 \pm .001$
$K^-$	$11.22 \pm .28$	$2.54 \pm .15$	$.08 \pm .04$
$\bar{p}$	$3.49 \pm .26$	$.47 \pm .11$	$91.99 \pm .04$
			DISC
			$.44 \pm .001$
			$92.69 \pm .03$
			$.03 \pm .03$

any six of the eight DISC phototubes (Table 2.1). DISC pion and proton efficiencies remained acceptably low.

Beam Cerenkov counter data included "tag bits", section 2.3.7, and scaler totals. The scalers required only a beam coincidence and hence recorded the number of times each counter fired for all beam particles. Tag bits were recorded

only with events, giving the pattern of counters that fired on a given event. To determine the beam composition and counter efficiencies, the Indiana group used a program [Be79a] adapted from E260. Using the Cerenkov scaler totals, the total beam scaler count, and accumulated Cerenkov counter tag bit patterns, the program determined counter efficiencies for each particle type,  $\pi$ ,  $K$ , and  $\bar{p}$ , particle fractions for unbiased beam, and similar fractions for "tagged" beam. Unbiased beam was the flux actually incident on the MPS, while "tagged" beam was recorded on events, and therefore distorted by relative cross sections for triggering. The tagged fractions were trigger dependent, but not the unbiased fractions (checked by comparing fits for  $\pi\pi n_T$  and  $K^0\pi p$  triggers). The fit results of Table 2.2 used only the  $\pi\pi n_T$  trigger.

Initially, fits were made for individual runs, but the statistical errors were large. Global fits, using only runs in which all the Cerenkov counters were at their nominal settings, were then made, Table 2.2. Since considerable run to run scatter was observed in the initial fits, we consider all particle fractions uncertain to .5%. Within this uncertainty, the unbiased fractions are consistent with those expected for our beam, (the expected  $\bar{p}$  fraction was 2.8%).

The raw  $\pi$  fractions of Table 2.2 include some muon and electron contamination. This was measured at 100 GeV as a fraction of the  $\pi$  flux by placing a module of the E260 calorimeters in the beam and triggering on the beam. From a sample of 1250 tagged pions, the muon fraction was found to be  $\mu = (3.2 \pm .6)\%$  of the  $\pi$  flux, and the electron fraction was found to be consistent with 0 (1 event).

MULTIPARTICLE SPECTROMETER PLAN VIEW MAY 1977

- 21 -

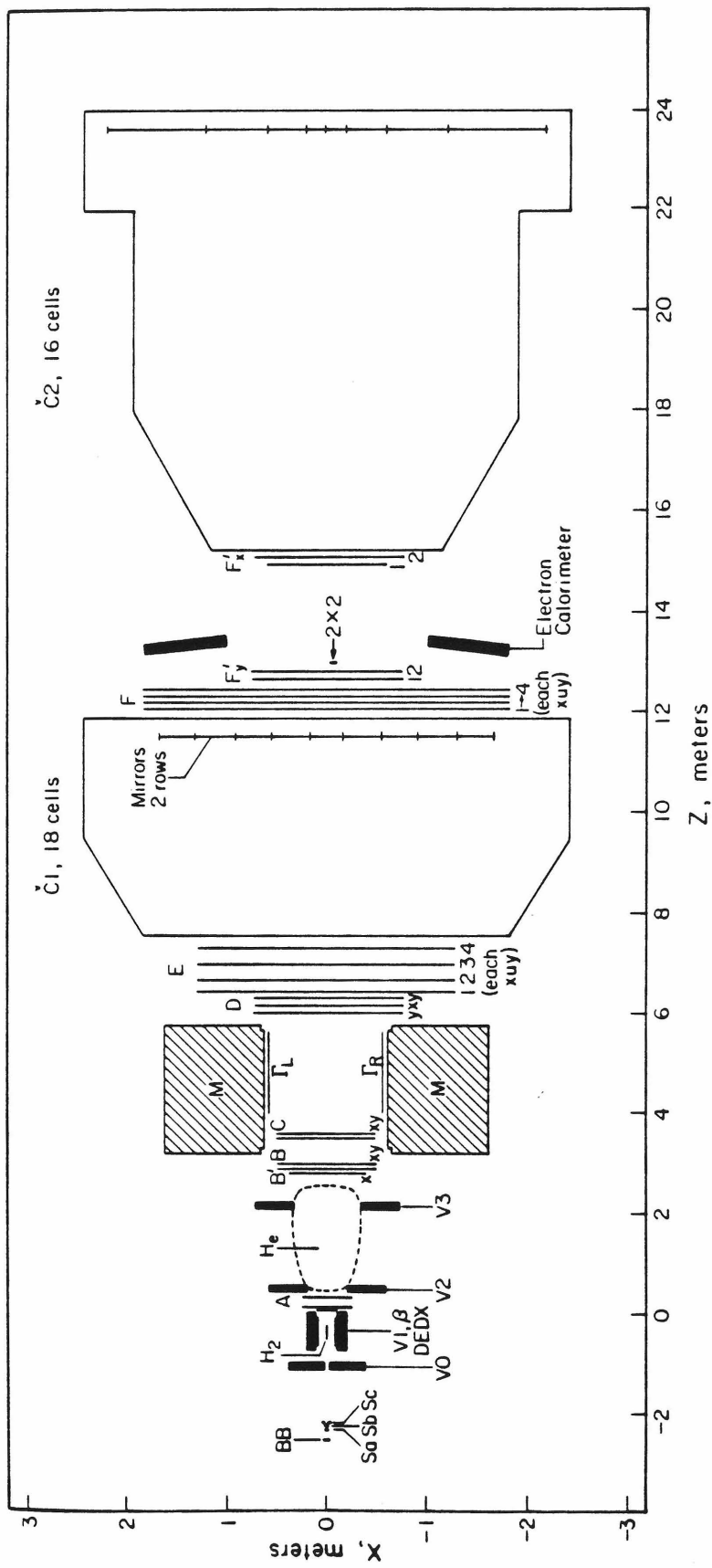


Figure 2-2. E110 Spectrometer, plan view, Run I configuration. For Run II, the major changes were addition of photon detectors, the "Lead Wall" and the E111 photon calorimeter behind C2. Also a pwc, BBW, was added at the 2x2 location, and the V3 counters and electron calorimeters were moved slightly.

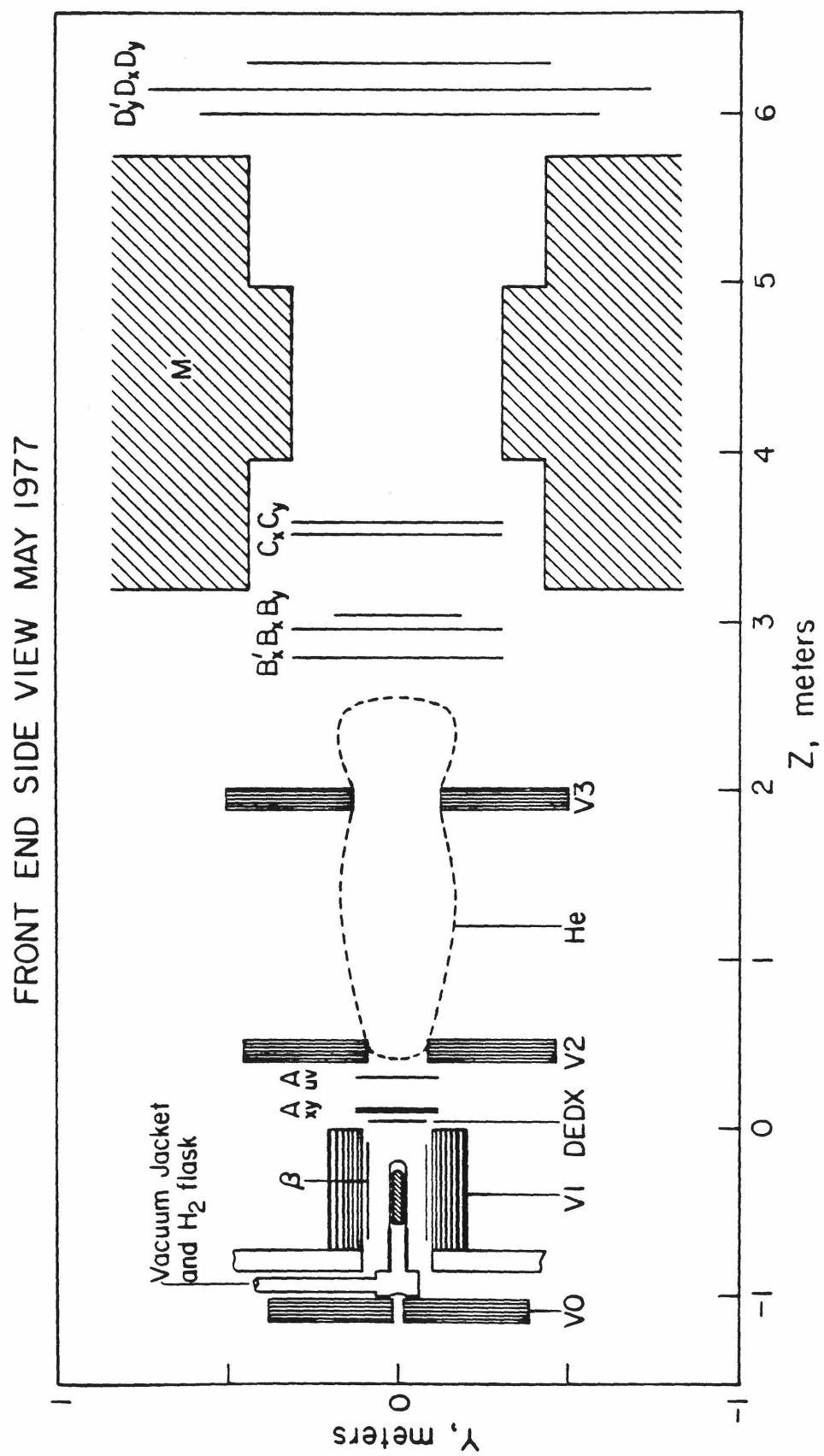


Figure 2-3. Front end region of the MPS for Run I, side view. The vertical aperture was determined by V3 in both runs.

### 2.3 The MPS

The MPS as used for the spring '77 run (Run I) of E110 is shown in figures 2-2 and 2-3. Upstream beam proportional chambers (BA), and a bank of neutron counters along side V1 are omitted. The main features of the spectrometer were a 12.00 inch long liquid hydrogen target surrounded by a photon/charged particle veto system, a large superconducting analyzing magnet, multiwire proportional tracking chambers upstream of the magnet, proportional and spark tracking chambers downstream of the magnet, two large multicelled atmospheric pressure gas Cerenkov counters, various scintillation counters and a triggering system which used multiplicity signals from several of the proportional chambers.

A PDP-11/45 computer running the MULTI on line system (as modified and maintained for the MPS by the Indiana group) [Dz76b], collected the data, wrote it to magnetic tape, and provided simple diagnostics for monitoring the experiment. After each event, shift register (tag bit and pwc) and spark chamber (VTD scaler) data were read in through direct memory access (DMA) units, and phototube (CAMAC ADC) data were read in through a BDO-11 branch driver. CAMAC scalers were read before and after each beam pulse. Event and scaler data were initially stored on disk as a buffer, and then written on tape as time allowed, mainly between pulses. A single data tape could hold about 10,000 events.

Diagnostic functions were performed as time allowed, and included event displays of the spark and proportional chambers (without track finding), histograms of requested quantities, and end run summaries. The summaries were printed and written to tape after each run. A set of visual scalers were used as a backup for the CAMAC scalers, readings being recorded by hand after each run.

The coordinate system used for E110 had z along the nominal, or surveyed, beam line (spectrometer centerline), y vertical, and x horizontal. The origin was taken directly above a survey bench mark near the downstream end of V1.

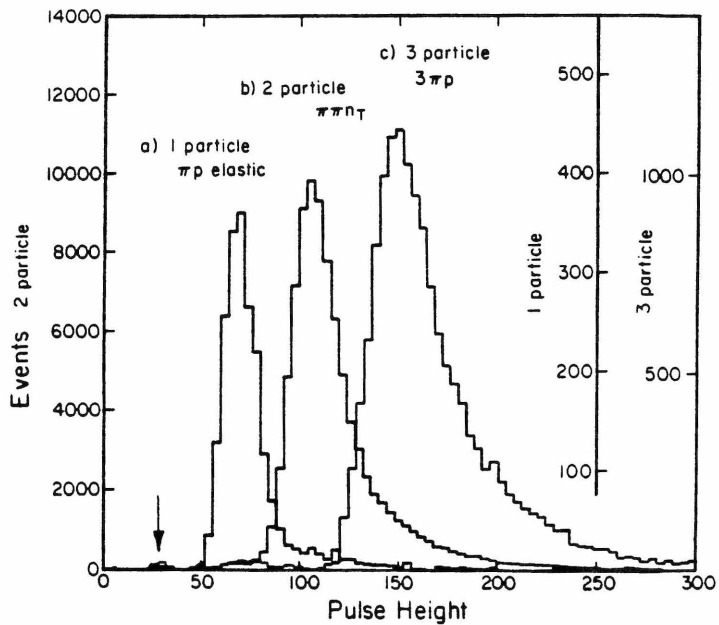


Figure 2-4. DEDX response for 1 to 3 particles. Data came from indicated triggers; only events of the desired topology were included. Arrow points to the ADC pedestal.

### 2.3.1 Beam and Interaction Counters

Beam and interaction definitions for the trigger electronics and scalers were made by five plastic scintillator counters, figure 2-2. Our beam was defined by a small three counter telescope, Sa, Sb, and Sc, located at  $z \sim -2.3$  m. Sa and Sb were thin 1" square counters ( $Sa = 1/8$ " thick,  $Sb = 1/16$ " thick). Sc was 2" square,  $1/4$ " thick and had a  $1/2$ " (x) by  $1/4$ " (y) hole. Sc rejected particles that missed the hole.

Interactions were detected by either pulse height in a thin counter, "DEDX", near the target, or by the absence of a signal in a veto counter, "2x2", downstream of the F station (both in coincidence with a beam particle). The DEDX counter  $8" \times 6" \times 1/16$ " (x,y,z) covered the exit of V1 and was viewed by two phototubes whose signals were added before discrimination and recording by ADC's. Figure 2-4 shows the DEDX response to 1, 2, and 3 particles. A two particle signal was used to indicate an interaction. The 2x2 counter was 2" square,  $1/4$ " thick, and viewed by a

single phototube (through a long light pipe to keep the phototube below the spectrometer fiducial volume). The phototube was attached to a motorized "table" which allowed easy adjustment of the counter location in x and y. The  $2 \times 2$  counter was aligned with the beam whenever the beam was retuned or the MPS magnet polarity reversed. For 175 GeV data, the  $2 \times 2$  counter was replaced by a 1" square counter to preserve our minimum  $p_t$  bias.

### 2.3.2 Target

Our liquid hydrogen target, figure 2-5, had a 12.0" long (room temperature) by 1.0" diameter flask made of .005" mylar, except for an upstream end made of Vespel with a .015" thick entrance window. The flask was supported by its fill and vent pipes which ran parallel to and below and above the beam, respectively. The flask, wrapped with 10 layers of .00025" aluminized mylar "super-insulation", covered  $-0.567 < z < -0.262$  meters. Temperature sensitive resistors monitored the liquid level (full/empty) of the flask. The hydrogen density is assumed to be the standard boiling point value of  $0.0708 \text{ gm/cm}^3$  with 1% error because the true pressure, temperature and bubble density are unknown.

The vacuum jacket shape and fill/vent pipe locations were dictated by the target location within V1. Proper aiming of the beam between the pipes was essential. The pipes were searched for by vertical and then horizontal beam sweeps across them, recording increases in reaction rates when they were hit. The midpoint between the pipes was determined in terms of the beam at the BB and A stations, and the beam counters, especially Sc, were then aligned with respect to this location to about  $\pm 1$  mm uncertainty.

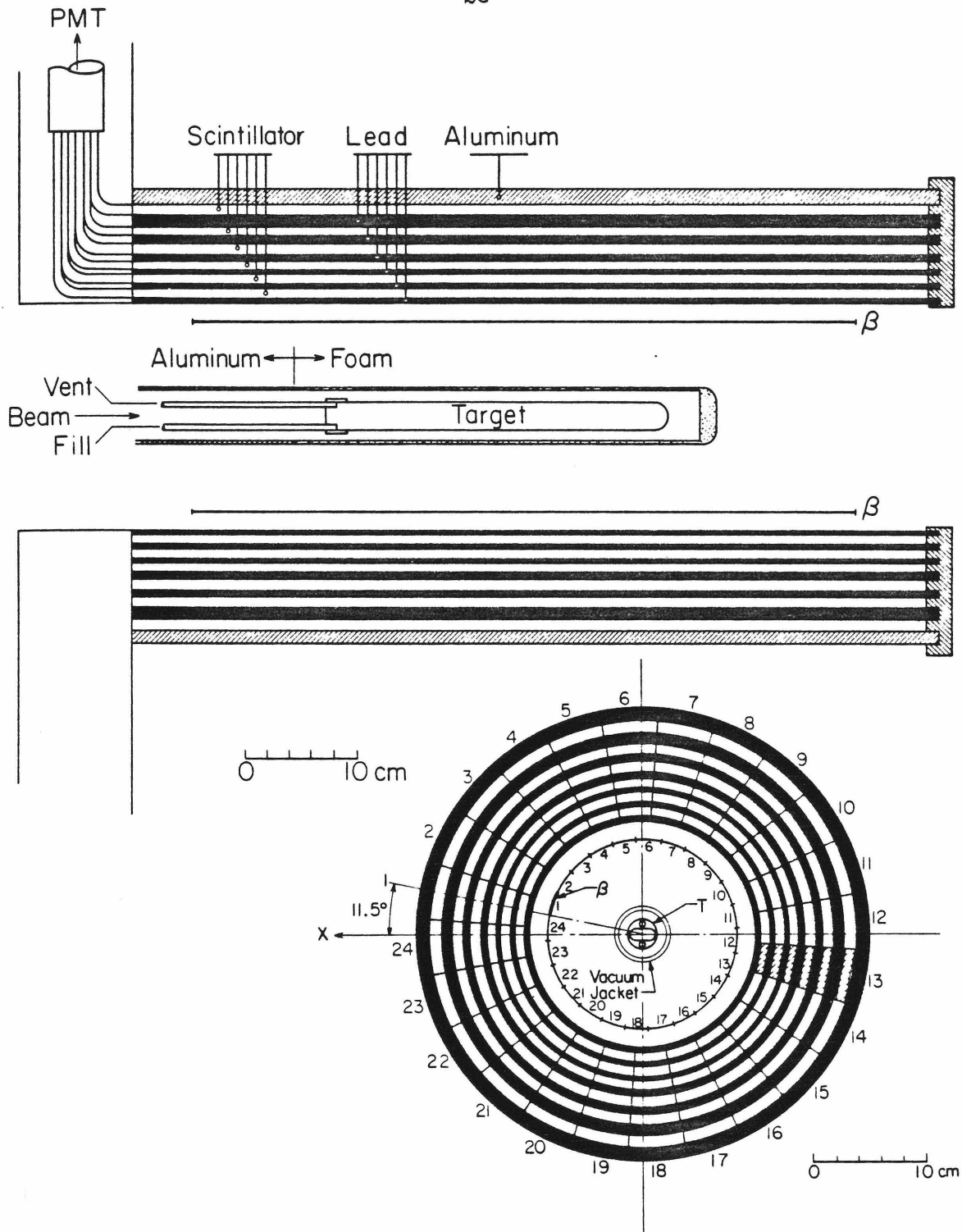


Figure 2-5. Side and front views of V1. Details of the target, vacuum jacket and counter orientation (surveyed at  $11.5^\circ$ ) are also shown. Signal cables for the  $\beta$  proportional chamber exit the front of V1. Numbered segments refer to tag bits for V1 and  $\beta$ . The  $\beta$  and V1 segments overlapped. In the trigger, a hit in any  $\beta$  segment turned off the two V1 segments behind it.

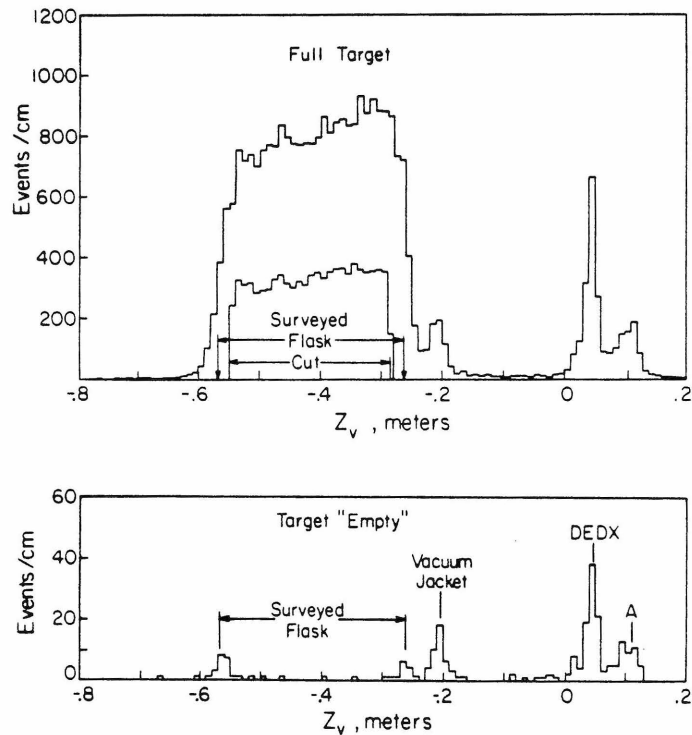


Figure 2-6. Vertex Distribution for the  $\pi\mu\mu_T$  trigger. 2-6a shows target full data for events written to PST's, (upper distribution) and for events satisfying essentially our full set of cuts (lower distribution). (The vertex cut shown is obsolete, but representative.) The lower figure is target "empty" data. Flask ends, the vacuum jacket, and nearby detectors are visible.

The small (1.0") diameter of the target flask was part of an effort to enhance the detection of recoil protons from  $\pi^- p \rightarrow K^0 K^- p$  and similar reactions. This effort also included a two inch diameter foam-mylar-glue low mass vacuum jacket .12 gm/cm<sup>2</sup> thick normal to the target (  $\sim 3 \times 10^{-3}$  radiation lengths). For structural reasons, the downstream end of the jacket was a 1/2 inch thick foam plug glued to the mylar end, about  $3 \times 10^{-3}$  radiation lengths thick. Upstream of the target flask, the jacket was a 1/8" thick, 2" diameter aluminum cylinder. The beam

entrance window was .005" mylar, about half a meter upstream of the target flask. Figure 2-6 shows the vertex distribution for  $\pi\pi n_T$  events. The vacuum jacket end cap is clearly resolved from the hydrogen flask. The shape of the vertex distribution results from a high rate of delta ray vetos, as discussed in section 4.8.

### 2.3.3 Target House, Forward Photon Detection

Surrounding the target and masking off all but the forward aperture through the magnet was a set of lead and plastic scintillator shower counters, V0, V1, V2 and V3, and a cylindrical pwc,  $\beta$ , figures 2-5 and 2-7. For  $\pi^- p \rightarrow \pi^+ \pi^- n$ , they were used to veto a large background of events with charged and/or neutral particles outside the magnet aperture.

The cylindrical  $\beta$  chamber, with 192 anode wires at a radius of 8.48 cm vetoed charged recoils. Interleaved pairs of wires were read out to the shift register giving 96 channels. A current division system using special amplifiers and CAMAC ADC's was included (to resolve which wire of a pair was struck) but was not needed for  $\pi\pi n$ , where  $\beta$  was used only as a veto. Groups of four consecutive shift register channels (8 wires) were fed to the trigger electronics for the veto. The sensitive length of the anodes was about 23.3 inches extending from  $z \approx -.670$  m. to  $z = -.076$  m. The cathodes were solid, the inner being thin and the outer being a .1 inch thick cylinder which provided the structural support for the chamber.

The main photon veto, V1 or the "Barrel," was cylindrical, figure 2-5, housing 24 counters and their 2" diameter RCA 6655 phototubes in a sealed nitrogen atmosphere (for target safety). Each counter had six 28" long, .25" thick fingers interleaved between lead cylinders of varying thickness. The fingers were radially tapered to insure close packing and were wrapped in optically graded aluminized mylar [Wa72] in a reasonably successful attempt to equalize light output along the finger length. Lead layer thicknesses were (from inner to outer) .135" (effective),

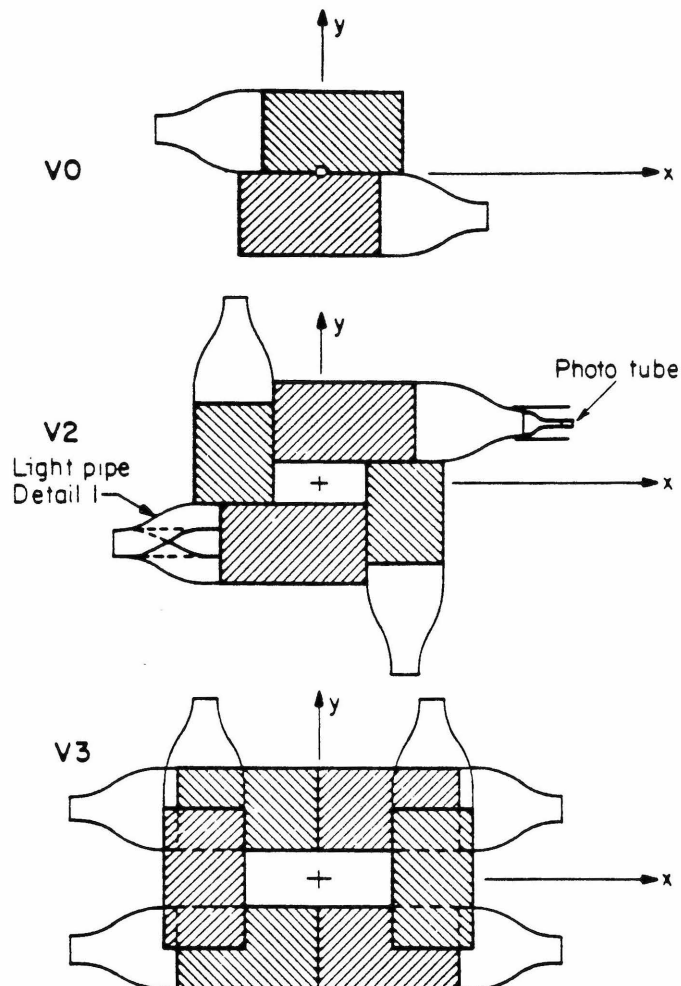


Figure 2-7. Jaw counters. V0 was upstream of the target and V1 was downstream, just after the A station. V3 was near the magnet.

.135", .135", .260", .260", and .385". The inner layer was actually a thin lead layer pressed onto a brass cylinder. The outer can of V1 was a half inch thick aluminum cylinder. The counter thresholds were set to  $\sim 1$  MeV, and gains were monitored with weak  $Bi^{207}$  sources glued to the light pipe ends directly in front of air gaps to the phototubes. A .003" mylar gas barrier covered the V1 exit.

The vetoes V0, V2 and V3, figure 2-7, collectively called the "Jaw" vetoes, had a total of 12 flat 14×25 inch counters. (Two counters in V2 were only 14×18 inches.)

Each was a layered sandwich of 6 lead and 6 scintillator sheets (both .25" thick) in a thin walled (.125") aluminum box. RCA 8055 phototubes (5" dia. cathode) were used. V0, upstream of the target, had a 1" diameter hole to allow for beam passage. V2 had four counters and a fixed aperture. V3, six counters, had an adjustable aperture, but this was kept fixed (along with the V3 location) during the entire run. In Run I, this aperture was set to mask off the magnet pole tips and rays traced to the magnet sides at its midpoint. For Run II, V3 was moved upstream of its Run I location somewhat, and the aperture adjusted. The vertical angular aperture was only slightly reduced, but the horizontal aperture for Run II masked off the entire magnet, including the downstream end. Jaw counter thresholds were set to 1/6 of the single muon pulse height. For this, beam stops relatively close to the MPS were closed to create a halo of muons about the beam line.

In Run I, shortly after the 50 GeV and first set of 100 GeV runs were made, one barrel counter, (B-8), failed with a short in the phototube base. Because of the danger of damaging other equipment, especially the target and  $\beta$  chamber, a group decision was made to not repair the counter, and we completed the run, including most of the 100 GeV data and all of the 20 GeV data, with only 23 barrel counters. A single barrel counter strike trigger,  $\pi\pi B$  was added to evaluate the background. As it turned out, this trigger was crucial for a neutron veto correction, but the loss of B8 had no noticeable effect on the veto house failure rate. B8 was repaired prior to Run II, and we had no further problems with the counter.

Between V2 and V3, we had a helium bag, figure 2-3, covering the  $K^0$  decay region of the Vee triggers. Its purpose was to reduce diffractive ( $3\pi$ ) backgrounds in the  $K^0\pi p$  trigger.

The electron modules and one hadron module (L1H) of the E260 calorimeters, figure 2-2, [see Ha75b] were maintained with increased phototube gains as a possible off line photon veto. The other hadron calorimeter modules were left

uninstrumented. At one point, the L1 electron and hadron modules were moved into the beam on curve through runs to measure muon and electron beam contamination, Section 2.2.1. Otherwise, the calorimeters were kept clear of the C2 entrance window, figure 2-2. This resulted in about half of each calorimeter being masked by the magnet flux return. We ultimately chose to not use the electron calorimeters as off line vetoes in the Run I data. However, preliminary studies indicated a reasonable sensitivity down to surprisingly low photon energies, and that if combined with a veto covering the rear of C2, we would have a viable off line veto setup for Run II. Also prompted by an extremely poor missing mass resolution at 175 GeV, a "lead wall" was added behind C2. The V3 aperture was reduced and the electron calorimeters were moved closer the beam. Also, the E111 photon detector [Ba80 and references therein] was installed behind C2 (mainly as a test for proposal P523, see chapter I). These adjustments gave us an off line  $4\pi$  veto coverage.

The lead wall covering the exit of C2 was roughly rectangular with dimensions 100" (x) by 80" (y). A single .75 inch layer of lead was backed by 20 horizontal scintillator counters (8.5" by 50" each) with 2 inch phototubes. Phototube signals were sent only to the ADC's. Since only one layer of scintillator was used, there was no active charged particle - photon discrimination and the lead wall could not be used as an active veto.

The E111 photon calorimeter was located just downstream of the lead wall. This calorimeter was a high resolution hodoscope with seventy 1.05 centimeter wide counters in x and seventy in y. Each counter had eight fingers along the beam direction interspersed between 6.4 mm thick lead layers, and the fingers from the opposite view counters. Since this calorimeter was to be used in P523 tests for  $\pi^0$  measurements, a hole matching the photon calorimeter size was left in the lead wall. The hole was actually about 140 cm in the x view, and had a movable lead cover to maintain veto coverage when the photon calorimeter was moved. This

occurred whenever we changed magnet polarities in Run II. The E111 counter was positioned along the MPS centerline with a slight offset in x so that the bent beam just missed the counter. Data from the photon calorimeter were read into ADC's adapted from E111 [Ba80], and buffered to the main on line computer with an LSI-11 micro computer and DMA access. Details of this are in Fredericksen's thesis along with the photon calorimeter analysis algorithms.

#### **2.3.4 Magnet**

The MPS analyzing magnet, figure 2-2, was a superconducting dipole with the flux return outside its large cryostat. Roughly a 48D48 dipole, the x-y aperture at the pole tips was 122 cm. (x) by 61 cm. (y). However, the distance between the upstream and downstream flux returns, was about 2.5 meters.

For this experiment we ran at full field,  $I_{mag} = \pm 180$  amperes giving  $\int B \cdot dl \cong 25 kG \cdot m$  for an effective  $p_x$  kick of  $p_K = .7510 \pm .0015 GeV/c$ . The main field was sufficiently uniform and fringe fields small enough that we could use a square field approximation for momentum analysis. However, the fringe fields did affect the y view pattern recognition, and vertical focusing corrections were applied in that view. A field map [Ha75, Ma78b], was used as input to these corrections, and for the acceptance calculations. During data taking, the field was monitored by recording the current before each run and at four hour intervals. Run by run  $K^0$  mass plots (from  $K^0\pi\pi X$  data) verified both the magnet stability and the field map.

#### **2.3.5 Spark Chambers**

Eight spark chambers were grouped behind the magnet in two stations, E and F, four chambers per station, figure 2-2. Except for a size difference, the E and F chambers were essentially identical in construction. An aluminum frame supported four planes of .005 inch aluminum wires at 32/inch. These were glued to G-10

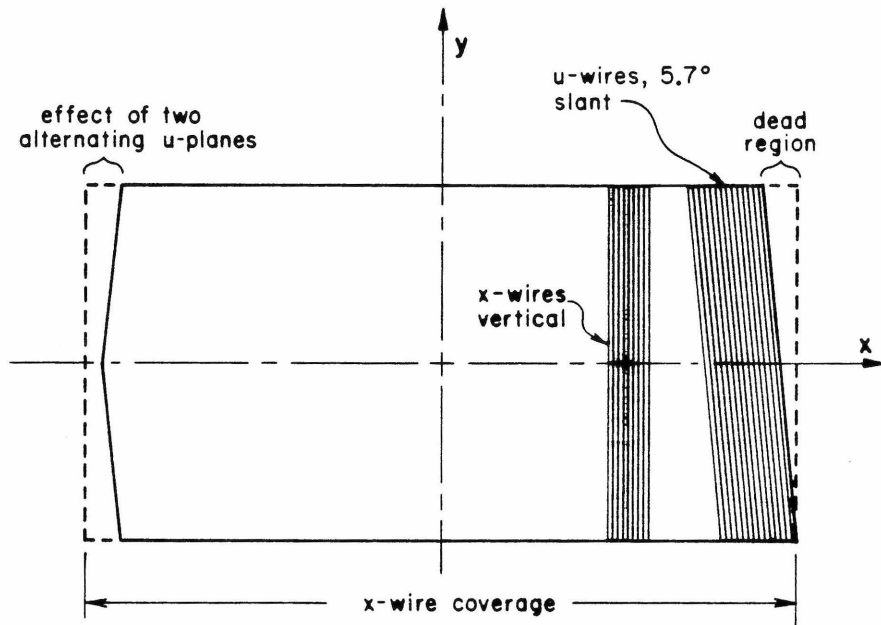


Figure 2-8. Spark chamber x-u plane. The u-cutoff was in all chambers, but was important only at the F station in Run II, where it set the fiducial volume limit, section 3.3.

boards attached to the frames. Active areas were  $\sim 2.4 \text{ m. (x)} \times 1.2 \text{ m. (y)}$  for the E-chambers and  $\sim 3.6 \text{ m. (x)} \times 1.8 \text{ m. (y)}$  for the F-chambers.

Each chamber measured x, u and y coordinates with two spark gaps, x-u and y-y, the u wires being inclined at an angle of  $\pm 5.7^\circ$  with respect to the x-wires, (four planes each way). As the chamber frames were rectangular, the slant u wires clipped off the edges of the x views a bit as shown in figure 2-8, reducing the regions where the x wires were fully sensitive to about 2.2 meters (Ex) and 3.2 meters (Fx). No plugs or intentional dead spots were installed in the chambers. The spark chamber gas, a mixture of 90% neon, 10% helium, and a trace of ethanol, was filtered through liquid nitrogen cooled traps and recirculated.

Spark chamber readout was by magnetostrictive wands with pickups and preamplifiers at each end, for a total of 48 signals. After discrimination each signal was digitized in time with a SLAC designed [Be72b] MTD scalar system running at 20

Table 2.3  
Spark Chamber Efficiencies  
Whole Chamber Average

Statistical Errors are all in Range .001 to .003

Chamber	Imag=-180	Imag=+180	Chamber	Imag=-180	Imag=+180
E1x	.910	.913	F1x	.926	.912
u	.938	.944	u	.939	.904
y	.930	.926	y	.828	.795
E2x	.939	.930	F2x	.680	.625
u	.921	.903	u	.772	.832
y	.909	.910	y	.675	.744
E3x	.918	.909	F3x	.881	.868
u	.916	.897	u	.819	.888
y	.918	.887	y	.629	.578
E4x	.877	.881	F4x	.892	.823
u	.890	.896	u	.902	.896
y	.940	.940	y	.926	.939

MHz. Up to 15 sparks per channel could be digitized with a .25 mm least count error; however, the position resolutions for each plane (after averaging the two pickups) was only  $\sim .7$  mm. for the E-chambers and  $\sim 1.0$  mm. for the F-chambers. Some saturation may have been present in either the pickup or main amplifiers, as evidenced by some residuals being slightly shifted with particle position.

High voltage pulses were produced by discharging coiled coaxial charge lines through thyratrons retired from use at SLAC. Each chamber had one such pulser, the eight pulsers being driven in parallel by a prepulser of similar design. Spark chamber dead times were initially set to 30 ms at the beginning of Run I, and improved to 20 ms about one third of the way through the data taking. During Run II, 10 ms dead times were quickly reached. The chambers had both pulsed, and d.c. clearing fields. Track memory times for the chambers were  $\leq 2\mu s$ .

Spark chamber efficiencies were  $\sim 90\%$  for the best chambers, Table 2.3 and Appendix D, but problems existed near the beam and some of the chamber edges. Track angles were large near the chamber edges and wand or amplifier problems might explain the efficiency loss. Near the beam, efficiencies were also poor and

sparks from "old" beam tracks could often be seen. Beam envelopes from curve through data are "pinched" slightly at the E-station, evidence that good and "old" sparks in the beam region were subject to merging. This probably contributed to the efficiency loss of some of the spark chambers near the beam. However, the poor efficiency regions were somewhat larger than the beam, probably meaning that spark formation and/or signal pickups also had problems.

### 2.3.6 Proportional Chambers

Sixteen multiwire proportional chambers (pwc's), with a total of 29 anode readout planes provided tracking data for the beam and secondary charged particles in front of the MPS magnet and supported the spark chamber tracking behind the magnet. Their properties are summarized in Table 2.4. Some of the pwc's were also used as hodoscopes to count particles for the trigger, section 2.4.

Construction techniques depended on the chamber. The B, D and F' chambers, had aluminum box frames, the BA, BB and A chambers had G-10 frames pressed into a sandwich by either G-10 (BA) or aluminum (BB,A) outer frames. The cylindrical  $\beta$  chamber was supported by its outer cathode, a .125" thick aluminum cylinder, and the magnet lining  $\Gamma$  chambers were basically an aluminum, foam and G-10 sandwich. Not all of the anode wires in some chambers (Bx, By, Dy, Dy', and Dx') were instrumented; but those that were covered the necessary apertures, so that except for a handful of dead channels, there were no holes in the pwc coverage.

The BA and BB stations gave the beam trajectory at the target. The BA station at  $z = -20.11$  m had two chambers each with x and y readouts. The BB station at  $z = -2.57$  m was one chamber with x, u ( $45^\circ$ ), and y readouts.

The A, B, and C stations tracked particles upstream of the magnet. The A station had six anode planes in two chambers, the first containing Ax1, Ax2 (staggered), Ay1 and Ay2. The second had slant ( $\pm 45^\circ$ ) planes Au, Av. The B and C

Table 2.4

Proportional Chamber Parameters

Type	Planes	Anodes <sup>(a)</sup>	Anode spacing	Cathode spacing	A-C gap		Anode Dia. <sup>(b)</sup>	Cathode Dia. <sup>(c)</sup>	Gas
					mm	mm			
BA	4	64	2.000	solid	6.9	20	solid	<i>ArCO<sub>2</sub></i> <sup>(d)</sup>	
BB	3	32	.977	solid	3.25	10	solid	<i>Magic</i> <sup>(e)</sup>	
<i>A</i> <sup>(f)</sup>	6	256	.977	.977	2.79	10	50	<i>Magic</i>	
B/C	5	512 <sup>(g)</sup>	1.954	1.06	6.86	20	100	<i>ArCO<sub>2</sub></i>	
D/F'x	5	320	4.618	1.599	9.53	50	100	<i>ArCO<sub>2</sub></i>	
F'y	2	130	6.350	1.599	9.53	50	100	<i>ArCO<sub>2</sub></i>	
$\beta$	1	192	1.837 <sup>(h)</sup>	solid	4.06	20	solid	<i>Magic</i>	
$\Gamma$	2	336	5.20	solid	8.0	20	solid	<i>Magic</i>	

notes: (a) total wires per plane including uninstrumented wires; (b) gold plated tungsten; (c) Wire cathodes: Be Cu alloy, solid cathodes either Aluminized mylar (BB,  $\beta$  inner) or Aluminum ( $\beta$  outer,  $\Gamma$ ); (d) 80% *Ar*, 20% *CO<sub>2</sub>*; (e) *Magic* Gas= 20% Isobutane, 4% Methylal, .5% Freon 13B1, balance Argon; (f) Ax1 and Ax2 share a cathode plane, so do Ay1 and Ay2; (g) 512 for x view, y view had 320 wires; (h) degrees.

stations had five planes, Bx', Bx, By, Cx, and Cy in three chambers. (Bx' was the odd man.) Bx', Bx and By were upstream of the magnet, while Cx and Cy were actually inside the magnet, just within the flux return (figure 2-3).

Lining the magnet sides were two chambers  $\Gamma_R$  and  $\Gamma_L$ , designed with current division electronics, that detected particles too soft to pass completely through the magnet. Very early in Run I,  $\Gamma_L$  failed with a broken wire. For the same reasons as with the B8 counter, we decided not to repair the  $\Gamma_L$  until after the run. These chambers were used in a "high mass"  $\pi\pi\pi$  trigger only, not the  $\pi\pi\pi_T$  trigger discussed here.

Table 2.5			
Proportional Chamber Efficiencies			
Whole Chamber Average			
Chamber	Chamber	Chamber	Chamber
Ax1	.898	Cx	.985
Ax2	.960	Cy	.980
Ay1	.947	Dy'	.893
Ay2	.963	Dx	.997
Au	.941	Dy	.991
Av	.918	F'y'	.950
Bx'	.951	F'y	.984
Bx	.987	Dx'(F'x1)	.867
By	.981	F''x(F'x2)	.953

Of the pwc's downstream of the magnet, only the D chambers, Dy, Dx and Dy', covered the aperture of the experiment. The four F' chambers, between the F-spark chambers and the C2 Cerenkov counter, supported beam region track finding, where the better time resolution of the pwc's was used to help distinguish good from "old" tracks in the spark chambers. The y chambers, F'y1 and F'y2, were between the F spark chambers and 2x2 counter. The x chambers F'x1, F'x2 (also referred to as Dx' and F''x for historical reasons) were hung from the front end of C2.

Whole chamber efficiency averages are given in Table 2.5, and position dependent efficiencies are plotted in Appendix D.

### 2.3.7 Shift Registers

The pwc readout system used preamplifiers located on each chamber (one preamp per wire) feeding a central 5921 element shift register through 200 ns long 50  $\Omega$  coaxial cables (RG174). Most of the preamps (including all those used in the trigger) were built by our group with a simple single transistor design as in figure 2-9. The preamps were grouped 32 to a card with the transistors in 5 RCA-CA3081

PWC PREAMP and SHIFT REGISTER

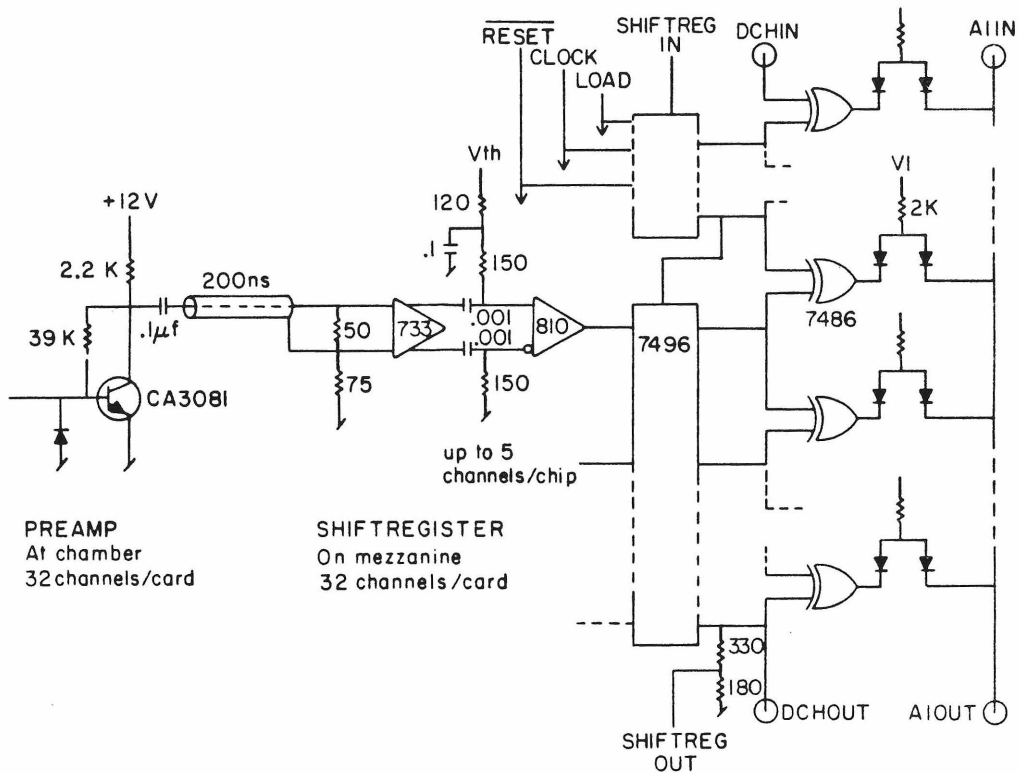


Figure 2-9. Shift register and pwc preamp. The signals SHIFTREG IN and OUT carried coordinate information, and the signals AIIN and AIOUT carried fast analog multiplicity information used for the E110 topological trigger.

chips. Except for the A-chambers, each preamp card fed a single shift register module. For the 1 mm wire spacing in the A-station, we read out alternate wires on both sides of the chamber and sorted the signals in four ended cables. The BA, Dy' and Dx' chambers used an older, more complicated preamp driving ribbon cables. The  $\beta$  and  $\Gamma$  chambers used special amplifiers located near the chamber which included analog outputs for current division analysis.

The shift register modules, figure 2-9, also built by our group, amplified, discriminated and, when in coincidence with a load pulse from the trigger

electronics, Appendix B, loaded the signals into the shift register. Upon loading, these signals were passed on to an analogue daisy chain in the same module. The daisy chain output current (AIOUT) was proportional to the number of "hits", or distinct groups of wires on a chamber that "fired". Reasonably fast multiplicity measurements, these outputs were the essence of our multiplicity trigger. In effect, the proportional chambers acted as thin hodoscopes.

A "hit" was any number of consecutive wires that fired. A single nonfiring wire was sufficient to separate two hits. About 5% of the time soft delta rays would cause two (or more) neighboring wires to fire in response to a particle. Because of the daisy chain design, the multiplicity logic was sensitive to only the number of hits, and not the total number of firing wires. This considerably lessened, but did not eliminate our sensitivity to delta rays in the pwc's. Only chambers used for the multiplicity trigger had their daisy chains fed to the multiplicity electronics.

If an interaction did not lead to spark chamber pulsing, the shift register, if loaded, was cleared with a fast reset pulse to await the next load. If a trigger occurred, shift register inputs were "clamped" during spark chamber pulsing to avoid spurious loads, and further shift register load pulses were suppressed while its contents were clocked into the on line computer via DMA access. The data recorded were the "width" and trailing "edge" of each group of firing wires, where "width" is the number less one of wires that fired in a group.

In addition to the pwc information, the shift register contained 144 "tag bits" (288 addresses). These recorded the condition (fire/not fire) of a large number of counters including the beam Cerenkov counters, the upstream photon veto counters (V1 to V3), and  $\beta$  chamber veto outputs; as well as recording which of our several pretriggers and triggers was responsible for the event.

### 2.3.8 Cerenkov Counters C1 and C2

Two large multicelled atmospheric pressure gas Cerenkov counters, C1 and C2 (figure 2-2), were used for secondary particle identification. A rather complete description of these counters is in Medinnis' thesis [Me80].

C1, between the E and F stations, was air filled with an index of refraction  $n - 1 = 2.9 \times 10^{-4}$ . It had a radiator length of 4 m and an active area of  $3.3 \times 1.5 \text{ m}^2$ . The counter had two rows of 11 mirrors each ( $4 \times 1.5 \text{ m}^2$ ) at  $z = 11.5 \text{ m}$ ; however, for this experiment only the inner 18 mirrors were instrumented. The mirrors were  $Mg F_2$  coated aluminized mylar backed by 3 cm urethane foam. Each mirror was viewed by a 5" phototube (either RCA 4522 or RCA 8854) with light collection by an ellipsoidal cone.

The entrance window was  $250\mu$  mylar followed by two sheets of  $100\mu$  black polyethylene. The exit window was  $500\mu$  aluminum except near the beam where it was mylar and polyethylene as in the entrance window. (Opaque diaphragms used in E260 to isolate the inner six cells, were removed for E110.)

Table 2.6		
particle	C1	C2
$\pi$	5.8	12.7
$K$	20.5	45.1
$p$	40.0	85.7

C2, behind the F station, was filled with a helium-air mixture with an index of refraction  $n - 1 = 6 \times 10^{-5}$ , corresponding to about 90% helium and 10% air. This was checked every four hours by comparing gas samples taken from C2 against pure helium in a small laser interferometer. C2 had a radiator length of 8.4 m. and an active area of  $4.0 \times 2.1 \text{ m}^2$  at  $z = 23.6 \text{ m}$ . It had 16 aluminized Lucite mirrors (.6 mm thick in two rows of 8) with  $Mg F_2$  overcoats. These directed light toward RCA 4522 phototubes via paraboloidal ("Winston") cones. The phototubes were protected

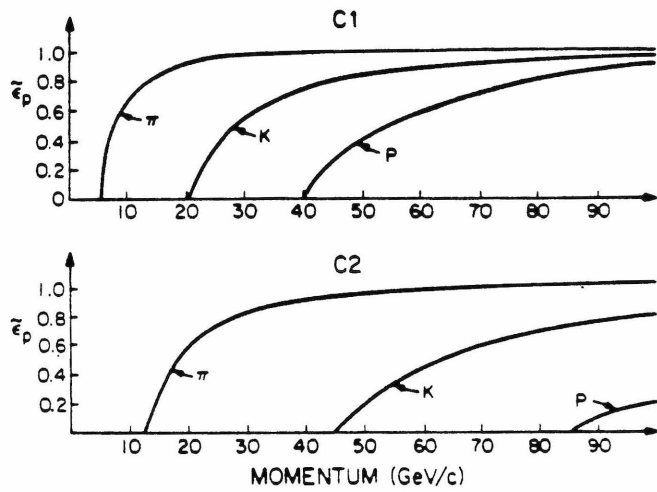


Figure 2-10. Ideal Cerenkov light yields normalized to 1 (see equation 2.1) as a function of momentum. In practice, pulse height analysis in threshold regions was of limited use.

from helium poisoning by quartz windows glued to the cones, a  $1/16''$  gap between windows and photo cathodes, and continuous flushing of the gas volume about the tubes with  $CO_2$ . The C2 entrance and exit windows were similar to C1's, although the exit window had no low mass region near the beam. Both counters were painted black on the inside to minimize reflections, and prior to E110, the C2 mirrors were refurbished at UCLA and reinstalled by M. Medinnis.

C1 and C2 outputs were capacitively coupled to the ADC's to eliminate a 60 cycle ripple, and loaded with an 85 ns gate. Pedestal slewing on high rate tubes was observed, but all attempts to eliminate it with or without the capacitors were unsuccessful.

Table 2.7 lists the  $\beta = 1$  photoelectron yields  $\langle N \rangle$  for C1 and C2 found [Da78], using  $\pi\pi n$  data. Where possible, one counter was used to tag pions for the other, and corrections for finite particle momenta and K contamination of pedestals have

been included. The momentum correction factor was

$$1/\varepsilon = (1-1/n^2)^{-1}(1-1/n^2\beta^2), \quad (2.1)$$

the relative yield of Cerenkov light as a function of  $\beta$  and is shown in figure 2-10, which also illustrates the counter thresholds (Table 2.6). The results for cells 2 and 13 are admitted "guesses" [Da78].

Table 2.7							
Mean Photoelectron Yields $\langle N \rangle$ , $\beta = 1$							
C1				C2			
Cell*	$\langle N \rangle$	Cell	$\langle N \rangle$	Cell	$\langle N \rangle$	Cell	$\langle N \rangle$
1	-	12	-	23	3.0	31	2.7
2	5.0	13	5.0	24	4.0	32	2.9
3	6.5	14	3.9	25	5.5	33	5.3
4	6.7	15	6.2	26	3.2	34	2.9
5	5.9	16	6.9	27	6.4	35	4.3
6	13.1	17	4.7	28	4.4	36	3.9
7	6.9	18	5.8	29	3.5	37	2.7
8	6.8	19	5.9	30	2.8	38	2.1
9	4.4	20	3.7				
10	10.0	21	2.7				
11	-	22	-				

\* Cells 1, 11, 12 and 22 were not instrumented.

## 2.4 Triggers

The E110 topological trigger was based on counting hits in several of the proportional chambers to assess the forward multiplicity. The  $\beta$  chamber, Barrel and Jaw counters were also used, as well as the DEDX and  $2 \times 2$  counters. Appendix B discusses in detail the trigger electronics, gives diagrams, and lists multiplicity requirements for all the triggers used. This section only reviews essentials in the context of the  $\pi\pi n_T$  trigger.

The trigger sequence began with the arrival and interaction of a beam particle at a time when the trigger electronics was "live", that is, not processing a previous trigger candidate or during data read in. Only particles satisfying

$$BEAM = S_a \cdot S_b \cdot \overline{S_c} \cdot BEAMGATE \quad (2.2)$$

were counted as "beam". An interaction was flagged by either no signal from the  $2 \times 2$  or a two particle signal in the DEDX counter (we use + for logical "or").

$$INTBM = IB_{2 \times 2} + IB_{DEDX} \quad (2.3a)$$

$$= (BEAM \cdot \overline{2 \times 2}) + (BEAM \cdot DEDX \geq 2). \quad (2.3b)$$

If these conditions were satisfied during the trigger live time, the electronics then checked that we had only a single beam particle within the pwc time resolution about the beam particle in question, that no previous interactions had occurred within the last microsecond, and that the photon veto counters were ready prior to the beam particle arrival. The above checks did not include the spark chambers. If a preset 20ms spark chamber dead time had not expired by the time the trigger electronics had declared a trigger based on the charged topology, the electronics were simply reset and started again. Thus not all triggers were recorded on tape. For normalization, we consider the recorded events a random sample of the actual triggers. With the interaction, the pwc shift registers were loaded, and their daisy

chain electronics provided multiplicity outputs which were analyzed for agreement with any of our several trigger topologies. If a topology requirement was satisfied, and if the spectrometer readiness checks were passed, we had a trigger.

Multiplicity measurements used the Ax2, Ay2, Au, Bx, By, Cx, Cy, Dx, Dy,  $\beta$ ,  $\Gamma_R$  and  $\Gamma_L$  chambers, with the DEDX counter providing limited (by Landau fluctuations) information for some triggers. Several groups of chambers, A, BCD, BC, BCD',  $\Gamma$ , and "special D" were defined to measure multiplicities at various locations by voting among the chambers in each group. In the absence of delta rays, a charged particle from the target would provide a single hit in most of the chambers it passed through.  $K^0$ 's decaying between the A and B stations were be detected by a change of two in the multiplicity between A and B.

For a given chamber, the multiplicity measurement was made with "daisy chain receivers" (DCR's) and "Window Discriminator Units" (WDU's) designed by our group, see figure B-4a in Appendix B. The DCR's shaped daisy chain outputs (AIOUT, see figure 2-9) from the shift registers, passing them along to the WDU's. DCR outputs were proportional to the number of hits in the chamber feeding them. WDU's contained several independent pairs of discriminators. Each pair tested preset minimum and maximum hit requirements and output a fixed pulse height if both were satisfied. The Ax = 2 requirement was a special case set up as at least 2 hits and less than 3 hits. WDU outputs for the various planes in a given requirement were linearly added and then discriminated in "Majority Logic Units", also designed by our group. These units gave a NIM standard output pulse if the total height of the input pulse was above a preset level. Thus, an A-station requirement of 2 hits in at least 2 of 3 planes was satisfied by any two of the WDU's for the A-station sending pulses to a Majority Logic unit set to require at least two pulse height units, figure B-4a. The NIM pulses were fed to standard Lecroy fast coincidence units along with pulses from other units and the veto counters to form the trigger for a given

topology, figure B-5.

The stiffness of each trigger was determined by the goals for the reaction, its cross section compared to potential backgrounds, and our willingness to lose good events to suppress them. Some compromises (reflecting the survey nature of the experiment) were also made to adjust live times. Delta rays, chamber inefficiencies, electronic noise and close tracks can all distort multiplicity measurements. For  $\pi\pi n_T$ , the biggest worries were considered to be reactions involving recoil  $N^*$ 's decaying to  $\pi^0 n$  or  $\pi^- p$ , which called for photon vetoes; low-t  $\pi\pi$  scatters, which called for use of the  $2\times 2$  veto; elastic scatters with accompanying delta rays in the pwc's; and three particle (diffractive) events with two particles unresolved by several chambers.

The last two effects caused us to set up particularly stiff forward multiplicity requirements for  $\pi\pi n_T$ , demanding exactly two particles at both A and BCD with only slight concessions for chamber efficiencies and delta rays, and expecting losses from these effects. Losses from close tracks merging in one view was another price of the trigger. We required two of three A chambers (Ax2, Ay2, Au) to have exactly two hits, "A(2)2/3", and five of the six BCD chambers (Bx, By, Cx, Cy, Dx and Dy) to have exactly two hits, "BCD(2)5/6".

The other  $\pi\pi n_T$  requirements were  $\overline{2\times 2}$ ,  $\beta=0$ , and all 12 Jaw counters and the 24 barrel counters have no hits, figure B-3. A  $\beta$  chamber inhibit existed on the barrel veto, but this was covered by the  $\beta = 0$  condition. The Barrel and Jaw requirement was called BRINHJAW = 0, to emphasize the  $\beta$  inhibit which turned off the two barrel counters behind any of the 24  $\beta$  sections that registered a hit. The  $\pi\pi n_T$  final trigger requirement was thus

$$Trig = \overline{2\times 2} \cdot (BRINHJAW=0) \cdot (\beta=0) \cdot (A(2)2/3) \cdot (BCD(2)5/6). \quad (2.4)$$

Our trigger selected only the topology of the event, not the types of the particles involved. Thus the  $\pi\pi n_T$  trigger included data from reactions such as  $K^-p \rightarrow K^-\pi^+n$ ,  $\bar{p}p \rightarrow \bar{p}\pi^+n$ ,  $\pi^-p \rightarrow K^+K^-n$ , and  $\pi^-p \rightarrow \bar{p}pn$ , as well as "junk" such as  $\pi e \rightarrow \pi e$  (at relatively high  $t$ ),  $\pi^-p \rightarrow \pi^-\pi^+\pi^0n$  where the  $\pi^0$  can come from either the upper or lower vertex (see figure D-1), and at a reduced level, some diffractive and delta ray induced events.

Except for alignment (curve through) and test runs, we had ten triggers operating simultaneously. Five of these,  $\pi\pi n_T$  (the subject of this thesis),  $K^0\pi p$ ,  $K^0\pi\pi X$ ,  $K^0K^0 X$ , and  $\pi\pi n_H$  ("high mass"  $\pi\pi n$ ) were considered major "physics" triggers. The other five,  $\pi p$  (elastic),  $3\pi p$ ,  $\pi\pi X$ ,  $\pi\pi n_P$  ( $\pi\pi n$  "paddle"), and IB (interacting beam) were background or calibration triggers, and were "prescaled" to preserve live time for the main triggers. As a result of a run plan change shortly after the Run I 50 GeV running, the  $\pi p$  and  $\pi\pi n_P$  triggers were removed and pre-scale factors for the other background triggers were adjusted to permit more live time for the major triggers. Late in Run I,  $\pi\pi B$  ( $\pi\pi$  "Barrel", section 2.3.3) which *required* exactly one barrel counter hit, but was otherwise the same as  $\pi\pi n_T$ , was added. In Run II we also had a  $\pi^-p \rightarrow \pi^0n$  charge exchange trigger.

## 2.5 Beam Momentum, Resolution

Ultimately, the source of all our various resolutions such as momentum, mass,  $t$ , missing mass, angle, and vertex, are the position measurement resolutions, locations of the various tracking chambers, and the material in the spectrometer. A detailed event simulation can, in principle, determine all relevant resolution parameters. However, most were measurable directly from data, although in some cases, their dependences on variables such as  $m_{\pi\pi}$  were not. Most variations, however, can be estimated from relatively simple formulae. The main exceptions are the  $\cos\theta_J$  and  $\varphi_J$  resolutions, and we used a simple simulator based on our acceptance Monte

Carlo for them. The simulation was checked with measured resolutions, and results were consistent with measurements. We prefer to use measured numbers for our claims wherever possible. We group in this section our  $100\text{GeV}/c$  resolution results. Kinematic symbols are defined in Appendix A.

Average track angular resolutions, in milliradians, are given in table 2.8.

Table 2.8	
Average Track	
Angle Resolutions	
View	$\sigma, \text{mR}$
Beam x	.033
Beam y	.034
After x	.086
After y	.097
Before x	.138
Before y	.155

In the table, before and after refer to upstream and downstream of the MPS magnet.

The momentum resolutions observed in curve through data at 20, 50, and 100 GeV are summarized by

$$\Delta p/p = \frac{.001p}{p_K} \sqrt{.037 + 8.60/p^2}. \quad (2.5)$$

The multiple scatter term  $(8.6/p^2)$  is only noticeable at low momenta. Ignoring it gives  $\Delta p/p = .00026p$ . This improvement over E260 (.0007p) came from increasing both the magnet  $p_K$  and front end lever arm.

The missing mass resolution was determined in a series of fits to the neutron missing mass spectrum. Neutron  $Mx^2$  plots, such as figure 1-3, indicate an average resolution,  $\sigma_{Mx^2}$ , of about  $2.5 (\text{GeV}/c^2)^2$  at  $100\text{GeV}/c$  beam momentum. The neutron peak after  $\pi\pi X$  subtraction is consistent with a Gaussian with event configuration dependent resolution. A quadratic expression using the variable

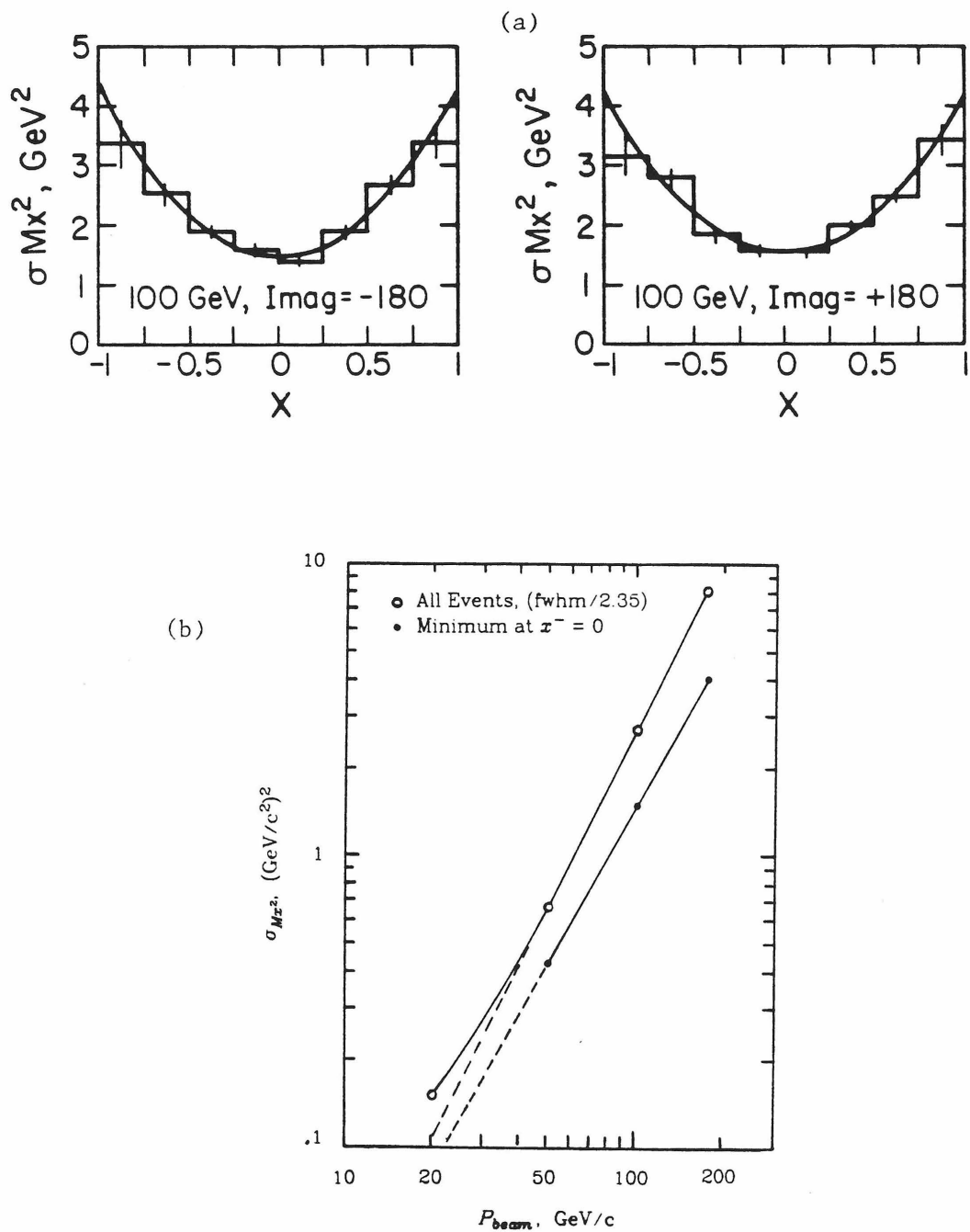


Figure 2-11. Neutron missing mass squared resolution. In (a)  $\sigma_{Mx^2}$  is plotted against  $x^-$  at 100  $\text{GeV}/c$ . Part (b) shows the beam momentum dependence of the minimum  $\sigma_{Mx^2}$  and average resolutions. These averages ("all events") follow a  $P_{\text{beam}}^2$  dependence above 50  $\text{GeV}/c$ .

$$x^- = (E^- - E_b/2) / (E_b/2) \quad (2.6)$$

where  $E^-$  is the forward  $\pi^-$  lab energy, and  $E_b$  is the beam pion energy, adequately describes  $\sigma_{Mx^2}$ . Background subtracted neutron missing mass distributions were fit to a Gaussian form in eight  $x^-$  bins from -1 to +1. The resolution, as a function of  $x^-$ , see figure 2-11a, was then fit to a quadratic function with the result

$$\sigma_{Mx^2} = (1.49 \pm .05) + (-.007 \pm .10) (x^-) + (2.67 \pm .20) (x^-)^2 \text{ (GeV/c}^2)^2. \quad (2.7)$$

at 100 GeV/c. Within our statistics, we found no magnet polarity or real  $\pi\pi$  mass dependence of the  $Mx^2$  resolution. (An apparent  $m_{\pi\pi}$  effect reflects the  $x^-$  dependence folded with changing decay  $\pi\pi$  angle distributions.) Figure 2-11b shows the beam momentum dependence of  $\sigma_{Mx^2}$ .

The fits that produced figure 2-11a and equation 2.7 also gave the beam momentum measurement, and evaluated an alignment kink (sections 3.2 and C.7) between the upstream and downstream sides of the MPS magnet. Our best beam momentum estimate (found by forcing the mean neutron mass to its accepted value of .93957 GeV/c<sup>2</sup>) is

$$P_{beam} = 100.05 \pm .04 \pm .10 \text{ GeV/c.} \quad (2.8)$$

The first error is the statistical fit error and the second one is the rms spread from a .8 inch momentum slit setting, section 2.2.

We have about 5800 examples of  $\pi^-e^- \rightarrow \pi^-e^-$  in the  $\pi\pi n_T$  data. While an easily removed background (just a total charge test), this reaction was extremely useful for resolution measurements. Being an elastic scatter (off an atomic electron), the kinematics are well defined and give a maximum electron energy of 85 GeV for a 100 GeV/c beam. For this reaction C1 and C2 are useless. This is dealt with by evaluating the  $\pi e$  mass for both possible particle assignments. The resulting  $\pi e$

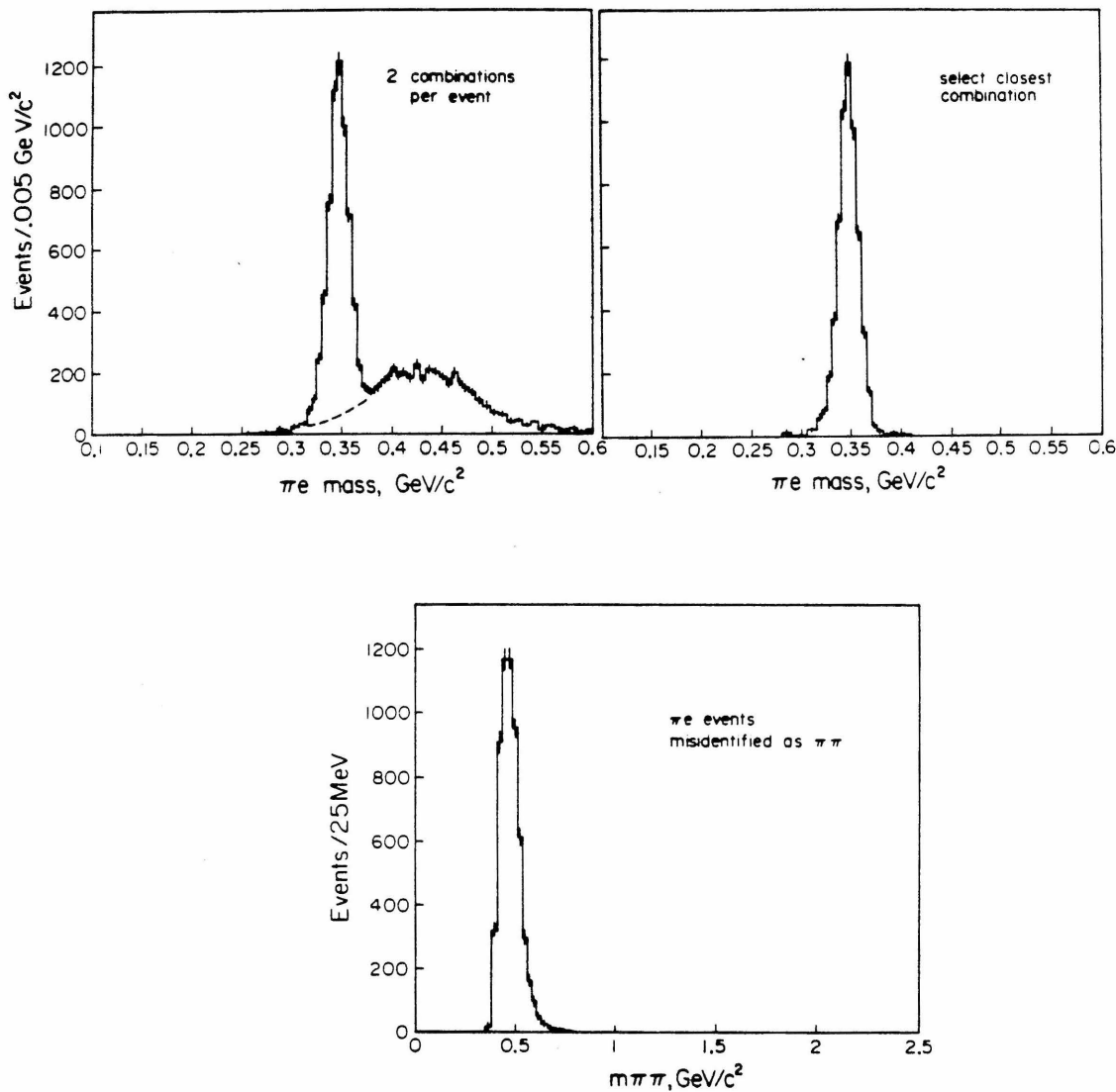


Figure 2-12. Pion electron scattering data. The events in 2-12b were used for  $t_{pn}$  resolution estimates. The same events when plotted as  $\pi\pi$  yield 2-12c.

mass distribution is shown in figure 2-12a. A very nice  $\pi e$  peak is seen, along with a mush resulting from wrong assignments. For our purposes, simply selecting the combination closest to the nominal  $\pi e$  mass or  $\sqrt{s}$  of the scatter, is acceptable, figure 2.12b. The width of the  $\pi e$  peak gives a forward mass resolution estimate of  $11.3 \pm 1$  MeV/c<sup>2</sup>. This resolution is applicable to any forward system with total

momentum near 100 GeV/c, vertex in the hydrogen target, and opening angles similar to those of the  $\pi e$  reaction. Figure 2-12c shows the " $\pi\pi$ " mass for the  $\pi e$  data, and indicates that this resolution maps to  $\pi\pi$  masses of about .47 GeV/c<sup>2</sup>. This compares favorably with the  $K^0$  mass resolution of  $\sigma(m_{K^0}) = 16 \pm 1$  MeV found in our  $K^0 K^\pm \pi^\mp X$  analysis [Br80]. The  $K^0$  momenta averaged about 30 GeV, but they decayed between the A and B stations.

Equation 2.5, the data in Table 2.8, and the approximate form  $m_{12} = \sqrt{p_1 p_2} \theta$  can be used to estimate the mass dependence of  $\sigma(m_{\pi\pi})$ . The form for  $m_{12}$  assumes massless decay products and a small lab opening angle  $\theta$ , but is adequate for the present purpose if we expect only to get  $d\sigma(m)/dm$  from it. Taking extreme cases for the effect of  $p_1$  and  $p_2$ , we have  $d\sigma_m/dm = (4.1 \pm 8)$  MeV/GeV. The large error covers nonlinearities expected in the resolution, and tying this onto the estimate at  $m_{\pi\pi} = .47$  GeV, we have

$$\sigma(m_{\pi\pi}) = (11.3 \pm 1) + (4.1 \pm 8)(m_{\pi\pi} - .47) \quad (2.9)$$

where the resolution is in MeV/c<sup>2</sup>, and  $m_{\pi\pi}$  is in GeV/c<sup>2</sup>. Both the  $\pi e$  and  $K^0$  masses give estimates of the systematic forward mass error. These estimates are 3 MeV and less than 1 MeV respectively.

Another important feature of the  $\pi e$  reaction is that since all final particles are observed (and the target electron was at rest),  $P_t = 0$ , where  $P_t$  is the transverse momentum of the forward  $\pi e$  pair measured with respect to the beam pion. We thus get a measurement of the  $p_t$  resolution, and hence the  $t_{pn}$  resolution for  $\pi^- p \rightarrow \pi^+ \pi^- n$ . To good approximation, the  $p_t$  resolution is constant, and also to a good approximation (especially when the recoil neutron mass is poorly measured) we can estimate  $t' = t_{pn} - t_{\min} = -p_t^2$ . This form implies that  $\sigma_t = 2\sigma_{p_t} \sqrt{|t'|}$ , and that  $\sigma_t = 0$  at  $t' = 0$ . Including a small zero point error gives

$$\sigma_t = \sqrt{\sigma_{t_0}^2 + 4|t'| \sigma_{p_t}^2} \quad (2.10)$$

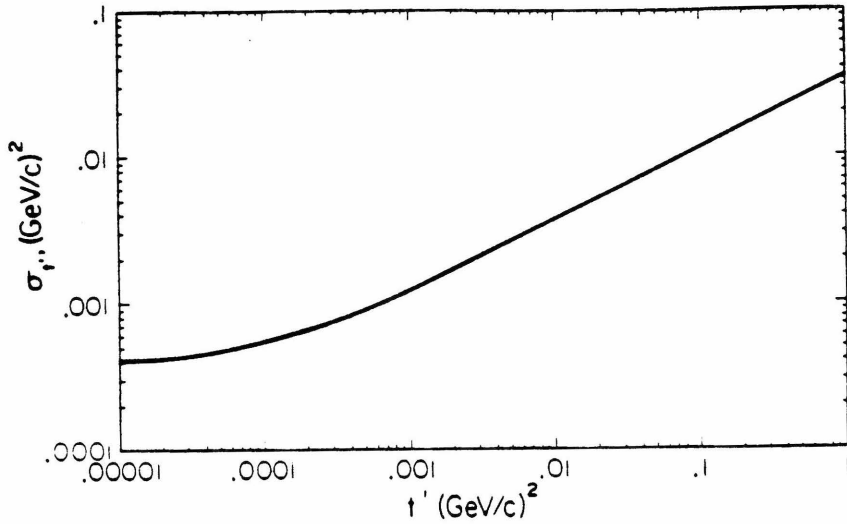


Figure 2-13.  $t_{pn}$  resolution estimate from equation 2.11.

For spectrometers of our type, this form is well born out at even moderate  $t_{pn}$  [Gr74]. Both parameters of equation 2.10 are available in  $\pi e$  scattering if we take  $\sigma_{p_t} = \langle P_t \rangle$ , and  $\sigma_{t_0} = \langle |t| \rangle = \langle P_t^2 \rangle$ . These values are  $\langle P_t \rangle = .018 \text{ GeV}/c$  and  $\langle P_t^2 \rangle = .00041 (\text{GeV}/c)^2$  so that our  $t$  resolution is (figure 2-13)

$$\sigma_t = \sqrt{1.7 \times 10^{-7} + 1.30 \times 10^{-3} |t'|} . \quad (2.11)$$

This equation applies at  $m_{\pi\pi} = .47 \text{ GeV}/c^2$ , but  $\sigma_t$  increases less than a factor of two from  $m_{\pi\pi} = .5$  to  $2 \text{ GeV}/c^2$ . The  $P_t$  measurements also give an estimate of our systematic  $p_t$  error resulting from alignment differences between the beam and MPS front end. The average  $P_t$  components were  $\langle P_{tx} \rangle = -.00125 \pm .002 \text{ GeV}/c$  and  $\langle P_{ty} \rangle = -.00218 \pm .002 \text{ GeV}/c$ . These errors are negligible. (The x-y difference reflects mistakes in setting up the BAY and AY chambers. Both had two y planes which were meant to be staggered but weren't. This was corrected for Run II. The x view planes were staggered.)

The above claims are consistent with results from a Monte Carlo study which used the track angle resolutions of Table 2.8. This study also gave us resolution estimates for  $\cos\theta_J$ , and  $\varphi_J$ , the Gottfried-Jackson frame  $\pi\pi$  decay angles. The  $\cos\theta_J$  resolution depends slightly on  $m_{\pi\pi}$ , falling from .03 to .01 between the  $\rho^0$  mass and 2.5 GeV/c<sup>2</sup>. The  $\varphi_J$  resolution was seen to be independent of mass, but  $t_{pn}$  dependent. At  $t_{pn} = -0.01 \text{ GeV}^2$ , it was 7° and at  $t_{pn} = -0.10$  it was 3°. At  $t_{pn} = t_{\min}$ , the  $\varphi_J$  resolution diverges since the neutron azimuth is indeterminate, but  $d\sigma/dt$  is falling below  $t_{pn} = -m_{\pi\pi}^2$ . The 7° estimate is an effective upper limit.

Figure 2-14 plots the vertex resolution,  $\sigma_z$ , against the  $\pi\pi$  mass. The observed mass dependence of  $\sigma_z$  reflects changes in laboratory opening angle distributions as the mass increases. The vertex errors in the figure are those reported by TEARS (section 3.2) with an additional factor of 1.5 applied. This factor was determined in vertex distribution fits with a series of  $\sigma_z$  cuts, figure 2-15, and is good to 10% of itself. This underestimate has been traced by Bromberg to a missing term in the vertex routines which had no effect beyond the error estimate. Our vertex routines have been compared against another fitter [De80] and found to be highly efficient and, within the adjusted errors, accurate. Because of the dependence seen in figure 2-14, no cut on  $\sigma_z$  was used. The TEARS vertex routines are described in Appendix C.

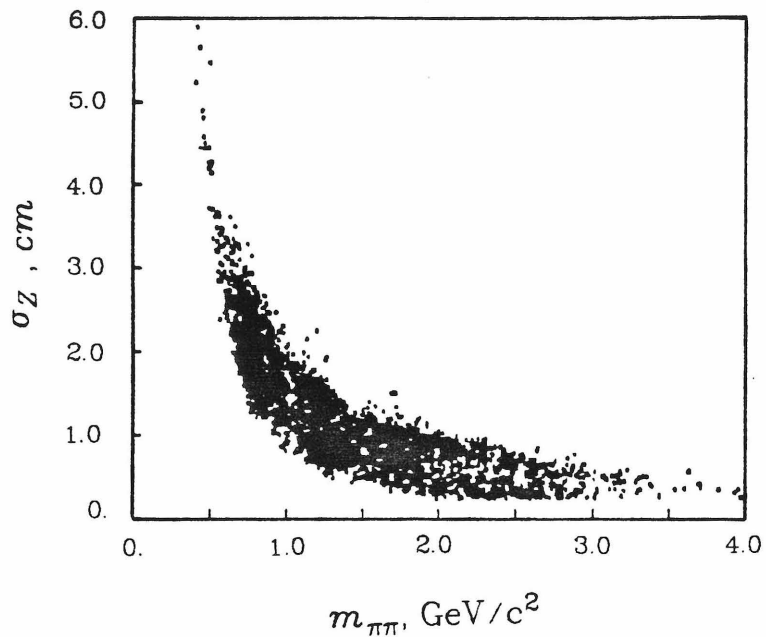


Figure 2-14. Vertex resolution versus  $\pi\pi$  mass at 100  $\text{GeV}/c$ . The resolution scale includes the correction of figure 2-15.

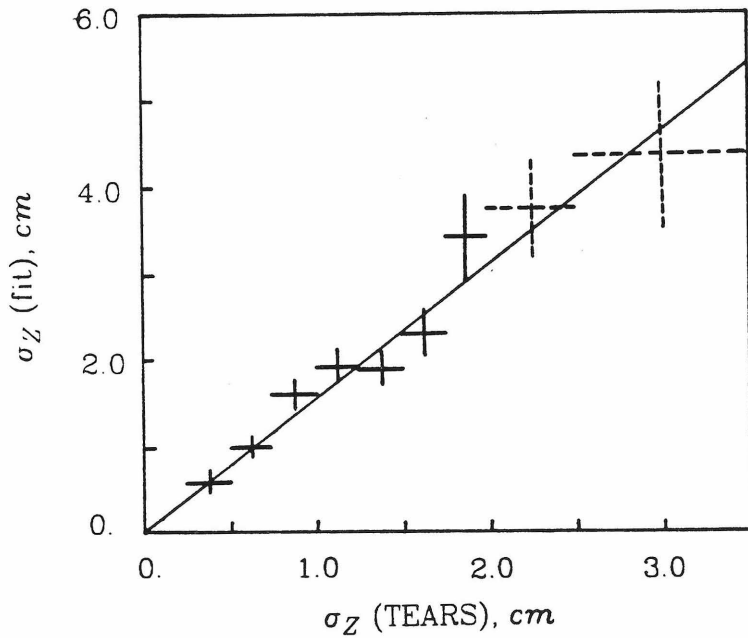


Figure 2-15. Vertex resolution scale adjustment. Even with the larger resolution estimate, vertex feed out losses (section 3.3) were negligible.

## Chapter III

### Event Reconstruction, Scaler Analysis

#### 3.1 Introduction

This chapter reviews our track finding analysis and the selections used to extract  $\pi^-p \rightarrow \pi^+\pi^-n$  events from the  $\pi\pi n_T$  trigger data.

The data processing went through several levels, DST, CST, PST, and CPR, each distinguished by the amount of data retained on each event, and the number of events kept. DST's, or data summary tapes, were the result of a track finding analysis on raw data with the program TEARS [Fo75]. DST's were actually 1600 bpi copies of 800 bpi raw data tapes with the track, momentum, and vertex results appended to each event. Although based on the program used for E260, E110 TEARS had substantial differences from the E260 version. For E110, TEARS was optimized for low multiplicity events and the algorithms for tracking upstream of the magnet bear little resemblance to those used in E260. DST's served mainly as a way station, holding tracking results enroute to more manageable formats with which data handling and physics analyses were more efficient. About two hundred DST's were needed to hold the Run I data.

From DST's, compressed summary tapes, or CST's, were created by removing all raw data records. Simplified format copies of the ADC, tag bit, and pwc shift register were included, but all spark chamber data was removed. Only results for matched tracks, and only the results of one of two independent before magnet analysis systems was included. Flags on the CST's recorded chamber responses (hit/no hit) for each good track. The CST format was compatible with all the triggers, and even allowed us to repeat the front end tracking at one point with some improvements to TEARS, without needing to recreate DST's.

CST's were split by trigger. The selection required only that the appropriate trigger tag bit be on. Hence no events were lost because of multiple trigger bit firing. This was allowed by the triggers, some of which overlapped. For  $\pi\pi n$ , CST's were used mainly for correction factor development, and performing Cerenkov counter analyses. Beyond the trigger splitting, no events were cut from the CST's. For Run I twenty 6250 bpi CST's were needed, five each for the three major triggers, and five more to hold the other triggers.

PST's, or physics summary tapes, had a format specialized to the two body topology of  $\pi\pi n$ . Scaler and some tag bit data were the only remnants of raw data on the PST's. The PST track data covered only the two good vertex particles, and only enough information was retained to make fiducial cuts, evaluate weights, and do kinematic analyses. At this level, we evaluated all event by event corrections, using factors developed with CST's, and performed our full kinematic event analysis. In creating PST's from CST's, preliminary selections were made. Events failing loose topology cuts and some basic trigger tests were rejected. Further cuts were made in the PST analysis and both sets are discussed in section 3.3. PST's were compact enough, to be maintained as Fermilab disk files, and not tapes.

If only weighted distributions were needed, PST's would be sufficient. However, weights were reevaluated every time the PST was read. A format more suitable to decay distribution analysis (fits) was used in CPR's, or condensed physics records. CPR's, which were created from PST's, held only kinematic analysis results, ( $m_{\pi\pi}$ ,  $t_{pn}$ ,  $Mx^2$ ,  $\pi\pi$  rest frame decay angles,  $t_{\pi\pi}$ , and  $u_{\pi\pi}$ ), and all correction weights for each event. No track information at all was written on CPR's, and only events passing all cuts used for PST analysis were written to CPR's. Both  $\pi\pi n_T$  and  $\pi\pi X$  trigger data were processed to the PST and CPR levels.

### 3.2 TEARS

TEARS created DST's after performing our tracking and vertex analyses. For  $\pi\pi\pi$  and other non-vee triggers, it made few judgements on the topologies of events beyond setting flags for successful operations such as vertex finding. Selection of good events from the TEARS results was left to later (CST and PST) analysis programs. For vee triggers, such as  $K^0\pi p$ , the desired topology was an integral part of the formalism. Appendix C gives a more detailed review of TEARS than given below, and tables in it are referred to here.

Track finding began downstream of the MPS magnet with independent straight line fits in the xz and yz views. Minimum spark requirements, Table C.1, included both overall and local group requirements. (An overall requirement spanned all chambers in a given view, for example the x view chambers downstream of the magnet. A group requirement covered only a subset of these, for example the Fx chambers.) Two passes were made in each view. In pass 1, sparks in the F-station were required; in pass 2, the F-station was ignored. Both because of having two passes and having relatively loose requirements in pass 1, single view cleanups were employed to remove redundant tracks (keeping the better of two tracks with essentially the same parameters). Next, the xz and yz tracks were matched, section C.3, using slant view spark chamber information and the requirements of Table C.2. More cleanups followed to remove spurious matches. This was our only view matching operation, and the term "match" will refer only to the track pairs found in it.

None of the downstream cleanups were 100% efficient. We preferred to have high efficiency for good track and match survival over high efficiency in spurious track and match removals. The single track and match cleanups were designed to compare tracks for duplicates and pick the best of a pair. If a track or match was reasonably unique, it survived these tests. Since the front end (between the target and MPS magnet) tracking chambers were all proportional, their superior time

resolution provided a strong "effective" cleanup when we sought upstream tracks corresponding to downstream matches. As a result, the appropriate measure of multiplicities is drawn from the front end results, not the downstream ones. Spurious matches typically had no corresponding front end tracks. Those that did were fairly rare and usually shared front end tracks with a good match.

After completing the downstream analysis we determined the beam trajectory, which was needed in the front end algorithms. One unique beam trajectory was found per event. The procedure used was not a fit since we had only two beam stations (BA and BB) about 19.5 meters apart. Instead, we used the beam pwc data to locate the beam position at each station, and connected these with straight lines. If hits in either view at either station were ambiguous, the event was flagged. The beam position and error were then drawn from averages of the beam location and beam spot width for the view and station in question. Although such suspect beam events were later cut from the data, this allowed a full analysis of them, and in the  $\pi\pi n$  case, they were found to be as good in all respects except for a poor  $t_{pn}$  measurement as the good beam data. Multiple beam particles were not a problem, although they would, without the strobe kill, dominate the two body  $\pi\pi n_T$  trigger. The strobe kill electronics, Appendix A, removed nearly all double beam within the resolving time of the beam pwc's, and removed all double beam where both particles were in the same *rf* bucket (at the cost of losing some effective flux, but the scalers accounted for that), and charge and momentum cuts removed any surviving remnants.

Having a beam track, TEARS turned to the front end analysis with the immediate goal of finding all possible "links", or front end tracks that joined to the downstream matches. The next goal was to locate main and (depending on the trigger) vee vertices. A general feature of the front end analysis was that it sought only linking tracks. With only one exception, if a particle failed to pass through the magnet

aperture, its tracks were not found. All but one of the the triggers were designed for all particles to pass the magnet and extra charged particles were heavily suppressed by the topological trigger. (The exception was the "high mass"  $\pi\pi n$  trigger in which a single slow particle (nominally a  $\pi^+$ ) was intended to strike the inside magnet wall in one of the  $\Gamma$  chambers. For that trigger, the slow particle tracking was meant to be done in a DST analysis separate from the one described here. We will not detail those operations.)

The front end analysis was performed twice on every event using the systems "Vtrig" and "Targtrk", optimized for topologies with and without secondary vertices (vees) respectively. Vtrig will be discussed in Appendix C. Both sets of results were written to DST's, but for CST's and beyond we specialized to the results of the system appropriate to a given trigger. On CST's, only Vtrig results were written for the vee triggers,  $K^0\pi p$ ,  $K^0\pi\pi X$ , and  $K^0K^0X$ . Targtrk results were used for all other triggers unless Targtrk failed. In that case Vtrig results were substituted as a backup. (This later proved unnecessary; all  $\pi\pi n$  events failing Targtrk reconstruction also failed Vtrig.)

The front end analysis of interest to  $\pi\pi n$  was not Vtrig, but Targtrk. In this system, only main vertex particles were sought. No fits to a specific hypothesis were made; all possible vertex particles were found. The tracking requirements for Targtrk are given in Table C.3. In this table, only *real* sparks are included.

An important feature of the front end algorithms was the use of information from the beam and matches to support the front end tracking. Since we had a  $K^0$  decay volume free of chambers, figure 2-3, and the A station was close to the target, the BC lever arm was not sufficient to always resolve the correct hit from two close A-station hits. Additional information was needed. This was provided by extrapolations of the matches to the magnet center and (in y only) to a point inside the decay volume, and of the beam track to the target. The y-view match extrapolation

used a vertical focusing correction but the x view extrapolation only needed a square field approximation. All extrapolations were assigned inflated errors, and were included in initial track fits. With the exception of the x-view mid magnet point, these extrapolated points were then removed from tracks in a refit. Refit tracks were then used to find momenta and charges using a square field approximation.

The beam extrapolation was especially important in selecting the correct A-station hits for a track. In the fits, the beam provided a vertex "spark", although vertex was unknown. Since a wrong vertex spark could lead to a bad selection at the A-station, Targtrk was structured as a loop over three possible vertex sparks along the extrapolated beam and sizable errors were assigned. After all front end tracks had been found by Targtrk for each of the three choices and a vertex had been found for at least one (and usually all three), the best set of Targtrk results was selected as the one that made best use of the A-station information. Secondary criteria were the number of vertex tracks and the vertex  $\chi^2$ .

The vertex fits were iterative  $\chi^2$  fits in both the xz and yz views to a common  $z_v$ . Forward track deletion was allowed independently in either view. For Targtrk, and for the main Vtrig vertex, beam tracks were included and could not be deleted.

Targtrk used one final cleanup, called Sclean. Sclean selected only the best match of any pair having two different y view tracks matching to the same x view track. Since the slant spark chambers were virtually x chambers (stereo angle of only  $\pm 5.7^\circ$ ), multiple x view tracks matching to the same y view track were allowed by Sclean. Next, Sclean sought to remove "old" or out of time beam region tracks by requiring F' pwc hits on any matched track within  $\pm 5\text{cm}$  of the 2x2 counter. There were two such chambers in each view and one hit in each view was required, amounting to two additional tracking requirements. In Run II, a BA type proportional chamber (called BBWV) was located with the 2x2 counter at a  $45^\circ$  slant. Hits

in this chamber were included in the match spark counting, and were also used in Sclean. A hit in BBWV on a track was enough for Sclean to approve a match.

For Targtrk, Sclean was used only after all tracks were found and the best vertex determined. In this case, Sclean (which was written for Vtrig) was an add on to flush spurious matches, especially in the beam region, that linked to the same front end tracks used by good particles. The Sclean processing in this case was on any match with a Targtrk link to the front end. The sequence "vertex then Sclean" was considered reasonable since spurious matches always used the same front end track as a good match so that the vertex fits were not much biased by the spurious matches. The average tracking efficiency exceeded 99% on good (real) particles, but as discussed in section 4.8, the appropriate tracking efficiency includes the effect of the trigger requirements and includes both particles in a configuration dependent calculation. Without Sclean, Targtrk was only about 90% efficient with respect to feed up problems in the vertex multiplicity. With Sclean, the feed up effects were less than 1.4%, while feed down losses were less than .3%.

Particle momenta were evaluated in TEARS using a square field approximation. The xz plane component of the momentum is

$$P_{zz} = P_K / |\sin\theta_b - \sin\theta_a| \quad (3.1)$$

where  $P_K = .7510 \text{ GeV}/c$  is the magnet's  $p_t$  kick and  $\theta_b, \theta_a$  are the xz plane angles before and after the magnet, respectively. The full momentum of the particle is then found as

$$P = P_{zz} \sqrt{1 + S_y^2 / (1 + S_z^2)} \quad (3.2)$$

where  $S_z$  and  $S_y$  are the before magnet slopes. Unfortunately, the momenta measured by TEARS have a systematic shift characteristic of a kink of  $\delta\theta = .084 \pm .007$  milliradians between the upstream and downstream (of the MPS magnet) chamber

alignments. The kink had no noticeable effect on the tracking and linking efficiencies. Monte Carlo studies have shown that this momentum error was not the result of the square field approximation, and that the square field approximation has no noticeable effect on the resolution. We accounted for the kink by a first order momentum correction at the PST level,

$$P = P_m (1 + \delta\theta/\theta) \quad (3.3)$$

where  $P$  is the true momentum,  $P_m$  the measured momentum,  $\theta$  the bend angle and  $\delta\theta$  the kink. Appendix C includes a discussion of the kink and the evaluation of  $\delta\theta$ .

### 3.3 Event Selection

Despite stiff multiplicity requirements for the  $\pi\pi n_T$  trigger, section 2.4, most of the recorded data was not  $\pi^- p \rightarrow \pi^+ \pi^- n$ . A large number of background reactions either had or could mimic the required two body signal. Examples of these include  $\pi^- p \rightarrow \pi^- \pi^+ \pi^0 n$ ,  $K^- p \rightarrow K^- \pi^+ n$ ,  $\pi^- p \rightarrow K^- K^+ n$ ,  $\bar{p}p \rightarrow \bar{p} \pi^+ n$ , and  $\pi^- e^- \rightarrow \pi^- e^-$  ( $\pi e$  scattering, or extremely stiff delta rays). To extract our sample of  $\pi\pi n$  events (with reasonably small and correctable backgrounds), a series of cuts listed in Table 3.2 and discussed here was made. In addition to insisting on the expected topology, charge, and particle species, some cuts insured that the intended trigger was actually satisfied and were designed to facilitate corrections.

Our basic topology cut required that two oppositely charged particles (total forward charge zero) come from a vertex found by Targtrk. Only Sclean approved particles were included in this accounting, and the total charge test came after the vertex particles were counted. (One cut we did *not* make was requiring exactly two matches. Studies found no differences in event distributions made with this, and those with our usual cut beyond an expected reduction of event totals of about 40%.

Most two body charge zero events had large missing masses, indicating considerable energy going into neutral particles (mainly  $\pi^0$ 's). A loose total forward momentum cut (75 to 125 GeV for the 100 GeV beam) was made in creating PST's, but for the final analysis, recoil neutrons were identified by a missing mass calculation requiring

$$-2.5\sigma(Mx^2) \leq (Mx^2 - m_n^2) \leq 2.5\sigma(Mx^2) \quad (3.4)$$

where

$$Mx^2 = (P_{\pi^-} + P_{\pi^+} - P_{beam} - P_p)^2. \quad (3.5)$$

The  $P_i$  are 4 vectors of the forward  $\pi^-$  and  $\pi^+$ , the target proton ( $p$ ), and the beam pion. For equation 3.4,  $\sigma(Mx^2)$  is evaluated according to equations 2.6 and 2.7. As shown by figure 4-3, virtually all 100 GeV events passing this cut fall between the limits  $-5 < Mx^2 < 7 \text{ GeV}^2$ . The  $Mx^2$  cut left us with a background of about 10% from events with unvetoed  $\pi^0$ 's. These background events, indistinguishable from good  $\pi\pi n$  events are accounted for by a background subtraction, section 4.2 and Appendix D, in the cross section measurement, but are left intact in decay distribution plots.

Cerenkov analyses were needed to remove  $\bar{p}p \rightarrow \bar{p}\pi^+n$ ,  $K^-p \rightarrow K^-\pi^+n$ , and  $\pi^-p \rightarrow K^-K^+p$  or  $\bar{p}pn$  backgrounds. For the first two, we required that the beam Cerenkov counters tag the beam as a pion according to

$$\pi = (C_0 + PRUSS) \cdot \overline{BDIFF} \cdot \overline{DISC} \quad (3.6)$$

when all counters were set. The tag was adjusted appropriately when one of the counters wasn't ready. For the pion induced backgrounds, C1 and C2 identified the forward particles whenever their momenta allowed. (The qualification is discussed in section 4.9 along with the details of the C1-C2 analysis.)

Table 3.1a  
Run I Apertures (meters)

Z	X limits	Y limits	Name
2.022	$\pm .3$	$\pm .12$	V3xy
3.042		$\pm .17$	Bxy
3.96	$\pm .55$		Pole tip upstream
4.47	$\pm .55$		Mid magnet
4.98	$\pm .55$		Pole tip downstream
5.70	$\pm .55$	$\pm .28$	Magnet exit
6.30		$\pm .311$	Dxy
11.5		$\pm .73$	C1
12.43	$\pm 1.10$		F4xy

Table 3.1b  
Run II Apertures (meters)

Z	X limits	Y limits	Name
1.943	$\pm .225$		V3x
1.689		$\pm .0921$	V3y
3.042		$\pm .17$	By
3.96	$\pm .55$		Pole tip upstream
4.47	$\pm .55$		Mid magnet
4.98	$\pm .55$		Pole tip downstream
5.70	$\pm .55$	$\pm .28$	Magnet exit
6.30		$\pm .311$	Dy
11.5		$\pm .73$	C1
12.43	$+1.60$		F4x
12.43	$-1.66$		F4x

In order that acceptance calculations be well defined, fiducial cuts, Table 3.1, were made. These outer aperture cuts required that particles land well inside the F station. For Run I data, we selected the F-x cut to avoid a region of rapidly falling reconstruction efficiency on one side of the spectrometer. This was unnecessary for Run II, spark chamber improvements having been made for that run. We also required both particles to miss a  $28 \times 28$  mm box (at  $P_{beam} \leq 100 \text{ GeV}$ ) centered on the  $2 \times 2$  counter. At 175 GeV, this cut used a 14.7 mm box surrounding the  $1 \times 1$  counter.

Table 3.2 100 GeV/c Event Cuts	
Cut	Percentage of Data Rejected
PST Creation	
Vertex Found	.5
Two Particle	42.
Loose Momentum Cut	56.
Charge Zero	32.
$A(2)2/3$ Multiplicity	.14
$BCD(2)5/6$ Multiplicity	3.2
BCD Hits on Tracks	1.1
PST Analysis (CPR creation)	
Beam Pwc	4.4
Beam Cerenkov	7.3
Apertures (10%)	15.
Pass 1	1.9
Vertex z	24.
$\Delta x \Delta y$	7.0
Bx radius	< .1
Veto House (V0 to V3)	2.4
$Mx^2$	45.
C1 C2	11.
Reconstruction	< .1
A - station	< .1

Cuts are listed sequentially. Percentages apply at the time the cut was made. The "vertex z" cut is a rough average two different cuts, see text. Final A-station cut requires tracks resolved in at least 2 planes of 3. "Apertures" includes outer and  $2 \times 2$  cuts only.

The last strictly fiducial cut was a requirement on the vertex z-coordinate. (No cuts were needed in the x and y views.) We actually used two different cuts, both designed to eliminate net feed out losses caused by a finite vertex resolution, section 2.5. For normalization, a cut inside the target flask requiring

$-.51m \leq z_v \leq -.30m$  was made to give a well defined target length. For data distribution analyses, we cut outside the flask, requiring  $-.65m \leq z_v \leq -.23m$ . In this case, the downstream cut is about halfway between the target flask and the vacuum jacket. These cuts were studied with a Monte Carlo, and the resulting feed out losses were found negligible. (The vertex cut number in Table 3.2 is actually for a cut about midway between the two just given. For these, the amounts of data rejected by the vertex cuts are 41% (tight cut) and 14% (loose cut).)

Trigger inefficiencies for close tracks motivated another "fiducial" cut, namely one at the Bx station requiring  $\Delta x \geq 5.85 \text{ mm}$  and  $\Delta y \geq 6.96 \text{ mm}$ , where  $\Delta x$  and  $\Delta y$  are track separations. These values require that the two pions be separated by at least 3 wires in all BCD trigger chambers except, possibly, the Dx chamber, where crossing tracks were allowed. These cuts were set after looking at the consecutive struck wire distributions to remove any need to account explicitly for events lost by soft delta rays causing tracks to merge (section D.4).

Another separation cut required that the radial distance between the two tracks at Bx be greater than 13 mm. This rejected little data above  $m_{\pi\pi} \approx 500 \text{ MeV}/c^2$ . It followed the  $\Delta x \Delta y$  cut which imposed an effective radius of 9.1 mm. The A station trigger efficiency was quite poor for events in which the two forward particles were resolved in only one or none of the three A station trigger planes, Table 4.4.1. This rarely occurred above  $\pi\pi$  masses of 500  $\text{MeV}/c^2$ . Although few events at any mass were involved, their correction weights were large. This motivated the above radius cut, and a cut requiring that the forward particles be resolved in at least two of the A station trigger planes. A few low mass events survived these redundant cuts. There wasn't enough low mass data for acceptance corrections below about 550  $\text{MeV}/c^2$ , and except for some weighted mass distributions and scatter plots, we generally ignored it.

A major block of cuts was designed to ease trigger efficiency corrections. (The B station separation cuts could also be included in this class). We used a software trigger following the hardware to insure that the  $\pi\pi m_T$  trigger was indeed satisfied. These cuts were that the  $\beta$  chamber have no hits, that the photon vetoes (V0 through V3) all be quiet, that the A station have exactly two hits in at least two of the three trigger planes, and that there be exactly two hits in at least five of the six BCD trigger planes. In addition, a more detailed cut was imposed for the BCD chambers. The BCD hardware requirement interacted with the reconstruction efficiency and was also quite sensitive to delta ray vetoes. The trigger requirements were significantly stiffer than the tracking requirements if we assume all hits were actually on tracks, even allowing one bad chamber. To provide for compatibility between the BCD delta ray and reconstruction efficiency corrections (sections 4.4 and 4.8), we required that the two forward tracks both have hits on them in at least five of the six BCD chambers, and if both tracks satisfied this in only five chambers, those had to be the same five. If one chamber was flagged as bad in the hardware trigger cut, then it was the only one allowed to fail this test. If the x view tracks crossed in the Dx chamber, then Dx was the only bad chamber allowed.

We only used events for which the two good tracks were pass 1, section 3.2. Pass 2 tracks hitting the F-station occurred at a rate consistent with interactions, and wide angle Pass 2 data had terrible reconstruction efficiencies. The track pass type selection was made after the charge and multiplicity cuts. A reconstruction efficiency cut at 50% was also made. Given the fiducial and pass cuts, failures of this cut were rare. When using event by event weights for acceptance, we used a 10% cut to avoid divergences. This cut was not used in decay distribution fits.

To insure a good measurement of the beam track, we required a good measurement of the beam coordinate at both stations (BA, BB) and in both views. This cut rejected any events using the average beam spot for any view.

In the 175 GeV/c data, additional cuts to remove events with photons detected in any of the E111 photon detector, lead wall, or electron calorimeters were made, [Fr82]. Counter elements along charged particle tracks and their neighbors were excluded from the cut. In the lead wall, and also the calorimeters, pulse heights from the remaining counters were added and the event was rejected if the total exceeded half the minimum ionizing pulse height. For the E111 photon detector, pulse height signals from charged tracks were removed. Photons were then identified by peaks seen in both (x and y) views, and if any were seen the event was rejected. These forward photon cuts were tuned to optimize photon rejection and maintain acceptable charged particle efficiencies. They reduced backgrounds at 175 GeV/c to the 100 GeV/c level.

### 3.3.1 Run Selection, Data Set

Important for the cross section analysis (as well as general data analysis) was the identification and exclusion of bad runs. Most bad runs were known from our logs. These runs were compromised by conditions such as lack of beam or C1C2 Cerenkov counter data, short run trigger electronics failures, and/or critical tracking and trigger chamber failures. These problem runs correlated well with large fluctuations in run by run diagnostic scaler ratio plots, especially plots of  $\sigma_{TL}$ , equation 3.10. Various other plots were also used, including a cross section evaluated using weights for all corrections, including acceptance. A few additional bad runs were flagged in these diagnostic plots and verified by our records.

Most of the bad runs found in these reviews were excluded from both our scaler and decay distribution analyses. Only a couple of runs, for which the STROBE scaler was unplugged were included in an expanded data set for distribution fitting only. This operation reduced our data set by about 15%, from 280000  $\pi\pi n_T$  events to 240000 events. Table 3.3 summarizes the 100 GeV data set fate from raw CST's to

Table 3.3 Run I, 100 GeV/c Data Set	
	Events
Total Recorded $\pi\pi n_T$	277924
Good Runs Only	239419
On PST (good runs)	38997
CPR*, Tight Vertex, total	7425
$ t_{pn}  < .15 \text{ (GeV/c)}^2$	5099
$\rho^0 (.60 < m_{\pi\pi} < .94 \text{ GeV/c}^2)$	1422
CPR*, Loose Vertex, total	10577
$ t_{pn}  < .15 \text{ (GeV/c)}^2$	7250
$\rho^0 (.60 < m_{\pi\pi} < .94 \text{ GeV/c}^2)$	2105

\* Cuts for CPR's are cumulative.

the final samples of  $\pi\pi n_T$  events used for our various results.

For our normalization, we divided the data into positive (+) and negative (-) magnet current groups. With this division a problem spanning the entire Run I data set emerged. The "triglog" cross sections  $\sigma_{TL}$ , see Table 3.4, depended on the magnet polarity. After considerable effort, we concluded that this did not represent a left right bias in the spectrometer for good  $\pi\pi n$  data. It seems that the trigger simply allowed more garbage in the trigger at one polarity than the other. The data cuts are "polarity blind", and after the full analysis, the cross sections were, within errors, consistent. While the source of the polarity problem has never been isolated, we believe it to be due to a number of small asymmetries in the spectrometer, none of which were large enough to cause the problem alone. Examples would be small misalignments of the 2x2 counter, possible fringe field magnetic effects on the V3 phototubes, and a paddle near the extreme edge of the Cx chamber that was left out of the trigger. Although outside of the fiducial volume, this paddle would flag no delta ray vetoes, while its symmetric partner could. This problem was found and fixed before Run II, and V3 was located farther from the magnet in that run. The polarity problem was absent from that run. While not proving the above

speculations correct, the lack of a problem in the Run II data showed that a small average lab beam angle ( $\approx 1/2mr$ ), and a half inch offset of the magnet with respect to the beam were not the culprits.

At 175 GeV/c, the number of  $\pi\pi n_T$  triggers was over 50% more than the Run I, 100 GeV/c total. This was more than balanced, however, by increased backgrounds, mainly the high  $Mx^2$  ("fast  $\pi^0$ ") background. The 175 GeV/c good run set included 481000  $\pi\pi n_T$  events, and yielded only 8408 events in the final sample. (About 75% of this was used in the 175 GeV/c cross section analysis [Fr82].) For decay distributions only, this was augmented by 1487 events (out of 75000 triggers) from a revised  $\pi\pi n_P$  trigger, giving a total of 9895 events. This additional data resulted from a desire to check the A station performance by removing it completely from the  $\pi\pi n$  trigger.

Late in Run II, we redesigned the  $\pi\pi n_P$  trigger (from the one described in Appendix B) and essentially replaced  $\pi\pi n_T$  by it. The  $\pi\pi n_T$  trigger was then heavily prescaled while  $\pi\pi n_P$  was not. To compensate for removing the A station from the trigger, we included stiff DEDX counter requirements both below and above the two particle peak. Other requirements were the same as for  $\pi\pi n_T$ . The resulting events were free of A station biases, and no corrections for them were needed. There were Landau fluctuation (in DEDX pulse height) losses, but for decay distributions, this did not matter. The revised  $\pi\pi n_P$  trigger overlapped  $\pi\pi n_T$  significantly, so for runs with the revision, we use the dominant  $\pi\pi n_P$  and ignore a much smaller sample of  $\pi\pi n_T$ .

### 3.5 Scaler Analysis

To obtain an absolute cross section,  $\sigma$ , for  $\pi^-p \rightarrow \pi^+\pi^-n$  within specified mass and  $t_{pn}$  cuts, we need an estimate,  $P$ , of the events produced by a total pion flux,  $B$ , incident on a target containing  $N_T$  protons/cm<sup>2</sup>. Then  $\sigma$  is given by

$$\sigma = \frac{P}{N_T B}. \quad (3.7)$$

The produced event estimate,  $P$ , is obtained from the corrected fraction of recorded triggers surviving all cuts:

$$P = TRIGLOG \frac{N_c}{N_r}. \quad (3.8)$$

*TRIGLOG* is a scaler total giving the number of times the  $\pi\pi n_T$  trigger was satisfied. The number,  $N_r$ , is the number of  $\pi\pi n_T$  events written on tape, and  $N_c$ , is the corrected number of events surviving the analysis. The ratio  $TRIGLOG / N_r$  is roughly a spark chamber dead time correction, as not all triggers lead to spark chamber pulsing, section 2.4. (In chapters 5 and 6, we will refer to  $N_c$  as a produced event total. This is admittedly at odds with (3.8) unless  $TRIGLOG = N_r$ . That condition was met in the Run II data, but in Run I, these numbers differed by a few percent. The term is convenient.)  $N_c$  depends on specific cuts, such as mass and  $t_{pn}$ , which we apply to the final data, but not on the biases of the spectrometer. Our cross section analysis naturally splits into two pieces, the evaluation of  $N_c$ , and everything else.  $N_c$  is obtained by applying our full set of event dependent and acceptance corrections to the observed event sample. The other factors group themselves into an exercise in scaler analysis yielding a number,  $\sigma_1$ . This section will concentrate on expanding equations 3.7 and 3.8 into the terms we used, then defining and evaluating  $\sigma_1$ . Section 5.3 will complete the cross section analysis and present results.

The pion flux,  $B$  is obtained from the scalers *EFFBM*, *PRETRIG*, *STROBE*, and the beam pion fraction,  $f_\pi$ .

$$B = f_\pi f_d \text{EFFBM} (\text{STROBE} / \text{PRETRIG}). \quad (3.9)$$

*EFFBM* scaled the "effective" beam flux onto the MPS, section 2.4.1. *EFFBM* was not scaled during evaluation of a trigger candidate by the electronics, or while the on line computer read in the data from an event. However, the name is slightly misleading since this scaler was located before the strobe kill electronics which, as discussed in section 2.4.1, could kill off trigger candidates for reasons dealing with spectrometer readiness. This amounted to a deliberate, but unbiased, rejection of part of the beam flux. The ratio *STROBE* / *PRETRIG* gives this reduction. The factor  $f_\pi$  is evaluated as

$$f_\pi = f_\pi^c (1-\mu) \quad (3.10)$$

where  $f_\pi^c$  is the "unbiased" pion fraction found from the beam Cerenkov analysis, section 2.2.1. The factor  $(1-\mu)$  accounts for a muon (and electron) contamination included in  $f_\pi^c$ . Beam decays and interactions between the beam counters and the upstream end of the target flask are accounted for by  $f_d$ .

It is useful to group equations 3.7 to 3.10 together to give

$$\sigma = \left[ \frac{\text{TRIGLOG} \cdot \text{PRETRIG}}{N_T f_\pi f_d \cdot \text{EFFBM} \cdot \text{STROBE}} \right] \frac{N_c}{N_r} \quad (3.10a)$$

$$= \sigma_{TL} \frac{N_c}{N_r} \equiv \sigma_1 N_c \quad (3.10b)$$

The term  $\sigma_{TL}$  is, roughly, the cross section for the  $\pi\pi n_T$  trigger to occur. We say "roughly" only because the target factor,  $N_T$ , applies to a fiducial cut and not to all the matter seen by the beam. Equation (3.10) is more applicable to this experiment than (3.7). It exposes a real distinction between the trigger, which includes

mainly garbage, and the physics we extract from recorded good events. The terms not included in  $\sigma_{TL}$  are necessary to convert it to a "physics" cross section. Another and important effect of using  $\sigma_{TL}$  is that it can be evaluated on a more restricted set of runs than used for making event distributions. In that case,  $N_c/N_r$  represents the (corrected) fraction of recorded events that survive our analysis, and both terms in this ratio are from all runs analyzed for event distributions.

Also useful is the "cross section per event",  $\sigma_1$ , given by the second half of (3.10b):

$$\sigma_1 = \frac{\sigma_{TL}}{N_r} \quad (3.11)$$

By virtue of the  $1/N_r$  term, the cross section per event depends on the run set used to evaluate it. However, it is independent of all corrections and any  $\pi\pi$  mass or  $t_{pn}$  cuts used. Both  $\sigma_{TL}$  and  $\sigma_1$  depend on the target fiducial cut through the factor  $N_T$ . Our cross section evaluation used both  $\sigma_{TL}$  and  $\sigma_1$  at various stages; however, the goal of the scalar analysis was  $\sigma_1$ .

Our decay distribution fits treat the positive and negative magnet data on an equal basis. For this reason, and to reduce errors, we used the following procedure for  $\sigma_1$ , Table 3.4. Large mass cut cross sections,  $\sigma^+$  and  $\sigma^-$  were obtained for positive and negative magnet polarities. A mass cut of .5 to 2.7 GeV/c<sup>2</sup>, and a  $-1.5$  (GeV/c)<sup>2</sup>  $< t_{pn} < 0$  cut was also applied. A target fiducial cut of  $-0.51 < z_v < 0.30m$  was used. Event by event weights for all corrections, including acceptance, were applied,  $N_c = \sum_{events} w$ . The liquid hydrogen density was taken as  $0.0708 \text{ gm/cm}^3$  [PDG80], with a 1% uncertainty, giving an inverse density of  $1/N_T = 11.25 \times 10^5 \mu b$ .  $\sigma^+$  and  $\sigma^-$  were then evaluated as

$$\sigma^\pm = \frac{\sigma_{TL^\pm}}{N_r^\pm} \sum w^\pm \quad (3.12)$$

Although the  $\sigma_{\pi}$  values for the polarities were quite different, the agreement between  $\sigma^+$  and  $\sigma^-$  was within errors. To eliminate the remaining asymmetry, at least to first order,  $\sigma^+$  and  $\sigma^-$  were averaged arithmetically,

$$\sigma = \frac{\sigma^+ + \sigma^-}{2}. \quad (3.13)$$

Equation 3.13 is our reason for introducing an  $N_c$  estimate at this level. We used acceptance weights as a first order correction to account for 2x2 counter location variations in a low statistics situation, where our decay distribution fits might have trouble. The cross section per event was then obtained by dividing by the total weight used for  $\sigma^+$  and  $\sigma^-$ ,

$$\sigma_1 = \sigma \left( \sum w^+ + \sum w^- \right)^{-1} \quad (3.14)$$

These calculations used essentially the entire set of good runs. Only a few good runs were excluded here (for lack of some scaler data) and included in the general decay distribution analysis.

The Run I, 100 GeV/c scalar analysis data is given in Table 3.4. Only statistical errors are given in the table. The  $\sigma^+$  and  $\sigma^-$  values agree, within statistics. Applying equation 3.13 gives a polarity averaged  $\sigma = 4.25 \pm .08 \mu b$ . And we have

$$\sigma_1 = .2160 \pm .005 \mu b.$$

This value is used for our  $\rho^0$  cross section, which used the tight target cut. A parallel analysis was made by Fredericksen for the Run II data, [Fr82].

The tight vertex cut cost us  $\approx 30\%$  of the good  $\pi\pi n$  data, and the  $t_{pn}$  cut was also significant, but the statistics were still sufficient. The true target flask length was poorly known, and the tight fiducial cut avoided a difficult to determine feed-in feed-out correction. Simple Monte Carlo studies showed that the tight target fiducial cut had negligible net data feed out and was insensitive to the true flask length.

Table 3.4  
100 GeV/c Scaler Analysis

Quantity	$I_{mag} = +180$	$I_{mag} = -180$
Events	2681	2179
EFFBM	$6.3689 \times 10^9$	$5.2352 \times 10^9$
B	$5.7180 \times 10^9$	$4.7005 \times 10^9$
STROBE	$6.4700 \times 10^8$	$5.0819 \times 10^8$
PRETRIG	$9.9481 \times 10^8$	$8.2026 \times 10^8$
TRIGLOG	178453	123930
$\sigma_{TL}$	$54.0 \pm 0.0024$	$47.9 \pm 0.0028$
$N_T$	141673	96414
$\sum w^\pm$	10995.64	8679.85
$\sigma^\pm$	$4.19 \pm 0.106 \mu b$	$4.31 \pm 0.121 \mu b$

Table 3.4b Special Data Cuts for Above	
Target	$-.51 < z_v < -.30$ m
Mass	$.5 < m_{\pi\pi} < 2.7$ GeV/c <sup>2</sup>
$t_{pn}$	$-.15 < t_{pn} < 0$ (GeV/c) <sup>2</sup>
Min. Acceptance	10%

To recover sufficient statistics for general decay distribution fits, we opened up the vertex cut to  $-.65$  to  $-.23$  m, actually outside the target. This cut was also insensitive to net feed out problems, and virtually all the data within it can justifiably be considered as actually coming from inside the target, see figure 2-6. From equation 3.11,  $\sigma_1$  must be adjusted for the expanded cut. Since we don't know the full target  $N_T$ , we scale  $\sigma_1$  by the increase in weighted data. (The result is consistent with  $N_T$  for a 12.0" target.) The expanded data set had 7215 events for the same mass and  $t_{pn}$  cuts with a total weight of  $\sum w = 29150$  events, giving

$$\sigma_1^e = .1458 \pm .0032 \text{ nb} \quad (3.15)$$

The 175 GeV/c analog of equation 3.15 is  $\sigma_1^e = .0471 \text{ nb}$ . These values apply to the moment and decay distributions of Chapters V and VI.

## Chapter IV

### Data Corrections

#### 4.1 Weights

About half of the  $\pi\pi n$  events allowed by the spectrometer dead time and acceptance were lost through a number of mechanisms. Also, backgrounds of order 10% persist in the final data sample. We review our event by event corrections in this chapter. Appendix D goes into the details of the evaluation of a number of the corrections discussed here. The major correction not discussed here is our acceptance, section 5.1, which has zeros in significant places. Global corrections, not applied on an event by event basis were discussed with the scaler analysis, section 3.4.

For this analysis, most non-acceptance corrections are accounted for by weights applied to each  $\pi\pi n_T$  event in our final sample. The major exception is a background subtraction for veto house failures. Except for particle decay, interaction and geometric acceptance, all of the correction factors were found through analyses of  $\pi\pi n_T$  and/or various background triggers, especially  $\pi\pi X$  and curve throughs.

If the chance an accepted event survives a series of independent losses is  $P$ , then the number of observed events,  $N_o$ , can be used to estimate the accepted event count, (the number we would have without losses),  $N_A$ , by

$$N_A = N_o / P = wN_o. \quad (4.1)$$

The weight,  $w$ , is just  $1/P$ . Equation 4.1 applies equally well to differential distributions as to total event counts.

Because most of the losses depend on laboratory variables not visible in plots such as mass distributions, the  $w$  in equation 4.1 is an average weight. More

directly, we can evaluate the weight appropriate to each event and use

$$N_A = \sum_{j=1}^{N_A} w_j \quad (4.2)$$

For each event,  $j$ ,  $w_j$  is found as a product of weights for each individual loss:

$$w_j = \prod_i w_j^i = \prod_i 1/p_j^i. \quad (4.3)$$

The  $p_j^i$  are the chances that event  $j$  survived the effect  $i$ . The counting error in a weighted distribution is estimated by  $\sigma = \sqrt{\sum w_j^2}$ . We have taken care to analyze the data and evaluate the corrections,  $w^i$ , to maintain independence of the corrections. Cases where mechanisms are coupled, such as chamber efficiencies in our pwc based trigger and track finding, were evaluated together.

If some of the  $w^i$  are "large", then it is probable that several things, any of which could cause a loss, could all "go wrong" on an event. However, each  $p^i$  is the probability a problem did not happen, and  $\prod p^i$  correctly calculates the chance nothing went wrong. Large weights in general are not desirable, but if all or at least a large fraction of the events have comparable weights, the situation is livable. In our case, the weight is built up from a number of weights most of which are about 1.1 or less. The largest weight is almost always the  $\beta$ -chamber delta ray correction which ranges from about 1.18 to 1.40. Still, unusually large weights are to be avoided as they distort distributions. Results are more reliable if the occasional high weight event is excluded from a distribution without further correction, [Ea71]. Our high weight cut is applied on individual corrections, which under some circumstances can become large. The most notable case of this is our reconstruction correction for which we cut at a reconstruction efficiency of .5, or a weight of 2.

In addition to weighting for losses, we include weights for backgrounds not removed by the beam and C1C2 Cerenkov analyses. Both these analyses remove the

greater part of their backgrounds but an estimable amount persists. In this case the weight is interpreted as the fraction of events that have the correct particle species. Veto house inefficiencies can be defined, and evaluated with the help of the  $\pi\pi X$  trigger. Under some circumstances, that data can then be used in a background subtraction. We begin with the veto house problem.

#### 4.2 Veto Failure Background

Other than a finite acceptance, the most obvious problem with our data is a background of order 10% at 100 GeV/c under the neutron in the missing mass squared ( $Mx^2$ ) spectrum of figure 4-1. Figure 4-2 illustrates the probable sources of the background. At  $Mx^2$  values near the neutron,  $N^*$  and  $\Delta$  resonance production dominates. Missing particle kinematics are mainly set by the missing energy  $\approx \frac{1}{2} Mx^2$ .

The  $\pi\pi X$  trigger, whose only significant difference from  $\pi\pi n_T$  was its lack of a veto house requirement, was used to estimate the background. The veto inefficiency, or "failure rate", including both instrumental and geometric effects, was measured by taking the ratio of known veto failures in  $\pi\pi n_T$  with the total  $\pi\pi X$  event rate as a function of  $Mx^2$ . The known failures were just  $\pi\pi n_T$  events with  $Mx^2$  above the neutron peak. None of these were examples of  $\pi^+ \pi^- n$ . Including corrections to the  $\pi\pi X$  total for prescaling and delta rays, the failure rate,  $F$ , in a given  $Mx^2$  bin is given by

$$F = \frac{(Events \text{ in } \pi\pi n_T) \cdot \delta}{(Events \text{ in } \pi\pi X) \cdot P} \quad (4.4)$$

where  $P$  is the  $\pi\pi X$  prescale factor, and  $\delta$  is the average  $\beta$ -chamber delta ray correction ( $\pi\pi X$  was not subject to delta ray vetos). Data at 50 and 20 GeV/c were crucial in obtaining the failure rate under the neutron  $Mx^2$  peak at 100 GeV/c. Indeed, 100 GeV/c data only to verified the consistency of the analysis. What we

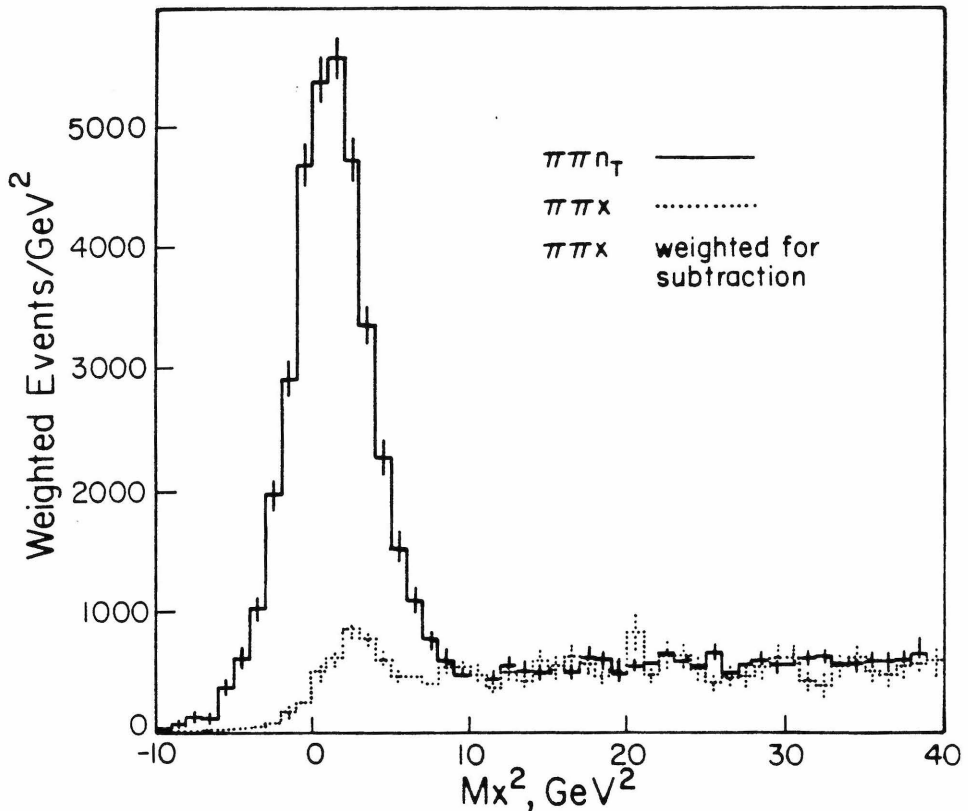


Figure 4-1. 100 GeV/c  $Mx^2$  spectrum for  $\pi\pi n_T$  and fully weighted  $\pi\pi X$  spectrum. By construction, the veto weight gives cancellation at high missing masses. (Deviations result from averaging inefficiencies measured at 20, 50 and 100 GeV/c.) Under the neutron peak, the shape is mainly determined by measured failure rates at 20 and 50 GeV/c, and has a small model dependent  $\Delta(1236)$  component.

needed was the failure rate under the neutron peak, which was, by definition, unobtainable at 100 GeV. The need for using 50 and 20 GeV/c data was the only reason we kept a fixed front end geometry for all energies (at the cost of reduced acceptances at the lower energies).

Failure rates as a function of  $Mx^2$  were found at each beam momentum and magnet polarity. These sets were then averaged as a function of  $Mx^2$  after determining that they were all consistent. For our background subtraction,  $\pi\pi X$  events passing the same missing mass cut as the  $\pi\pi n_T$  data were then given the additional weight,  $w_b = -P \cdot F$ . Figure 4-3 shows our final  $F$  as a function of  $Mx^2$ . The very first

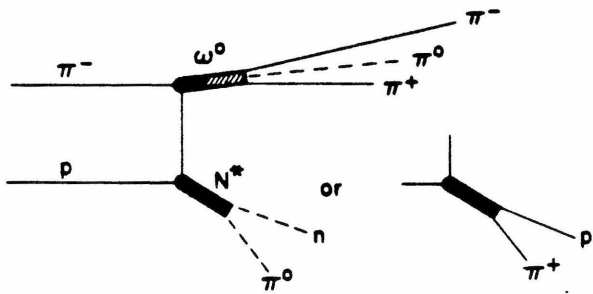


Figure 4-2. Major background sources. The major source of background under the neutron peak is  $\Delta$  and  $N^*$  resonances, although a tail of  $\omega^0$  production is also present. At high  $Mx^2$  values, mesons decaying to  $\pi^+\pi^-$  and one or more  $\pi^0$  should dominate, with lower vertex processes yielding  $\pi^0$ 's also present and significant. Charged decays of  $N^*$ 's are allowed because of the finite efficiency of the  $\beta$  chamber.

bin applies only to the  $\Delta(1236)$  mass region, as discussed in Appendix D. The jump at the  $\Delta$  presents a problem in actually applying this correction. We have dealt with it by smearing that bin according to our  $Mx^2$  resolution, and applying an effective  $F$  built from the smeared  $\Delta$  bin and the relatively flat other values. For the smearing, one needs an estimate of the amount of  $\Delta(1236)$  relative to the rest of the  $\pi\pi X$  spectrum. The  $\Delta(1236)$  fraction and the overall background levels depend on  $m_{\pi\pi}$ , but measured failure rates were independent of the  $\pi\pi$  mass. Details of the model and evaluation of  $F$  are given in Appendix D.

Figure 4-4a, shows the  $\pi\pi X$   $Mx^2$  spectrum at 100 GeV/c after correction for losses. After removing a small amount of  $\pi\pi n$  data from the  $\pi\pi X$  sample, it can be weighted for veto house inefficiencies and prescale factors and subtracted from the  $\pi\pi n_T$  data. Figure 4-4b, shows the resulting background  $Mx^2$  distribution and figure 4-5, is the subtracted  $\pi\pi n$   $Mx^2$  distribution.

One problem that, rather surprisingly, didn't affect the veto failure rate was the failure of the B8 counter, one of the 24 counters in the cylindrical Barrel veto,

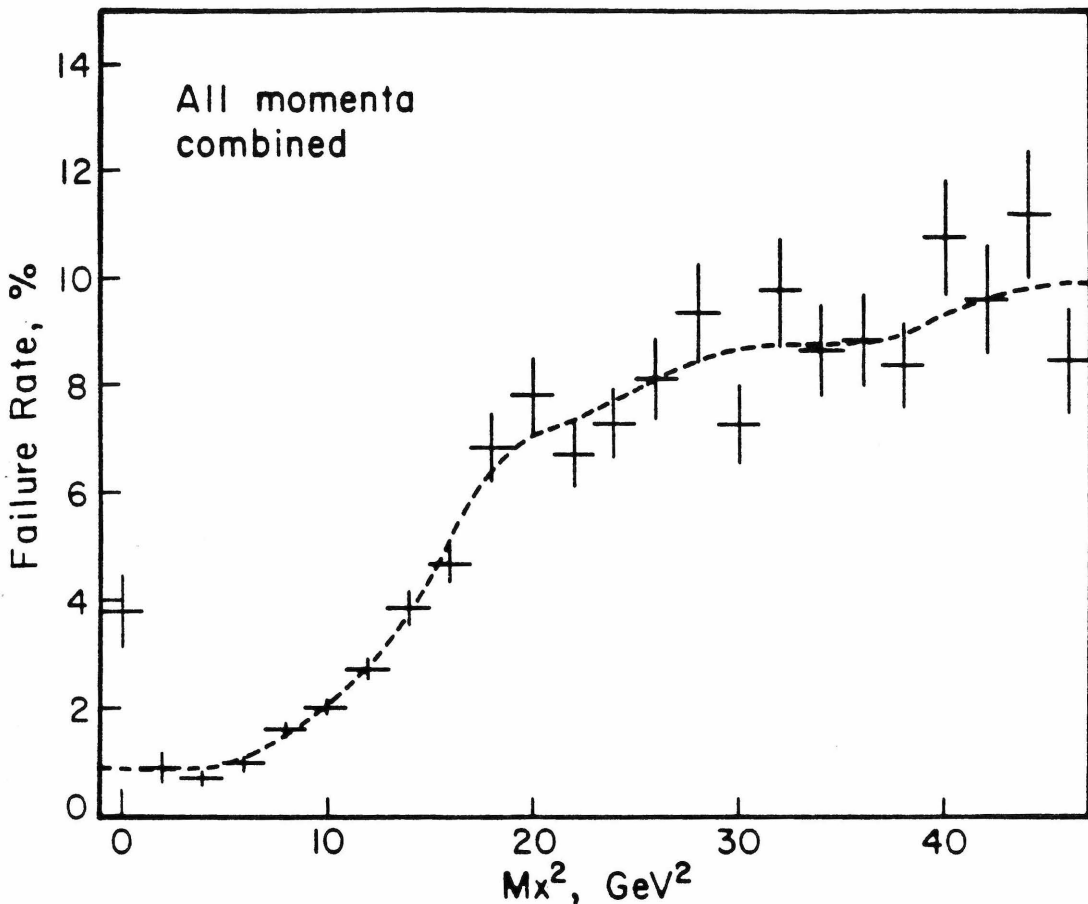


Figure 4-3. Measured veto house inefficiency. Data at 20, 50, and 100 GeV/c were combined for this figure. The curve, from a one pass smoothing, was not used for corrections.

Chapter 1. The rates were consistent before and after the failure. As discussed in Appendix D, this follows from the fact that an increase in failure rate would only be for the special class of vetos detected by a single photon interaction in the Barrel. This is a small class, and the B8 failure would only change that partial inefficiency by 4% of itself.

Most of the  $\pi\pi X$  events were not  $\pi\pi n$  events, but our trigger design did allow some  $\pi\pi n$  events in the  $\pi\pi X$  data. These were mainly neutron vetos,  $\beta$ -chamber delta ray vetos, and some events also passing the  $\pi\pi n_T$  trigger. The total of such good  $\pi\pi n$  data in the  $\pi\pi X$  trigger is small, both as a fraction, and as an absolute number since the  $\pi\pi X$  trigger was heavily prescaled. These were removed from the

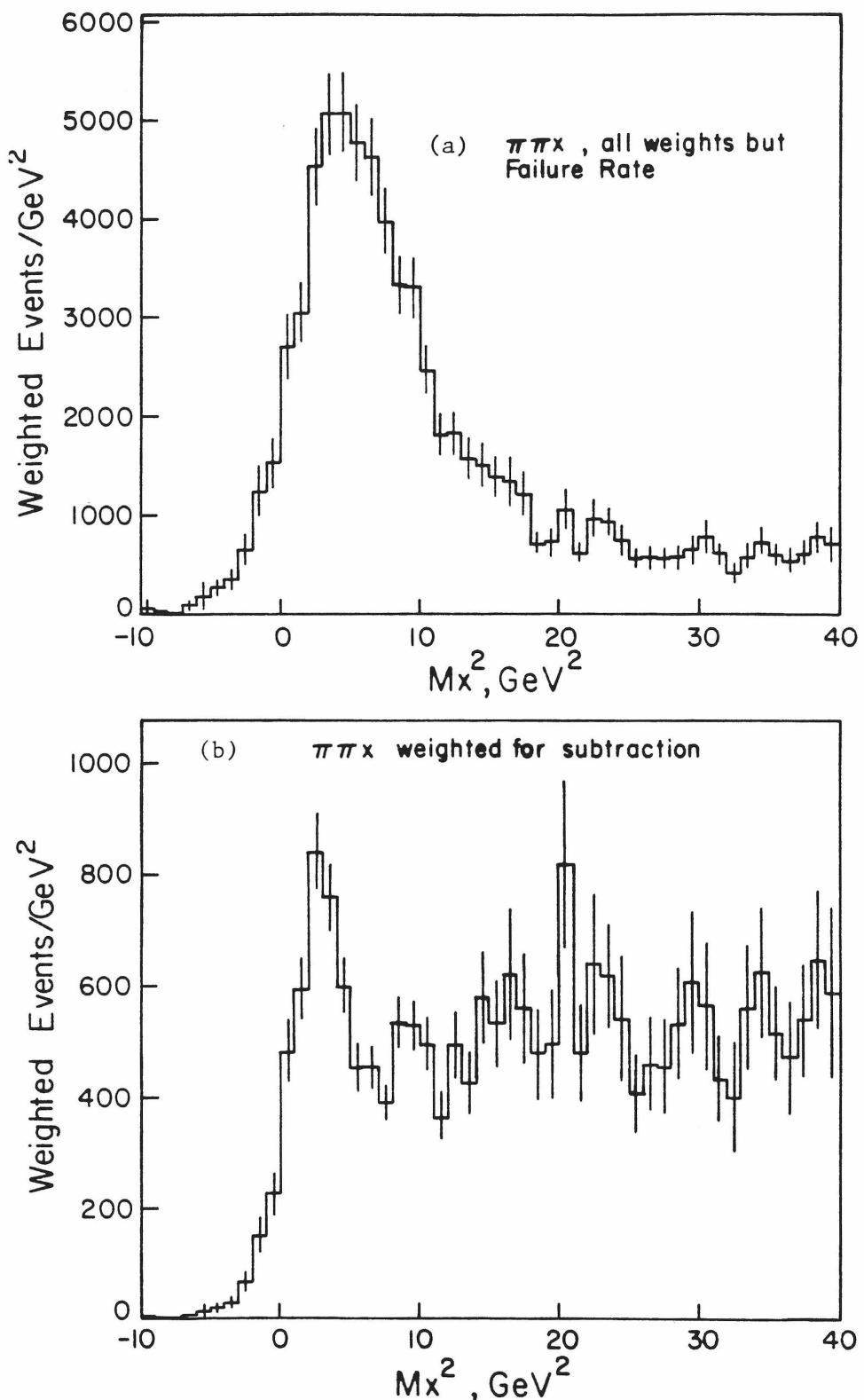


Figure 4-4.  $\pi\pi X$  Distributions. 2-4a shows the  $\pi\pi X$   $Mx^2$  spectrum with all weights except the veto failure rate. This is included in 2-4b. The data of 2-4b are included, to scale, in figure 2-1.

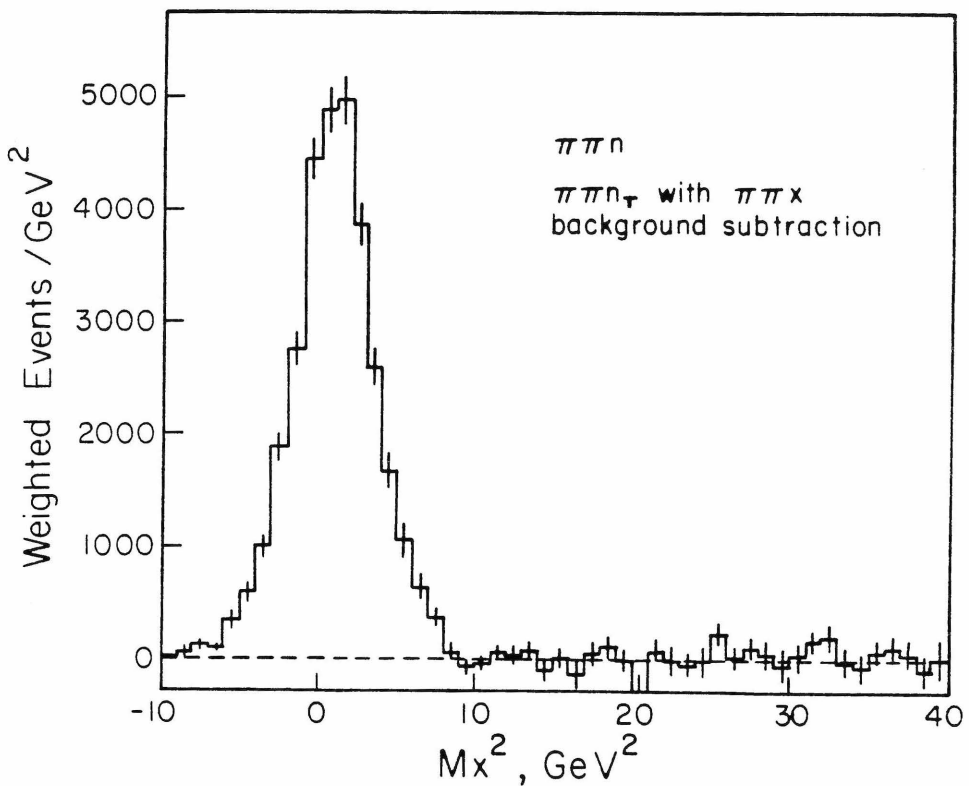


Figure 4-5. Subtracted  $\pi\pi n$   $Mx^2$  spectrum.

$\pi\pi X$  data before weighting to avoid subtracting good events, and to avoid double counting (with a minus sign) the neutron veto and  $\beta$ -chamber delta ray effects.

The veto failure background subtraction was mainly needed for our  $\rho^0$  cross section measurement and our  $t_{pn}$  distributions. The effect of the background on our decay distribution fits was minimal. We have chosen to not do the subtraction for those fits. The background was greatest at the  $\rho$  and decreased with increasing  $\pi\pi$  mass.

The above formalism can be applied to both our 100 and 175 GeV/c data. In the latter case, the "veto house" definition is extended to include the forward photon vetoes (electron calorimeters, lead wall, and E111 photon calorimeter, section 2.3.3). After the additional off line veto cuts are made at 175 GeV/c, section 3.3,

the veto failure background, as a fraction of the neutron peak, is comparable to that seen at 100 GeV/c. In this case, however, corrections for good event losses due to the photon cuts must also be made. The loss was found by using  $\pi\pi B$  trigger data from Run II.  $Mx^2$  and recoil neutron angle cuts, were used to get a clean sample of  $\pi^-p \rightarrow \pi^+\pi^-n$  events. The forward photon detector response to these events set a good data loss of 12.5% [Fr82].

### 4.3 Neutron Veto

Neutrons interacting in the Barrel (labeled V1 in figures 2-2 and 2-5) veto about 10% of our  $\pi\pi n$  data. The correction for this loss was found in a study of the  $\pi\pi B$  background trigger. The main feature of this trigger was a requirement that one and only one of the counters in V1 fire. Otherwise the requirements for  $\pi\pi B$  were the same as for  $\pi\pi n_T$ . We checked this equality by turning off the B=1 requirement for a run, and noted that the trigger was identical to  $\pi\pi n_T$ .

The most striking feature of this trigger was a strong recoil neutron signal, identifiable through  $Mx^2$  and  $\Delta\varphi$  cuts, where

$$\Delta\varphi = \varphi_{forward} - \varphi_{Barrel} \quad (4.5)$$

is the difference between predicted and observed Barrel hits. Figure 4-6, shows a 100 GeV/c  $\Delta\varphi$  plot for the  $Mx^2$  cut  $-5 < Mx^2 < 2.5$  (GeV/c<sup>2</sup>)<sup>2</sup>. This peak is centered on  $\Delta\varphi = -1.2^\circ$ , indicating a small error in the surveyed Barrel counter azimuth. (The surveyed orientation was 11.5° between the x-axis and the B-1 counter center, figure 2-5.)

The neutron detection efficiency,  $E_{nv}$ , was found from ratios of  $\pi\pi B$  and  $\pi\pi n_T$  data. The two triggers are complementary, one having a veto on detected neutrons and the other not.  $N^*$  backgrounds under the neutron differed slightly, but other corrections are the same, and in principle they cancel. The background

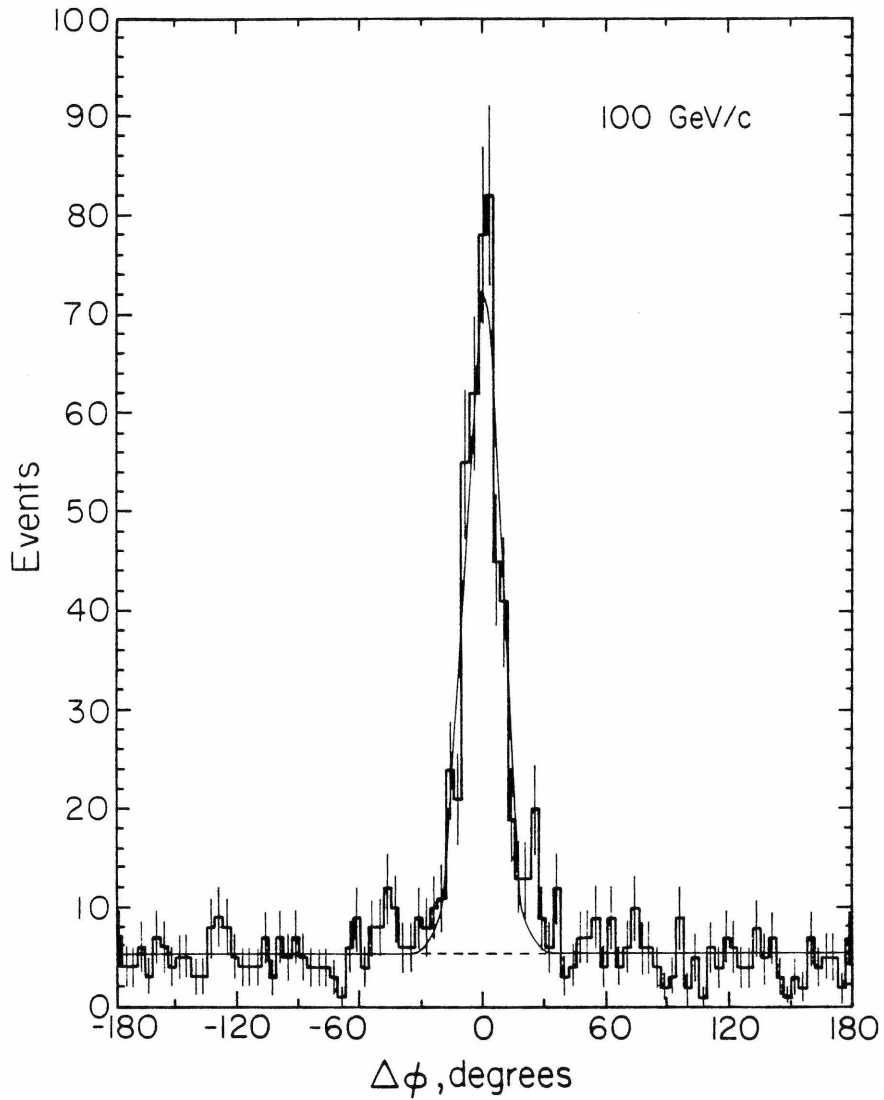


Figure 4-6. Recoil neutron signal. Both the flat background level and peak width depend on  $\sqrt{-t_{pn}}$ . Data are unweighted, and no  $t_{pn}$  cut was used for this plot.

subtraction for  $\pi\pi B$  was internal, using the  $\Delta\phi$  distribution, while the  $\pi\pi n_T$  background subtraction used  $\pi\pi X$  data.

Figure 4-7, shows the  $E_{nu}$  distributions. Owing to limited running time with  $\pi\pi B$ , the errors are rather large.

The neutron efficiency measurement is discussed in section D.3. Our fits demanded a flat  $\sqrt{-t}$  dependence above threshold, so we averaged the above threshold rate to get (statistical error only)

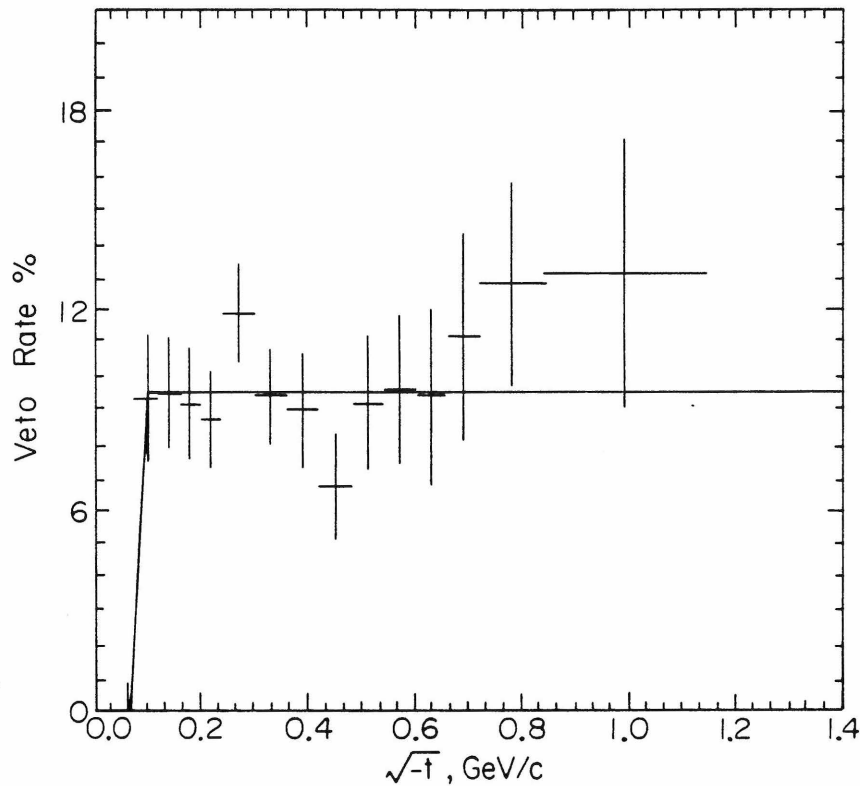


Figure 4-7. Neutron Veto rate,  $E_{nv}$ .

$$E_{nv} = \begin{cases} 0. & \sqrt{-t} < .08 \text{ GeV/c} \\ .0981 \pm .005 & \sqrt{-t} \geq .08 \text{ GeV/c} \end{cases} \quad (4.6)$$

For the early runs, before B8 failed,  $E_{nv}$  is scaled up by a factor of 24/23.

The neutron veto weight for  $\pi\pi n_T$  is just  $w_{nv} = \frac{1}{1 - E_{nv}}$  and has the values

$$w_{nv} = \begin{cases} 1.00 & \sqrt{-t} < .08 \\ 1.109 \pm .006 \pm .022 & \sqrt{-t} > .08, \text{ late runs} \\ 1.114 \pm .007 \pm .023 & \sqrt{-t} > .08, \text{ early runs} \end{cases} \quad (4.7)$$

where the first error is statistical, and the second systematic. Early and late refer to before and after B8 failed.

The systematic error in  $w_{nv}$  represents a 20% error for  $E_{nv}$ . Neutrons can re-scatter and register in a second Barrel counter, or nuclear reaction fragments might register in a second counter. Such "double" neutron vetos were excluded by the  $\pi\pi B$  trigger. Unfortunately, the signal for them is similar to that for some  $\Delta^0$  decays, and we have been unable to distinguish at any reasonable level between these sources for the two Barrel hit signal. The 20% error estimate is about midway between a  $\Delta^0$  dominated two barrel hit signal and a naive estimate of  $(E_{nv})^2$ .

#### 4.4 BCD Delta Rays

The only trigger correction for the B, C, and D chambers that may be treated in isolation is the delta ray correction. Chamber efficiency losses must be done in the track finding correction, section 4.8, as the same hits are used for both triggering and track finding. Close track losses are best treated as an acceptance effect after close track cuts, section 3.3, are made.

The BCD trigger cuts, section 3.3, remove any events "saved" by delta rays. The high BCD chamber efficiencies insure that relatively few recorded events are lost by these cuts.

For this correction, we deal only with delta rays separated from tracks by one or more "quiet" wires. Delta rays unresolved from the track that created them were treated by adjusting the close track cuts.

As far as the trigger was concerned, "delta ray" includes not only real delta rays (penetrating electrons recoiling from a fast particle - atomic electron collision), but also random chamber noise coincident with events, and recoil protons from low  $p_t$  elastic scatters that occurred in the BCD region and were detected by a chamber. It is not useful to bother distinguishing these other mechanisms from true delta rays.

Table 4.1	
BCD Delta Ray Weights	
6ok	$w = 1.1244 \pm .0117 \pm .0124$
5ok	
chamber	weight
Bx	$1.386 \pm .012 \pm .039$
By	$1.420 \pm .013 \pm .042$
Cx	$1.432 \pm .013 \pm .043$
Cy	$1.428 \pm .013 \pm .043$
Dx	$1.400 \pm .012 \pm .040$
Dy	$1.383 \pm .012 \pm .038$

The BCD delta ray correction relies heavily on the stiff  $\pi\pi\pi$  topological trigger requirements to conveniently deal with correlations between chambers. Only the cases of 0, 1, and "many" chambers seeing delta rays need to be distinguished. We do have to consider two types of trigger condition. Cases where all six chambers (Bx, By, Cx, Cy, Dx, and Dy) have hits on both tracks, "6ok", and cases where one chamber fails to have a hit on one or both tracks, "5ok", need different corrections. Delta rays are more serious in the latter case, as a delta ray seen by just one of the five "good" chambers would cause a veto. In the 6ok case, at least two chambers must see delta rays to cause a veto. The development of the BCD delta ray correction, along with a discussion of the effect of delta rays unresolved from tracks, is given in Appendix D. Table 4.1 gives the correction weights. The errors are statistical then systematic.

#### 4.5 A-Station Trigger Correction

The A-station trigger correction was developed by D. Petersen and F. Fredericksen of Indiana. The correction accounts for both inefficiencies and "noise" (mainly delta rays) in the three A-station trigger planes. The point of view is that all events satisfying the hardware trigger, A(2)2/3, are acceptable regardless of where the hits came from. Noise is allowed to save events that would not pass trigger tests on the strength of hits on tracks alone. This is looser than the approach we use at the BCD stations.

Having a 2 planes out of 3 trigger requirement, with one a slant plane, there is no "absolute" trigger suppression if tracks are unresolved in one view. The angular coverage of a wire pair at A is greater than at BCD. If tracks are very close, we do have problems with the trigger, but if the tracks are resolved at Bx, and not Axy, we have a significant, but not disastrous suppression.

Data losses from a separation cut for particles unresolved in only one A-station plane would be excessive, owing to the relatively large solid angle covered by an A-station wire pair. We thus choose to not make such a cut, and to weight for inefficiencies in the trigger for single unresolved views at A. It follows that we don't make acceptance corrections for forbidden regions as in the BCD region. This approach does pull the A-station trigger requirements out of the track finding efficiency calculation of section 4.8, but errors resulting from this split are second order and minimized by not requiring that hits on the tracks themselves satisfy the trigger.

The correction accounts for a multitude of trigger sins. We label cases of 0, 1, 2, or 3 planes with resolved tracks as 0ok, 1ok, 2ok, and 3ok. The assignment of cases has nothing in principle to do with the hits on tracks, just whether the tracks are separated in the various views. The 3ok case can be both saved or killed off by chamber noise (the latter being more likely.) If all planes have hits on both tracks,

noise in two planes kills the event, but noise in one plane is no problem. If one plane misses a hit on a track, then noise in that plane cannot hurt. Indeed, one noise hit will make the plane satisfy the trigger again. But, unless that plane has exactly one noise hit, then noise in either of the other two planes will cause a trigger failure. In the 2ok case, where the tracks are unresolved in one plane, a single noise hit in the unresolved plane will help, but noise hits in the other two planes will only hurt unless accompanied by missing hits ("on" tracks). The 1ok and 0ok cases simply require noise hits in order to trigger. The correction depends on which plane(s) actually have unresolved tracks.

A number of tools were used to obtain this correction [Pe78, Pe80b, and Fr82]. These included curve through and  $3\pi p$  data, a Monte Carlo simulation, and data from the revised  $\pi\pi n_P$  trigger described in section 3.3.1. The curve through data gave the response, especially noise response, of the A-station chambers to a single track. The  $3\pi p$  data allowed a measurement of two particle cases (with one extra track's worth of noise) when the hits on one of the tracks were "erased". At this stage, iterative (to account for correlations) hand calculations could be used to evaluate the trigger efficiencies, but Frederickson found that the correlations involved were better dealt with by using the data as input to a Monte Carlo simulation of the A-station response. Finally, the  $\pi\pi n_P$  data gave a direct measure, since the A station was not even in the trigger.

Table 4.2 lists the efficiencies found for Run I and the trigger condition A(2) 2/3. Event weights are just one over the efficiency. An error of .04 is assigned to the efficiencies. Although the analysis determined efficiencies for all cases, only the 3ok and 2ok cases are used in  $\pi\pi n$  analysis, and the average weight on events is  $\langle w_A \rangle = 1.16$ . Few events were found in the 1ok and 0ok classes, and cutting them out is relatively unbiased. (All but two such events were removed by other cuts, namely the B station radial separation and  $\Delta x \Delta y$  cuts.)

Table 4.2  
A-Station Trigger Efficiencies

Class	Unresolved plane(s)	Efficiency
3ok	none	.888
2ok	x	.809
	y	.766
	u	.739
1ok	x+y *	.104
	x+u *	.090
	y+u *	.075
0ok	x+y+u *	.104

\* not used

#### 4.6 Target Region Delta Rays

The last delta ray correction concerns the cylindrical  $\beta$  chamber. A delta ray detected by it will veto an event, and about 30% of accepted  $\pi^+\pi^-\pi^0$  events are vetoed there. This veto rate shows a strong vertex location (z) dependence; it is the main effect producing the uncorrected vertex distribution shape of figure 2-6. The vertex dependence results from a variation of total track length in the hydrogen target with vertex location. The beam and forward  $\pi^-$  tracks add up to a single track over the full target length. The track length variations then come from the  $\pi^+$  track. Delta ray vetos, both from the beam and forward particles is an absorption process. If the delta ray rate were small, the veto rate would be virtually a linear function of z-vertex.

Correction weights for this loss were found using data from curve through runs, in which the  $\beta$  chamber recorded hits passively, and a simple model. The model assumes that the rate of delta ray production and detection by  $\beta$  is constant in z. A constant term is provided for delta rays produced in the vacuum jacket end cap. For each particle we find the probability that it passed through its part of the

target without producing detected delta rays.

The curve through measurements found a rate of .533/meter that a single track in hydrogen would create one or more detected delta ray. The chance that a particle passes through the end cap *without* releasing any detected delta rays was .989. Combining terms for the beam, forward  $\pi^-$  in the target, and for the two forward particles in the vacuum jacket, a constant of .8313 results. The chance that an event survives a delta ray veto is then

$$P_s = .8313 e^{-0.533(z_d - z_v)} \quad (4.8)$$

Each observed event is then given the weight  $w_s = 1 / P_s$ . Further details are given in Appendix D.

#### 4.7 Interaction and Decay Losses

Hadronic interactions of the secondary particles in the target or spectrometer material result in both trigger losses and event reconstruction "failures". Correction weights for this were found using appropriate path lengths,  $\pi^\pm p$  cross sections for the target, and the  $\pi^\pm$  absorption length of the spectrometer through the F-station. Cross sections and absorption lengths used parameterizations from the review article of Giacomelli, [Gi76]. These agree well with data down to  $\sim 2$  GeV/c, the low momentum cutoff of the spectrometer.

Beam attenuation in the target by hadronic processes has the same form as secondary interactions with only the path length changed. Because beam flux loss depends on the vertex, we combined it with the secondary losses. The average hadronic loss weight, including both beam and secondary losses was  $\langle w_I \rangle = 1.11$ .

D. Petersen studied losses expected from  $\pi \rightarrow \mu\nu$  decays and found that in most cases the  $\mu$  is deflected from the  $\pi$  path by an amount sufficient to cause a reconstruction failure. The correction weight for this is

$$w_d = e^{-L \frac{m_\pi}{c\tau} \left( \frac{1}{P_\pi^+} + \frac{1}{P_\pi^-} \right)} \quad (4.9)$$

where  $c\tau = 780$  cm, and L is the distance over which a reconstruction failure would result. We use  $L = 9$ m, the average decay weight being  $\langle w_d \rangle = 1.016$ .

#### 4.8 Chamber Efficiency Correction

The reconstruction system described in section 3.2 and Appendix C, along with our topological cut (two good vertex particles with total charge zero) has been found highly efficient. Limited statistics event scans found the efficiency to be over 90% and dominated by chamber efficiencies. Failed two body events (in which both particles passed the magnet aperture) observed in these scans occurred at a rate consistent with expectations from decays and interactions. The observed reconstruction success rate in the scans depended on the event configuration, mainly through the location of particles at the F-station. The most prominent effect was a beam region problem resulting from both reduced spark efficiencies and from old beam tracks. The latter was a problem only in scans made without the Sclean track cleanup. At the level of statistics in the scans (a couple hundred events), no problems with our matching or match cleanups were found with Sclean in the system.

A high statistics search for match problems was conducted on CST's with the help of the DEDX counter. We found that the feed down of two body events to single body events was at a rate less than .3%, and that the feed up to higher multiplicities was less than 1.4%. These estimates are from event totals where we second guessed the topology and tried to construct "good" events (two body, total charge zero, and  $Mx^2$  within our cuts) out of available tracks, either by addition in the case of single particle events, or by deletion in the case of multiplicities greater than two. Normalization of the rates was by the good two body set seen in the same study. The number of "saved" events was quite small, and mass or other dependences could

not be determined reliably. We include no correction for them but do use the above numbers as systematic errors. Feed up from true single particle events to two particles was also quite small, less than .3%. This latter number was taken from the two particle DEDX distribution of figure 2-4, and includes all the  $\pi\pi m_T$  events with pulse heights less than 70. Such events also include timing errors for the DEDX counter electronics; in which case our DEDX cut has lost some good events at a level less than .3%. This is also included in our systematics.

The DEDX study implies that virtually all the events rejected by the two particle cut, a substantial 42% (see Table 3.2), were indeed junk.

To correct for reconstruction and trigger losses due to our finite chamber efficiencies, we use a brute force calculation by C. Footman of Cal Tech. This calculation indicates an average loss of about 3.4%, but more significantly, it accounts for configuration dependent losses by using measured chamber efficiencies as a function of position. For Run I, this calculation indicated severe losses for events with particles beyond  $x \approx +1.1m$  at the F-station. Because of that, we chose a more restricted fiducial volume than we would have on the basis of chamber sizes alone. This problem was resolved for Run II, and a larger F-station fiducial cut was used for the 175 GeV/c data.

Given measured chamber efficiencies (see Appendix D), the chamber efficiency correction calculates the chance that both particles had at least enough hits along their paths to satisfy the various track finding, view matching, and BCD trigger requirements. The track finding requirements are listed in Appendix C, and the BCD trigger requirements are given in section 2.4. The efficiency correction gives a weight,  $w = 1/E$ .

The calculation is equivalent to grinding through the binomial expression

$$E = \sum \left[ \prod_i^{\text{hit}} p_i \prod_{i \neq j}^{\text{miss}} (1-p_j) \right] \quad (4.10)$$

where the sum is over all possible patterns of hits and misses that satisfy the various requirements. The  $p_i$  are individual chamber efficiencies and vary with position as well as chamber. Note that we do not calculate the chance of having the actual recorded pattern of hits and misses on an event. What we want is the chance of success, which includes all possible patterns that meet or exceed the requirements. We follow the intent of the above expression, but with two tracks, 44 chambers, and 24 requirements to satisfy for track finding, and the BCD trigger requirement (the A-station trigger correction used Indiana method, section 4.6), a straightaway naive calculation would be prohibitive. The actual calculation realizes that the tracks are independent as far as the tracking is concerned. It also takes advantage of our group requirement structure and the separate track finding stages (x-after, y-after, match after, x-before, and y-before) to save several orders of magnitude in computer time.

The calculation loops over the particles in an event. For each particle position dependent chamber efficiencies are evaluated for all chambers. The track finding (including trigger effect) success probability for the particle is then found. For reasons discussed below (the BCD trigger), seven "partial probabilities" are found, the first six corresponding to patterns of all hits except for a miss in one particular BCD chamber, and the seventh for no BCD misses at all.

The concept of partial probability permeates the calculation, usually referring to the probability for a group of chambers, independent of other groups, to have any pattern of hits and misses yielding a given total hit count. Partial probabilities for individual groups are found separately. The probability for each allowed (by minimum hit requirements) multiplicity within the group is saved, indexed by the multiplicity. For each view, we then find overall partial probabilities for each allowed (by minimum hit requirements for the view) multiplicity by taking the product of the various group partial probabilities when the sum of the group hit counts

in the view is the desired multiplicity. The total probability for a view is the sum of its overall partial probabilities (now indexed by overall hit count). "Finally", the total probability for a track is the product of the individual view probabilities, corrected for a few hit patterns that didn't easily fit into the loops used. The use of partial probabilities was designed to avoid double counting of efficiencies and to speed the calculation. It was crucial for making the calculation with anything resembling reasonable computer times.

"Finally" was in quotes because of the BCD trigger. We allow only one of the six trigger chambers to miss a track. When considering two tracks, misses on both must be confined to a single chamber. Without this restriction, the efficiency for an event would simply be the product of two single particle probabilities:  $E = P^1 P^2$ . With this restriction, we can include only single track patterns that have either no BCD misses, one miss for both tracks, or both tracks having a miss in the same chamber. Letting  $i = 1, \dots, 6$  indicate which chamber ( $B_x, \dots, D_y$ ) misses a hit (all others having a hit) and  $i = 7$  indicate no misses, the single track routines calculate probabilities  $P_i^k$  through  $P_7^k$  for each particle  $k$ . For a two particle event, the  $P_i^k$  combine as

$$E = P_7^1 P_7^2 + P_7^1 \sum_{i=1}^6 P_i^2 + P_7^2 \sum_{i=1}^6 P_i^1 + \sum_{i=1}^6 P_i^1 P_i^2 \quad (4.11)$$

to give the reconstruction and (BCD) trigger efficiency.

#### 4.9 Background Rejection by C1 and C2

The rejection of  $K^+ K^- n$  and  $p\bar{p}n$  final states by the Cerenkov counters C1 and C2 used likelihood calculations developed by W. Danchi for this experiment. These are described in detail in references [Da78]. In brief, the light seen by C1 and C2 is compared to the light expected under a given mass hypothesis for the final state particles. Geometric and momentum dependent effects such as light sharing

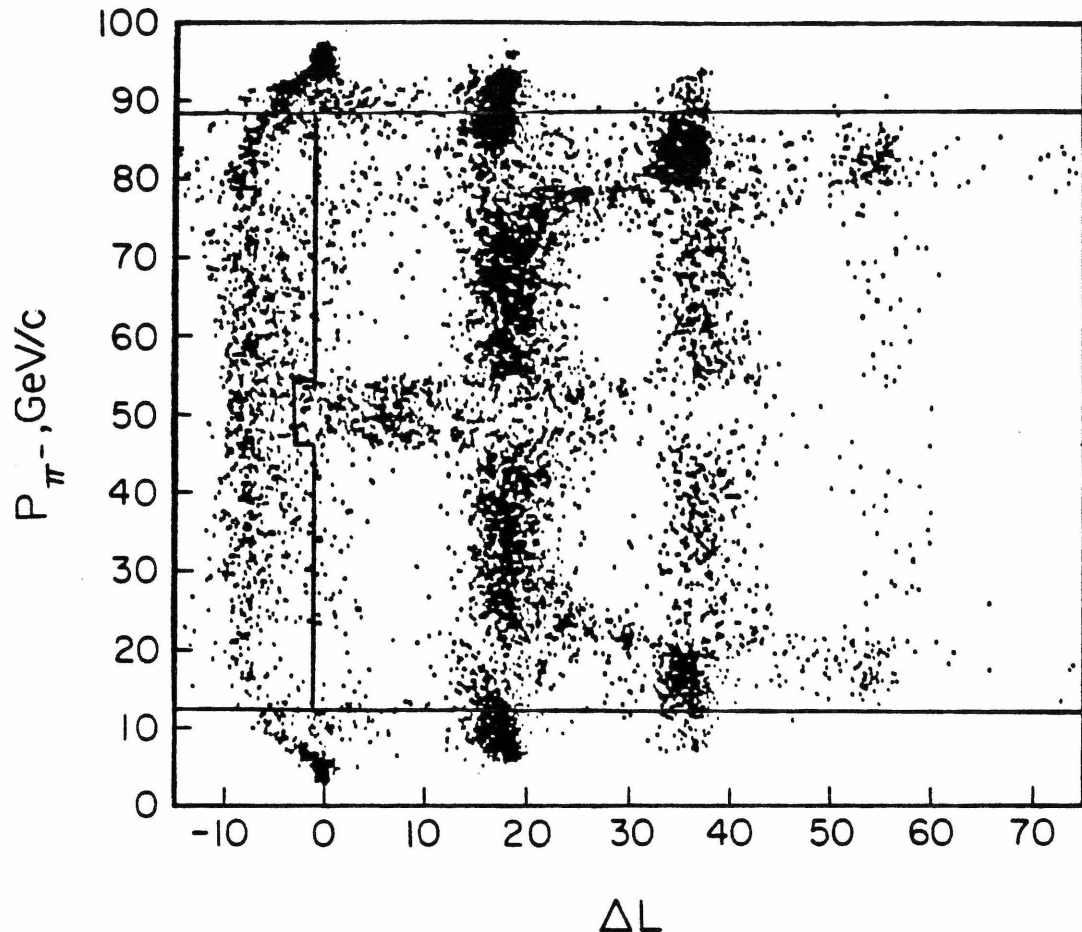


Figure 4-8. Likelihood difference  $L_{\pi\pi} - L_{KK}$  versus  $p_{\pi^-}$ .  $p\bar{p}$  combinations are included with  $KK$  in this plot.

among cells and the  $\beta$  dependence of light production above threshold (figure 2-10) are included. The hypothesis with the largest likelihood, or probability, to produce the observed light is the one preferred by the Cerenkov counters. Our actual cuts, given below, basically follow this.

Advantages of the likelihood method are that it allows natural and convenient evaluation of cases where two particles strike the same cell (light added) or cases where a particle's light is shared among more than one cell, and it gives some selection power (from pulse heights) in kaon threshold regions. The method is fooled, as is a simple on/off method, by simple inefficiencies in a cell, delta rays near a

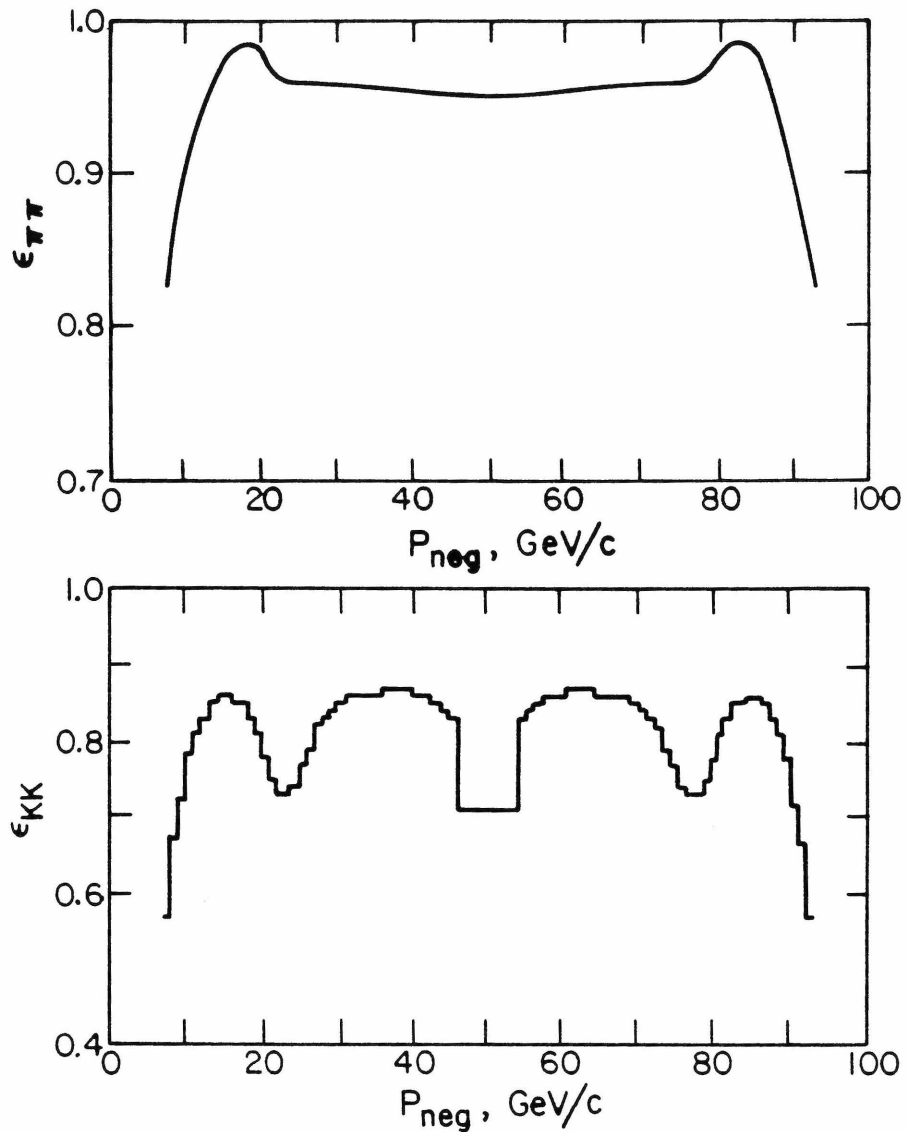


Figure 4-9. C1 C2 efficiencies for  $\pi\pi$  and  $KK$  combinations, from [Pe80a].

mirror giving light,  $K \rightarrow \mu\nu$  decays, and has no sensitivity at all if one particle is below the C1  $\pi$  threshold and the other is near  $100 \text{ GeV}/c$ .

In using the likelihood method, Danchi found that the preferred way to make a choice and display the C1 C2 response was to use the difference of the logarithm of the likelihoods of a pair of hypotheses. Figure 4-8 shows this difference,  $\Delta L$  vs.  $P_{\text{neg}}$  for our  $100 \text{ GeV}/c \pi\pi n$  data, along with the cuts used. Three problem regions are seen. We lose all discrimination when one particle is at or below the C1  $\pi$  threshold. The counters have no preference and  $\Delta L = 0$  is returned. The other particle is well

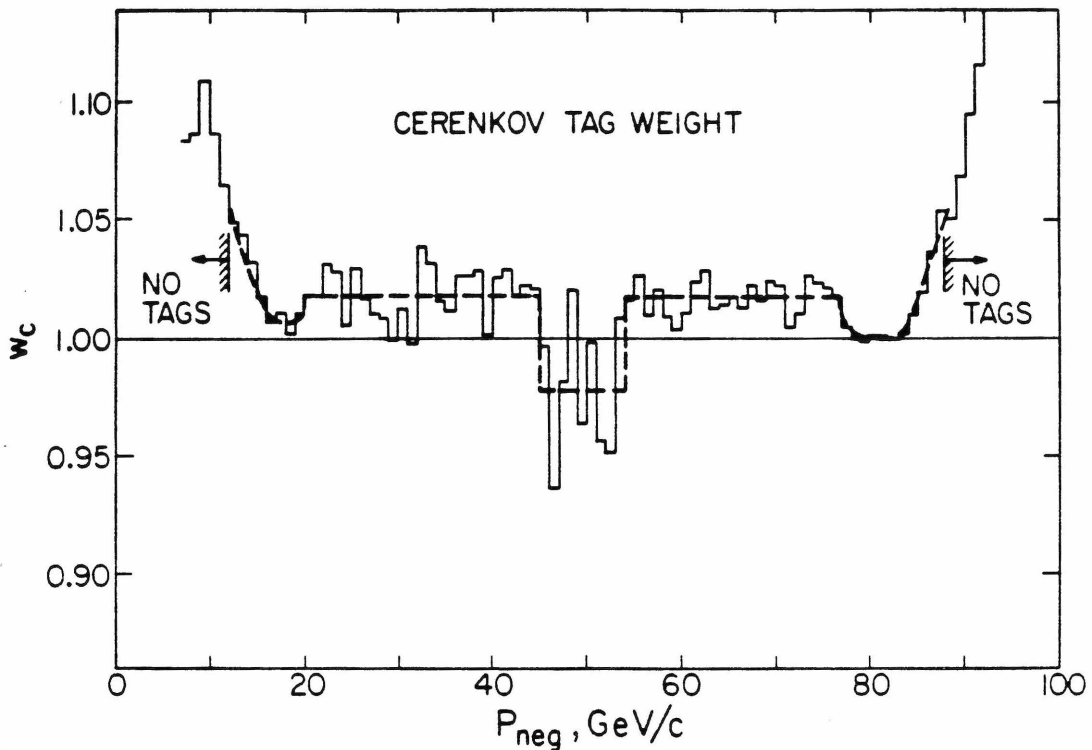


Figure 4-10. Weight for the C1 C2  $\pi\pi$  tag. Dashed curve is the value actually applied. The data curve is from equation 4.13, the efficiencies in figure 4-9, and observed  $\pi\pi n_T$  events.

above all thresholds. The 50 GeV/c region, where both particles are above the C2  $K$  threshold is also a problem. Here we have only the pulse heights for a selection, and low asymptotic photoelectron levels make life hard.

The banded structure of the plot reflects a net of zero to four selections in favor of  $\pi\pi$  over  $KK$ . The band at  $\Delta L < 0$  is  $KK$  preferred, the bands at  $\Delta L > 0$  are one to four (last off scale) net votes for  $\pi\pi$ . The  $\Delta L$  contribution from cells that cannot choose is  $\approx 0$ , and the band widths are from photon counting statistics. The contribution to  $\Delta L$  for a given particle - counter combination is zero if the particle missed the counter completely. If one particle - counter combination favors  $KK$  and the other three favor  $\pi\pi$ , then the net number of votes is 2 for  $\pi\pi$  and  $\Delta L \approx 55$  (see figure 4-8) would result. A mistake, e.g.,  $KK$  misidentified as  $\pi\pi$ , will often look like solid  $\pi\pi$  selections. The scale of the plot or distance between bands, is set

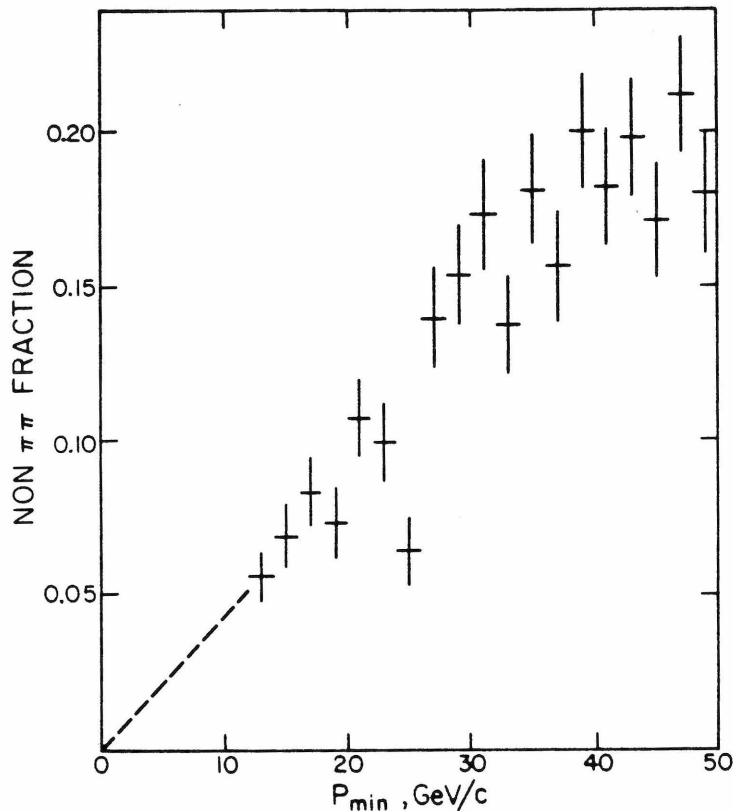


Figure 4-11. Non  $\pi\pi$  fraction. Data points use the C1 C2 tag. Dashed line follows equation 4.14.

arbitrarily by an assumed probability of  $e^{-20}$  for below threshold kaons to make light. (This is an unreasonably small number if one considers delta rays and  $K$  decays, but the line widths are also affected by the scale and no bias results.)

Because the 100 GeV/c beam momentum was not well matched to the thresholds in C1 and C2, the Indiana group undertook a study [Pe80a] to develop a statistical background subtraction. The study was never finished, but efficiency measurements were obtained. Using these, we have found event by event tagging acceptable for most  $\pi^-$  momenta. In regions where  $\pi\pi$  losses are  $\gtrsim 5\%$ , likelihood based tags are reasonable. A weight based on  $P_{\min}$  (slowest particle momentum) is used elsewhere.

he likelihood cuts used are ( $L = \log$  of likelihood)

$$\Delta L = L(\pi\pi) - L(KK) = \begin{cases} \text{None} & P_{neg} < 12 \text{ GeV/c} \\ -1 & 12 < P_{neg} < 46 \text{ GeV/c} \\ -3 & 46 < P_{neg} < 54 \text{ GeV/c} \\ -1 & 54 < P_{neg} < 88 \text{ GeV/c} \\ \text{None} & 88 \text{ GeV/c} < P_{neg} \end{cases} \quad (4.12)$$

Active tagging is used from 12 to 88 GeV/c. The cut change between 46 and 54 GeV/c is to minimize  $\pi\pi$  losses in the C2  $K^-$  turn on region. The efficiencies for our cuts were found [Pe80a] by studying the  $\pi^-p \rightarrow K^0 K^-p$  and  $K^-p \rightarrow K^0 \pi^-p$  reactions. In these, charged kaons and pions could be selected without C1 or C2. Single particle efficiencies were found, and then combined in a way compatible with the likelihood formalism to produce the efficiency plots of figure 4-9, which are *two* particle efficiencies, indexed by  $P_{neg}$ .

The hole in the KK efficiency near 50 GeV/c reflects the cut shift to avoid  $\pi\pi$  losses. The  $\pi\pi$  loss in the cut region is  $\sim 5\%$  while the KK contamination of the tagged sample is  $\gtrsim 8\%$ . For the tagging region, we apply a weight for  $\pi\pi$  losses and KK feed-in of

$$w = \frac{1}{\varepsilon_{\pi\pi}} \left( 1 - \frac{(1-\varepsilon_{KK})f_{KK}}{f_{tag}} \right) \quad (4.13)$$

where  $f_{tag}$  is the fraction of events tagged as  $\pi\pi$ ,  $f_{KK}$  is the fraction tagged as KK, and  $\varepsilon_i$  is the efficiency to properly tag type  $i$ . The weight is a function of  $P_{neg}$  only (largely because  $f_{KK}$ ,  $\varepsilon$  and  $f_{tag}$  were parametrized in that variable only). Figure 4-10 shows the weight in 1 GeV/c bins. Efficiencies used for the figure have been smoothed, but not the  $\pi\pi$  and KK fractions. We apply a simple crude smoothing (dashed curve) for the weights actually used, and consider them uncertain to  $\pm 0.01$  or roughly half the difference from 1.

In the nontagging region, we follow the Indiana group and use a simple extrapolation of the  $f_{KK}$  distribution of figure 4-11, in terms of  $P_{\min}$ , essentially  $P_{\text{neg}}$  folded about 50 GeV/c:

$$w = 1 - (.056 - .0043(P_{\min} - 13)). \quad (4.14)$$

We have checked that the  $\Delta L$  cut shift near 50 GeV/c, and the transitions from tagging to non-tagging at  $P_{\min} = 12$  GeV/c introduce no discontinuities into the (weighted)  $P_{\min}$  distributions. We might also add that the  $\rho^0$  decay kinematics insure that very few  $\rho^0 n$  events are outside the tagging region, even at extreme  $\cos\theta_J$ . Events outside the tagging region are found mainly at higher  $\pi\pi$  masses. The average 100 GeV/c C1C2 weight is 1.00, meaning that  $\pi\pi$  losses are almost exactly matched by KK contamination.

At 175 GeV/c, tagging by C1 and C2 was much less effective. Although limited tagging regions were available, more emphasis on weights for contamination was needed. Details of the 175 GeV/c analysis are given in Fredericksen's thesis [Fr82].

#### 4.10 Beam Corrections

Corrections for both our beam pwc cut and Cerenkov counter tagging are needed. In the former case, we excluded otherwise good events because of ambiguous data in one or more of the beam pwc measurements. The cut events had a poorly determined beam trajectory, hence a poor  $t$  measurement. As described in Appendix C, we could, and did, analyze the bad beam events fully in order to determine that this loss was independent of the forward event configuration, and that a suspect  $t$  measurement was their only problem. The correction for this loss merely weights each event for an overall fractional loss of 4.4%. The resulting weight is  $w = 1.046$ , with a statistical error of .002.

The beam Cerenkov counter analysis was more involved. At 50 and 100 GeV/c, our nominal (all counters set)  $\pi$  tag was

$$\pi = (C_0 + PRUSS) \cdot \overline{DISC} \cdot \overline{BDIFF} \quad (4.15)$$

Events not passing this tag were removed from the data sample. The pion efficiency for this tag was high, (>99 %), and  $K^-$ ,  $\bar{p}$  contaminations were insignificant. Although the beam flux has been corrected for the pion fraction, we need also correct for the efficiency and contaminations resulting from the beam tagging requirement. The correction weight accounts for both pion losses and the contaminations, and is given by (either of) equations 4-16,

$$w = \frac{1}{\varepsilon_\pi} - w \left( \frac{\varepsilon_K f_K}{\varepsilon_\pi f_\pi} + \frac{\varepsilon_{\bar{p}} f_{\bar{p}}}{\varepsilon_\pi f_\pi} \right) \quad (4.16a)$$

$$w = f_\pi / (\varepsilon_\pi f_\pi + \varepsilon_K f_K + \varepsilon_{\bar{p}} f_{\bar{p}}) \quad (4.16b)$$

where  $\varepsilon_i$  is the efficiency for the tag pattern (equation 1) for particle type  $i$ , and  $f_i$  is the tagged beam fraction for  $i$ . The first form shows the roles of inefficiency and contamination in the weight, but  $w$  is found on both sides. Form (4-16b) is the one actually used.

The weight equation (4-16b) does not depend on the tag pattern used, but the efficiencies,  $\varepsilon_i$  do. For the tag (4-15),

$$\varepsilon_i = (E_i^{C_0} + E_i^{PRUSS} - E_i^{C_0} E_i^{PRUSS}) (1 - E_i^{DISC}) (1 - E_i^{BDIFF}) \quad (4.17)$$

where the 100 GeV/c  $E_i$  are the efficiencies found in Table 2-2.

Most of our data runs had all beam Cerenkov counters up and working. For those runs, the above tag, (4-15) is applicable. However, a painfully significant number of runs (about 20% of our data) were made with one or more beam Cerenkov counters not ready, and we cannot afford to exclude them. These were

typically runs made after several hours of beam or accelerator down time, and we took data with one or two of the counters not quite ready. The differential counters BDIFF and then DISC were usually the last ones "tuned". For such runs, we exclude the unprepared counter(s) from the tag, and adjust the expression for  $E_i$  accordingly. In such cases pion losses can be large (when, for example,  $C_0$  is not set), or contaminations up to half a percent (DISC not set). The average beam weight was  $\langle w \rangle = 1.017$ .

#### 4.11 Weight Summary

Studies of our vertex resolution, section 2.5, found that no correction (within a 1% error) was needed for either of our vertex cuts. Our missing mass cut, equation 3.4, required a small correction. Accounting for events in a Gaussian tail beyond 2.5 standard deviations gave constant weight of 1.034. Corrections for pion the fraction of our beam flux were made in the scalar analysis of section 3.4.

The average weight was roughly independent of  $\pi\pi$  mass, figure 4-12. Over all masses, it was 2.39 at 100 GeV/c and 2.56 at 175 GeV/c. Table 4.3 lists 100 GeV/c weight averages for  $|t_{pn}| \leq .15$ , and  $.64 \leq m_{\pi\pi} \leq .9$  GeV/c<sup>2</sup>, and the 175 GeV/c forward photon veto weight. Observed ranges and systematic error estimates are included. The latter were obtained from statistical errors in weight measurements, and systematic error estimates in those measurements. The errors are combined in quadrature for our cross section, section 5.3.

Correction	$\langle w \rangle$	100 GeV/c Average Weights		
		Low	High	Error
A-station	1.16	1.12	1.35	.02
BCD Delta Ray	1.16	1.12	1.43	.02
$\beta$ Delta Ray	1.30	1.20	1.41	.013
Neutron Veto	1.10	1.00	1.11	.024
Beam Pwc	1.05	1.05	1.05	.002
Hadronic Interact	1.11	1.09	1.14	.01
C1 C2	1.002	.94	1.06	.005
Reconstruction	1.034	1.00	1.48	.01
Vertex cut	1.00			.01
$M_{\pi\pi}^2$ cut	1.013			.01
Beam Cerenkov	1.017	.995	1.16	.005
Forward $\gamma$ Veto (175 GeV/c only)	1.125			.015

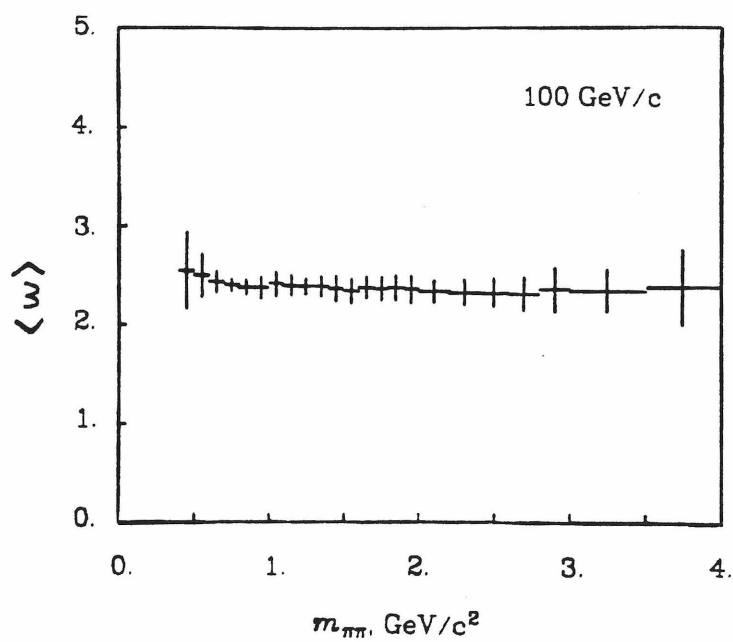


Figure 4-12. Average weight as a function of  $\pi\pi$  mass at 100 GeV/c. Error bars are statistical only.

## CHAPTER V

### Acceptance, Cross Section, Moments

#### 5.1 Acceptance

Losses from finite geometric acceptance and the mechanisms discussed in Chapter IV distort the data for  $\pi^-p \rightarrow \pi^+\pi^-n$  into the distributions we actually observe. The acceptance is the most important correction if we seek to recover "produced" distributions from our data. This section reviews our acceptance calculation. A comprehensive acceptance correction is intimately connected with decay distribution fits. Section 5.2 gives the formalism used for the fits and indicates the role of the acceptance in them.

The outer edges of the tracking chambers and the magnet aperture impose a set of limits within which particles must pass in order to be detected. Next, the  $2 \times 2$  beam veto presents a small "hole" which particles must miss. In addition, our BCD trigger requirements are sufficiently rigid that if particles are unresolved at the B station in either view, the trigger losses are almost total. The most reliable way to deal with this was to impose separation (" $\Delta x \Delta y$ ") cuts on the data at the Bx station and include the effect in our acceptance.

Each observed event is viewed as a member of a class having the same kinematic variables in the  $\pi\pi$  rest frame,

$$x_K = \{m_{\pi\pi}, t_{pn}, \cos\theta_J, \varphi_J\}, \quad (5.1)$$

or an equivalent set. In (5.1)  $m_{\pi\pi}$  is the  $\pi^+\pi^-$  effective mass,  $t_{pn}$  is the squared four momentum transfer from the proton to recoil neutron,  $\cos\theta_J$  is cosine of the Gottfried - Jackson frame [Ja64] polar angle, and  $\varphi_J$  is the azimuthal angle in the same frame, see Appendix A. Averaging over target proton and recoil neutron spins, for a given beam energy, these variables completely specify a  $\pi^-p \rightarrow \pi^+\pi^-n$

event in the  $\pi\pi$  rest frame. To complete the event description one needs a set of laboratory variables, for example,

$$\mathbf{x}_L = \{P_{Lab}, \mathbf{x}_v, y_v, z_v, \varphi_L, \theta_B, \varphi_B\}. \quad (5.2)$$

The lab azimuth,  $\varphi_L$ , can be taken as either the recoil neutron or the  $\pi\pi$  azimuth with respect to the beam (they differ by  $\pi$ ).  $P_{Lab}$  is the beam particle momentum,  $\mathbf{x}_v, y_v, z_v$  are vertex coordinates, and  $\theta_B, \varphi_B$  are beam angles with respect to the VPS z-axis.  $\{\theta_B, \varphi_B, \varphi_L\}$  form a set of Euler angles.

The geometric acceptance is the fraction of events for which all required particles fall within the fiducial volume of the spectrometer. Table 3.1 gave these limits. If *all* variables, kinematic and laboratory, are specified, the acceptance is 0 or 1 only. If an average over some variables is made, the acceptance becomes a continuous function of the others and has limits of 0 and 1.

Our acceptance was found in the Gottfried Jackson frame with a Monte Carlo event simulation built around an event rotation technique developed by the Indiana group, [Ma78a, St82]. The Monte Carlo was run at  $\pi\pi$  mass intervals of 50 MeV/c<sup>2</sup> from 550 to 2000 MeV/c<sup>2</sup>, and larger mass intervals up to 4000 MeV/c<sup>2</sup>. At each mass, grids of 40  $\cos\theta_J$  bins and 18  $\varphi_J$  bins covering the intervals  $-1 < \cos\theta_J < 1$  and  $-\pi < \varphi_J < \pi$  were created at each of 14  $t_{pn}$  values from  $t_{pn} = t_{\min}$  to  $t_{pn} = -1.0$  (GeV/c)<sup>2</sup>. The  $t_{pn}$  values were  $|t_{pn}| = -t_{\min}, .01, .025, .05, .075, .100, .125, .15, .2, .3, .4, .5, .8, \text{ and } 1.0$  (GeV/c)<sup>2</sup>.

Events were generated in the x-z plane ( $\varphi_L = 0$ ) using the z-axis as the "beam".  $\cos\theta_J$  and  $\varphi_J$  were randomized within each bin. Next, the vertex coordinates ( $x_v, y_v$ , and  $z_v$ ) and the beam angles ( $\theta_B, \varphi_B$ ) were randomized. The  $x_v, y_v$ , and beam angle distributions were drawn from observed data, but the  $z_v$  distribution was taken as flat over the length of the target. Explicit beam and secondary particle absorption corrections are made to the data. The 2x2 was centered on the

projection of a beam particle with average beam angles passing through the average vertex.

The lab azimuth,  $\varphi_L$ , was *not* randomized. The Indiana event rotation accounted for this. For each generated event, an acceptance equal to the fraction of rotated (in  $\varphi_L$ ) events to pass all apertures was found. The net acceptance for a bin in  $m_{\pi\pi}$ ,  $\cos\theta_J$ , and  $\varphi_J$ , was the average (including zeros) of all Monte Carlo event acceptances for that bin.

Not needing to rotate in  $\varphi_L$  reduced significantly the required statistics, but randomizing in the other laboratory variables was needed to track their effects. The number of events generated depended on the observed event distributions and known acceptance zeros. The bin sizes were small enough that flat decay angle distributions within a bin could be used. Positive and negative magnet acceptances were sufficiently similar and the actual data sample low enough that we could allow ourselves to make one grid applicable to both polarities. As a first order average for polarities, the magnet polarity itself was randomized, the relative amount of positive and negative polarity events generated being equal to the recorded data ratio.

The Indiana calculation is not a literal event rotation, and particles are not tracked in it. Instead, the calculation exploits the following observations. Even though particles receive a considerable  $p_z$  kick by the magnet, when viewed in transverse momentum ( $p_t$ ) space, the limits of acceptance for the 2x2 and outer apertures are, to an excellent approximation, rectangles. When an event is rotated, each forward particle follows a circle in  $p_t$  space. The angle between the  $p_t$  vectors, and their magnitudes are completely determined by the variables  $x_K$  and  $P_{Lab}$ . In the absence of vees, events rotate about the beam as rigid bodies. For a given vertex location, the  $p_t$  limits are well defined, indeed linear functions of the particle's momentum at all but the lowest momenta. While separate  $p_t$  limits apply to the 2x2

and to the outer apertures, the many chamber edge limits are reduced to one set of two limits in  $p_z$  and two in  $p_y$ . More significantly, since no literal event rotation is required, particles do not have to be retracked through the magnet at each new azimuth. There is no worry that not enough examples of the azimuth were sampled since literally all azimuths are done at once.

The acceptance for a two particle event is calculated by first evaluating accepted arcs of rotation for the two particles with respect to the outer fiducial limits (the "MPS" limits), and setting the net accepted arcs as those for which both particles are allowed. The arcs are stored as a set of angles for end points, and careful accounting maintains the correlation between particles in a "rotated" event. The effect of the  $2\times 2$  is found by finding arcs forbidden by it and removing them from the accepted MPS arcs. Although the  $\Delta x \Delta y$  effect does not naturally lend itself to rotations in  $p_t$  space, it was possible to incorporate it into the arc formalism with proper correlations with the other effects. The A-station radial separation cut, section 3.3, was azimuthally symmetric. Events failing it had no good arcs at all. The acceptance is the net angular coverage of the final allowed arcs.

The  $p_t$  limits used in the MPS and  $2\times 2$  calculations were drawn from previously evaluated tables of acceptance limits versus momentum. These tables were made by tracking simulated particles through the spectrometer and searching for momentum space acceptance limits. In the simulation, all tracks were generated from a single "vertex" located at the target center, and the  $2\times 2$  counter was located by a "beam" track along the z-axis before the magnet and at the nominal beam momentum. The magnet field map [Ha75,Ma78b] was used to track particles through the magnet. In the two particle acceptance calculation, limits for actual momenta were evaluated by linear interpolation between the nearest values given in the tables. The (small) effects of the actual vertex and  $2\times 2$  locations, and the real beam angle were accounted for by first order corrections to the limit values.

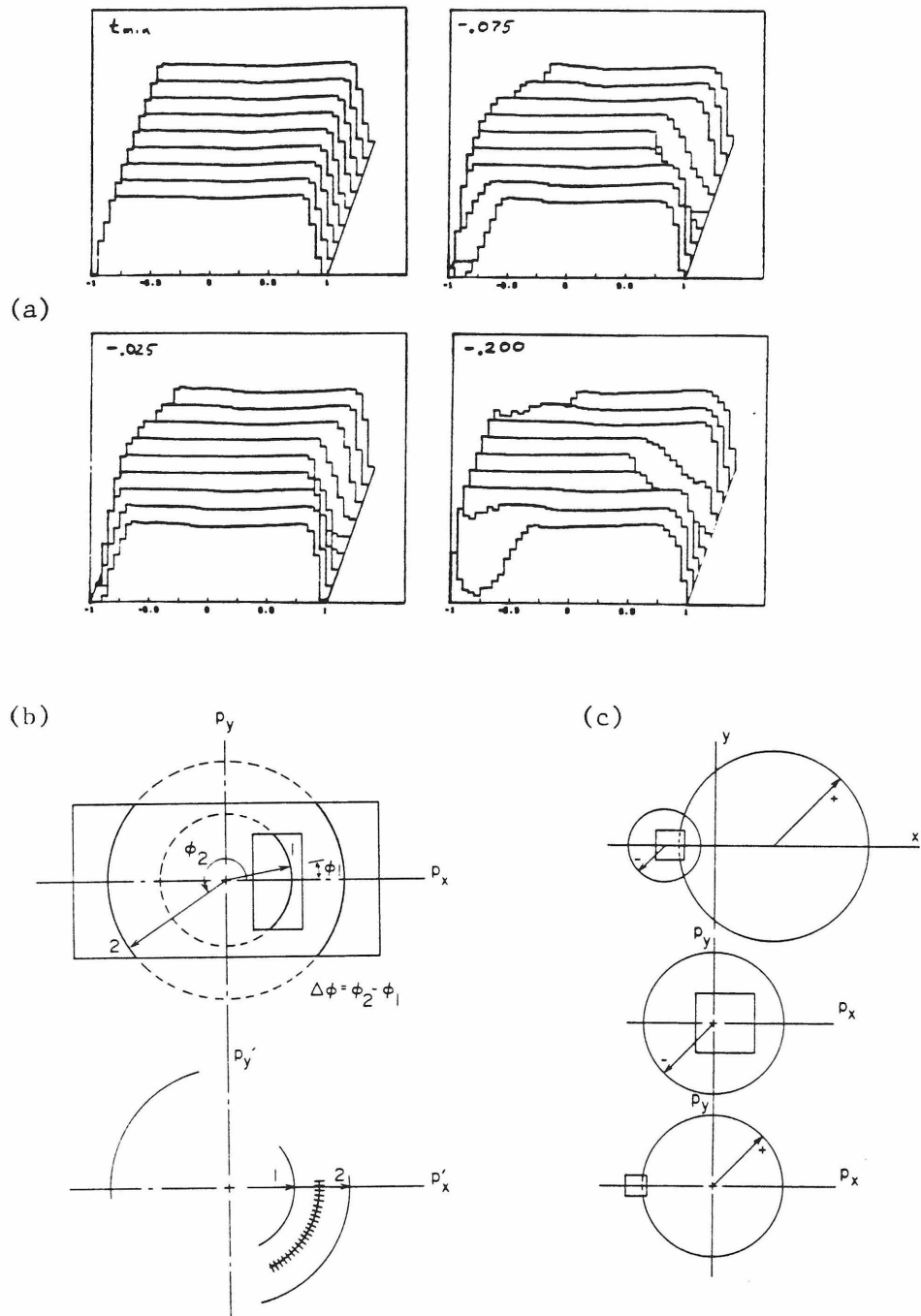


Figure 5-1. (a) 100 GeV/c acceptance at  $m_{\pi\pi} = 1.25$  and several  $t_{pn}$  values. Nine slices in  $\varphi_J$  are shown, the nearest one at  $-180^\circ$ , and the farthest at  $+180^\circ$ . Each  $\varphi_J$  slice shown is an average of two neighboring slices in the grid. The horizontal axis is  $\cos\theta_J$ . (b, c) Arcs for MPS and  $2 \times 2$  apertures, arbitrary scale. Dashed arcs are forbidden. For the  $2 \times 2$ , the upper drawing is in position space, all other arcs are in  $p_t$  space. A rigid body rotation keeps  $\Delta\varphi$  constant. Correlation calculations are shown for MPS arcs only (hatched arc is net accepted).

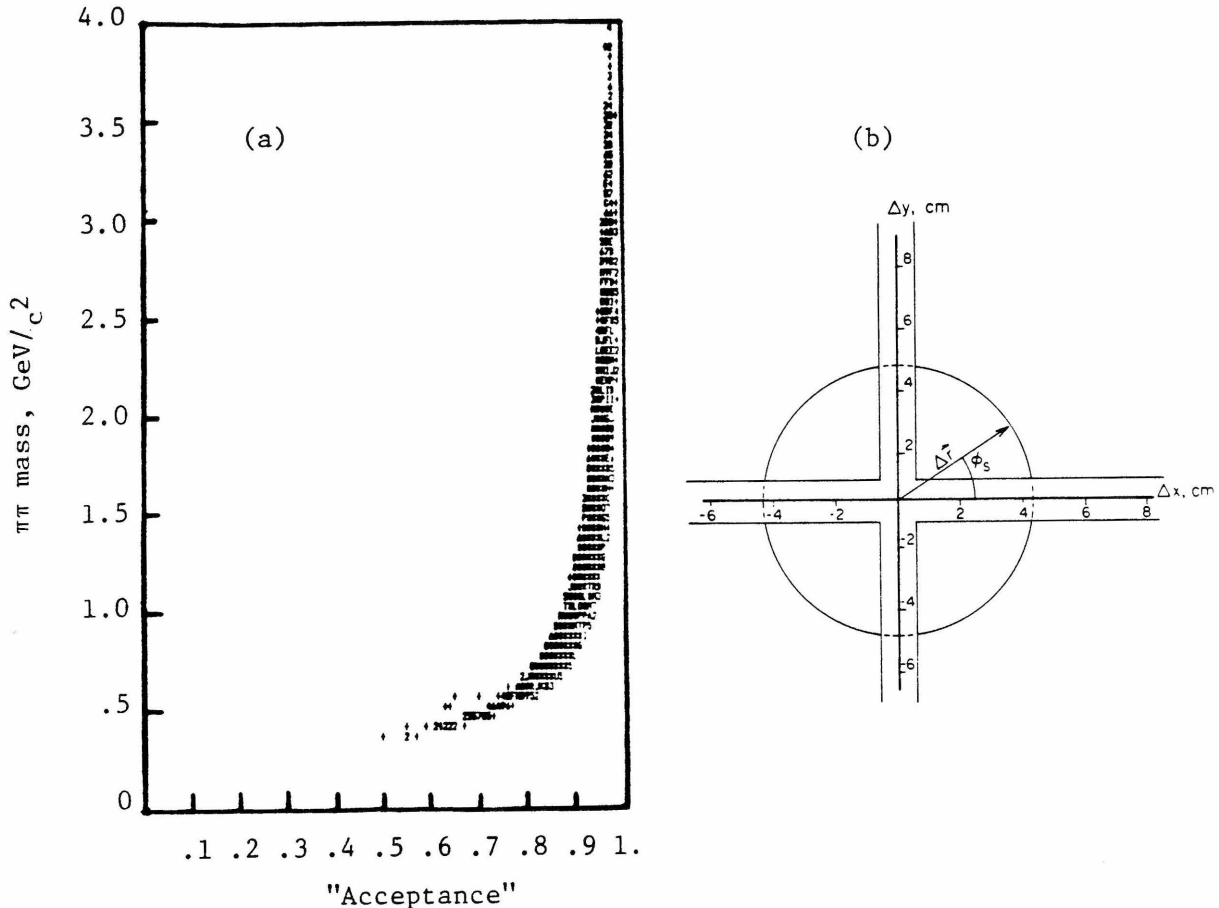


Figure 5-2. (a) "Acceptance" for the BCD  $\Delta x \Delta y$  cut at 100 GeV/c. The points are observed events, and the spread at each mass reflects decay distributions. Effects of the 2x2 and "MPS" apertures are not included in this figure. The BCD loss sets the upper limit on our acceptance at each mass. (b) Arcs for BCD effect,  $m_{\pi\pi} \approx .65 \text{ GeV}/c^2$  and  $P_{Lab} = 100 \text{ GeV}/c$ .

The Monte Carlo was checked by comparison with results from a more traditional Monte Carlo in which tracks were traced through the MPS. All lab variables, including  $\varphi_L$ , were randomized, and all fiducial cuts were applied. No difference in the results were seen.

Examples of the acceptance at 100 GeV/c are given in figures 5-1 and 5-2. In figure 5-1, examples of the grid at the  $f^0$  are shown. The forward ( $\cos\theta_f \approx 1$ ) hole is the most serious, since the  $\pi\pi$  decay distribution is peaked there at low  $t_{pn}$  and almost all masses. The 175 GeV/c acceptance is similar, although the fall offs are

smoother. Figure 5-2 shows the effect of the  $\Delta x \Delta y$  cut on our acceptance.

### 5.1.1 Acceptance Weights

In addition to use in our Monte Carlo, the  $p_t$  space rotation can be used to provide an event by event acceptance weight. Although such weights cannot correct for forbidden configurations, the correction is reasonable in regions with no absolute acceptance zeros. Used in this way, we find many observed high ( $\gtrsim 2$  GeV/c<sup>2</sup>)  $\pi\pi$  mass events have acceptance of order 10 to 20%. This implies acceptance weights up to 10, by far our largest. To avoid divergences, a 10% acceptance cut is applied when acceptance weights are applied.

## 5.2 General Correction Formalism

The formalism discussed in this section follows the one used by Grayer *et al.*, [Gr74], with modifications appropriate to our experiment. The acceptance modifies the differential distribution of produced events to create an "accepted" distribution,  $I_A$ , given by

$$I_A(\mathbf{x}_K) = A(\mathbf{x}_K) I_P(\mathbf{x}_K) , \quad (5.3)$$

where  $\mathbf{x}_K$  are kinematic variables as in equation 5.1.  $I_P$  is normalized so that

$$N_c = \int I_P(\mathbf{x}_K) d\mathbf{x}_K \quad (5.4)$$

where  $N_c$  is the fully corrected event count in equation 3.8. The acceptance  $A(\mathbf{x}_K)$  is an average over the laboratory variables,  $\mathbf{x}_L$ .

$I_A$  can also be given in terms of the observed event distribution,  $I_{obs}$ . Correcting for the losses and contaminations discussed in Chapter IV, with a weight,  $w$ , we have

$$I_A(\mathbf{x}_K) = \int w(\mathbf{x}_K, \mathbf{x}_L) I_{obs}(\mathbf{x}_K, \mathbf{x}_L) d\mathbf{x}_L \quad (5.5)$$

The forms (5.3) and (5.5) allow us to obtain  $I_P$ . If the acceptance is nonzero, they can be solved for  $I_P$ . This is the method of acceptance weights, section 5.1.1. To extrapolate  $I_P$  through acceptance zeros, one needs a good model for the reaction, or at least an expansion in a reasonably complete set of functions. That is, we express  $I_P$  as a function,  $F(\mathbf{x}_K, c_i)$ , where the  $\{c_i\}$  are parameters to be determined. A well chosen  $F$  will provide useful information on the structure of the reaction, as well as provide a reasonable extrapolation.

To apply these ideas, we bin the accepted distributions of equations (5.3) and (5.5) to give

$$f_k \equiv \int_k I_A(\mathbf{x}_K) d\mathbf{x}_K = \int_k A(\mathbf{x}_K) I_P(\mathbf{x}_K) d\mathbf{x}_K = \int_k A(\mathbf{x}_K) F(\mathbf{x}_K, c_i) d\mathbf{x}_K \quad (5.6)$$

and

$$d_k \equiv \int_k I_A(\mathbf{x}_K) d\mathbf{x}_K = \sum_{j=1}^{N_0} w_j \quad (5.7)$$

for a bin,  $k$ , in  $\mathbf{x}_K$ .  $N_0$  is the number of observed events in the bin (see equation 4.2).

To estimate the  $c_i$ , we used  $\chi^2$  minimization. The fits minimized the sum

$$\chi^2 = \sum_k \frac{(d_k - f_k)^2}{\sigma_k^2}, \quad (5.8)$$

with  $\sigma_k$  given by [Gr74]

$$\sigma_k^2 = \frac{\langle w_k^2 \rangle}{\langle w_k \rangle} f_k. \quad (5.9)$$

The average (over observed events) weight,  $\langle w_k \rangle$ , and the average square,  $\langle w_k^2 \rangle$ , in

(5.8) do not vary significantly with  $\cos\theta_J$  or  $\varphi_J$ , and  $\pi\pi$  mass variations are slight above 600 MeV/c<sup>2</sup>. We have actually used  $\sigma_k^2 = \langle w \rangle_{eff} |f_k|$ , where  $\langle w \rangle_{eff}$  is an average over all masses of  $\langle w^2 \rangle / \langle w \rangle \approx 1.01 \langle w \rangle$ . Our fits are fairly insensitive to the value of  $\langle w \rangle_{eff}$ . The claimed errors were affected more than the parameters. Using  $|f_k|$  helped to stabilize the fits when a number of bins were empty, and also helped to satisfy the physical constraint  $I_P \geq 0$ . A few violations were found in moment fits, but these corresponded to empty bins and were generally slight.

In practice, we fit on only a subset of the  $\mathbf{x}_K$ . The fits were then repeated in successive bins of the remaining variables. Our decay distribution fits have only the decay angles explicit in  $F$ . In this case, the bins,  $k$ , are  $\Delta\Omega_k = \Delta\cos\theta_J \Delta\varphi_J$ . Equation (5.6) then becomes,

$$f_k = \int_k A(\cos\theta_J, \varphi_J) F(\cos\theta_J, \varphi_J, c_i) d\Omega_k \quad (5.10)$$

Prompted by our small data sample, we took advantage of the expected symmetry about  $\varphi_J = 0$  (section 5.3), folded the data, and fit only  $0 \leq \varphi_J \leq \pi$ . The acceptances at  $\varphi_J$  and  $-\varphi_J$  were averaged, and the right hand side of (5.10) was multiplied by 2. The bin size in our moment fits (section 5.3) matched the acceptance grid,  $\Delta\cos\theta_J \Delta\varphi_J = (.05 \frac{2\pi}{18})$ , so  $A(\mathbf{x}_K)$  was pulled out of the integral. Thus for our actual fits, (5.10) was replaced by

$$f_k = 2A_k \int_k F(\cos\theta_J, \varphi_J, c_i) d\Omega_k. \quad (5.11)$$

$A_k$  was set by averaging the acceptance grids according to our mass and  $t_{pn}$  distributions. The small data sample also caused us to use relatively large bins in variables not explicit in a given fit.

Having  $f_k$  in  $\sigma_k$ , equation (5.9), makes the  $\chi^2$  problem nonlinear, although linearization can be recovered near a minimum. To deal with this efficiently, most

of our  $\chi^2$  fits used an iterative linear fit written by F. Fredericksen [Fr82]. On the first iteration  $\sigma_k = \max(\langle w \rangle_{eff}, \sum_{bin} w)$  was used to initialize the fit. On all later iterations, equation 5.9 was used. Convergence was rapid; only three iterations were needed in most fits.

Linearization of the  $\chi^2$  problem carried the benefit that the full error matrix, and hence parameter errors, followed immediately from the matrices involved. Errors for the  $c_i$  were given by the error matrix diagonal elements and were defined such that changing any  $c_i$  to  $c_i \pm \sigma_{c_i}$  shifts  $\chi^2$  by 1. A drawback of the fit was that physical constraints, such as  $I_P \geq 0$ , were not naturally incorporated. For the moment fits, (next section) we did not include this constraint. For the "high mass" fits of section 6.3, we included it only in a clumsy manner.

The iterative fit was tested on Monte Carlo data created by running events of known mass and moments (taken from [Gr74] and [Al78]) through our spectrometer simulation. The results from these tests were consistent with the input moments down to statistical levels comparable to our data.

The iterative fitter had stability troubles if the net weight in a number of bins was negative. Such cases resulted from statistical fluctuations when event by event  $\pi\pi X$  subtraction (with negative weights defined as in section 4.2) was used. For the  $\rho^0$  cross section, there was enough  $\pi\pi X$  data to fit it separately and then subtract the  $\pi\pi X$  produced event total from the  $\pi\pi n_T$  results. However, for the mass dependence of the moments, this was impractical. We can either appeal to the general similarity of the  $\pi\pi X$  decay distributions to those of  $\pi\pi n_T$  and leave the background in, or we can use negative weights for  $\pi\pi X$  and set bin contents to zero when negative counts are seen. We have chosen to leave the background in.

### 5.2.1 Moments

Any reasonable function of polar angles,  $\theta$  and  $\varphi$ , can be expanded in a series of spherical harmonic functions,  $Y_L^m(\cos \theta, \varphi)$ , [Ma70]. For particle decays, the expansion coefficients contain information on the spin of the initial state [Gr74], and can be used as input to an amplitude analysis. The Gottfried-Jackson and s-channel helicity systems both have the y-axis normal to the production plane. Parity conservation implies that for such systems,  $I_P(\theta, \varphi) = I_P(\theta, -\varphi)$ , [Ja65a]. This implies that only the real parts of the  $Y_L^m$ 's and only  $m \geq 0$  are needed, so the harmonic expansion we use is

$$I_P(m_{\pi\pi}, t_{pn}, \Omega) = \sum_L \sum_{m=0}^L t_L^m \operatorname{Re} Y_L^m(\Omega) \quad (5.12)$$

where  $\Omega = (\cos \theta, \varphi)$  and  $m_{\max} = l$ . The  $t_L^m$  are real functions of  $m_{\pi\pi}$  and  $t_{pn}$ , but are assumed constant in each mass and  $t_{pn}$  bin fit. The normalization condition (5.4) is

$$N_c = \sqrt{4\pi} t_0^0 \quad (5.13)$$

Normalized spherical harmonic moments, given by

$$\langle \operatorname{Re} Y_L^m \rangle = \frac{1}{N_P} \int I_P(\Omega) \operatorname{Re} Y_L^m(\Omega) d\Omega = \frac{t_L^m \varepsilon_L^m}{N_P} \quad (5.14)$$

are frequently used. The use of only  $\operatorname{Re} Y_L^m$  requires the term  $\varepsilon_L^M$ , where  $\varepsilon_L^0 = 1$  and  $\varepsilon_L^{m \neq 0} = \frac{1}{2}$ . The normalized moments tend to remove the mass dependences of resonant amplitudes and display more clearly the relative importance of the various moments than unnormalized moments do.

If only a finite number of moments are present, or at least significant, the series in equation 5.7 may be truncated at some  $l = l_{\max}$  and  $m = m_{\max} \leq l$ . At  $\pi\pi$  masses below about 2 GeV/c<sup>2</sup>,  $\pi\pi$  angular distributions are well described by such a series. At higher masses, the usefulness of moment expansions becomes limited,

mainly because of the uncertainties in fitting large numbers of moments (see section 5.5) with limited data sets.

Spin information in the moments is contained in the indices  $L$  and  $m$ . The highest  $L$  moment generated by a state of angular momentum  $l$  is  $L = 2l$ , which should project out more pure  $l$  intensity than moments with  $L < 2l$ . Odd  $L$  moments contain information on interference between neighboring even  $L$  moments. The index  $m$  combines information on the nucleon helicity flip and the spin of the exchange involved. If just  $\pi$  exchange without absorptive effects were present, only  $m = 0$  would be needed. In this case, the  $\varphi_J$  distributions would be flat [Tr62]. Spin 1 exchange yields moments with  $m = 0, 1$ , and  $2$ . In the Williams model (PMA), see [Wa73], moments with  $m = 1$  measure interference between pure  $\pi$  exchange and absorptive corrections to it, and furthermore,  $m = 2$  moments are forbidden [Oc73]. Pure  $\pi$  exchange is mainly nucleon helicity *non*-flip in the Gottfried-Jackson frame, while spin 1 exchanges are dominately helicity flip. The moment distribution thus reflects not only the spin of the decaying system, but the spins of the exchanges that formed the  $\pi\pi$  final state.

### 5.3 Cross Section Results

Before considering the general decay distribution results, we complete our normalization. The  $\rho^0$  region of the mass spectrum is known to be dominated by the spin 1  $\rho^0$  resonance, but a small s-wave background is also present, as well as interference effects with D-waves. In addition, effects of  $\rho$ - $\omega$  interference have been observed in high statistics experiments at high  $t_{pn}$ . This relatively low mass region is thus rather complex. Even separating the resonant intensity from the s-wave background is a nontrivial, model dependent affair. For these reasons, we chose to follow Grayer *et al.* and quote only the cross section for the same mass and  $t_{pn}$  cuts used at 17.2 GeV/c, [Gr74].

The mass interval is  $.60 \leq m_{\pi\pi} \leq .94 \text{ GeV}/c^2$  and the  $t_{pn}$  interval is  $|t_{pn}| \leq .15 \text{ (GeV}/c)^2$ . Data from the  $\pi\pi n_T$  and  $\pi\pi X$  triggers were fit separately with moments having  $L_{\max} = 2$  and  $m_{\max} = 1$ . The  $\pi\pi X$  veto failure weights, section 4.2, were set *positive* for these fits. The background correction was made by subtracting the  $\pi\pi X$  produced event count from the  $\pi\pi n_T$  produced event count. No scalar analysis was done on the  $\pi\pi X$  data. The veto failure weight was designed to scale the  $\pi\pi X$  data for a direct subtraction from  $\pi\pi n_T$ . Five mass bins,  $.60\text{--}.70$ ,  $.70\text{--}.77$ ,  $.77\text{--}.84$ , and  $.84\text{--}.94 \text{ GeV}/c^2$ , were used, for the fits, and their results added. A single  $t_{pn}$  bin was used. These bins were selected to maintain reasonable statistics for both the  $\pi\pi n_T$  and  $\pi\pi X$  fits. The tight target cut,  $-.51 \leq z_v \leq -.30 m$ , with a cross section per event of  $\sigma_1 = .216 \mu b$  at  $100 \text{ GeV}/c$  was applied. Data from both magnet polarities were combined for these fits.

Our  $\rho^0$  region cross section result is

$$\sigma_{\rho^0} = (.934 \pm .040 \pm .053) \mu b, \quad (5.15)$$

where the first error is statistical, and the second systematic. Table 5.1 summarizes the fit results. We emphasize that what we call the " $\rho^0$ " cross section is actually the cross section for the reaction  $\pi^- p \rightarrow \pi^+ \pi^- n$  with the cuts  $.60 \leq m_{\pi\pi} \leq .94 \text{ GeV}/c^2$  and  $|t_{pn}| \leq .15 \text{ (GeV}/c)^2$ .

We note that the  $\pi\pi X$  background at the  $\rho^0$  is about 13% of the  $\pi\pi n_T$  signal. This is a worst case. The background as a fraction of  $\pi\pi n_T$  falls with mass to negligible amounts above  $2 \text{ GeV}/c^2$ . (Figure 1-2 indirectly implies this.)

Our cross section at  $175 \text{ GeV}/c$  for the same mass and  $t_{pn}$  cuts was evaluated by Fredericksen, [Fr82]. His result is  $\sigma_{\rho^0} = (.229 \pm .012 \pm .010) \mu b$ . Our 100 and  $175 \text{ GeV}/c$  cross sections along with the low energy result of Gr74 are given in figure 5-3. PMA includes a basic  $1/P_{lab}^2$  dependence for the cross section, and this is often used as a benchmark for the  $\rho^0 n$  cross section. The line in figure 5-3 passes

Table 5.1		
100 GeV/c $\rho^0$ cross section		
Trigger	Events	$N_c$
$\pi\pi m_T$	1414	$4972.3 \pm 140.5$
$\pi\pi X$	416	$647.5 \pm 58.2$
$\pi\pi m$		$4324.8 \pm 152.1$
$\sigma_1$		$.216 \pm .008 \text{ nb}$
$\sigma = N_c \sigma_1$		$.934 \pm .066 \text{ } \mu\text{b}$

through the 17.2 GeV/c point and falls as  $1/P_{lab}^2$ .

Low energy  $\rho^0$  cross section measurements have shown a persistent lack of consistency in method for background subtraction and mass and  $t_{pn}$  interval selection. Also,  $t_{\min}$  effects are significant at beam momenta below about 10 GeV/c. Compilations of low energy  $\rho^0 n$  cross sections find dependences in the  $1/P_{lab}^{1.89 \pm .09}$  [Br72] to  $1/P_{lab}^{2.07 \pm .04}$  [Gi72] range. Since we use the same mass and  $t_{pn}$  cuts, we feel that the Gr74 point is the only published low energy cross section directly comparable to our values.

The 100 GeV/c point is within errors of the line in figure 5-3, but the 175 GeV/c point is significantly lower. Taking our two points together, we find that the cross section falls off more quickly, not slower, than  $1/P_{lab}^2$ . In terms of PMA, the extra drop off of the  $\rho^0 n$  cross section requires a steepening of the  $d\sigma/dt_{pn}$  distribution. This can be obtained by having larger exponential slopes for the collimating factors of PMA at the higher energies. The high precision results of Wicklund *et al.* [Wi78] require just such an effect. We note that our  $t_{pn}$  distribution fits, though not

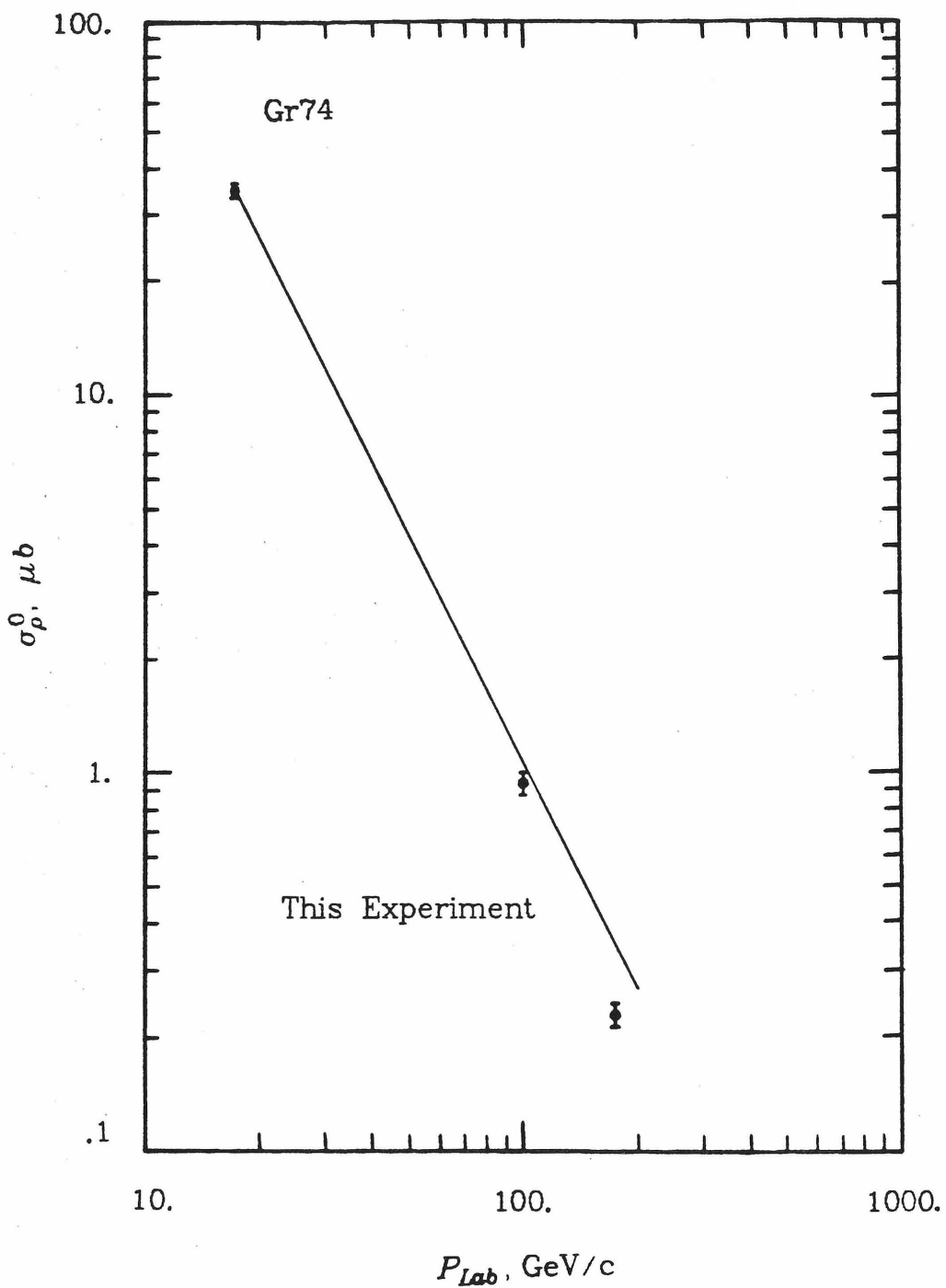


Figure 5-3. Cross section results for the  $\rho$  mass band and  $|t_{pn}| < .15$   $(\text{GeV}/c)^2$ . Also shown is the Cern Munich 17.2  $\text{GeV}/c$  result, [Gr74]. The line follows  $1/P_{Lab}^2$  and passes through the low energy point.

reliable, do show such an increase in the exponential slopes, and are roughly at values expected by extrapolating the trends of Wi78. In more basic terms, if  $\pi$  exchange is still dominant at our energies, and the effective  $\pi$  trajectory,  $\alpha(t)$ , is negative, then the  $s^{2\alpha-2}$  dependence of the cross section exceeds  $1/P_{lab}^2$  ( $s \approx 2m_\pi P_{lab}$ ). An effective  $t_{pn}$  averaged  $\alpha$  of about -.06 is sufficient to bring both our values within errors of a straight line through the 17.2 GeV/c point.

In the sections that follow, we relax the target vertex cut from the one used above to  $-.65 \leq z_v \leq -.23$  m. Although outside the flask, virtually all the data passing this cut came from interactions in the hydrogen, and as for the tight cut, feed-in feed - out losses are negligible. We scale the cross section per event for the expanded cut, yielding .146 nb at 100 GeV/c and .047 nb at 175 GeV/c. An error of 10% should be assumed for these numbers, mainly because the  $\pi\pi X$  background has been left in.

#### 5.4 The $\pi\pi$ Mass Spectrum

As discussed in Chapter I, the uncorrected  $\pi\pi$  mass spectrum shows prominent  $\rho^0$  and  $f^0$  peaks, as well as a weak  $g^0$  and a high mass continuum. Figures 5-4ab show  $\pi\pi$  mass spectra from our moment fits (next section) at 100 and 175 GeV/c. A  $|t_{pn}| \leq .15(GeV/c)^2$  cut was used, and  $m_{max} = 1$  was imposed. The lower curve in each figure is the uncorrected final event sample in 50 MeV/c bins.

In these figures, the  $\rho^0$  and  $f^0$  are clear. The  $g^0$  is a weak presence, especially at 175 GeV/c, but it seems real. At the mass spectrum level, the  $h^0$  is a lost cause in both uncorrected and corrected distributions. We note that Corden *et al.* [Co78] needed an amplitude analysis to pull out convincing  $g^0$  and  $h^0$  signals. Only a mere hint of the  $g^0$  was visible in their corrected mass spectrum, and the  $h^0$  was invisible at that level. Having not done an amplitude analysis, we will not be able to make any claims for the  $h^0$ , but will refer to the 2 GeV/c<sup>2</sup> region as the  $h^0$  region, and

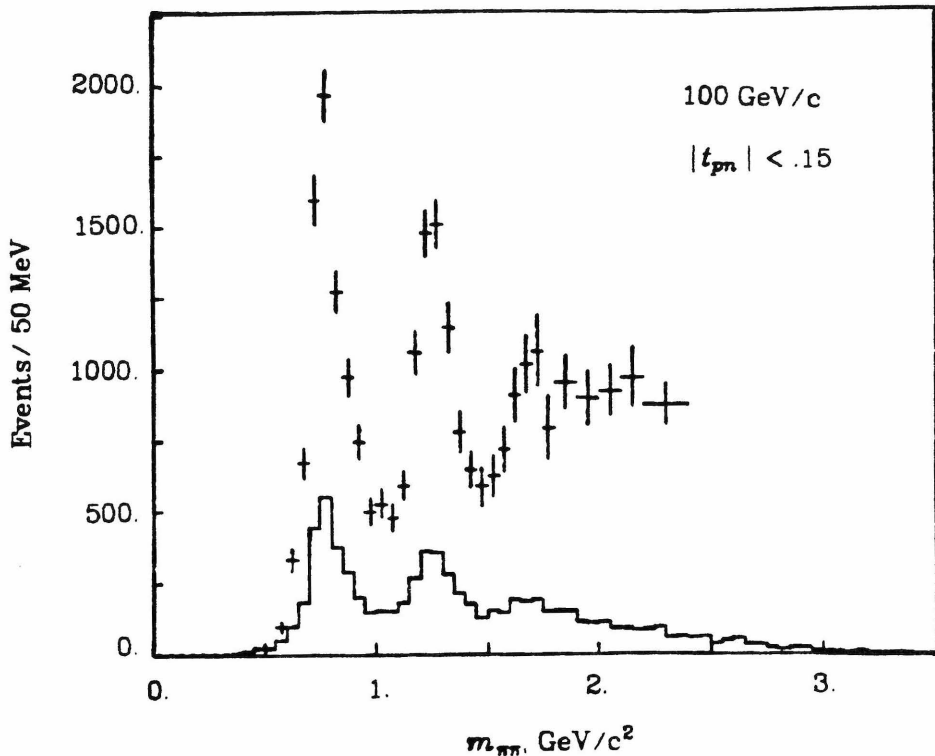


Figure 5-4a 100 GeV/c  $\pi\pi$  mass spectrum for  $|t_{pn}| < .15$  (GeV/c) $^2$ . Points with error bars are produced event totals from moment fits with  $L_{\max} = 8$  and  $m_{\max} = 1$ . The histogram is the uncorrected event total in 50 MeV/c bins from figure 1-2.

note features of the data there.

Above the  $g^0$ , we observe a slowly increasing distribution at 175 GeV/c, and a flat distribution at 100 GeV/c. With few exceptions, the individual bins are not statistically incompatible. The better high mass statistics and acceptance at 175 GeV/c imply that figure 5-4b is a better estimate of the mass spectrum above  $m_{\pi\pi} \approx 1.9$  than figure 5-4a. However, as noted in the next section, we expect that moment fits generally underestimate the high mass distributions. The high mass decay distribution seems more compatible with an exponential (in  $\cos\theta_J$ ) than a sum of harmonic moments.

This inspired another set of fits, described in section 6.3, which first fit just the  $\varphi_J$  dependence in slices of  $\cos\theta_J$ . The  $\varphi_J$  fits were to the form  $I_0 + I_1 \cos\varphi_J$ . Since

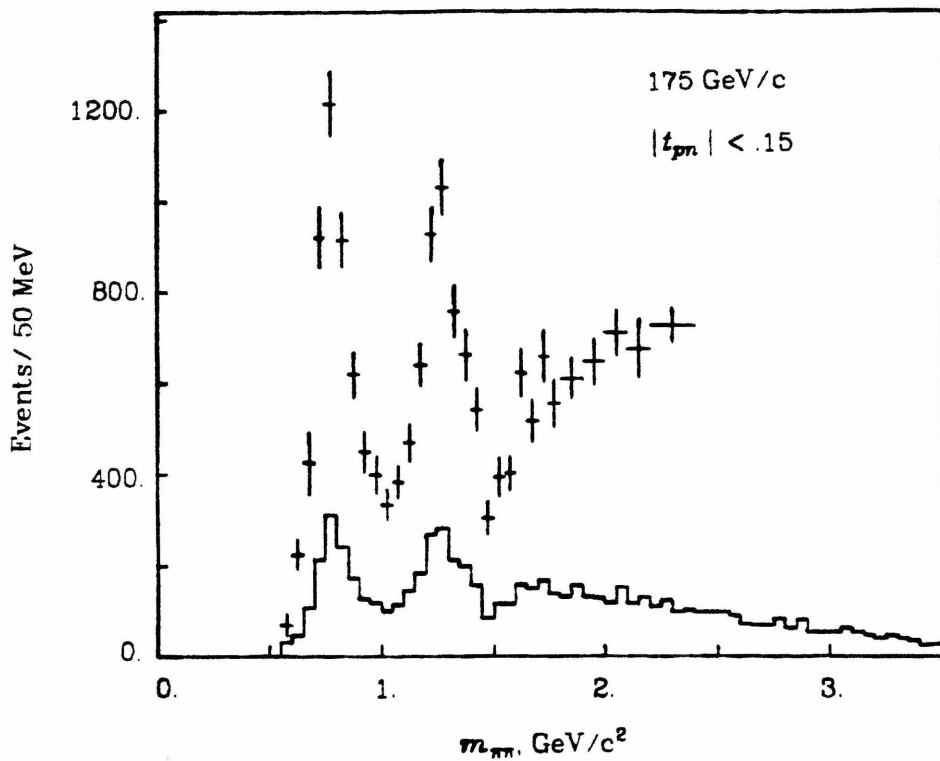


Figure 5-4b 175 GeV/c  $\pi\pi$  mass spectrum for  $|t_{pn}| < .15$  (GeV/c)<sup>2</sup>. Points with error bars are produced event totals from moment fits with  $L_{\max} = 8$  and  $m_{\max} = 1$ . The histogram is the uncorrected event total in 50 MeV/c bins from figure 1-2.

$\int_{-\pi}^{\pi} \cos\varphi d\varphi = 0$ , only the  $I_0$  term appears in the  $\cos\theta_J$  projection, and this term was used in a second set of fits. At low  $\pi\pi$  masses, we fit  $I_0$  to a sum of Legendre polynomials, and at masses above 1.9 we fit only the forward peak to an exponential. This method makes more demands on the data than a moment fit, and at low masses 100 MeV/c mass bins were used. The mass spectra from these fits are shown in figures 5-5ab. We observe that the high mass spectra run a bit above the moment results, although the 100 GeV/c results weren't "helped" that much. These fits run slightly below the moment results at the  $\rho^0$ , but the disagreement is not as bad as it appears in the figures. Rebinning the moment fit results, we find that the " $\varphi$  fits" are just over one standard deviation low at the  $\rho^0$ , and are in complete agreement with moments in the  $f^0$  and  $g^0$  regions. We feel that the moment results are more

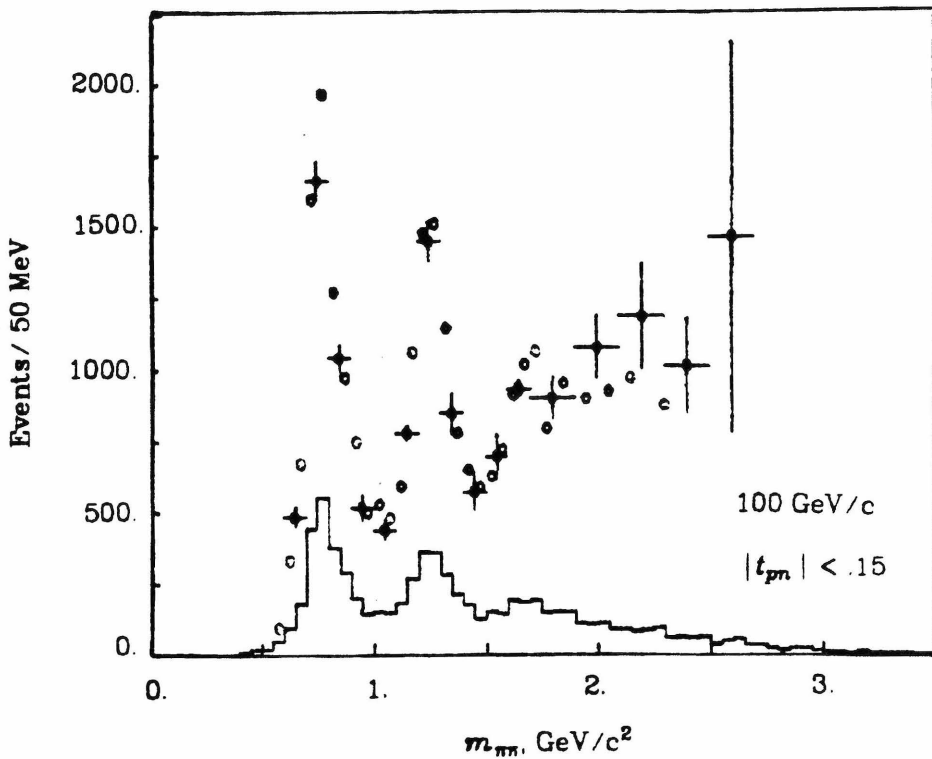


Figure 5-5a 100 GeV/c  $\pi\pi$  mass spectrum for  $|t_{pn}| < .15$  (GeV/c) $^2$ . Points with error bars are produced event totals from fits described in section 6.3. The fits were in 100 MeV/c $^2$  bins at low masses, but we plot the results as events/50 MeV for comparison to the moment fits (open circles). The vertical scale is the same as in figure 5-4a. Error bars for the moment fit results were excluded here for clarity.

reliable whenever a moment sum (equation 5.12) can be used. For our data, this means moment results are preferred below  $\approx 1.9$  GeV/c $^2$ . Above about 2.0 to 2.2 GeV/c $^2$ , the  $\varphi$  fit method is preferred if we accept an exponential forward peak.

Figures 5-5ab are consistent with high statistics results of the ACCMOR collaboration at 63 GeV/c [Da79], which were obtained by similar methods. The exponential  $\cos\theta_J$  dependence claim is much more compelling for their data than ours. Their data also give an indication of what we might expect to see at the  $g^0$ . With our data set, statistical errors would almost wash their  $g^0$  out of the mass spectrum.

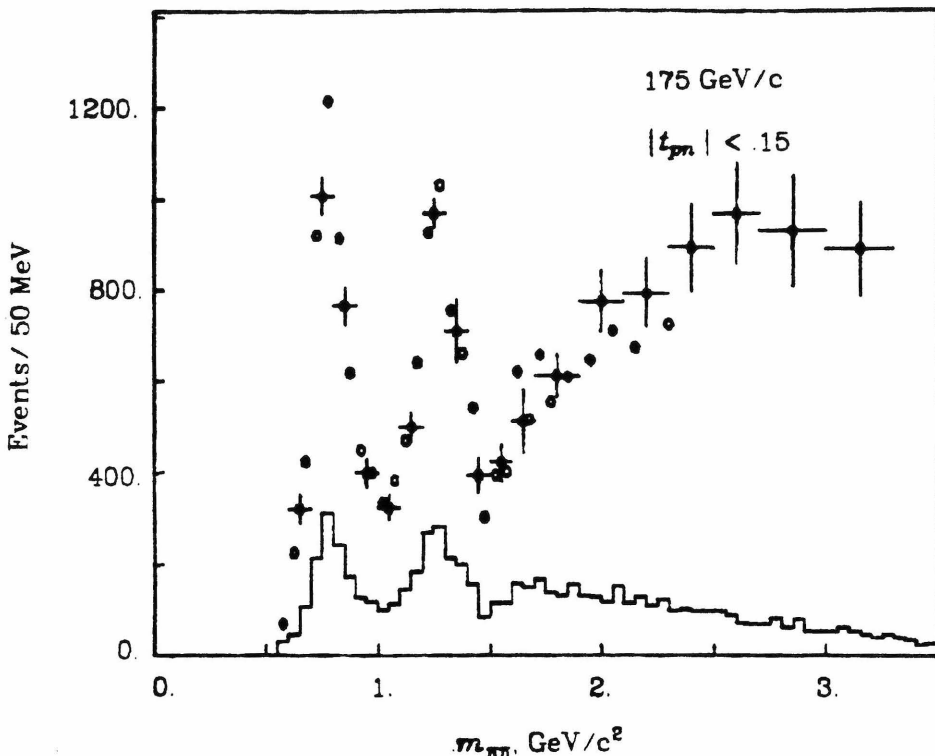


Figure 5-5b 175 GeV/c  $\pi\pi$  mass spectrum for  $|t_{pn}| < .15$  (GeV/c) $^2$ . Points with error bars are produced event totals from moment fits described in section 6.3. The open circles are the produced event totals of figure 5-4b. Error bars were excluded here for clarity.

Our mass distributions at high masses run a bit above those of Co78 at 15 GeV/c, but their data stops at 2.2 GeV/c $^2$ . Our mass spectra seem at odds with the results of Robertson *et al.* at 25 GeV/c, a low statistics bubble chamber experiment.

Figures 5-6ab are mass plots for a  $.15 < |t_{pn}| < 1.0$  (GeV/c) $^2$  cut. In this case, only moment fits were used for the acceptance correction. 100 MeV/c $^2$  mass bins were used,  $L_{\max}$  values stopped at 6, and  $m_{\max}$  was 2. These selections were motivated by the low event counts at high  $t_{pn}$ . The  $\rho^0$  and  $f^0$  are prominent again. A reasonable  $g^0$  is seen (this time its better at 175 GeV/c). We note that the high mass region does not increase with mass. This may be due to the  $L_{\max}$  used in the high  $t_{pn}$  fits. The high  $t_{pn}$  acceptance is relatively better, when compared to decay

distributions, than at low  $t_{pn}$ , but the raw event totals were much lower.

The plots given so far are too coarse to show a number of fine scale features reported by Grayer *et al* at 17.2 GeV/c. These features are shoulders on the high side of the  $\rho^0$  and  $f^0$  peaks at  $\approx 980$  and  $1460$  MeV/c $^2$ , respectively, and effects from  $\rho$ - $\omega$  interference at large  $t_{pn}$ . We searched for these in fine binned, weighted mass plots, but our small data set washed out any effects with fluctuations. In particular, we can neither confirm nor deny the presence of  $\rho$ - $\omega$  interference in our data. Effects related to the shoulders are seen in the moment results, and we turn to them now.

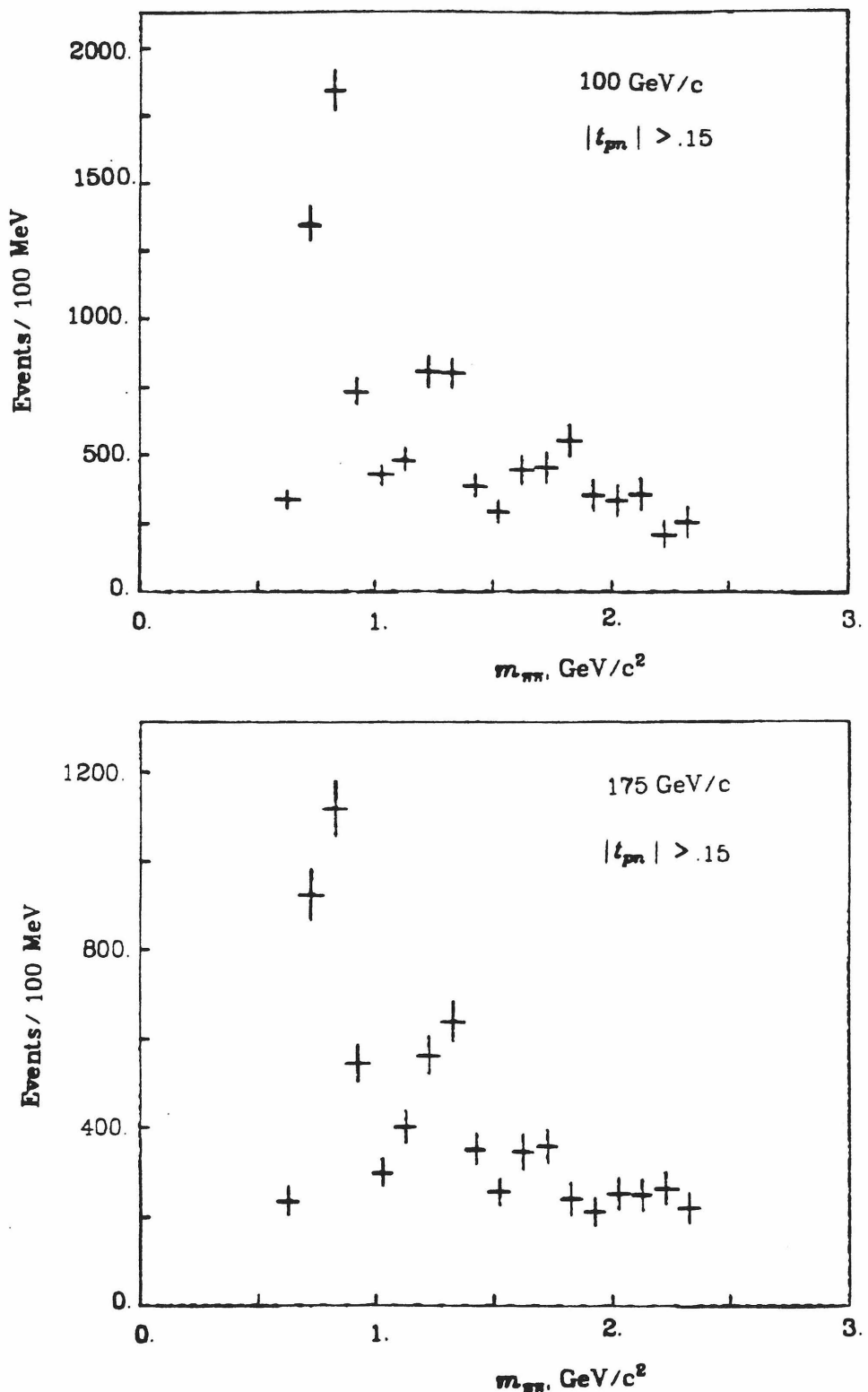


Figure 5-6. High  $t_{pn}$  mass spectra at 100 and 175  $\text{GeV}/c$ .  $.15 < |t_{pn}| < 1.0$   $(\text{GeV}/c)^2$ .

### 5.5 Moments versus Mass

Data up to  $\pi\pi$  masses of 2.4 GeV/c<sup>2</sup> were fit in the Gottfried - Jackson frame to the form (5.12). Figures 5-7 to 5-10 show  $\langle \text{Re } Y_L^m \rangle$  and  $t_L^m = \varepsilon_L^m N_P \langle \text{Re } Y_L^m \rangle$  at 100 and 175 GeV/c as a function of mass for  $|t_{pn}| < .15 \text{ (GeV/c)}^2$ .

Because of our small data sample, a single  $t_{pn}$  bin was used for these fits, and the smallest mass bin was 50 MeV/c<sup>2</sup>.  $L_{\max}$  values given in Table 5.2 were used, as well as  $m_{\max} = 1$ . Higher moments than those used were found consistent with zero in preliminary fits and excluding the high moments improved the fits. ("Threshold" means the first bin fit, usually 550 MeV/c<sup>2</sup>.) Figure 5-11a shows 100 GeV/c  $\langle Y_L^2 \rangle$  results from preliminary fits with  $|t_{pn}| < .15 \text{ (GeV/c)}^2$ . Figure 5-11b shows  $L = 9$  and 10 results from another preliminary fit on the same  $t_{pn}$  interval. In both cases, the moments are, within our statistics, consistent with zero, and were excluded in later fits. In the high  $L$  case, we interpret this not as meaning the absence of the moments from the produced distributions, but rather that our small data set is unable to extract such moments. We're better off constraining them to zero to reduce the number of parameters in the fits.

Table 5.2 Moment Constraints			
$L_{\max}$	Mass	$L_{\max}$	Mass
0	Threshold	5	1300 MeV
1	Threshold	6	1300 MeV
2	Threshold	7	1700 MeV
3	700 MeV	8	1700 MeV
4	900 MeV	$\geq 9$	unused

In some regions, especially the 175 GeV/c  $\rho^0$ , the moments are not well determined. Errors and fluctuations are large. Our results are "fragile" in the sense that including extra moments or going to much smaller mass bins can cause the fits to go berserk. Patently unacceptable results can be obtained if some caution is not

used. This was our primary motive for allowing only moments that were either well established in lower energy experiments or were required by our data. Our low statistics, compared to the complex and often rapid dependence of the  $\pi\pi n$  reaction on *all* kinematic variables, is the primary reason for our troubles. Our confidence in the results rests on reasonable  $\chi^2$  per degree of freedom values, and also on the agreement between fit results and weighted data in good acceptance regions. With these caveats, we consider some of the features seen in figures 5-7 to 5-10, and compare our results to lower energy results.

Our mass dependence results for 100 and 175 GeV/c seem consistent with each other, and generally similar to low energy results at 17.2 GeV/c [Gr74], and 15 GeV/c [Co78]. Above the  $g^0$  mass, we are more consistent with the 15 GeV/c results than those at 17.2 GeV/c. The data in figures 5-7 and 5-8 ( $N\langle Y_L^m \rangle$ ) show few surprises. The  $\rho$  and  $f$  signals are present in moments expected for their known spins. In the preliminary fits, no peaks were seen for these states in moments higher than  $L = 2l$ , where  $l$  is the spin of the resonance (1 for the  $\rho$  and 2 for the  $f$ ). The shoulders and rapid falls on the high sides of the  $\rho^0$  and  $f^0$  reported by Gr74 (at  $\approx 1$  and 1.4 GeV/c<sup>2</sup>) seem present in our data. Perversely, the  $\rho^0$  shoulder is best seen in the 100 GeV/c  $L=0, m=0$  plot, and the  $f^0$  shoulder is seen only in the 175 GeV/c  $L=2, m=0$  data. The  $g^0$  seems to be present, but puzzling. As with the  $\rho^0$  and  $f^0$ , the  $g^0$  mass region has bumps, admittedly small, in low order moments. However, in the crucial  $L = 6$  moments, the  $g^0$  is again perverse. At 100 GeV/c, we see fluctuations consistent with the  $g^0$ . At 175 GeV/c, the  $L = 6, m = 0$  moment does not have the desired bump. The absence might be blamed on statistical fluctuations, but is nonetheless disappointing.

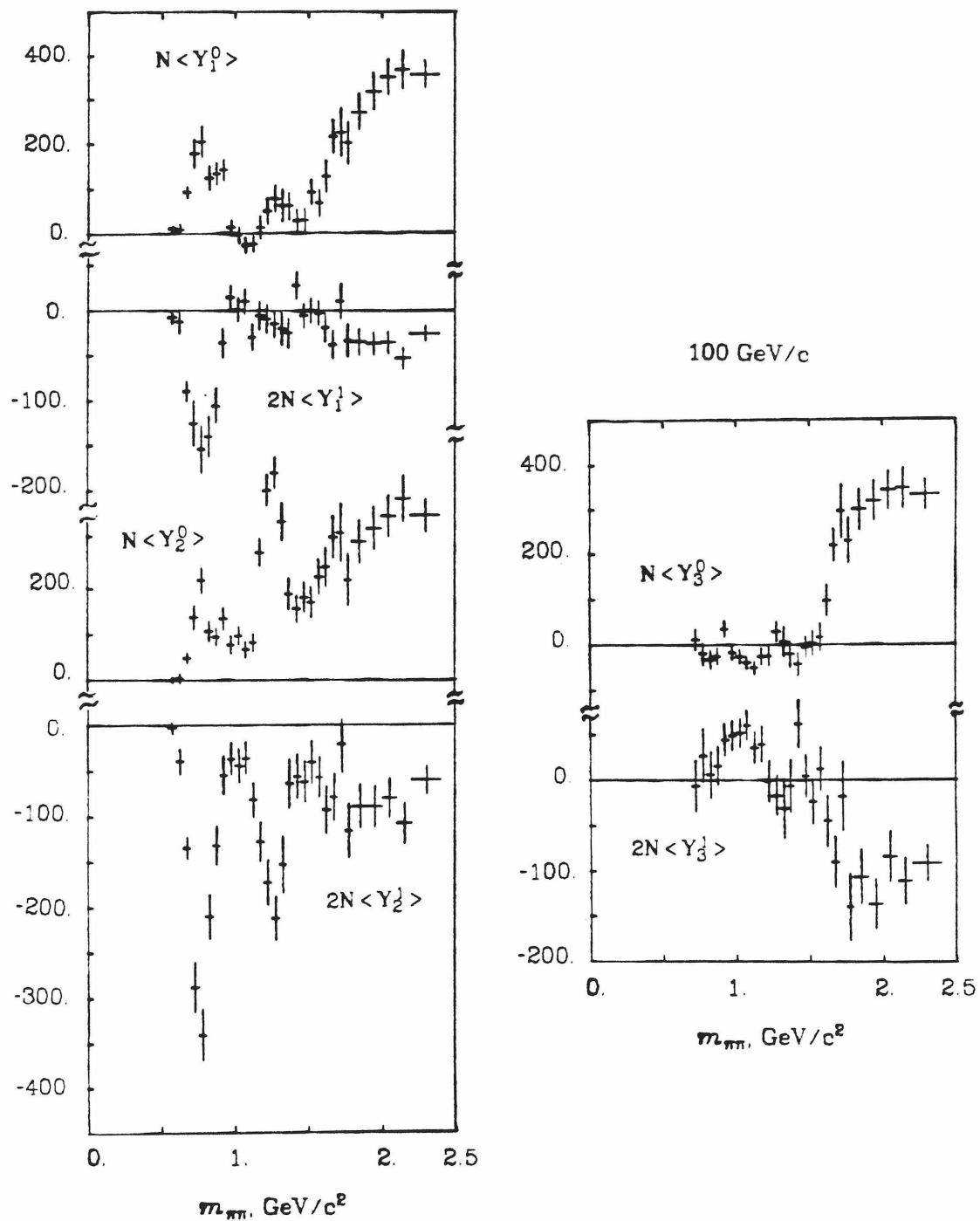


Figure 5-7a Unnormalized moments at 100 GeV/c.  $N < Y_0^0 >$  was plotted in figures 5-4ab. A  $|t_{pn}| < .15 \text{ GeV/c}$  cut was used for these fits.

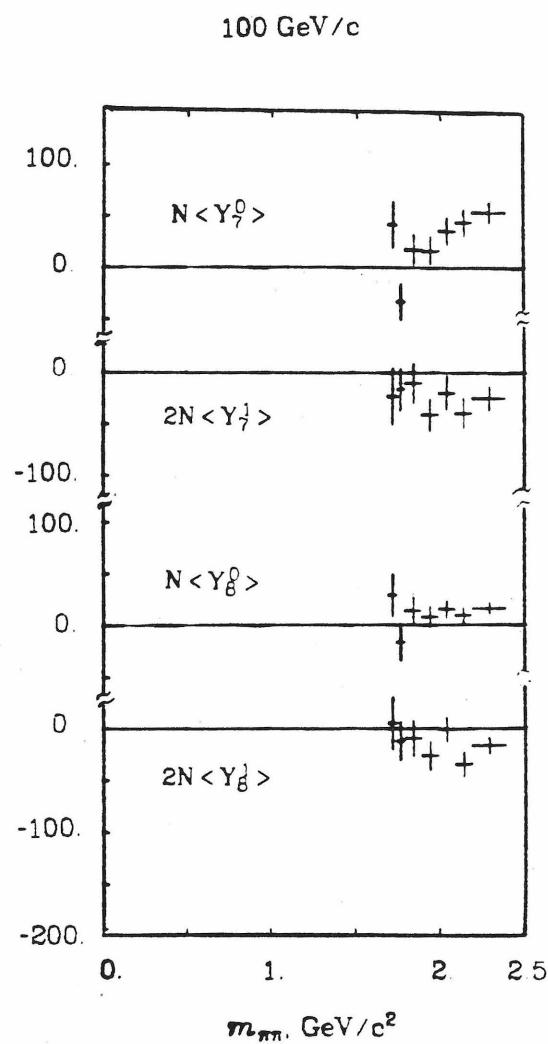
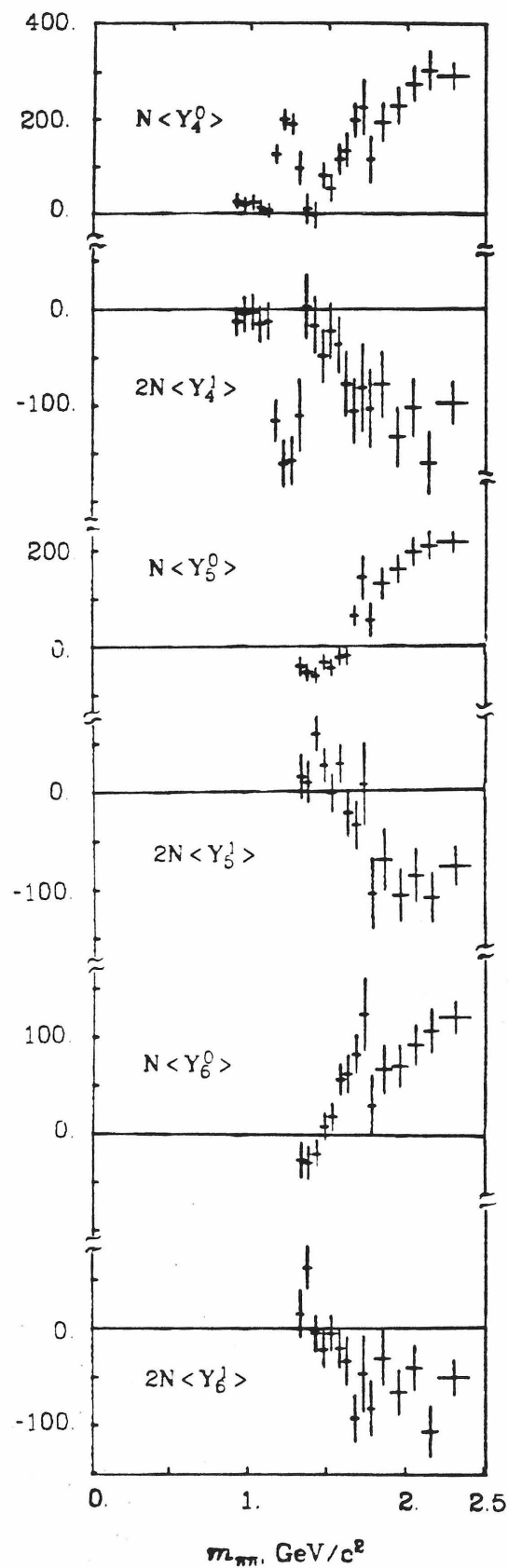


Figure 5-7b. See previous caption

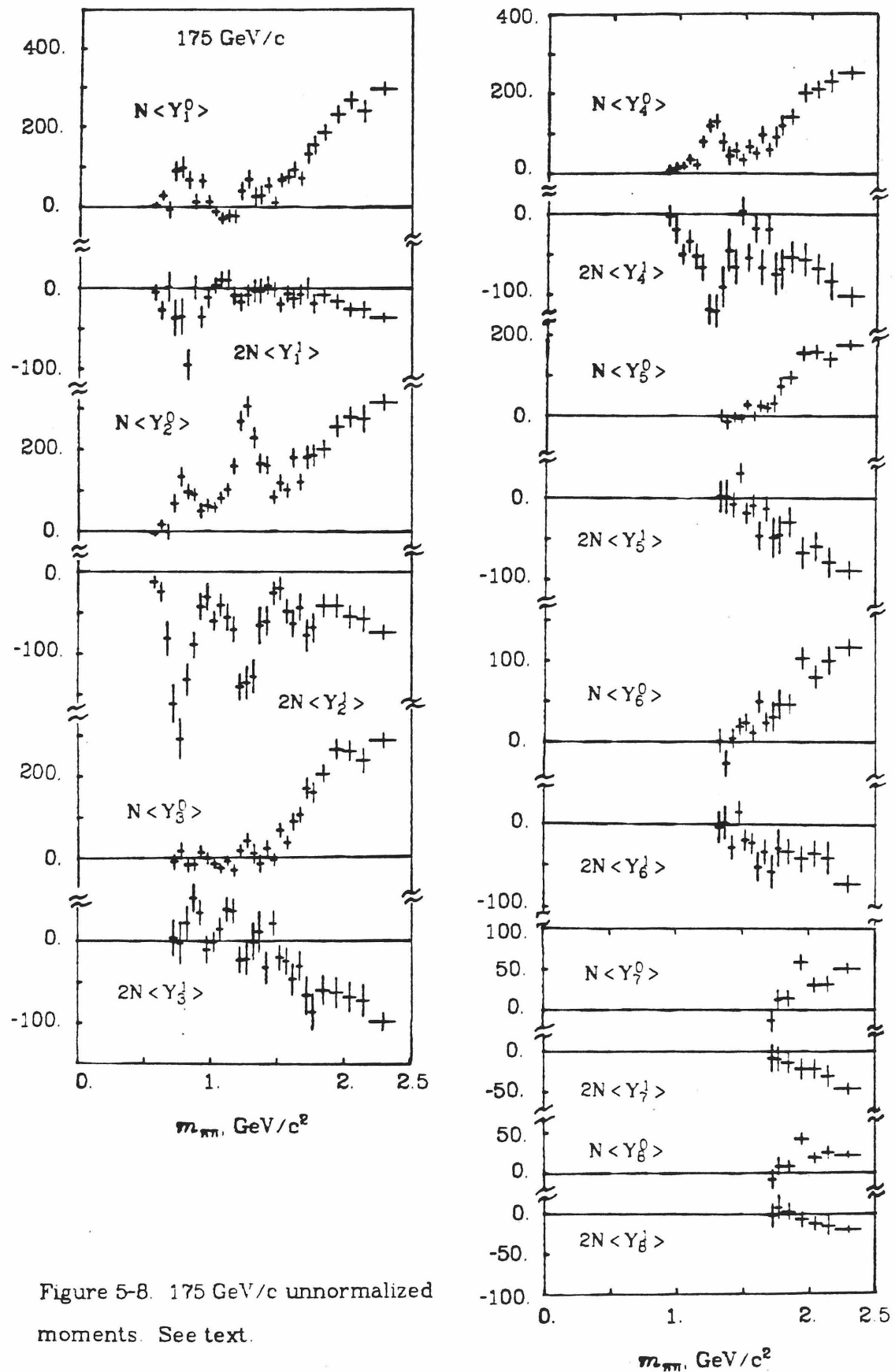


Figure 5-8. 175  $\text{GeV}/c$  unnormalized moments. See text.

The 175 GeV/c data may contain hints of the  $h^0$ . Fluctuations of the type one would expect are present in a number of moments, even the  $L = 8$  moments. However, our binning is quite large at the  $h^0$  mass, and a one bin fluctuation does not make a resonance. The fact that it is seen in a number of moments can also be explained as propagating fluctuations in the fit. This caution might also be applied in the 100 GeV/c  $g^0$  signal. No obvious  $h^0$  signal seems present in the 100 GeV/c moments.

We note that the  $m = 0$  and 1 moments are largely of opposite sign, a condition consistent with PMA and the more sophisticated Regge models for  $\pi\pi n$ . Also, with the exception of the 100 GeV/c  $L = 8$  moments, all the moments we have plotted in figures 5-7 and 8 are solidly non zero at all masses above 1.6 to 2 GeV/c<sup>2</sup>. The noted exception may very well have been a case like the  $L = 9$  and 10 moments. That is, our data is not good enough to sense its presence.

Figures 5-9 and 5-10 give our normalized moments for the two beam momenta. Since produced event counts are removed from the averages, these moments are directly comparable with those at 15 and 17 GeV/c. We note that the rapid drops already discussed become more prominent in the normalized moments. For the most part, we appear quite consistent with the lower energy results. Some of the caveats of the proceeding paragraphs still apply, but the broad agreement, spanning an order of magnitude in beam momentum from the other experiments to ours, speaks strongly for the stability of the  $\pi\pi n$  reaction.

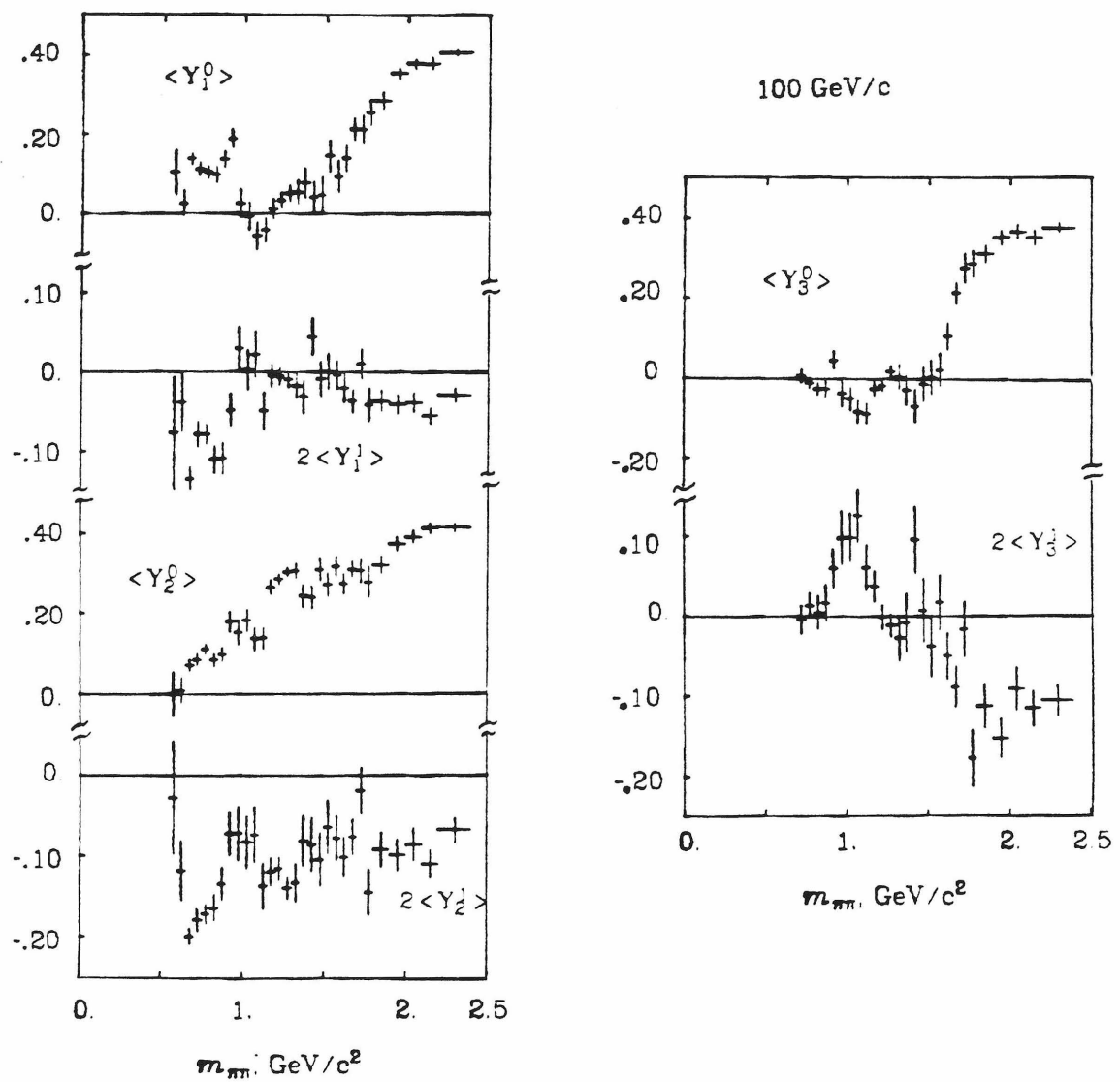


Figure 5-9a.  $100 \text{ GeV}/c$  normalized moments for  $|t_{pn}| < .15 \text{ (GeV}/c)^2$ .

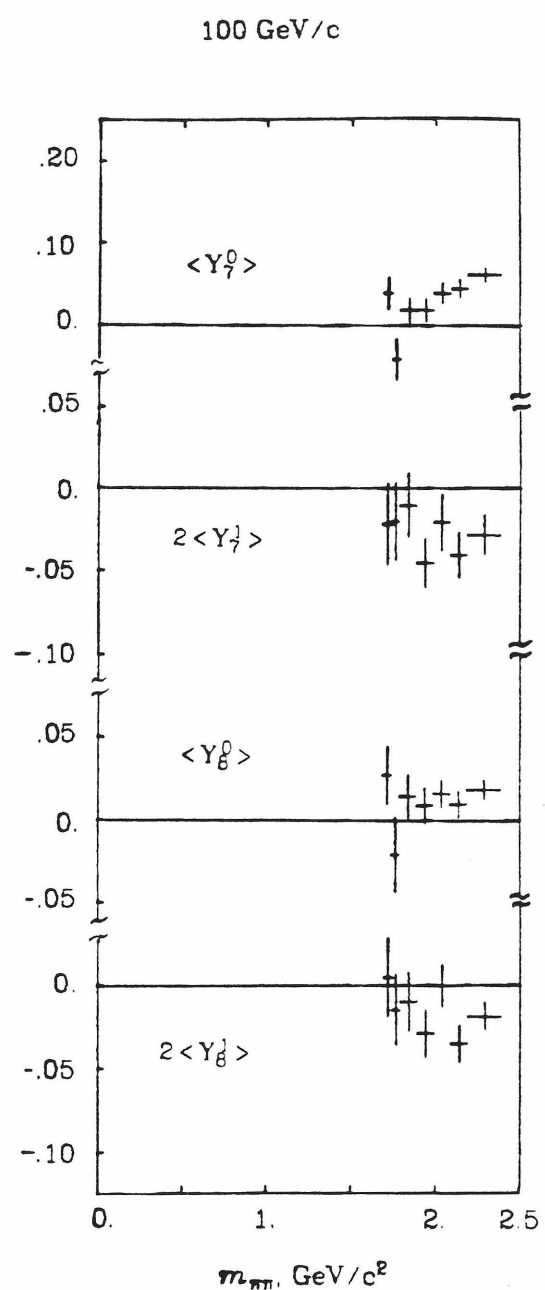
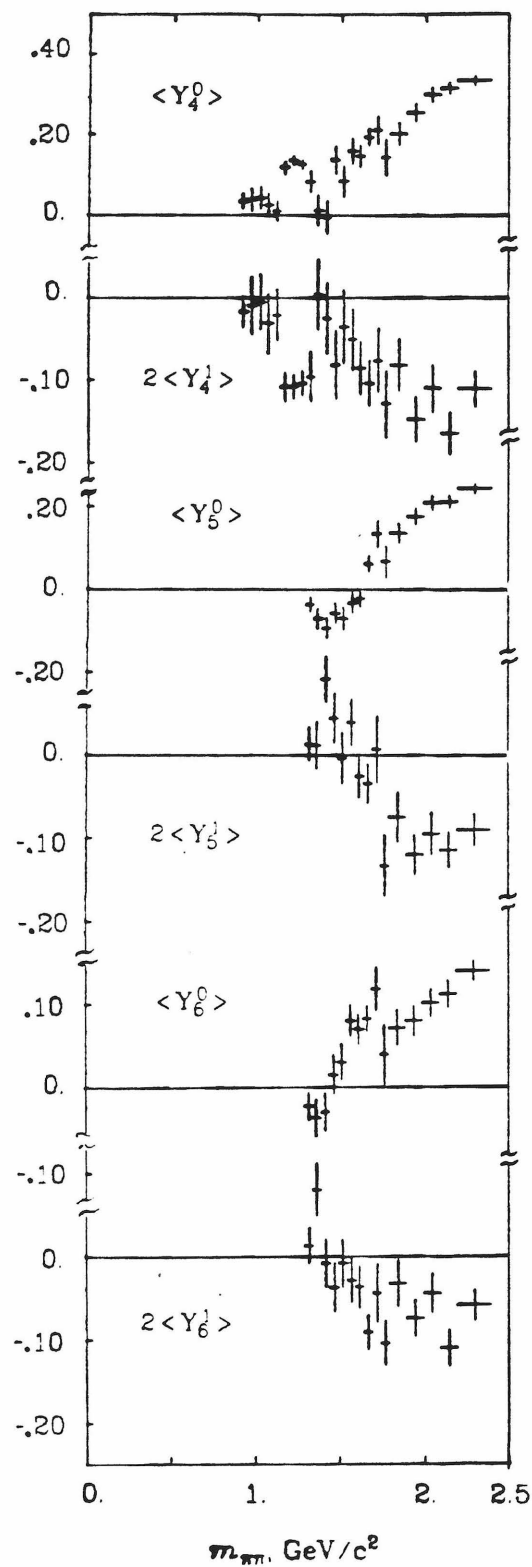


Figure 5-9b.

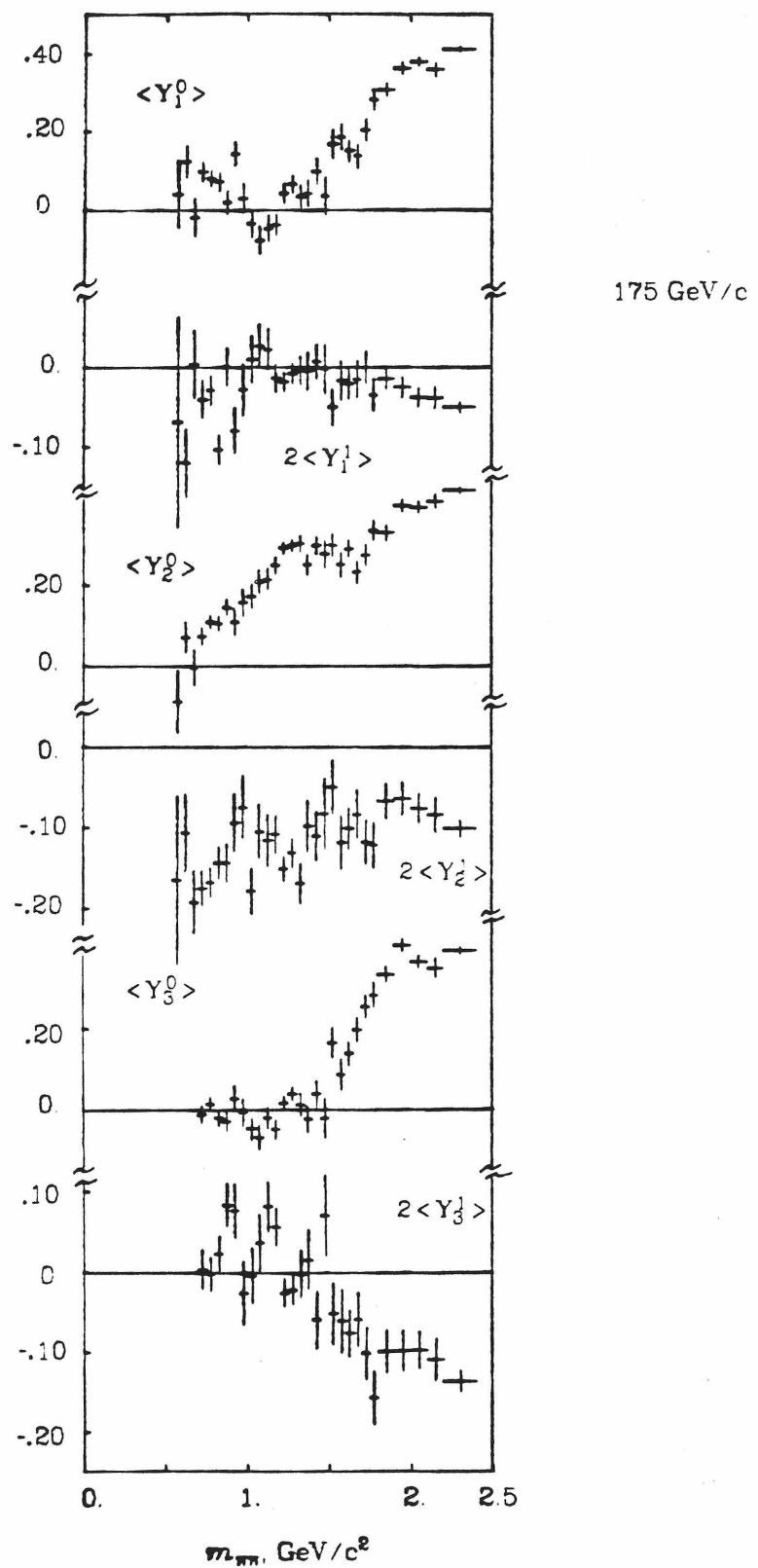


Figure 5-10 a. 175 GeV/c normalized moments for  $|t_{pn}| < .15$  (GeV/c) $^2$

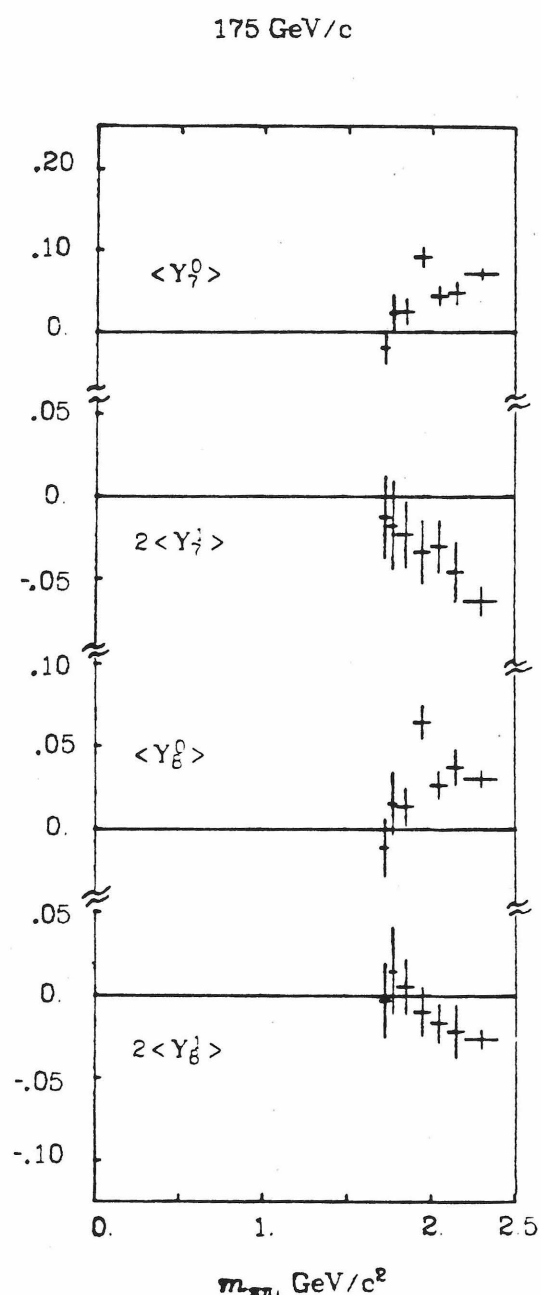
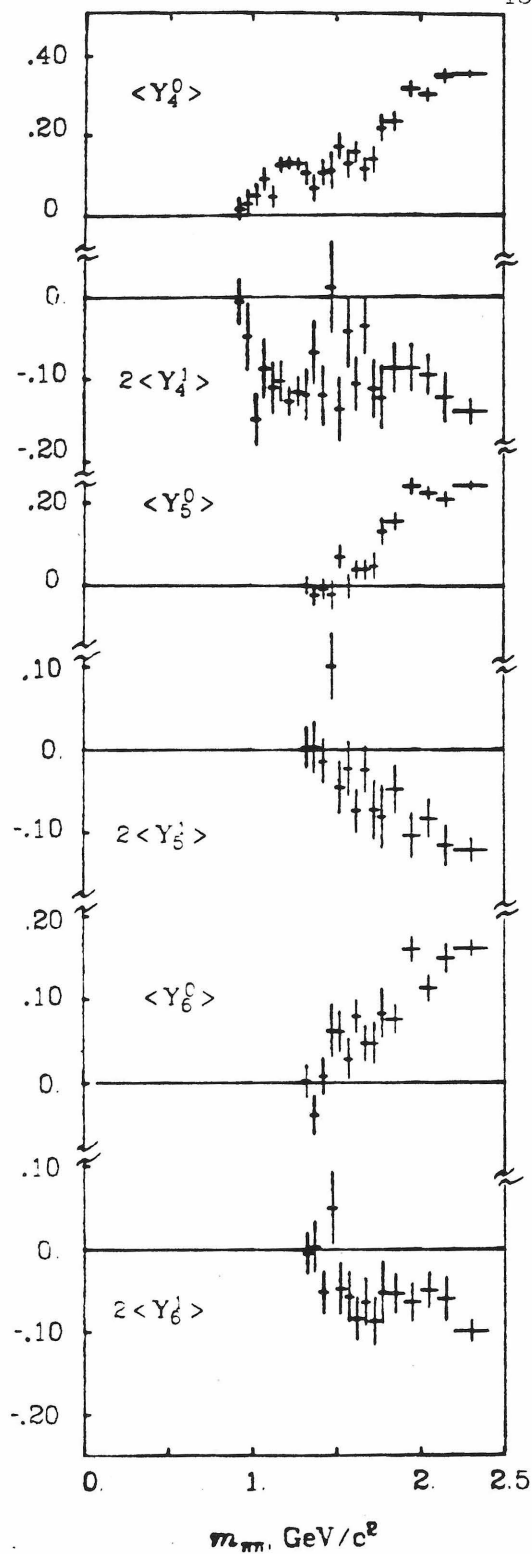


Figure 5-10b.

At masses near  $2.0 \text{ GeV}/c^2$ , results, especially  $Y_6$ , are in accord with the  $15 \text{ GeV}/c$  results of Corden *et al.*, and in disagreement with those of Grayer *et al.* at  $17 \text{ GeV}/c$ . We believe that this reflects acceptance limitations in the latter experiment at masses above the  $g^0$ . Both our, and the  $15 \text{ GeV}/c$  experiment had relatively good acceptance at high masses, while the  $17 \text{ GeV}/c$  experiment lost all forward peaking in their high mass raw data. Certainly, our data sample is tiny when compared to the  $17 \text{ GeV}/c$  data set. We believe we are viable at the higher masses only because our acceptance allows a substantial part of the forward peak. However, we note that our  $\langle Y_L^m \rangle$  moments are only about half those of Corden *et al.* Since the  $L = 9$  and  $10$  moments were consistent with zero in our data and not theirs, this may reflect a gradual degradation in the moments with  $L$ .

At  $\pi\pi$  masses above about  $2.2 \text{ GeV}/c^2$ , our fits to  $Y_L^m$ 's become inadequate. Even with only  $m = 0$ , and 1 large numbers of moments are needed to describe a sharp forward ( $\cos\theta_J \approx 1$ ) peak and little or no backward peak. (See the distributions of section 6.2.) The high frequencies (in  $\cos\theta_J$ ) of the highest moments are not well followed by our low statistics data. One might reasonably expect the needed spin content in the moment fits to parallel the Chew - Frautschi plot for the  $\rho$  trajectory. This has worked at masses up to the  $g^0$ . Extrapolating figure 17-9 of Perl [Pe74] to  $m_{\pi\pi} = 2 \text{ GeV}/c^2$ , we find a spin of  $\approx 4$ , implying an  $L_{\max}$  value of 8. Also, the spin content rises like the (mass) $^2$ . By this criterion, fits with  $L_{\max} = 8$  break down at  $m_{\pi\pi} \approx 2.0 \text{ GeV}/c^2$ . The  $15 \text{ GeV}/c$  data of Corden *et al.* [Co78] show that the  $L = 8$  moment becomes significant in the  $1.7$  to  $1.8 \text{ GeV}/c^2$  region, and that  $L = 10$  opens up by  $m_{\pi\pi} \approx 2 \text{ GeV}/c^2$ . Thus the  $\rho$  trajectory argument places only a lower bound on the needed moments. We expect that the low order  $L \neq 0$  moments are not unduly distorted by these failings, but that forward peaks will not be properly followed and produced event totals will be underestimated.

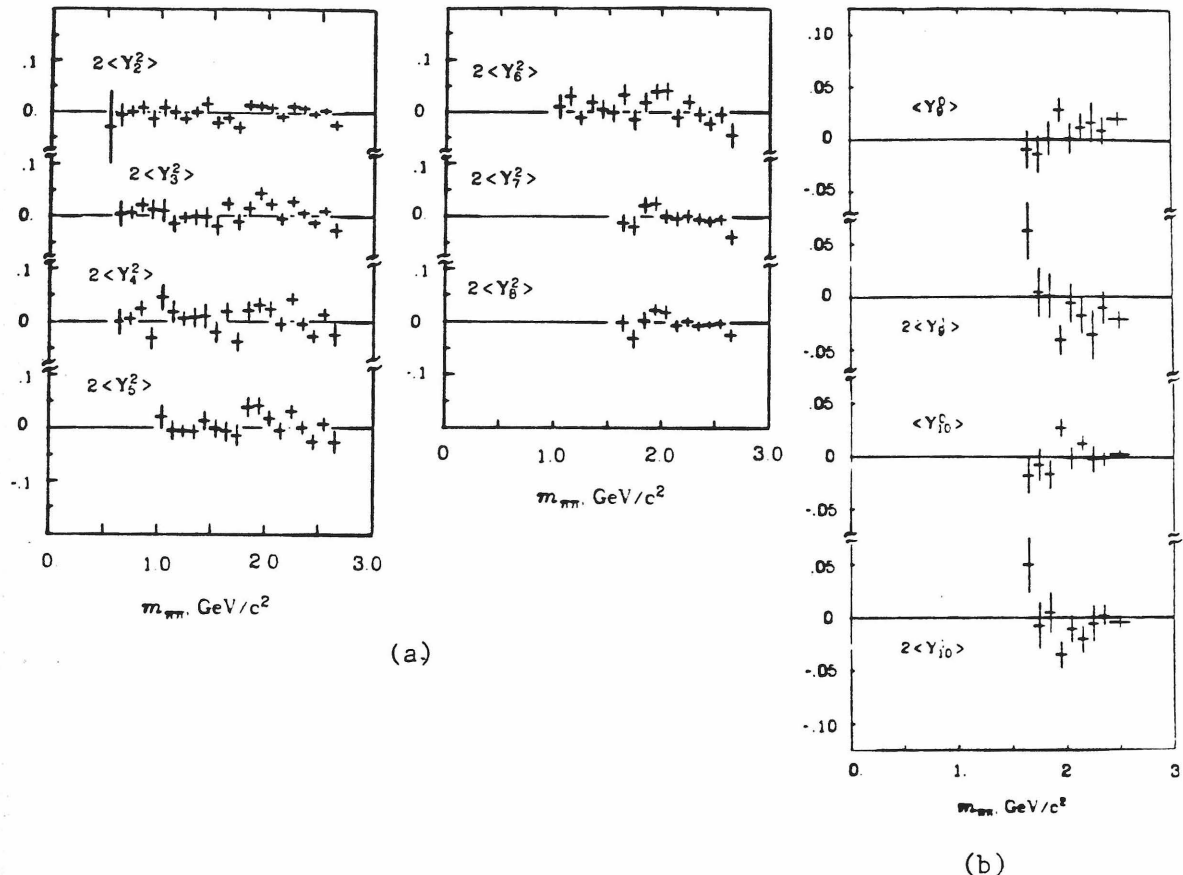


Figure 5-11. Constrained moments. Figure 5-11a shows low  $t_{pn}$   $m = 2$  moments, and 5-11b shows low  $t_{pn}$  moments with  $L = 9$  and  $10$ . These moments are consistent with zero and were constrained to zero in our final fits.

### 5.5.1 A PMA Test

Relations between  $m = 0$  and  $1$  moments are evident in the distributions of figures 5-9 and 5-10. Most obvious are the consistently opposite signs. Ochs and Wagner [Oc73] found that PMA predicts that the ratio

$$r_L = \frac{-(m_{\pi\pi}^2 - m_\pi^2)}{m_{\pi\pi}} \frac{1}{\sqrt{L(L+1)}} \frac{\langle Y_L^1 \rangle}{\langle Y_L^0 \rangle} \quad (5.16)$$

does not depend on  $L$ . They further noted that  $\rho_L = r_L(m_{\pi\pi})/r_1(m_\rho)$  gives the mass dependence of the PMA absorption parameter  $ReC_A$ . Using the 17.2 GeV/c data of Grayer *et al.* they then found  $ReC_A$  as a function of  $m_{\pi\pi}$ . We repeat this operation

with our moment results. Figure 5-12 shows the 100 GeV/c ratios. The curve in figure 5-12 is the  $\text{Re}C_A$  result of Oc73. We assume, as Ochs and Wagner did, that  $\rho_L(m_\rho) = \text{Re}C_A(m_\rho) = 1$ . As an attempt to avoid distortions from poorly determined moments, we used only moments where both the  $m = 0$  and 1 moments were at least 1.5 standard deviations from zero.

The agreement of these 100 GeV ratios with Ochs and Wagner's results is satisfactory. The excess of  $L = 2$  ratios below 900 MeV/c<sup>2</sup> was also noted by Ochs and Wagner. They felt it was due to neglecting a density matrix term ( $\rho_{11}^{11}$ ) in deriving equation 5.16 [Oc73]. At masses above 2 GeV/c<sup>2</sup>,  $\text{Re}C_A$  seems roughly constant. This agrees with results of Shimada and Wagner [Sh80] who used 63 GeV/c data from the ACCMOR group to measure  $\text{Re}C_A$ . Similar plots (not shown) at 175 GeV/c also find that  $\rho_L$  is independent of  $L$ . However, the overall magnitude of the 175 GeV/c ratios is about twice the curve and the 100 GeV/c values. We believe that the problem is poorly determined  $\rho^0$  moments at 175 GeV/c (see figure 5-10a). The ratio  $\rho_L$  is quite sensitive to errors in the moments, and our 175 GeV/c values at the  $\rho^0$  are not precise enough to use in this case. It would, perhaps, be more prudent to normalize the 175 GeV/c ratios elsewhere along the Ochs and Wagner curve. We feel that equation 5.16 is verified by our data, but a measurement of  $\text{Re}C_A$  has not been made. The 175 GeV troubles with these ratios should not be held in conflict with PMA.

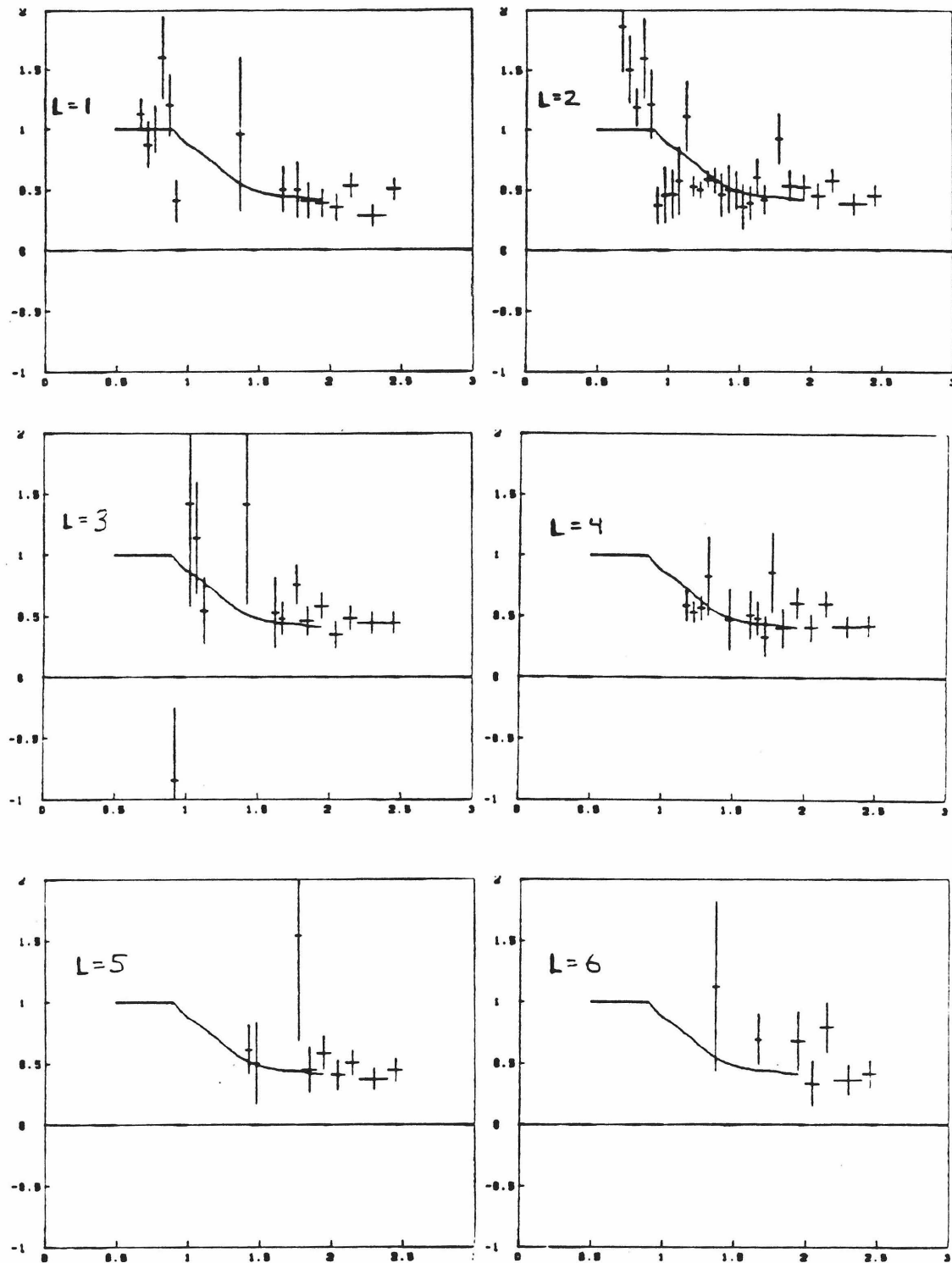


Figure 5-12. Moment ratios  $\rho_L$  at 100 GeV/c. All ratios are normalized by setting  $\rho_1(775 \text{ MeV}/c^2) = 1$ .

### 5.6 Moments versus $t_{pn}$

To obtain the  $t_{pn}$  dependence of the moments, we have fit several large mass bins, centered on the  $\rho^0$ ,  $f^0$ , and a large mass bin from 1.6 to 2.1 GeV/c<sup>2</sup>. The  $L_{\max}$  values were set according to Table 5.2 and the highest mass in each fit. For all of these fits,  $m_{\max} = 2$ . Figure 5-13 shows our  $\rho^0$  region results. Below  $\sqrt{-t_{pn}} \approx .40$ , only  $m = 0$  and  $m = 1$  moments are significant. Above that value,  $m = 2$  becomes nonzero. Around this value, the other moments also change dramatically. The low and high  $t_{pn}$  values of these moments are in fair agreement with lower energy results, [Gr74 and Al78], but a slight shrinkage is noticeable in this transition between our data and the low energy data. This qualitative feature is predicted by the Regge model of Kimel and Owens [Ki77], which includes  $\pi$ ,  $A_1$ , and  $A_2$  exchanges, and cut contributions for the  $\pi$  and  $A_1$ . To illustrate the shrinkage, figure 5-14 shows the zero crossing point of the  $\langle Y_2^0 \rangle$  moment. In this plot, we have included 17.2 and 63 GeV/c points taken from [Al78]. We note that the effect slows at our energies.

In the low  $t_{pn}$  region, absorbed  $\pi$  exchange has also described the  $\pi\pi n$  reaction well at lower energies. Indeed, PMA has been highly successful. Other exchanges, specifically  $A_1$  and  $A_2$  exchanges, are clearly present, but they do not become dominant until the "high"  $t_{pn}$  region. Since PMA contains no other exchanges and no moments with  $m \geq 2$ , the shrinkage in  $t_{pn}$  is not predicted by it. The transition point does, however, give us a limit on the region where PMA can be tested and applied with few reservations.

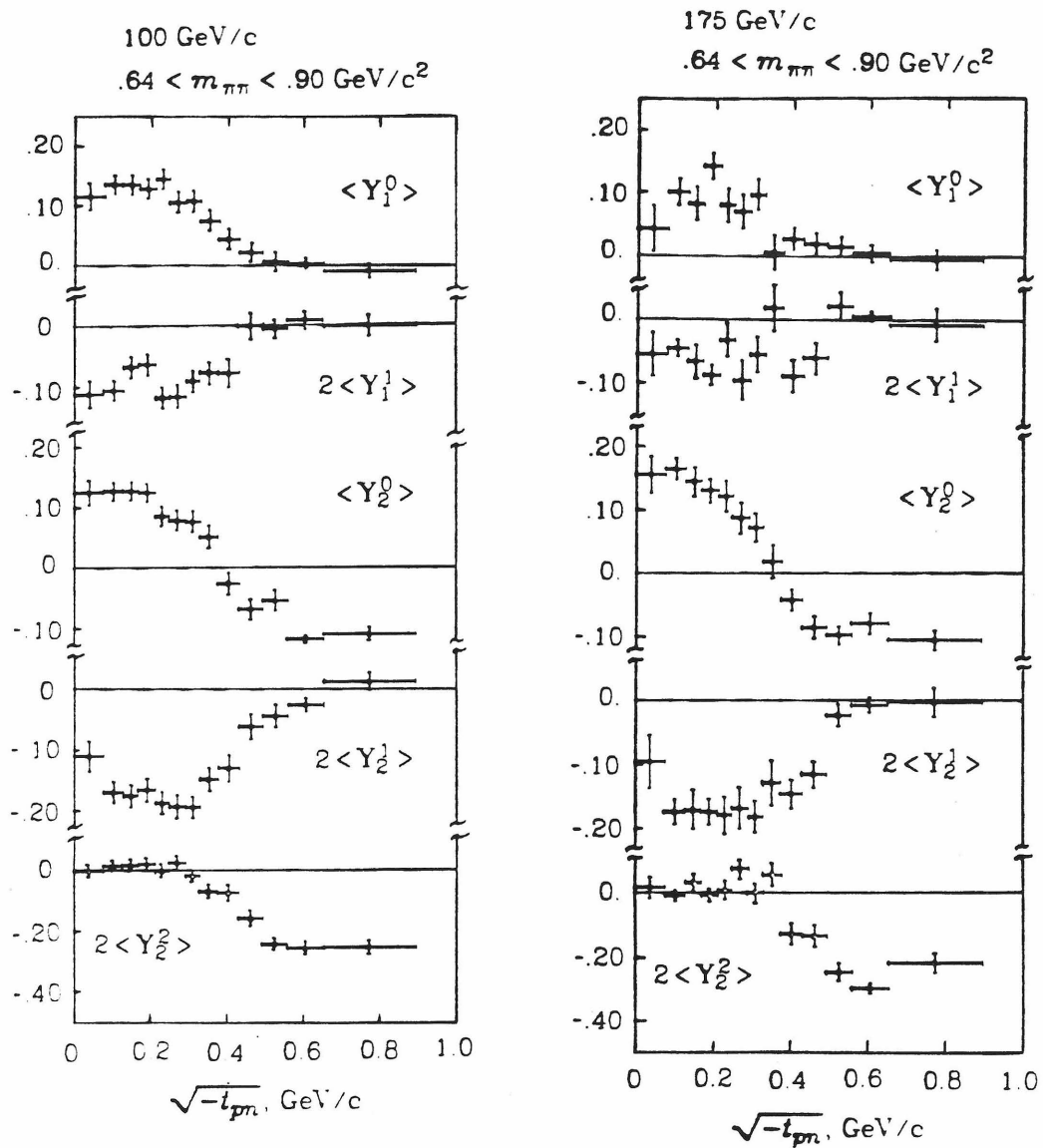


Figure 5-13. 100 and 175 GeV/c moments versus  $t_{pn}$  for the  $\rho^0$  region.

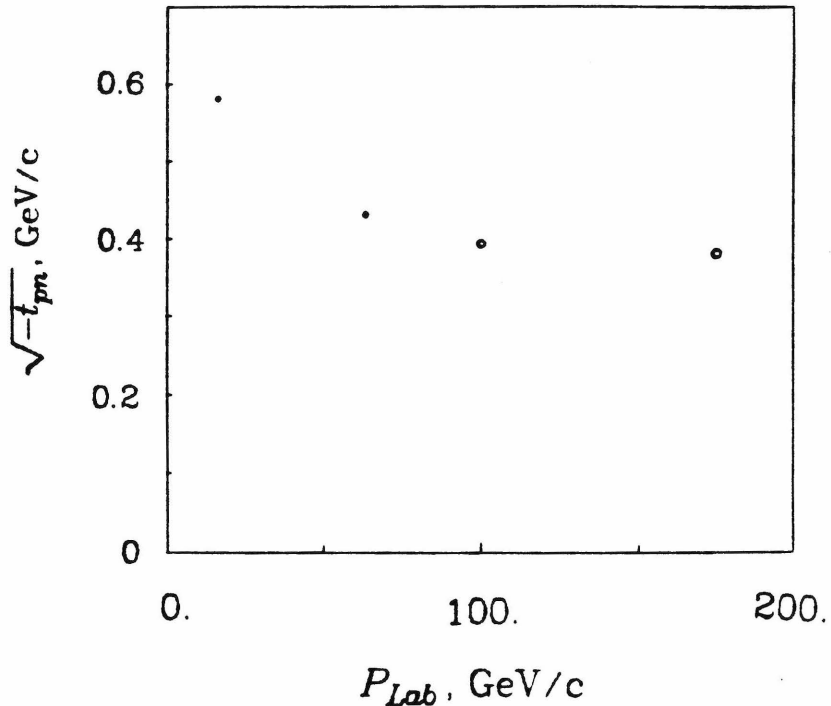


Figure 5-14. "Shrinkage" of the  $\rho^0$   $\langle Y_2^0 \rangle$  versus  $t_{pn}$  zero crossing point from 17 to 175 GeV/c. See text.

### 5.7 $\frac{d\sigma}{dt}$ Distributions

Figures 5-15ab display 100 GeV/c  $\frac{d\sigma}{dt}$  distributions for mass bands centered on the  $\rho^0$ ,  $f^0$ , and also the 1.6 to 2.1 GeV/c<sup>2</sup> bin. Both moment fit results, and acceptance weighted data appear in the plots. The acceptance weights chronically underestimate the data at low  $t_{pn}$ , but give a reasonable showing at higher values, allowing us to continue the plots beyond our last fits. Figure 5-15a is plotted with  $-t_{pn}$  to show a transition between the low and "high"  $t_{pn}$  regions near  $-t_{pn} \approx .15$ . The effect is not too clear in  $\frac{d\sigma}{dt}$  at the  $\rho^0$ , but it is striking in the 1600 to 2100 MeV/c<sup>2</sup> area.

Above and below the transition, the slopes appear roughly exponential, especially at the higher masses. Also, a very slight turnover is seen below  $|t| \approx m_\pi^2$ .

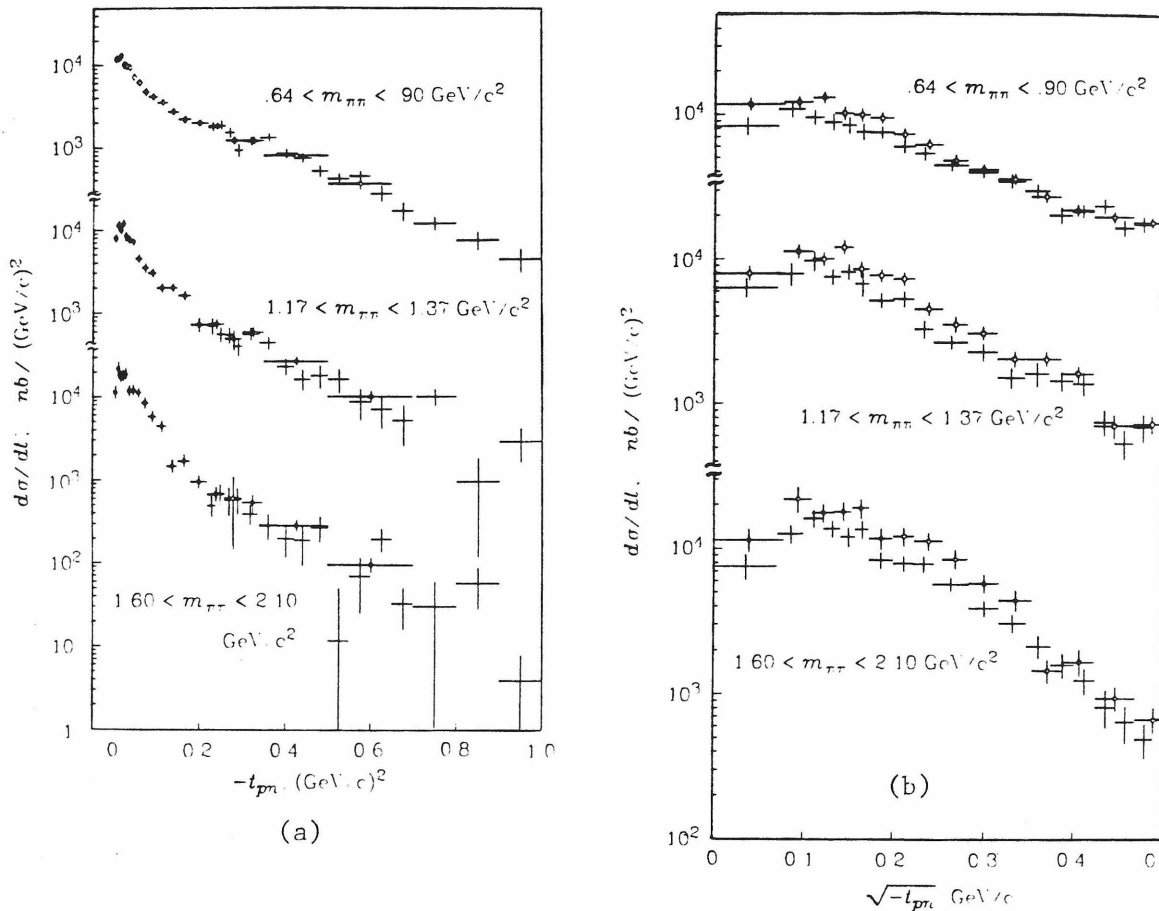


Figure 5-15. 100 GeV/c  $d\sigma/dt$  distributions. In (a), the vertical scale is offset slightly to positive  $t_{pn}$  only for clarity. No data were measured with  $t_{pn} > 0$ . In (b) we expand the low  $t_{pn}$  region.

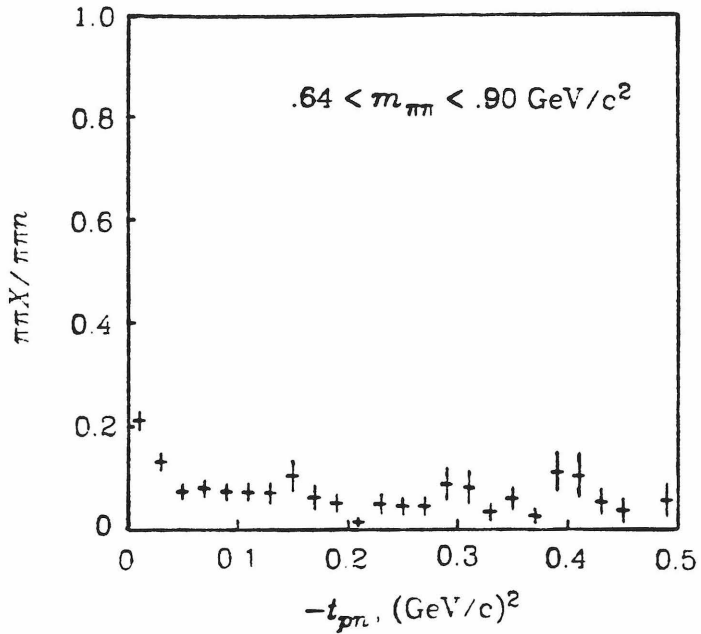


Figure 5-16. 100 GeV/c  $\rho^0$  region  $\pi\pi X/\pi\pi n_T$  ratio.

This is better seen in figure 5-15b, which expands the low  $t_{pn}$  region by using  $\sqrt{-t_{pn}}$  as the horizontal axis. The turnover is expected in  $\pi$  exchange dominated reactions with neutron recoils. The small  $t_{pn}$  region does not go to zero, in agreement with the PMA model and disagreement with simple OPE. This is also a feature of the Regge models of Kmel *et al.* We included weighted data in figure 5-15b as a check on the moment fits. Although weights underestimate  $d\sigma/dt_{pn}$  and the underestimate is  $t_{pn}$  dependent, the effect is slow compared to the bin size.

The forward dip is not a strong feature of the low  $\pi\pi$  mass data and some care (a  $\pi\pi X$  background subtraction) was needed to observe it. Figure 5-16 plots the ratio of  $\pi\pi X$  data over  $\pi\pi n_T$ . The peak at low  $t_{pn}$  is enough to wash out the  $\rho^0$  dip. The dips at the higher masses are stronger and  $\pi\pi X$  subtraction, though used, was not needed to observe them.  $\Delta$  resonance recoils, unlike neutron recoils, do not have a low  $t_{pn}$  dip. Hence our background peaks somewhat at low  $t_{pn}$  relative to  $\pi\pi n_T$ . The problem is worse at the  $\rho$  than at higher masses because the backgrounds are larger.

## CHAPTER VI

### Decay Distributions

#### 6.1 Scatter Plots

In this chapter we present  $\pi^+\pi^-$  decay angular distributions in the Gottfried - Jackson frame for  $\pi^-p \rightarrow \pi^+\pi^-n$ . We also consider  $t_{pn}$  distributions, and draw a few limited conclusions about  $\pi\pi$  scattering. We begin with a pair of 100 GeV/c scatter plots in  $\cos\theta_J$  versus  $\pi\pi$  mass. Figure 6-1 is at low  $t_{pn}$ . To reduce the point density, this plot uses a restrictive  $|t_{pn}| < .08$  (GeV/c)<sup>2</sup> cut. Our forward acceptance zero is present at all masses. Though heavily populated at all  $\cos\theta_J$ , inspection reveals that the  $\rho^0$  density is reduced near  $\cos\theta_J \approx -0.4$ . The  $f^0$  band shows three distinct clusters of events. The  $g^0$  region seems undistinguished in the forward direction, but contains a significant cluster of events near  $\cos\theta_J \approx -0.7$ . Above the  $g^0$ , the backward or  $\cos\theta_J \approx -1$  region quickly dies while a strong forward peak is established. The forward peak survives until our acceptance zero cuts it off completely. No mass band above the  $g^0$  is notable for local increases in the event density.

Figure 6-2 shows the  $\cos\theta_J$  versus mass distribution for  $|t_{pn}| > .15$  (GeV/c)<sup>2</sup>. At high masses, we still see forward peaking, structure at the  $g^0$  mass is less distinct, the  $f^0$  has only two broad clusters at extreme  $\cos\theta_J$  values, and finally, the  $\rho^0$  region shows clear clustering towards the middle, not the ends of the plot. The forward acceptance zero is much less evident in figure 6-2. The presence of clusters of events in these figures implies dips between them. One can easily visualize a number of possible contours for the dips that "connect" the various mass values. We will map the low  $t_{pn}$  dips in section 6.4.

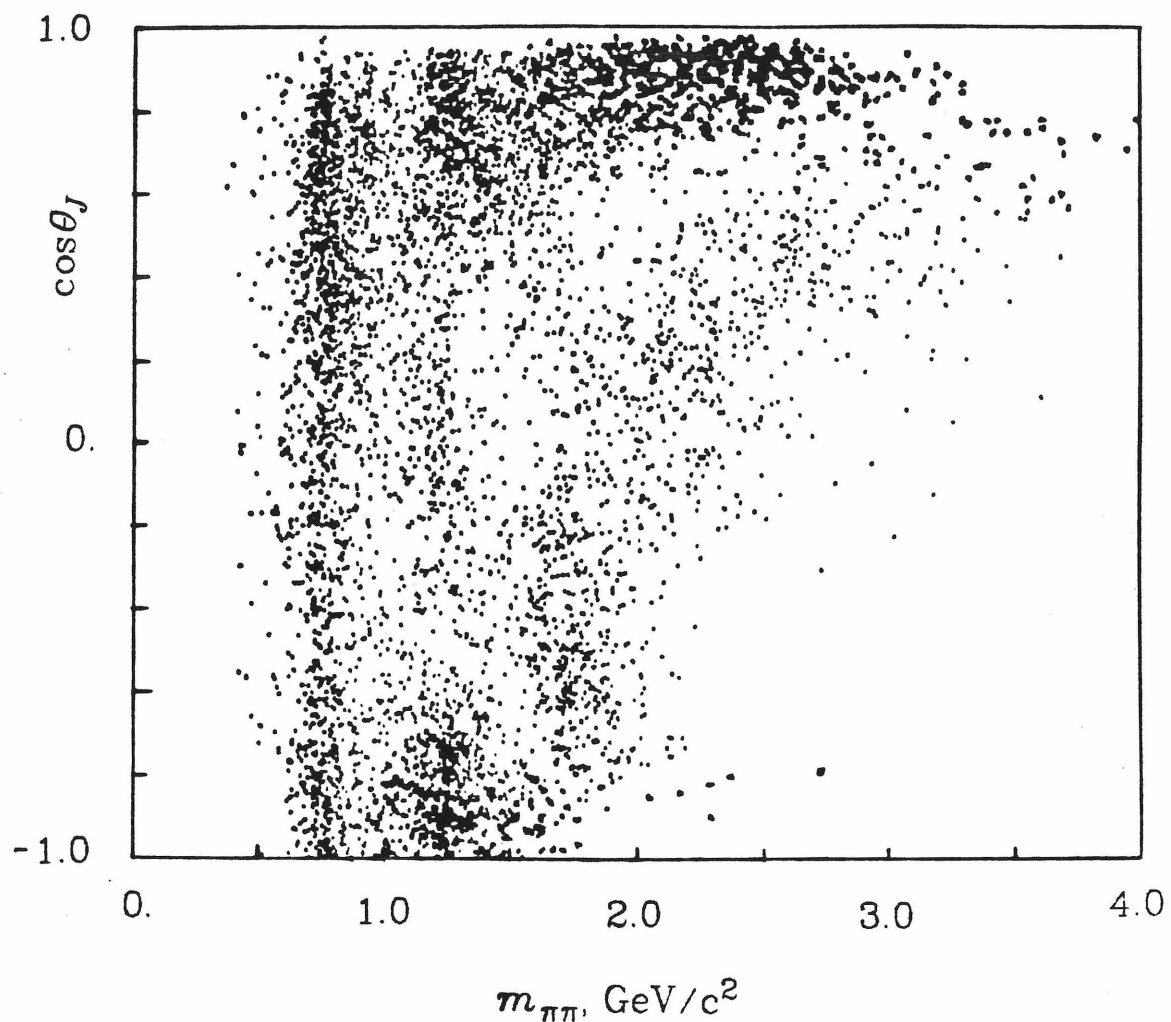


Figure 6-1. 100  $\text{GeV}/c$  scatter plot of  $\cos\theta_J$  versus  $m_{\pi\pi}$  for  $|t_{pn}| < .08$   $(\text{GeV}/c)^2$ . (An isolated small point corresponds to a single observed event. The point size corresponds to both the relative weight, including acceptance, of an event, and to the event density. This applies to all scatter plots of this chapter.)

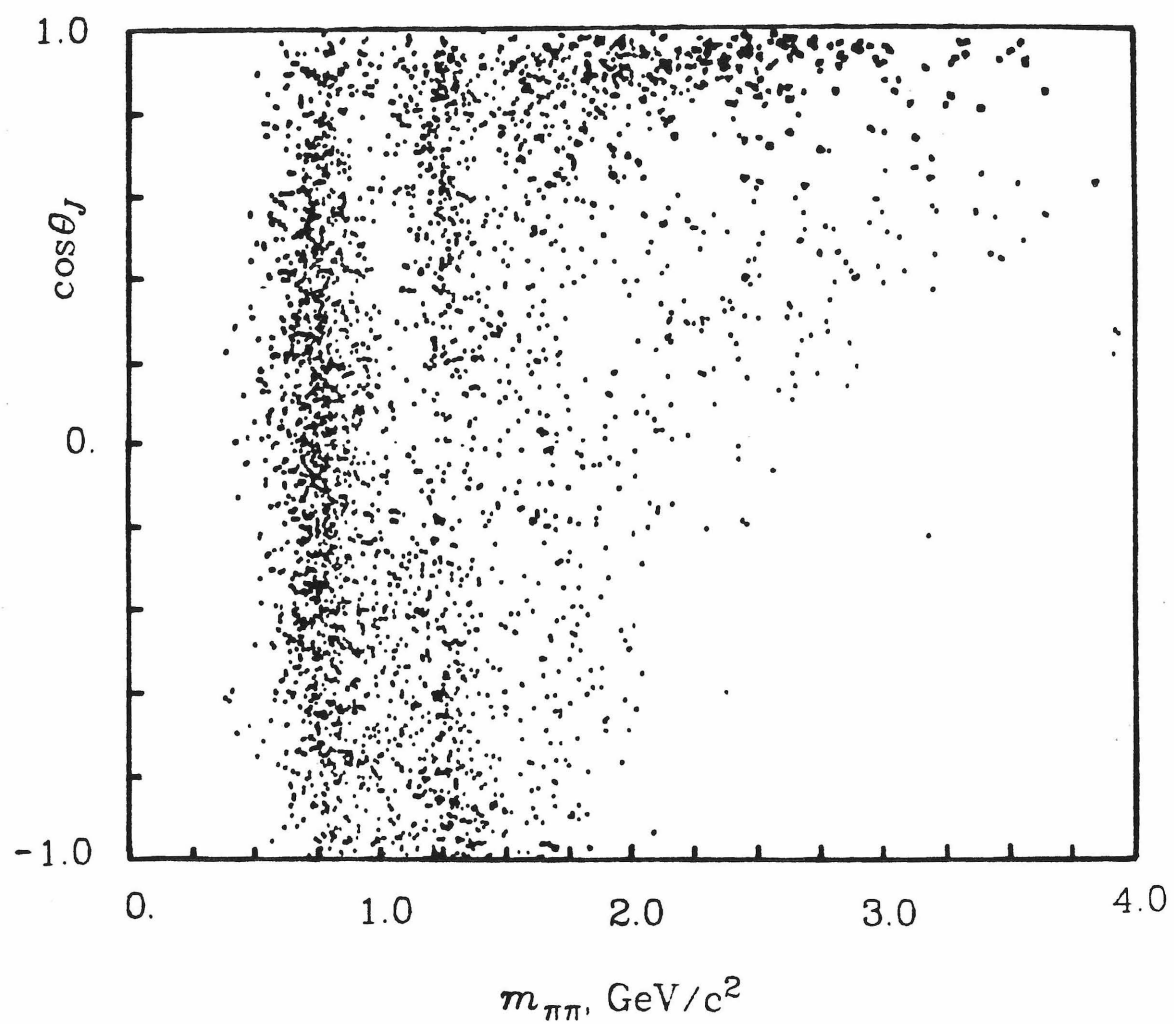


Figure 6-2. 100  $\text{GeV}/c$  scatter plot of  $\cos\theta_J$  versus  $m_{\pi\pi}$  for  $|t_{pn}| > .15$   $(\text{GeV}/c)^2$ .

## 6.2 Resonance Region

In this section we consider decay distributions for the  $\rho^0$ ,  $f^0$ ,  $g^0$ , and  $h^0$  mass bands. The same sequence of plots is given for each mass band. We include scatter plots (100 GeV/c only) and projections (both energies) in  $\cos\theta_J$  and  $\varphi_J$  of the  $\pi\pi$  decay distributions. The projections show fully weighted data as points with error bars. Smooth curves on the projections are moment fit results and represent produced distributions. The weighted data follows the fit result in  $\cos\theta_J$  fairly well in good acceptance regions, but falls away from it in acceptance zeros. The acceptance zeros at low  $t_{pn}$  are mainly in the peaks of the produced distributions. As figure 5-1 illustrates, they also tend to be broad in  $\varphi_J$ , and the forward zeros are centered on  $\varphi_J \approx 0$ . The effect of all this on  $\varphi_J$  projections is to make weighted data appear systematically below the produced distribution curve. Another effect is to make weighted data at low  $t_{pn}$  suggest that  $m = 2$  moments are significant when they are negligible. Histograms without error bars on each projection are uncorrected distributions of the final event sample. For each mass band, both low ( $|t_{pn}| < .15$ ) and high ( $.15 < |t_{pn}| < 1.0$  (GeV/c) $^2$ ) plots are presented. The information content of this section is contained in moment coefficients, but decay distribution displays allow one to see more clearly their implications.

Figures 6-3 and 6-4 show this sequence for a  $\rho^0$  mass band of 690 to 840 MeV/c $^2$ , or about  $\pm .5\Gamma$  about the  $\rho^0$  mass of .770 GeV/c $^2$ , with  $\Gamma = 158$  MeV/c $^2$  [PDG80]. In figure 6-3, a single broad minimum passing through  $\cos\theta_J \approx -.4$  and  $\varphi_J = 0$  is seen. The lack of events near  $\cos\theta_J = +1$  in figure 6-3 reflects the forward acceptance zero. The minimum position depends on both these variables. Projecting the data onto  $\cos\theta_J$ , we see a considerable forward-backward asymmetry resulting from interference between the S-wave background and the resonant P-wave  $\rho$ , [Eg74]. The interference term,  $Y_1^0$  is proportional to  $\cos\theta_J$ .

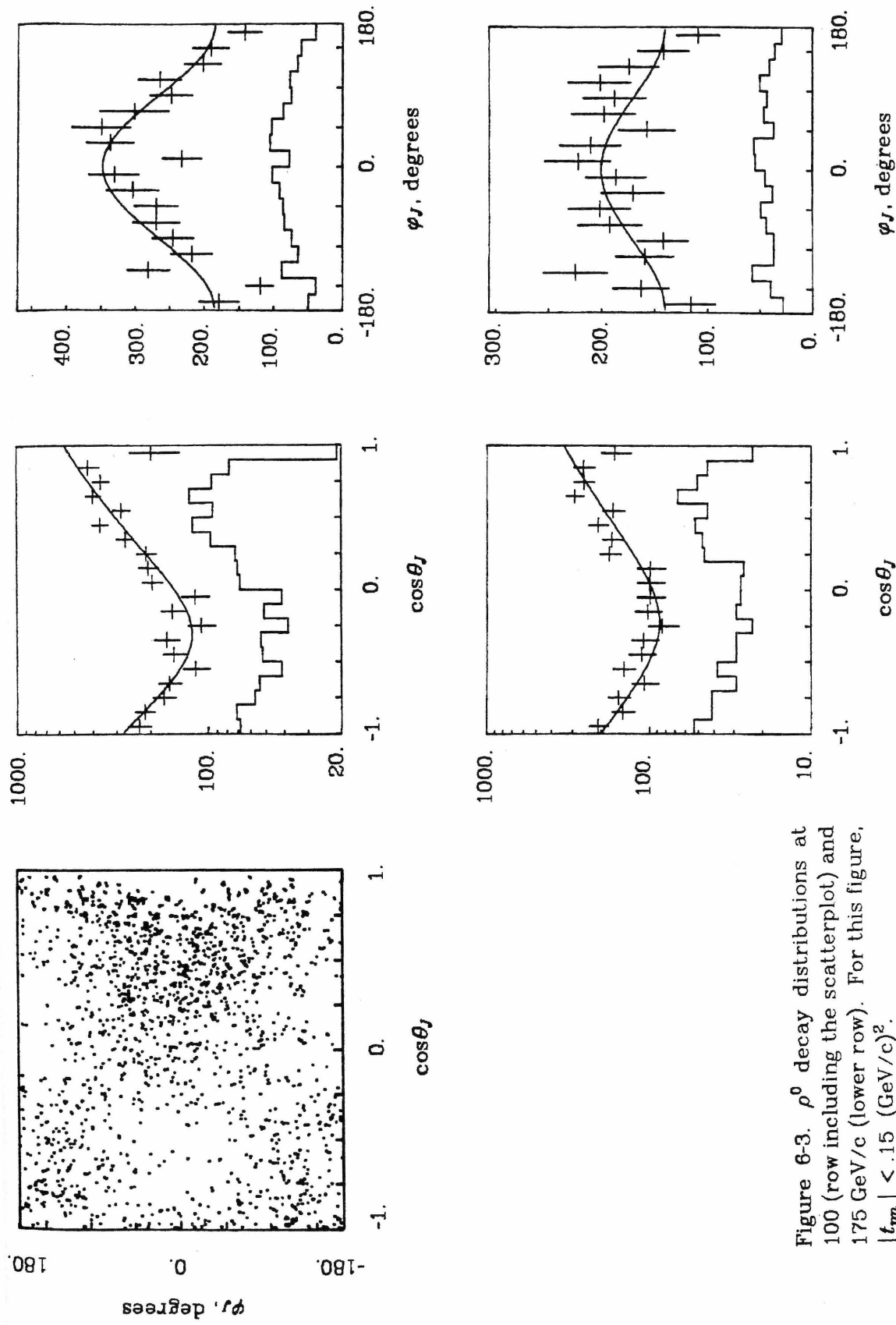


Figure 6-3.  $\rho^0$  decay distributions at 100 (row including the scatterplot) and 175 GeV/c (lower row). For this figure,  $|t_{pm}| < .15$  (GeV/c) $^2$ .

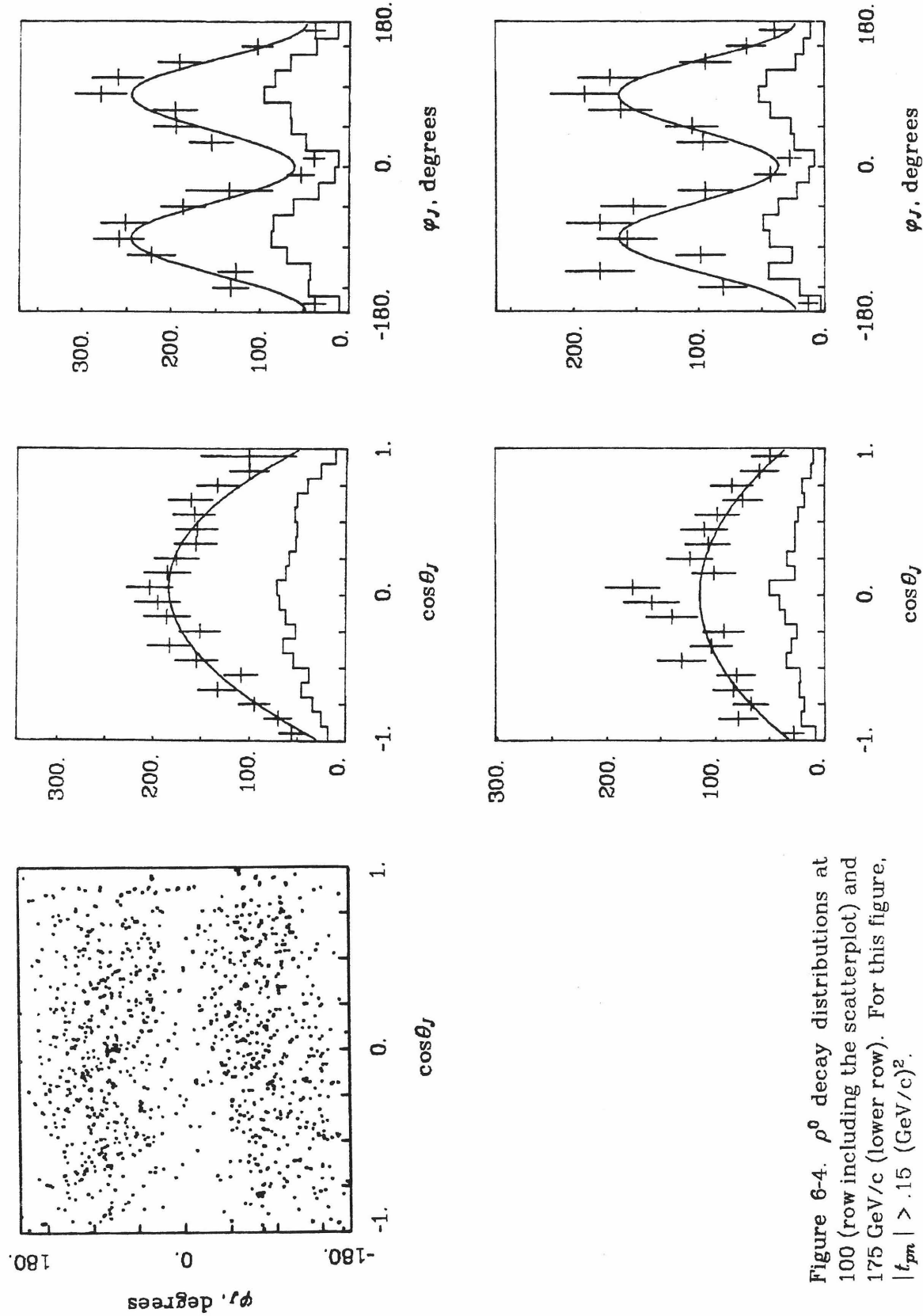


Figure 6-4.  $\rho^0$  decay distributions at 100 (row including the scatterplot) and 175 GeV/c (lower row). For this figure,  $|t_{pn}| > 1.5$   $(\text{GeV}/c)^2$ .

Because  $\int_{-\pi}^{\pi} \cos(m\varphi) d\varphi = 0$  for  $m \neq 0$ , only moments with  $m = 0$  appear in  $\cos\theta_J$  projections. Projections in  $\varphi_J$  are a bit more involved, and not often shown. The curves in our  $\varphi_J$  views are numerical integrals of the moments on  $\cos\theta_J$ , but several patterns are worth reviewing. First,  $\int Y_L^0 d\cos\theta_J = 0$  unless  $L = 0$  (orthogonality of Legendre polynomials). For  $m = 1$ , only odd  $L$  moments survive in the  $\varphi_J$  view. In general, the only  $m \neq 0$  moments seen in the  $\varphi_J$  view have even values of  $L + m$ . This follows from observing  $P_L(x)$  is even (odd) in  $x$  if  $L$  is even (odd), and that  $Y_L^m(x, \varphi)$  is  $(d/dx)^m P_L(x) \cos(m\varphi)$  times numbers. As a corollary, moment terms with  $m \neq 0$  and  $L + m$  odd are not seen in either projection, both variables must be used to extract such terms.

The  $\varphi_J$  projection of the  $\rho^0$  at low  $t_{pn}$  clearly shows the  $\cos\varphi$  dependence of a significant  $m = 1$  contribution.

The  $\rho^0$  high  $t_{pn}$  plots of figure 6-4 are a radical change from those in figure 6-3. In the  $\cos\theta_J$  view, we have lost the forward and backward peaks. Replacing them is a near perfect  $\sin^2\theta_J$ , with only small constant and  $\cos\theta_J$  terms. The  $\varphi_J$  distribution now has two peaks centered at  $\varphi_J = \pm 90^\circ$ . The shape is mainly  $\cos 2\varphi_J$ , with a comparable constant term and a small  $\cos\varphi_J$  term. The double  $\varphi_J$  peak is characteristic of  $m = 2$  moments. Indeed, recalling figure 5-13 we see that the moment content of the  $\rho$  mass band has changed completely. At high  $t_{pn}$ , the only nonzero moments are a  $Y_2^0$  that has changed sign, a now nonzero  $Y_2^2$ , and a (constant)  $Y_0^0 \propto N_c$  that "keeps" the distribution positive.

The decay angle distribution reflects not only the spin of the decaying state, but also its production. In the absence of interference effects, Lichtenberg [Li65] notes that a spin 1  $\rho$  decaying to two pions has  $I(\theta_J) \propto \cos^2\theta_J$  if the nucleon spin is not flipped, and  $I(\theta_J) \propto \sin^2\theta_J = 1 - \cos^2\theta_J$  if the nucleon spin is flipped. In the Jackson frame,  $\pi$  exchange is non flip, but spin 1 exchanges are spin flip [Wi78]. S-wave  $\pi\pi$  scattering just gives a flat term, and interference effects can bring in other

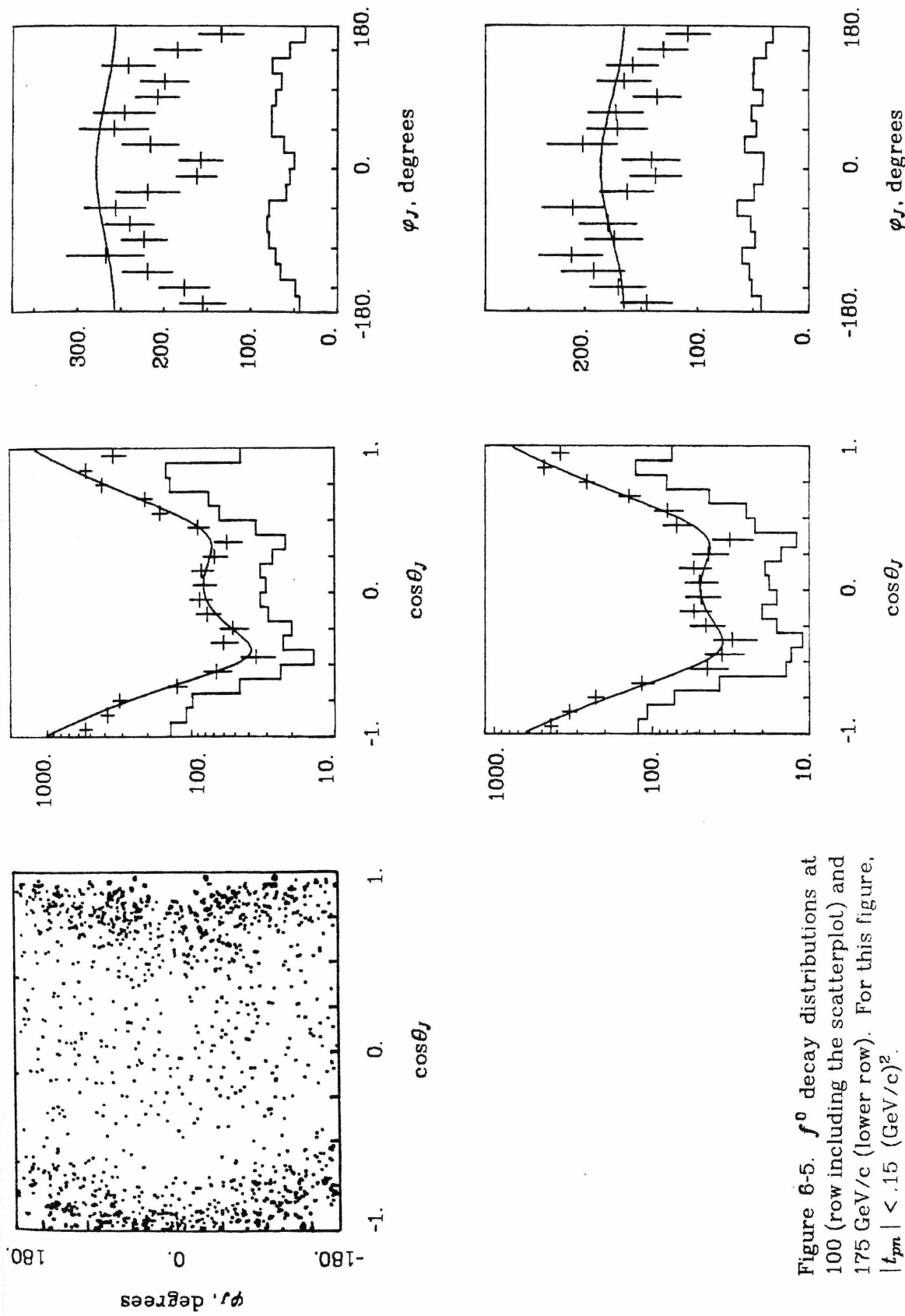


Figure 6-5.  $f^0$  decay distributions at 100 (row including the scatterplot) and 175 GeV/c (lower row). For this figure,  $|t_{pn}| < .15$   $(\text{GeV}/c)^2$ .

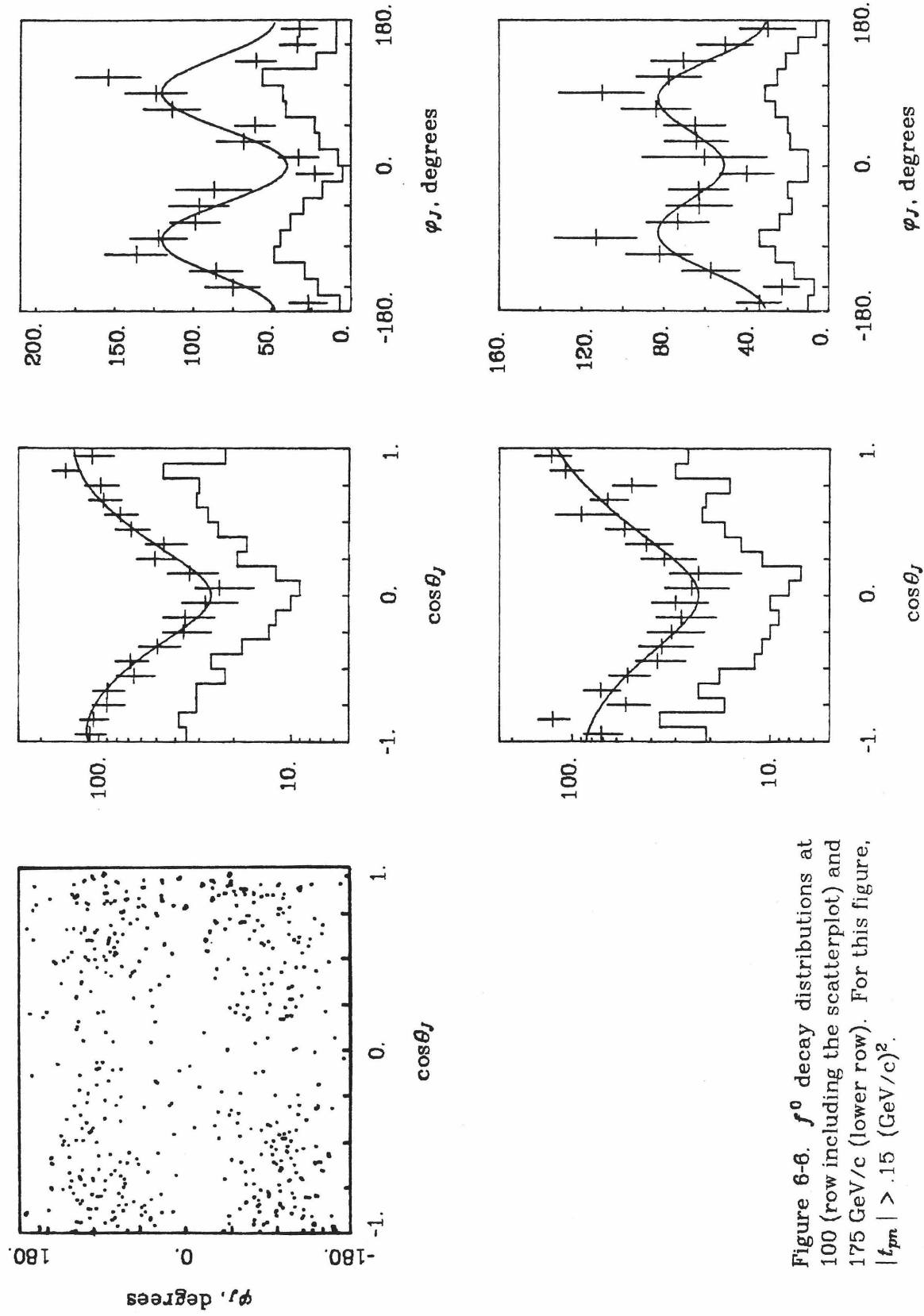


Figure 6-6.  $f^0$  decay distributions at 100 (row including the scatterplot) and 175 GeV/c (lower row). For this figure,  $|t_{pn}| > .15$   $(\text{GeV}/c)^2$ .

(especially linear in  $\cos\theta_J$ ) terms. Evidently, the high  $t_{pn}$  region of the  $\rho^0$  is dominantly spin flip with relatively little interference, while the low  $t_{pn}$  region is mainly non flip and has considerable interference.

The  $f^0$  mass region, 1180 to 1360 MeV/c<sup>2</sup>, is shown in figures 6-5 and 6-6. The acceptance holes of figure 5-1 are clearly visible in the low  $t_{pn}$  scatter plot of figure 6-5. Multiple dips are seen in the low  $t_{pn} \cos\theta_J$  projection, and there is only a small forward backward asymmetry. Eguchi *et al.* [Eg74] attribute this to the relative absence of interfering  $\pi\pi$  amplitudes. We note that the change between the low and high  $t_{pn} \cos\theta_J$  distributions, while significant, is not the total reversal seen at the  $\rho^0$ . The double dip of the low  $t_{pn}$  plots has become just a single dip in figure 6-6. An  $m = 2$  double peak in  $\varphi_J$  is quite prominent at high  $t_{pn}$ .

Figures 6-7 through 6-10 repeat this exercise for  $g^0$  and  $h^0$  mass bands of 1590 to 1790 and 1900 to 2060 MeV/c<sup>2</sup> respectively. The  $g^0$  displays a large forward - backward asymmetry, but does muster a backward peak. The backward peak at the  $h^0$  is required by our fits although we have no data in the last  $h^0$  bin. The changes from low to high  $t_{pn}$  become less pronounced as the mass increases from the  $\rho$  to the  $h^0$ . In particular,  $m = 1$  moments return beginning at or above the  $f^0$ , and  $m = 2$  moments fall with mass. Except for the dramatic  $Y_2^0$  sign reversal at the  $\rho^0$ , the  $m = 0$  and 1 moments retain their low  $t_{pn}$  signs, (once  $m = 1$  recovers), and the generally negative  $m = 2$  moments eventually die off.

The low  $t_{pn} \cos\theta_J$  distributions have changed dramatically as the mass increased from the  $\rho$  to the  $h^0$  region. The forward peak sharpens, the backward peak at first sharpens but then essentially disappears in the high masses, more dips enter, and the dips seem to move around with mass.

We note in passing that at low  $t_{pn}$  and intermediate masses ( $f^0$  and  $g^0$ ), the  $\varphi_J$  distributions seem to flatten out and become more consistent with the Treiman-Yang condition for  $\pi$  exchange dominance, namely a flat  $\varphi$  distribution [Tr62]. This

is illusory. The  $\pi^- p \rightarrow \pi^+ \pi^- n$  reaction fails the test almost everywhere. The reduction in the  $\varphi_J$  dependence of the integrated (in  $\cos\theta_J$ ) distributions results from a cancellation of strong  $\varphi_J$  dependences of both signs. The signs and magnitudes of the  $\varphi_J$  dependences couple to the slopes of the  $\cos\theta_J$  distributions. This is a prediction of PMA, and is seen in our data when we make  $\cos\theta_J$  slices. The Treiman-Yang test failure for  $\pi\pi n$  should be immediate upon considering what an  $m \geq 1$  moment means, but it is amusing to note that the only places flat  $\varphi_J$  distributions are found are in dips of the  $\cos\theta_J$  distributions, and these have been shown to correspond to zeros in the  $\pi\pi$  scattering amplitude [Pe73].

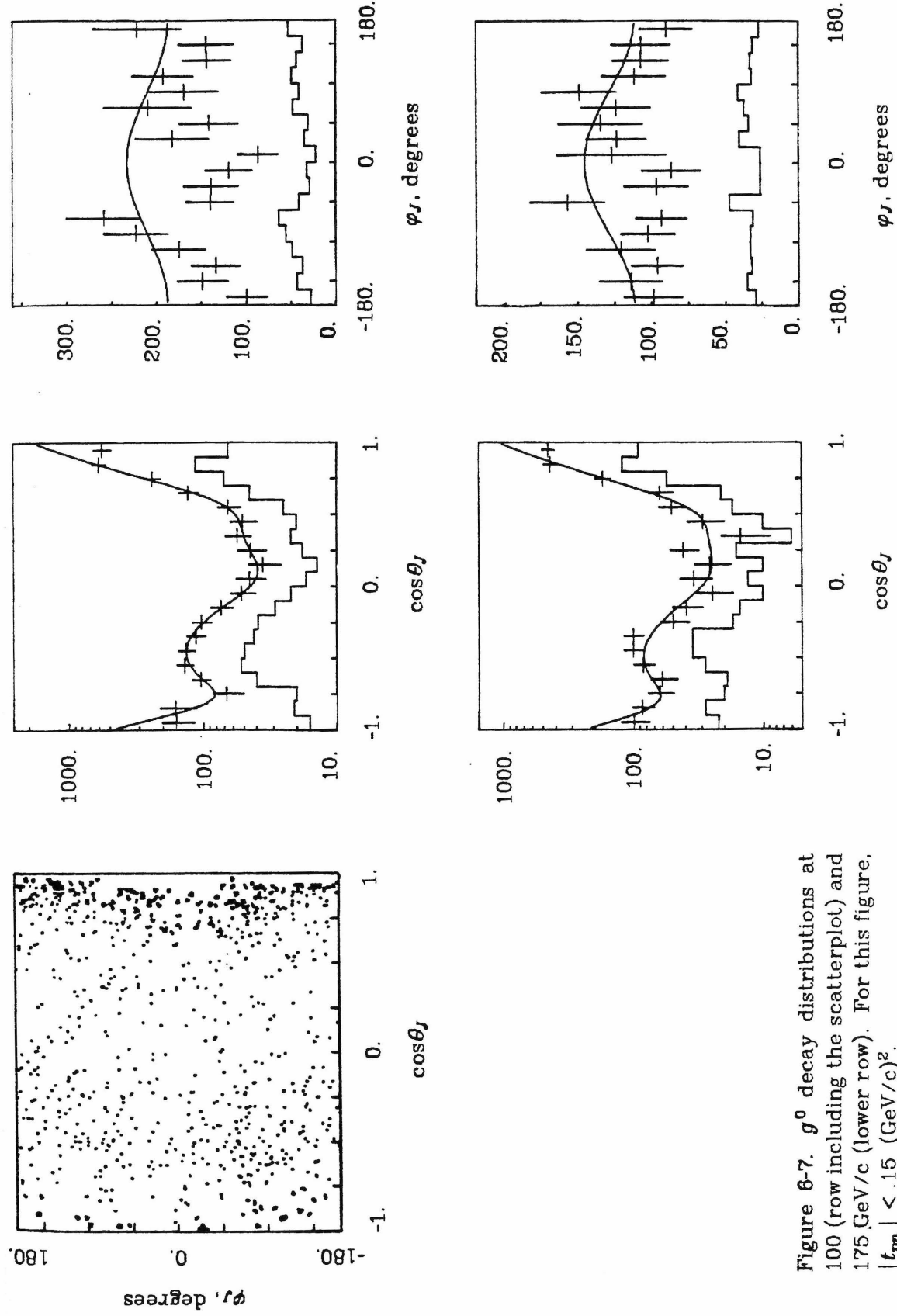


Figure 6-7.  $g^0$  decay distributions at 100 (row including the scatterplot) and 175 GeV/c (lower row). For this figure,  $|t_{pn}| < 15$   $(\text{GeV}/c)^2$ .

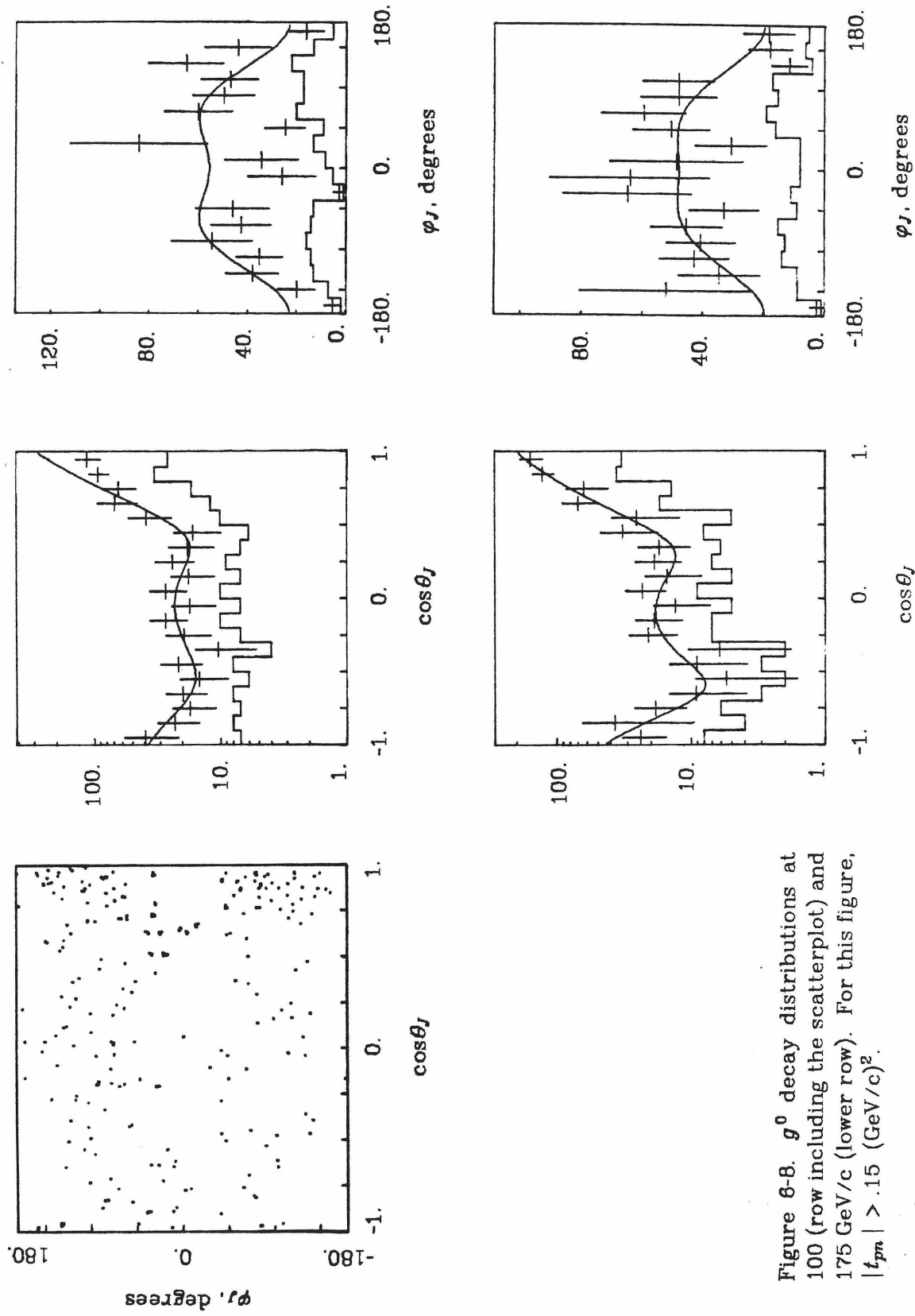


Figure 8-8.  $g^0$  decay distributions at 100 (row including the scatterplot) and 175 GeV/c (lower row). For this figure,  $|t_{pn}| > .15$  (GeV/c) $^2$ .

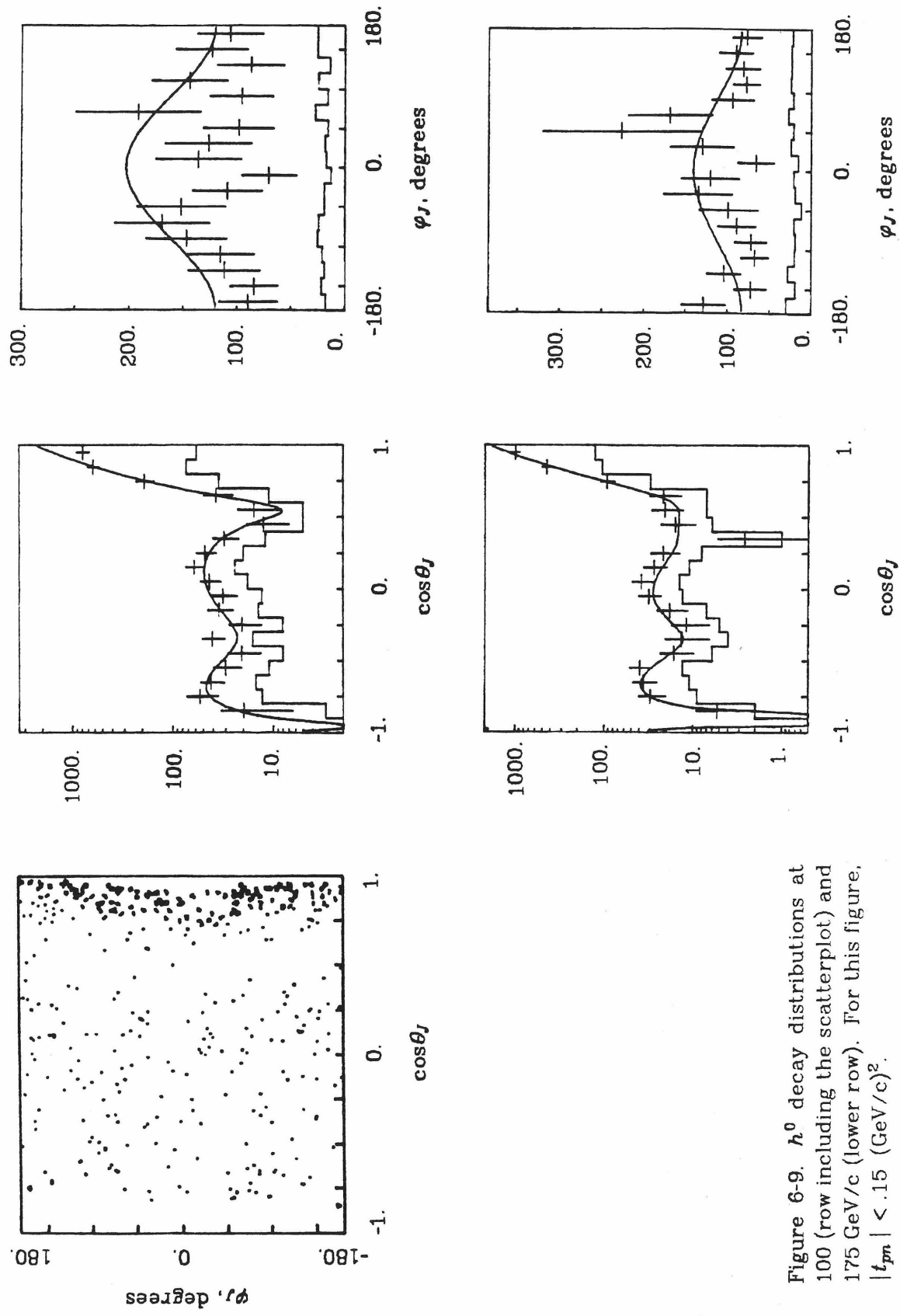


Figure 6-9.  $h^0$  decay distributions at 100 (row including the scatterplot) and 175 GeV/c (lower row). For this figure,  $|t_m| < .15$   $(\text{GeV}/c)^2$ .

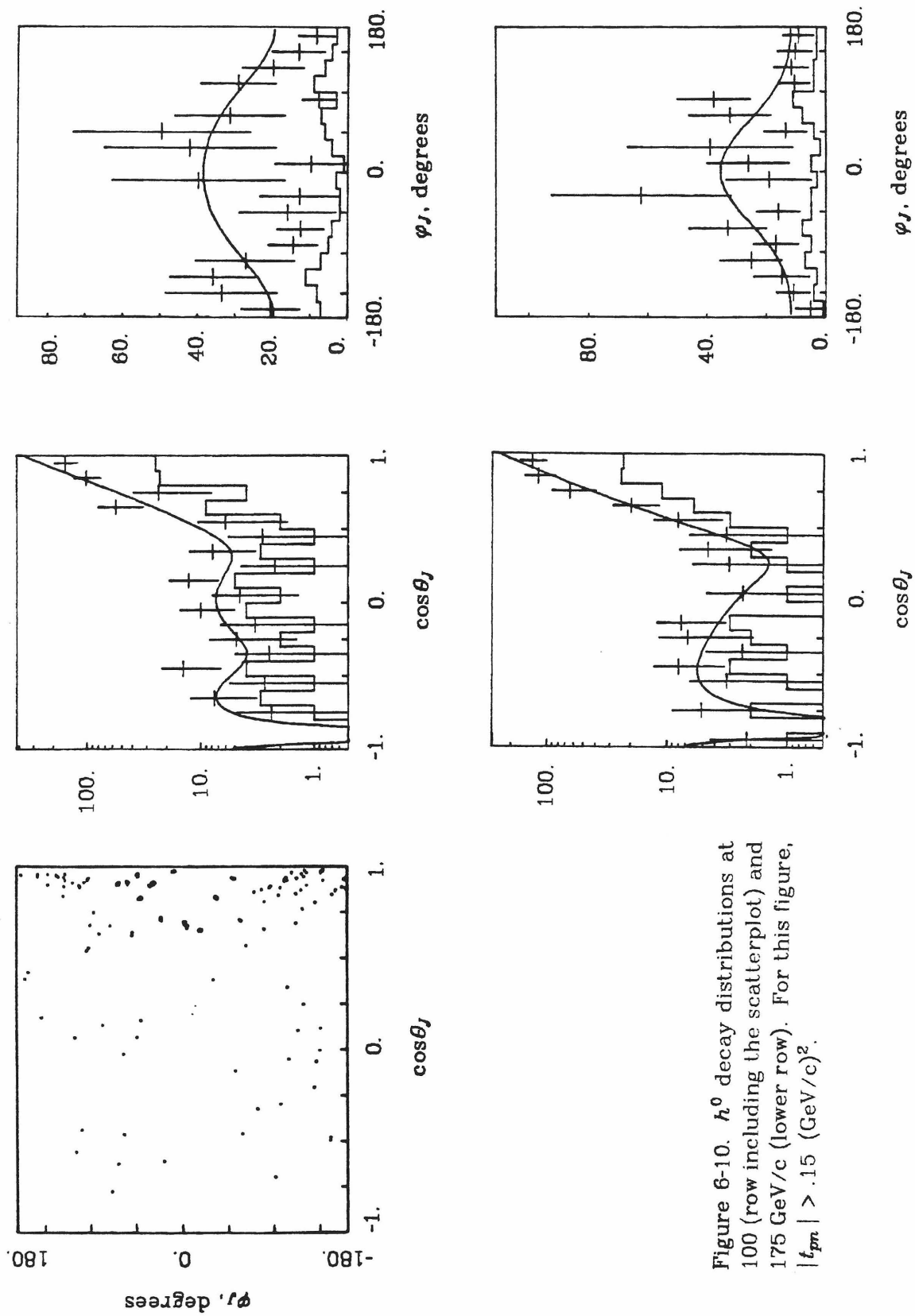


Figure 6-10.  $h^0$  decay distributions at 100 (row including the scatterplot) and 175 GeV/c (lower row). For this figure,  $|t_{pm}| > .15$  (GeV/c) $^2$ .

### 6.3 High Mass, Low $t_{pn}$ Fits

At  $\pi\pi$  masses above  $\approx 2 \text{ GeV}/c^2$ , our  $\cos\theta_J$  plots bear a strong resemblance to diffractive scattering distributions. These distributions show a strong forward ( $\cos\theta_J \approx 1$ ) peak, little or no backward peak, and a single dip next to the forward peak. The dip moves toward  $\cos\theta_J = 1$  as the  $\pi\pi$  mass increases, but seems to disappear near  $m_{\pi\pi} = 2.7$ , becoming (at best) a break in the distribution. The resemblance to diffraction is enhanced if we plot the data in  $t_{\pi\pi}$  rather than  $\cos\theta_J$ , section 6.4. In this case, the dip, and later break, is roughly fixed at  $t_{\pi\pi} \approx -1$ . The high mass forward peak appears roughly exponential in either  $\cos\theta_J$  or  $t_{\pi\pi}$ .

The  $\pi\pi n_T$  trigger was not optimized for high masses, and we clearly suffer from forward acceptance problems and low statistics. The high mass region is in somewhat better shape at 175 than at 100  $\text{GeV}/c$ . However, due to acceptance differences both data sets must be fit separately. This mass region is of considerable interest when viewed as a case of diffractive  $\pi\pi$  scattering, and we extend our analysis as far as possible. (The methods described below are quite data intensive. We have not attempted them at all at high  $t_{pn}$ .) The ACCMOR group at CERN recently investigated  $\pi\pi$  masses up to  $4.0 \text{ GeV}/c^2$  at  $63 \text{ GeV}/c$  with good high mass acceptance [Da79]. The fitting strategy here is motivated by their methods.

As discussed in section 5.5, spherical harmonic fits are not generally well matched to the high mass region. However, figure 5-11a shows that moments with  $m = 2$  are consistent with zero for  $|t_{pn}| \gtrsim 1.5 (\text{GeV}/c)^2$ .

With only  $m = 0$ , and 1 moments present, the produced distribution at constant  $\cos\theta_J$  follows the form,

$$I_P(\cos\theta_J, \varphi_J) = I_0 + I_1 \cos\varphi_J. \quad (6.1)$$

In a  $\cos\theta_J$  projection, only  $I_0$  survives. This allows us to make acceptance corrections at high masses without committing ourselves to a spherical harmonic fit. A

physical constraint is  $|I_1| \leq I_0$ . (Otherwise,  $d\sigma/d\Omega < 0$  would occur.)

We have used (6.1) in (5.6) for a series of  $\varphi_J$  dependence fits. Up to 20  $\cos\theta_J$  slices of varying size at each mass were fit. The iterative linear fit of Chapter V was used. The  $\varphi_J$  range was folded as in the moment fits, and bins with an acceptance of less than .02 were excluded from the fit. If less than five of the nine  $\varphi_J$  bins had acceptances greater than .02, no fit at all was tried. The  $t_{pn}$  cutoff for these fits was  $|t_{pn}| < .15$  to insure a minimal  $m = 2$  presence. We fit only this one large  $t_{pn}$  bin. The acceptance used in the fits was first averaged for mass and  $t_{pn}$  intervals according to weighted data. For  $\cos\theta_J$  bins larger than our grid, a second average among the affected bins was then made according to the weighted data distribution. Because of our relatively small data set, and the demands of a sharp forward peak, we needed fairly large mass bins in order to obtain even marginal statistics in each mass bin. The  $\cos\theta_J$  bin size selection was constrained near  $\cos\theta_J = 1$  by the steep forward peak, and our eventual need to fit  $I_0$  in  $\cos\theta_J$  (see below). On the other hand, our small data set required the largest bins we could bear. A number of sets were tried at each mass, in addition to trying different size mass bins before our final bin selections were made.

In the extreme forward direction, the  $\varphi_J$  fits usually failed for poor acceptance. The highest  $\cos\theta_J$  bin was always rejected, and as the  $\pi\pi$  mass increased, more high  $\cos\theta_J$  bins were added to the rejection list.

We were not able to obtain  $I_1$  in all the fits, but a reasonable  $I_0$  could still be obtained in good acceptance, low statistics cases if  $I_1$  were "abandoned", and we sought only  $I_0$ . In some other bins, the two component fit gave  $|I_1| > I_0$ , sometimes by a wide margin. Physically, these cases clearly had  $|I_1| \gtrsim I_0$ , but the fits badly over estimated the  $I_1$  component, which in turn distorted the  $I_0$  result. To ignore the  $\varphi_J$  dependence completely in such cases would unnecessarily increase the  $I_0$  errors. For them, we set  $|I_1| = I_0$  by fitting  $I_P = I_0(1 + s \cos\varphi_J)$ , where  $s = \pm 1$ .

The sign of  $s$  was taken as the sign of  $I_1$  found in the first pass fit. Unfortunately, these last tricks did not help the high  $\cos\theta_J$  problem. In the light of the above compromises, it might seem we're no better off than with moment fits. The improvement over moments is slight, but useful, and allows us to push our acceptance corrections above masses where the moments fits fail.

The acceptance correction with (6.1) required a second fit. In this, we fit the  $\cos\theta_J$  dependence of  $I_0$ , and extrapolated the result to  $\cos\theta_J = 1$ . An exponential fit to the forward  $I_0$  peak was used for masses above  $1.9 \text{ GeV}/c^2$ . This extended our results to about  $2.6 \text{ GeV}/c^2$  at  $100 \text{ GeV}/c$  and to about  $3.0 \text{ GeV}/c^2$  at  $175 \text{ GeV}/c$ . Away from the forward peak, the high mass  $I_0$  values were added to the integral of the exponential to obtain the produced event count. Below  $1.9 \text{ GeV}/c^2$ , we used a Legendre polynomial series

$$I_0 = \sum_L a_L P_L(\cos\theta) . \quad (6.2)$$

(The  $a_L$  are related to the  $t_L^0$  of equation (5.12) by  $a_L = \sqrt{\pi(2L+1)} t_L^0$ .) Produced event results from these fits were given in figure 5-5 and comparisons to the moment results were made there. The  $I_0$  results along with curves from these fits are shown in the next section.

#### 6.4 Transformation to $t_{\pi\pi}$

The main motive for doing the fits of section 6.2 was not just to extend our acceptance correction a few hundred  $\text{MeV}/c^2$ , but also to provide input for a study of  $\pi\pi$  scattering at the highest masses possible in our data, and specifically to measure the diffractive slope of the forward peak. Additional objectives were to document the approximately fixed position of the lowest  $|t_{\pi\pi}|$  dip, and, possibly, to measure the high mass  $\pi\pi$  elastic scattering cross section.

A number of problems have prevented the latter measurement. First, we do not have enough data to make a "traditional" Chew - Low pion pole extrapolation [Ch59] of, for example, the Colton-Malamud-Schlein type [Co71a, Co71b], or with any of the common form factors. In our case, reliable acceptance corrections for our small data set required much larger binning, especially in  $t_{pn}$ , than was tolerable in these methods. We then appealed to PMA as a model for the "target" pion  $t_{pn}$  dependence. In this case also, a number of ingredients were missing. First, the exponential slope  $B$ , of the PMA form factors is not yet reliably known from our data. Our fits so far for  $B$  (they have not been discussed) give values of about 10 to 15  $\text{GeV}^{-2}$  in  $d\sigma/dt_{pn}$  for our beam momenta. Figure 5-15a may also show a mass dependence to  $B$ , so extrapolating the low energy results of Wi78, which apply to the  $\rho^0$ , are not much use at the higher masses. Our need for a large  $t_{pn}$  bin is again our bane. We are unable to use differing  $t_{pn}$  dependences of the absorptive and  $\pi\pi$  scattering terms to separate them. A formal solution of PMA is possible if  $B$  is known, but without detailed fits using well determined  $I_1$  values, the separation (whether valid or not) is useless.

Although a  $\pi\pi$  cross section is not reported, we can still make useful observations about the decay distributions and determine an exponential slope. We begin by reconsidering the scatter plots that began this chapter. Figures 6-11 and 6-12 are the analogues of figures 6-1 and 6-2, but now we use measured  $t_{\pi\pi}$  values in place of  $\cos\theta_f$ . The variable  $t_{\pi\pi}$  is the squared four momentum transfer from the beam pion to the forward  $\pi^-$  (see Appendix A). It can be measured directly or approximated at low  $t_{pn}$  by equation 6.3 (see below). For the scatter plots, we use directly measured values of  $t_{\pi\pi}$ . In figure 6-11, the high mass dip has indeed become roughly straight in  $-t_{\pi\pi}$  at a value of roughly 1  $(\text{GeV}/c)^2$ . This dip runs into a concentration of events at the  $g^0$  and it is not clear from the scatter plot whether it penetrates them, goes around them, or turns away from them. Another clear dip

is seen running along the backward kinematic boundary. In the scatter plot its path from  $m_{\pi\pi} \approx 1$  and  $-t_{\pi\pi} \approx 1$  up the edge is clearly seen. This much implies that the dip survives through the  $f^0$  resonance. Whether it also passes through the  $\rho^0$  or exits the kinematically allowed regions at  $m_{\pi\pi} \approx 1$  and either  $-t_{\pi\pi} = 0$  or  $-t_{\pi\pi} \approx 1$  is not clear from the plot. A third dip, running roughly parallel to the second, but farther into the plot is also seen, but in the scatter plot it may not be convincing. (It is clear in the projections.)

We next consider briefly the high  $t_{pn}$  scatter plot of figure 6-12. The backward kinematic boundary is much fuzzier here because of the now large range of  $t_{pn}$  values included. Only one dip is clearly obvious in this plot. It "starts" at  $-t_{\pi\pi} \approx 0$  and  $m_{\pi\pi} \approx 1$  and runs roughly parallel to the kinematic  $t_{\pi\pi}$  limit. Other possible dips are evidently fairly weak, and not readily traced by this plot, but it seems clear that no dip can penetrate the  $\rho^0$  mass region and stay kinematically allowed. In both these plots, most dips are found at roughly constant  $u_{\pi\pi}$ . The major exception is the high mass dip in figure 6-11. Section 6.5 considers them in more detail.

Figures 6-13 (100 GeV/c) and 6-14 (175 GeV/c) present the  $I_0$  results of the previous section. We again use  $-t_{\pi\pi}$  instead of  $\cos\theta_J$  to represent the Gottfried - Jackson polar angle. The former is more directly a dynamical variable than  $\cos\theta_J$ , but the reference frame remains the same. Since the  $t_{\pi\pi}$  range expands as roughly  $m_{\pi\pi}^2$ , the high  $|t_{\pi\pi}|$  cutoff is the last bin completely inside the physical  $|t_{\pi\pi}|$  range at the low end of the mass bin. At low  $t_{pn}$ , the approximation

$$t_{\pi\pi} = -2q^2\sqrt{1 - \cos\theta_J} \quad (6.3)$$

where  $q = .5\sqrt{m_{\pi\pi}^2 - 4m_\pi^2}$  is the final state pion momentum in the  $\pi\pi$  rest frame is excellent. Equation 6.3 is exact at  $t_{pn} = m_\pi^2$  and corrections to it at small  $t_{pn} < 0$  are small enough to ignore. Bounds on  $t_{\pi\pi}$  are set by  $m_{\pi\pi}$ , the limits  $\cos\theta_J = \pm 1$ , and  $t_{pn}$ , see Appendix A.

The vertical scales in these figures should be considered arbitrary. They are essentially the produced event scale for events binned in  $\cos\theta_J$  bins of size .1. The transformation to  $t_{\pi\pi}$  has merely squeezed or stretched the horizontal axis. We should also caution that the decade scales in the plots vary from mass bin to mass bin.

These plots track quite nicely the  $m_{\pi\pi}$  evolution of the dips. In some cases, dips in one mass bin map to an inflection or break in the curve in the next, but the effect is still traceable. At the lower masses, no dips are fixed in  $t_{\pi\pi}$ . However, beginning at  $m_{\pi\pi} \approx 1.7 \text{ GeV}/c^2$ , the low  $t_{\pi\pi}$  dip is clearly established at  $\approx -1$ . Furthermore, even though it is seen to fade into a break at masses above about 2.6  $\text{GeV}/c^2$ , the break is at the same location.

The points in figures 6-13 and 6-14 are the  $I_0$  results of our  $\varphi_J$  fits. The curves are fits to the Legendre polynomial series of equation 6.2 ( $m_{\pi\pi} \leq 1.9 \text{ GeV}/c^2$ ) or to an exponential in the forward,  $-t_{\pi\pi} \approx 0$  region ( $m_{\pi\pi} \geq 1.9 \text{ GeV}/c^2$ ). Exponentials are not statistically compelling in our data, but we believe polynomial fits at high masses in principle underestimate the forward peak. Reasons for this have been discussed in Chapter V. We remark that exponentials are preferred in the high statistics ACCMOR group's 63  $\text{GeV}/c$  data.

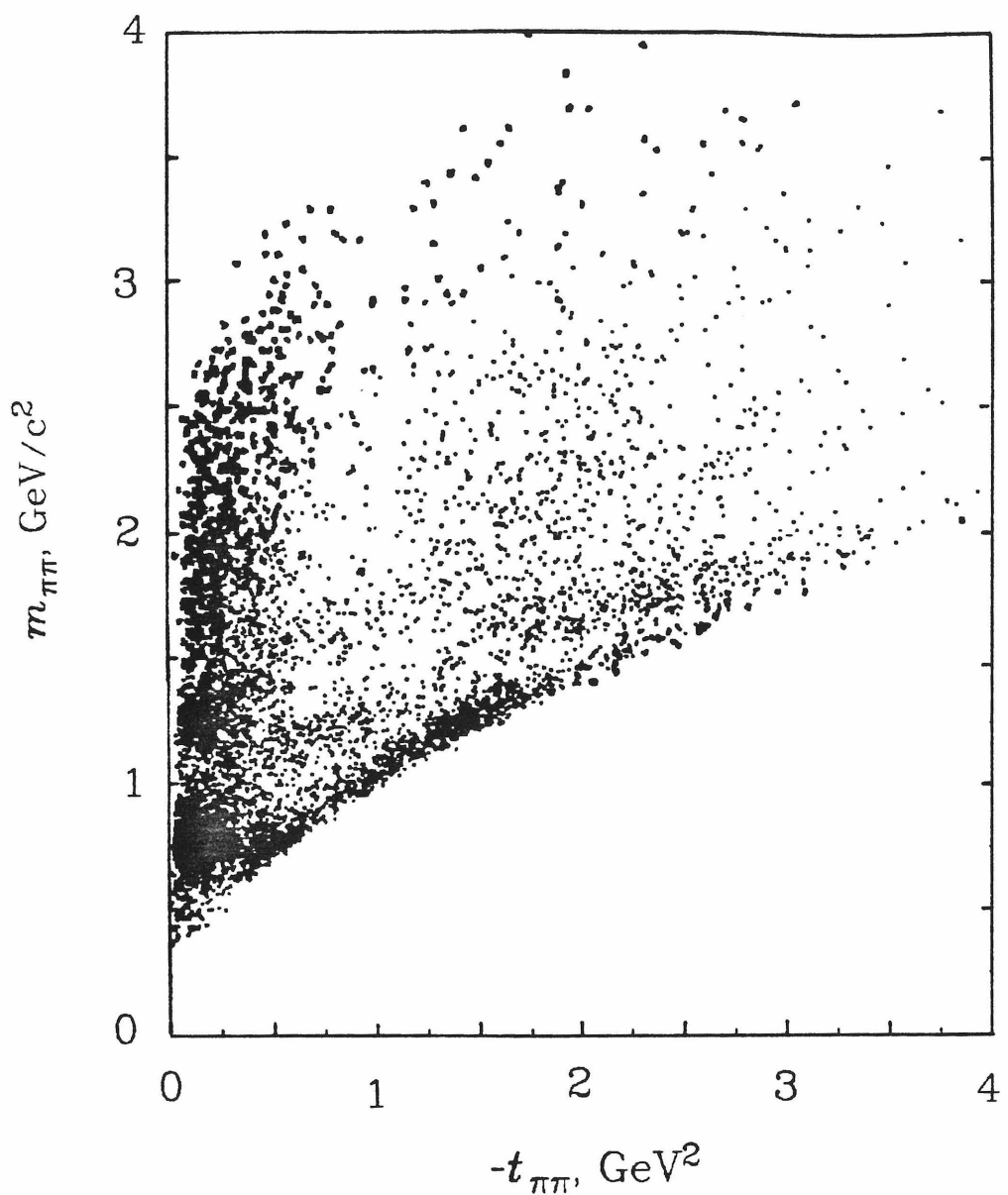


Figure 6-11. 100  $\text{GeV}/c$  scatter plot of  $-t_{\pi\pi}$  versus  $m_{\pi\pi}$  for  $|t_{pn}| < .08$   $(\text{GeV}/c)^2$ . The backward kinematic of  $\cos\theta_J = -1$  maps to the  $\pi\pi$  mass dependent limit seen, and the limit  $\cos\theta_J = +1$  maps to  $t_{\pi\pi} = 0$ .

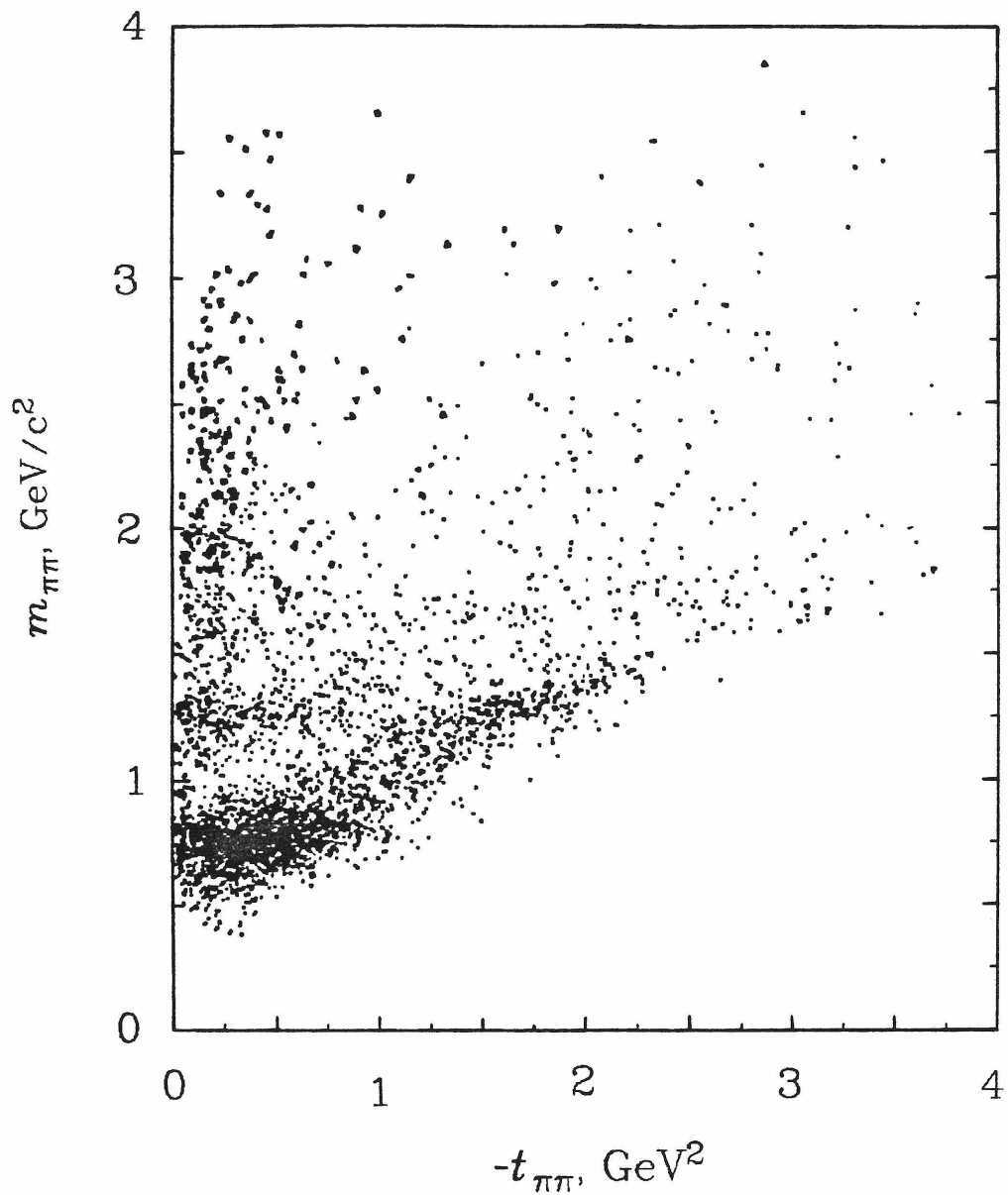


Figure 6-12. 100  $\text{GeV}/c$  scatter plot of  $-t_{\pi\pi}$  versus  $m_{\pi\pi}$  for  $|t_{pn}| > .15$   $(\text{GeV}/c)^2$ . Since no upper limit was placed on  $|t_{pn}|$ , the backward kinematic limit for  $-t_{\pi\pi}$  is not sharply defined for this plot.

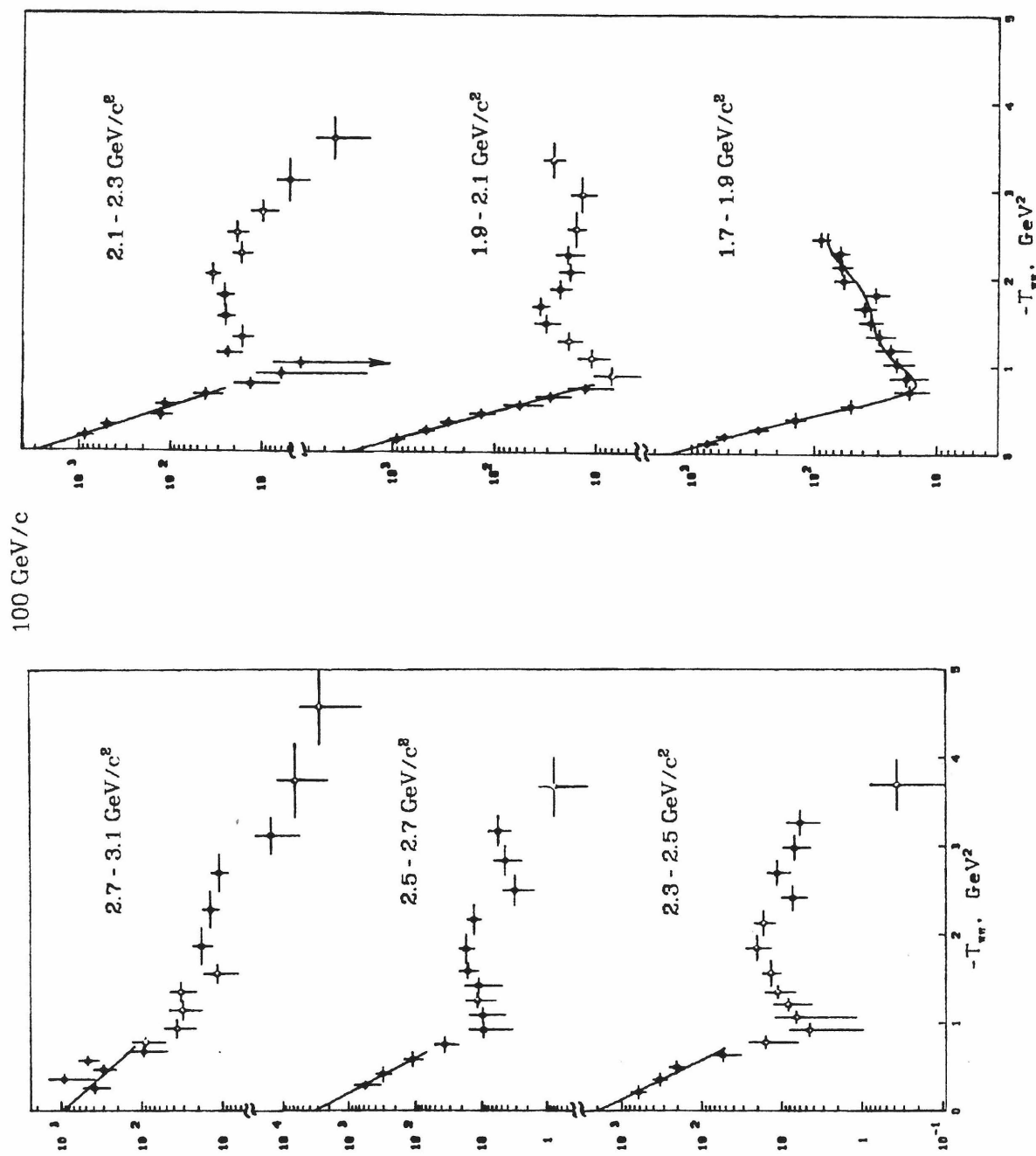
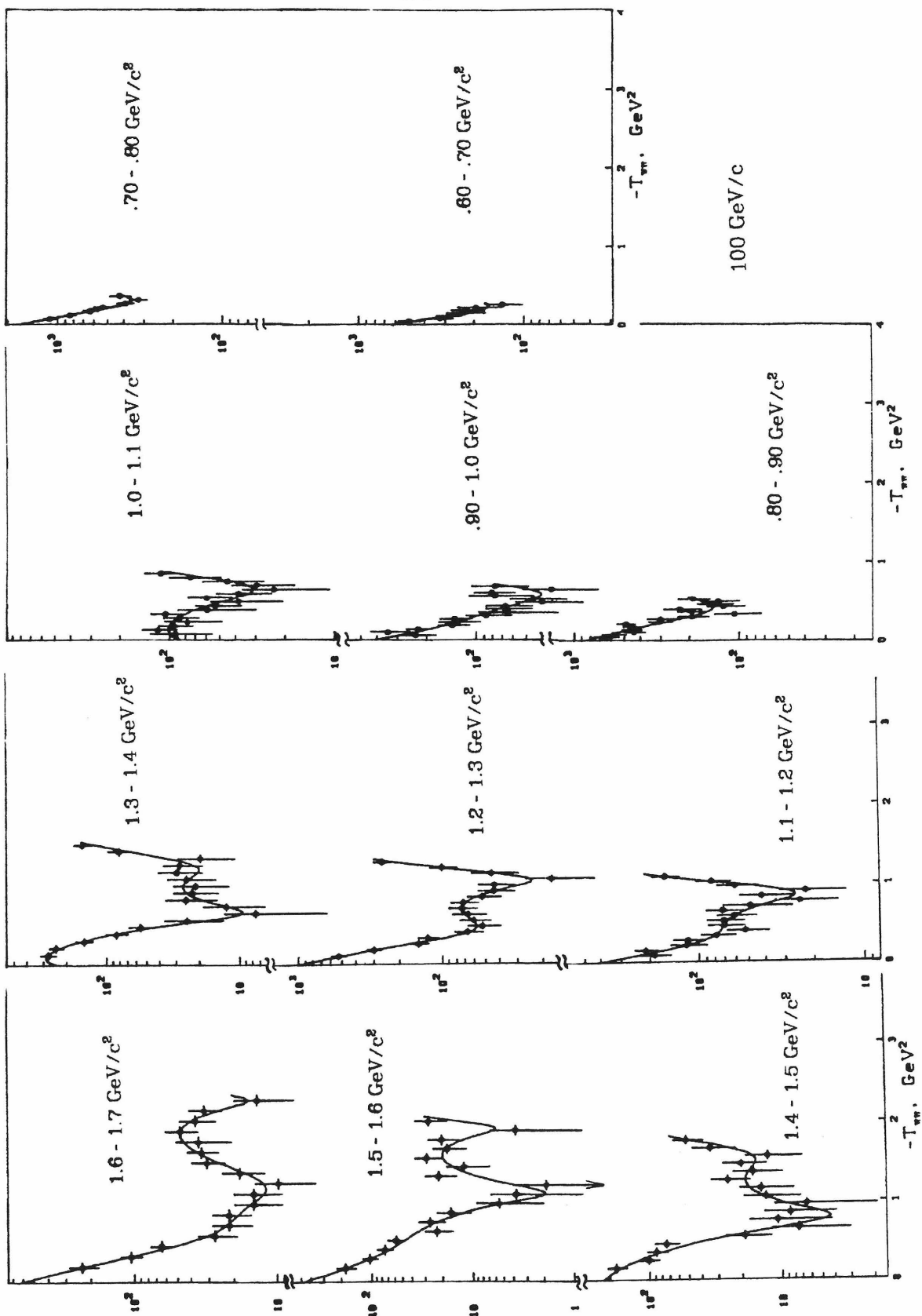


Figure 6-13.  $100 \text{ GeV/c}$  decay distributions in  $t_{\pi\pi}$  for  $|t_{pn}| < 0.15 \text{ (GeV/c)}^2$ . The points are  $I_0$  values and the curves are from fits described in section 6.2.



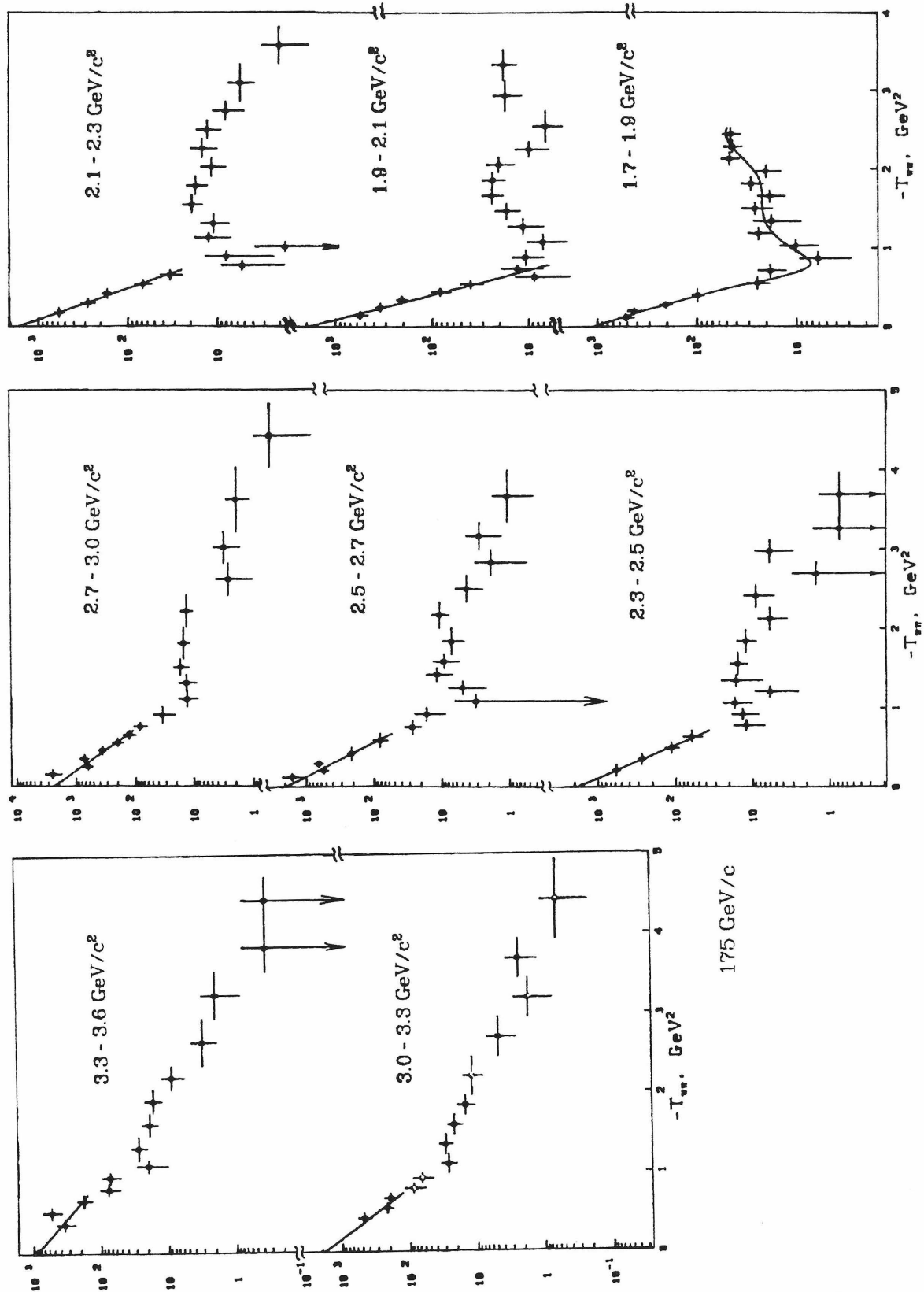
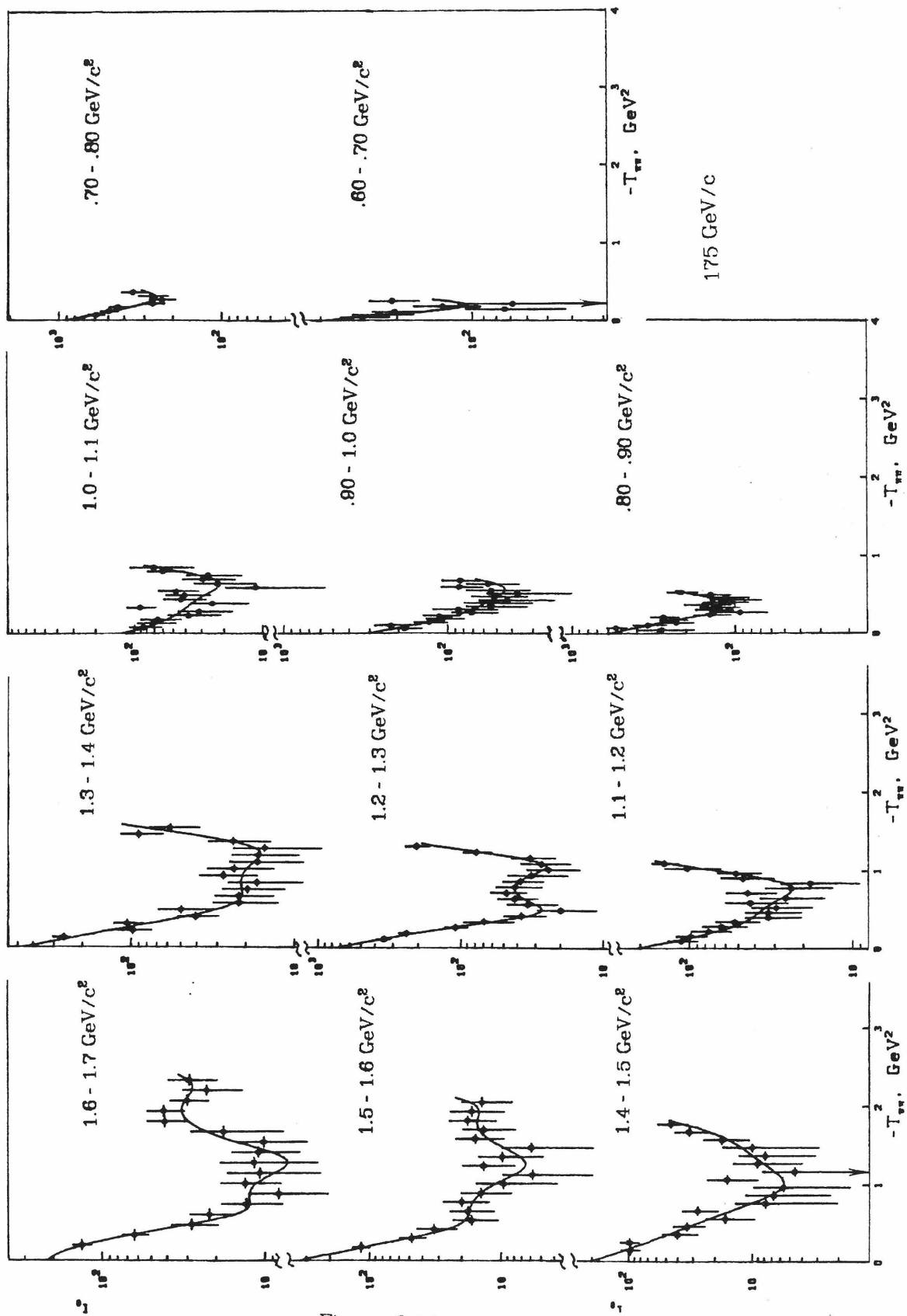


Figure 6-14.  $175 \text{ GeV}/c$  decay distributions in  $t_{\pi\pi}$  for  $|t_{pn}| < .15 (\text{GeV}/c)^2$ . The points are  $I_0$  values and the curves are from fits described in section 6.2.



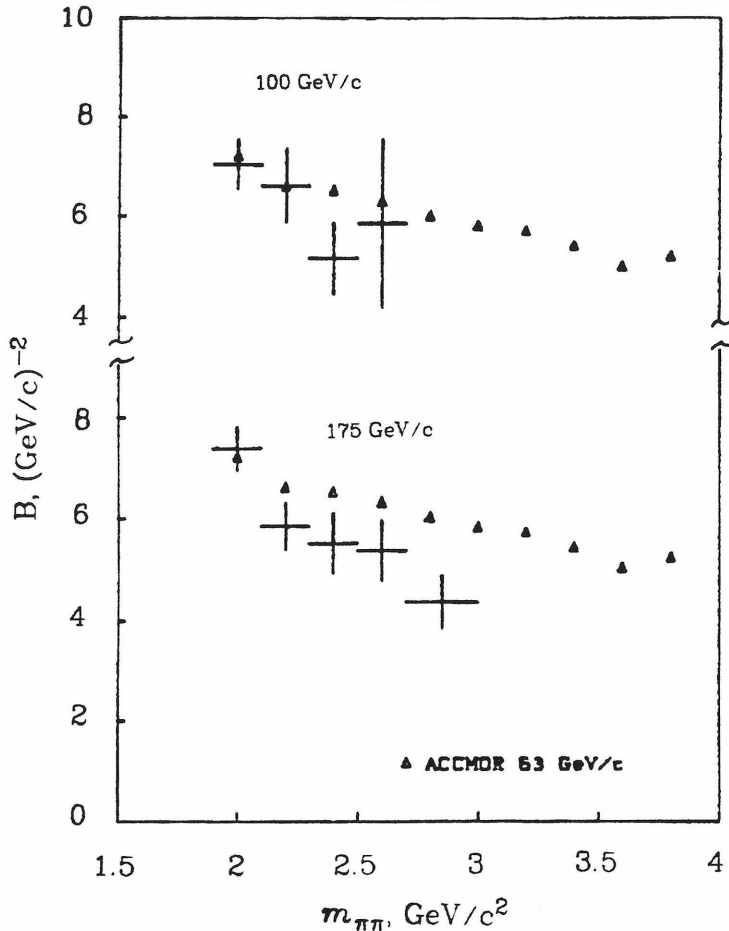


Figure 6-15. Exponential slopes (in  $t_{\pi\pi}$ ) for the high mass forward peaks of figures 6-13 and 6-14. Also plotted are slopes found by the ACCMOR group for the  $\pi\pi$  scattering intensity [Da79]. The errors claimed by Da79 are comparable to the symbol size.

#### 6.4.1 High Mass Exponential Slope

Figure 6-15 shows the exponential slopes from our high mass fits, along with values found by the ACCMOR group. We have excluded the highest 100 GeV/c mass band and the two highest at 175 GeV/c as unreliable. Reasonable fits were obtained in the other mass bands. Our results are reasonably consistent with the ACCMOR values. We both have roughly the same B values, and both experiments see a fall in B with  $\pi\pi$  mass. Our values appear to fall faster than theirs and are systematically lower. However, they were able to analyze their data much more fully, including a

pole extrapolation using PMA [Da79]. In our data, we found that our slopes increased (as did errors) when we made smaller  $t_{pn}$  cuts and dropped a bit when we expanded the cut. This leads us to believe that we probably underestimate the pole extrapolated slopes. (The slopes of figure 6-15, and not pole extrapolated values, are appropriate for acceptance corrections.) We do see that our slopes are, within errors, independent of  $P_{lab}$ . Such behavior is expected if off shell  $\pi\pi$  scattering is a meaningful process. Note that the slopes of figure 6-15 are in terms of  $t_{\pi\pi}$ . Plotted in this way a significant factor of  $q^2$  is removed from slopes in terms of  $\cos\theta_J$ . Despite a slight antishrinkage, the relatively constant slope in  $t_{\pi\pi}$  is characteristic of diffraction.

### 6.5 Dips

Virtually every polar angle ( $\cos\theta_J$ ,  $t_{\pi\pi}$ ) distribution given so far has one or more dips in it. A number of authors, Odorico [Od71, Od72ab], Pennington [Pe73], and Eguchi *et.al.* [Eg74] have all stressed the importance of amplitude zeros in any global understanding of  $\pi\pi$  scattering. Pennington emphasized that  $\pi\pi$  amplitude zeros are closely related to the dips seen in the decay distributions. The apparently smooth evolution of our dips makes such an interpretation attractive. Taking observed quantities as the real part of the dynamic variables, dip locations track the real parts of the amplitude zeros. The depth of the dip is related to the imaginary part of the amplitude in the case of observed data. Alternately, the depth is related to the imaginary part of the zero, which is not observed and can only be obtained by amplitude fits. The presence of backgrounds may move the dips relative to the  $\pi\pi$  zeros, but if these are small, we can get a reasonable map of the real parts of zeros by following the dips in our distributions. The net  $\pi\pi$  scattering amplitude is almost surely a complicated sum of different amplitudes, and if dips in decay distributions track anything, it is zeros or minima in the net amplitude.

Pennington warns that following dips in  $d\sigma/d\Omega$  is not by any means general enough for a full understanding of the  $\pi\pi$  amplitude zeros. The exercise still seems a useful first approximation for observing the dominant patterns.

Figure 6-16 shows our patterns. In this figure,  $s_{\pi\pi} = m_{\pi\pi}^2$  and  $-t_{\pi\pi}$  are used as the dynamic variables. Lines of constant  $u_{\pi\pi}$  are parallel to the diagonal  $\cos\theta_J = -1$  line. The kinematic boundaries are this line and the  $-t_{\pi\pi} = 0$  axis. The dots (·) were obtained from projections of our 100 GeV/c moment results since 50 MeV/c<sup>2</sup> binning was available. The points labeled "I" were from the same source. The dots locate clear dips, while the I's locate breaks in the  $\cos\theta_J$  projection of the fit results. Since the points in figure 6-16 were obtained by hand, errors for the I's (in  $t_{\pi\pi}$ ) are large, and some of them, especially the ones clustered at  $s = 1$ , may not be real. The arrows locate mass bins where the 100 GeV/c moment distribution was falling as  $\cos\theta_J = 1$  or  $\cos\theta_J = -1$  was approached. The open circles are dips and breaks taken from high mass 100 GeV/c slices of figure 6-13, and the x's are 175 GeV/c data from figure 6-14. From figures 6-13 and 6-14 we can continue the map of the leading dip but have essentially no information on the others. We see at least three families of dips (breaks are included), labeled A - D, B - C, and E - F, in the figure. The patterns are sufficiently striking that some discussion in terms of models seems appropriate. For this, we assume that our dips follow  $\pi\pi$  amplitude zeros, and will try to understand the observed patterns in terms of either of two dominating amplitude structures. Without detailed fits, the following discussion must be considered somewhat speculative.

An appealing dynamic origin for zeros is found in the Lovelace - Veneziano model which has the amplitude structure

$$V(s, t) = \frac{\Gamma(1-\alpha_s)\Gamma(1-\alpha_t)}{\Gamma(1-\alpha_s-\alpha_t)} \quad (6.4)$$

where  $\alpha_x = \alpha_x^0 + \alpha_x^1 \cdot x$ . In equation 6.4,  $s$ ,  $t$ , and  $u$ , are  $s_{\pi\pi}$ ,  $t_{\pi\pi}$ , and  $u_{\pi\pi}$ . For real

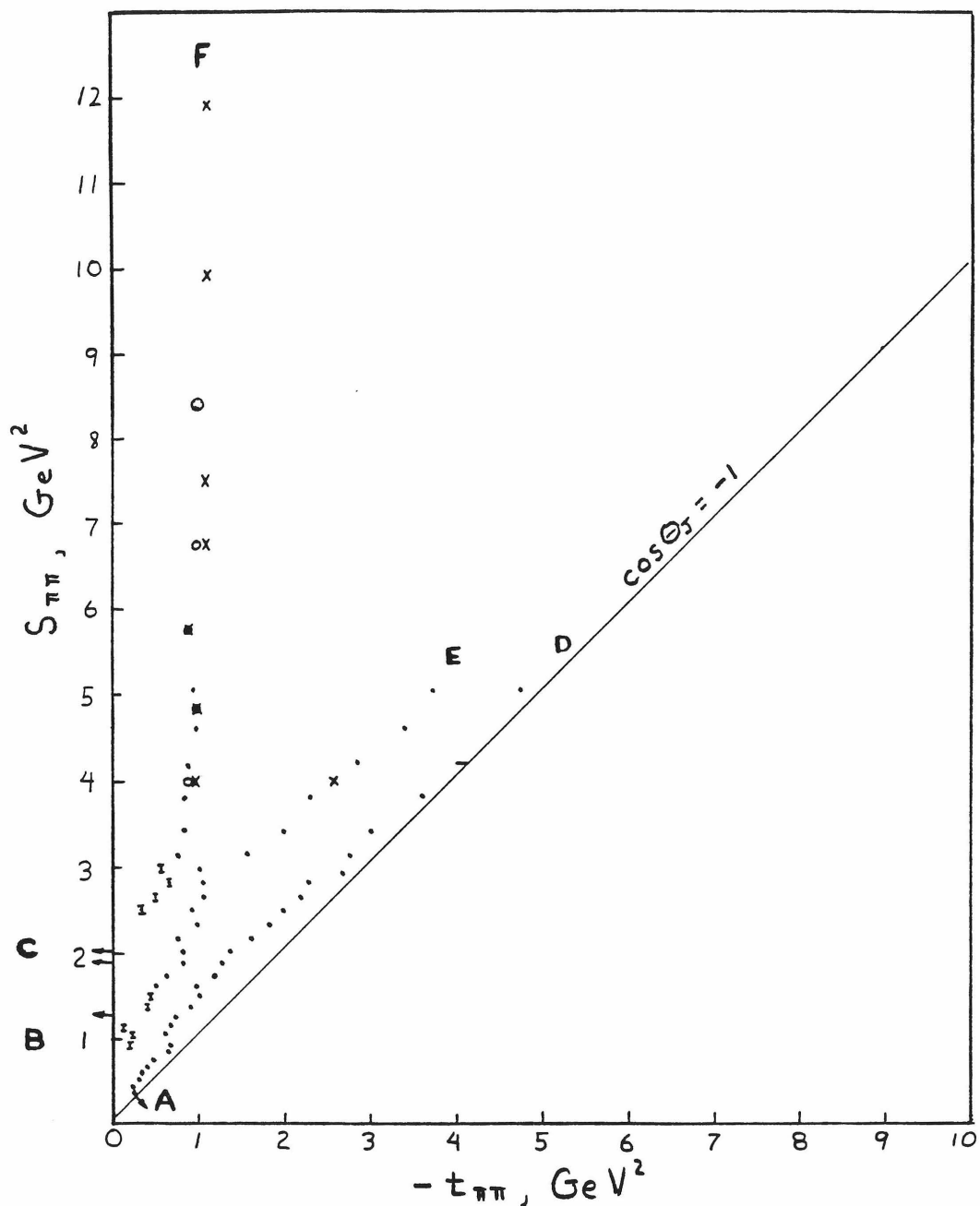


Figure 6-16. Pattern of decay distribution dips seen in our data. Symbols are explained in the text.

pion targets and  $\pi\pi \rightarrow \pi\pi$ ,

$$s_{\pi\pi} + u_{\pi\pi} + t_{\pi\pi} = 4m_\pi^2. \quad (6.5)$$

Forbidden double poles in the numerator of (6.4) are killed off by the denominator [Ve68]. This process creates zeros away from the double poles, and their dependence on  $s_{\pi\pi}$ ,  $t_{\pi\pi}$ , or  $u_{\pi\pi}$  depends on the condition (6.5) and the  $\alpha^i$ . Assuming constant  $\alpha^i$  leads to zeros at constant  $u_{\pi\pi}$ . Small deviations from this may be related to finite resonance widths or variations in  $\alpha^0$ , and  $\alpha^1$ . Large deviations are presumably effects not contained in (6.4). Odorico noted that the zero associated with the  $\rho-\rho$  double pole enters the kinematically allowed region at  $m_{\pi\pi} \approx 1 \text{ GeV}/c^2$ . He argued that this was the dominant reason for rapid drops in event distributions and moments at this mass. This explanation of the effect was contrary to assertions that the drops just reflected the coincidence with the  $\pi\pi \rightarrow K\bar{K}$  kinematic threshold. Odorico supported his position by finding similar effects in other reactions where the  $K\bar{K}$  threshold is not a factor, but the Veneziano amplitude is active [Od72b]. The dip series B - E is consistent with this first Odorico zero. Equation 6.4 contains one extra fixed  $u_{\pi\pi}$  but non double pole killing zero, the Adler zero, which passes through the point  $s_{\pi\pi} = t_{\pi\pi} = u_{\pi\pi} = 0$ . The  $K\bar{K}$  threshold does lead to a wiggle in the Adler zero [Pe73], and this is reflected in our dip patterns. In figure 6-16, the Adler zero corresponds to the dip series A - D.

At  $\pi\pi$  masses above the resonance region, where the decay distributions resemble diffraction scattering, a more convenient way to consider  $V(s,t)$  is explicitly in terms of exchange models. In this case, the amplitude is the sum of amplitudes for allowed exchanges including  $\rho$ ,  $f$ , and Pomeron. Such models could lead to fixed  $t_{\pi\pi}$  dips although their actual location would reflect the full amplitude and no single part. In figure 6-16, the dip series C - F is consistent with a fixed  $t_{\pi\pi}$  dip at  $s_{\pi\pi}$  values above about 3.5.

Our low  $s_{\pi\pi}$  pattern of dips is in reasonable accord with the zero patterns given in Pe73 and Eg74, and our identifications were based on these sources. Our dips agree with Pennington in sending the Adler zero (line A - D) outside the kinematic boundary in the backward ( $\cos\theta_J = -1$ ) rather than forward ( $\cos\theta_J = +1$ ) direction. Our dip shows a sharp wiggle near  $s = 1$ . Pennington remarks that such behavior is expected for a smoothly varying P-wave and rapidly varying S-wave, and is characteristic of the  $K\bar{K}$  threshold. The gross behavior of this dip is roughly along constant  $u_{\pi\pi}$  though. The B - E series of dips also follow roughly constant (though deviations are larger)  $u_{\pi\pi}$  and evidently leave the plot at about  $s_{\pi\pi} = 1$ . The third line (C - F) of points is a series of breaks near  $t_{\pi\pi} = 0$ . These and the arrows near  $s_{\pi\pi} = 2$  seem consistent with constant  $u_{\pi\pi}$  behavior. We see no dips that could be easily identified with higher mass double poles, for example the  $f-f$ ,  $f-g$ , and  $\rho-g$  double poles. If present, these presumably have large imaginary parts and we are not sensitive to them.

We see two entries to the plot from the left; one (point B) at  $s_{\pi\pi} \approx 1$ , and another (point C) at  $s_{\pi\pi} \approx 2$ . (The two arrows here are in neighboring mass bins.) The first has been identified by Odorico and others with the  $\rho-\rho$  double pole killing zero. The second exits the physical region nearest the the  $\rho-f$  double pole intersection [Eg74]. We note (as did Odorico [Od72b]) that the entry of this zero coincides with the rapid changes in moments at  $m_{\pi\pi} \approx 1.4$ . (The agreement here is better than at 1 GeV/c<sup>2</sup>.) In this case, unlike the first Odorico zero, no convenient threshold is available to compete with the explanation. This observation in turn lends support for the presence of the Odorico mechanism at 1 GeV/c<sup>2</sup>.

The B - E and C - F series of dips approach each other at  $s_{\pi\pi} = 3$ , and we might consider whether or not the actual pattern is C - E, and B - F, or something completely different. The rest of this section is speculation on this question. The fixed  $u_{\pi\pi}$  hypothesis implies that the zeros do not cross, and analyses of lower energy

data [Eg74] indicate no zero crossing. On the other hand, a sharp turn of the C - F series is difficult to understand from (6.4) with constant or even near constant  $\alpha^i$ . We might speculate that C - F is not one zero but two, consisting of an Odorico zero and a fixed  $t_{\pi\pi}$  zero not included in the amplitude (6.4). The Odorico zero would continue on at roughly constant  $u_{\pi\pi}$  but gather an imaginary part sufficient to obscure it in our low statistics data. (This seems inconsistent with low energy data.) Similarly, the fixed  $t_{\pi\pi}$  zero would continue down in  $s_{\pi\pi}$ , and while not particularly strong at low masses, be capable of distorting the patterns associated with other zeros. We note that in the region of  $-t_{\pi\pi} \approx 1$  both the Adler and first Odorico zeros deviate and run parallel to a fixed  $t_{\pi\pi}$  path for several mass bins each. Since the "constant"  $u_{\pi\pi}$  zeros clearly have distortions of up to  $\pm .5$  (GeV/c)<sup>2</sup>, we might admit such a possibility for any "fixed"  $t_{\pi\pi}$  zero and allow it to move a bit closer to  $t_{\pi\pi} = 0$  at the lowest masses, crossing the  $s_{\pi\pi} = 0$  axis at about  $-t_{\pi\pi} = .5$ . This slight bending increases the number of points along this dip significantly at low masses and may explain some of the distortions seen in the first two "fixed  $u_{\pi\pi}$ " zeros. It would also add an alternative mechanism for the Adler zero wiggle. One final benefit might be to indicate how  $\rho$  exchange, whose trajectory crosses zero at  $t \approx -.6$ , contributes to a high mass dip which is closer to  $t_{\pi\pi} = -1$ . These speculations imply that exchange diagrams play a significant part in the low mass region. At any rate, while gross patterns can be "understood" from simple applications of some models an amplitude analysis is called for, but resolving ambiguities in such an analysis requires high statistics data. It will be interesting to see what the ACCMOR collaboration might say about the zero patterns.

## 6.6 Review

In the previous chapters we have described our measurements of, and results on the  $\pi^- p \rightarrow \pi^+ \pi^- n$  reaction. We have presented the cross section in the  $\rho^0$  region, Gottfried - Jackson frame spherical harmonic moments for the  $\pi\pi n$  reaction as a function of  $\pi\pi$  mass and as a function of  $t_{pn}$  at the  $\rho^0$ , decay distributions in  $\cos\theta_J$ ,  $\varphi_J$  and  $t_{\pi\pi}$ , and the high mass diffractive slope for the forward  $\pi\pi$  peak. (Fredericksen's thesis also includes effective pion trajectories at the  $\rho^0$ .) We have confirmed the ACCMOR group observation of the fixed  $t_{\pi\pi}$  dip at high  $\pi\pi$  masses, and considered its mass dependence into the resonance region. Our low mass dip patterns are consistent with low energy results.

Our basic conclusion from all this is that reaction (1.1) is highly stable. That is, the gross features and many fine ones too, haven't changed much in the  $P_{lab}$  interval of  $\approx 15$  to  $175$  GeV/c. The cross sections at  $100$  and  $175$  GeV/c are in rough accord with simple extrapolations from lower energies. The slowing of the shrinkage in  $\langle Y_2^0 \rangle$  might be considered a change from low energy trends, but a calculation of the Kimmel and Owens model [Ki77] is needed. The high mass fixed  $t_{\pi\pi}$  dip was probably visible in some of the low energy experiments, but the ACCMOR group was the first to publish its observation [Da79]. The analysis reported here has been more a survey of reaction (1.1) than a detailed study of one topic. For this thesis the survey approach was adopted in the hopes of finding either significant changes in the reaction or demonstrating a general "stability" with  $P_{lab}$ . For the most part, we found the latter.

**APPENDIX A**  
**Kinematics, OPE, PMA**

**A.1 Kinematics**

A brief review of kinematics for  $\pi^- \rightarrow \pi^+ \pi^- n$  and some notation definition are useful. Needed approximations are also given. We then discuss one pion exchange and the Poor Man's Absorption model (PMA). PMA has been used as a method for isolating  $\pi$  exchange; that is, as a model for the "target" in  $\pi\pi$  scattering [Da79]. Our ability to use PMA is limited by our small data sample.

Our track finding analysis provided measurements of charges and momentum vectors ( $\vec{P}$ ), for the beam and the forward charged particles. Mass identification was provided by our Cerenkov counters once the momenta were found. The beam pion will be denoted by the subscript  $b$ , the target proton by  $p$ , the forward pions by  $f$  and/or charges, and the recoil neutron by  $n$ . The total forward system ( $\pi^+ + \pi^-$ ) will use  $f$  with no sign. Laboratory frame four vectors  $P = (p_x, p_y, p_z, E)$  satisfying

$$m^2 = P^2 = E^2 - \vec{P}^2 \quad (A.1)$$

are known, where  $m$  denotes the rest mass. These, along with the charges and a lab four vector for the target proton,  $P_p = (0, 0, 0, m_p)$ , are our kinematic data. We use units with the limiting velocity  $c = 1$  throughout. The total forward four momentum is  $P_f = P_f^+ + P_f^-$ , and the total energy is  $E_f = E_f^+ + E_f^-$ .

Mandelstam invariants for  $\pi^- p \rightarrow \pi^+ \pi^- n$  are

$$s \equiv (P_b + P_p)^2 = (P_f + P_n)^2 \quad (A.2a)$$

$$t \equiv (P_p - P_n)^2 = (P_b - P_f)^2 \quad (A.2b)$$

and  $u \equiv (P_b - P_n)^2 = (P_p - P_f)^2 \quad (A.2c)$

with

$$s + t + u = m_b^2 + m_p^2 + m_n^2 + m_f^2. \quad (A.3)$$

$P_f^2 = m_f^2$  is the  $\pi^+\pi^-$  effective mass. In a pattern used throughout the thesis, we use  $t_{pn}$  to distinguish  $(P_p - P_n)^2$  from  $t_{nn} = (P_b - P_f)^2$ .

The recoil neutron is undetected. We determine that the unseen system was a recoil neutron by evaluating the squared missing mass,

$$Mx^2 = (P_b + P_p - P_f)^2 \quad (A.4a)$$

or

$$Mx^2 = m_p^2 + t_{pn} + 2m_p(E_b - E_f) \quad (A.4b)$$

and requiring, within the limits of our resolution, that  $Mx^2 = m_n^2$ .

Equation (A.4a) was used for the missing mass calculation. At momenta above 30 GeV/c, our missing mass resolution, figure 2-11, causes the neutron  $Mx^2$  peak to include negative values.  $Mx$  is not useful and  $Mx^2$  is the proper variable. (A.4a) is also as good as we can do for  $Mx^2$ . The missing mass necessarily involves differences between two large and poorly measured numbers, essentially  $E_b$  and  $E_f$ , and there are just no clever tricks to use for  $Mx^2$  with an unmeasured recoil system. Our  $Mx^2$  resolution is essentially the  $E_f$  resolution. The contribution from the error in  $E_b$  from the finite momentum slit width is negligible on an event by event basis.

The effective rest mass,  $m_{\pi\pi}$ , of the forward pions is given by

$$m_{\pi\pi}^2 = (P_f^+ + P_f^-)^2 \quad (A.5)$$

The  $\pi\pi$  mass measurement using (A.5) is as good as we need get. The  $m_\pi = 0$  approximation,  $m_{\pi\pi} = \Theta \sqrt{P_{lab}^+ P_{lab}^-}$  is not useful, except to illustrate that the  $m_{\pi\pi}$  resolution is set by both the lab momenta of the pions and the lab opening angle,  $\Theta$ .

In practice, this form distorts the mass spectrum noticeably. The mass resolution can be improved slightly if we force  $Mx^2 \equiv m_n^2$  by adjusting the forward momenta according to their resolutions. None of our other measurements were noticeably improved by this trick (actually attempted to improve on  $\varphi_J$ , defined below) and we abandoned it.

Assuming we have isolated neutron recoil events (with only a small background), we can easily improve on the  $t_{pn}$  measurement, (A.2b). A more reliable and accurate estimate of  $t_{pn}$  is

$$t_{pn} = -p_t^2 + t_{\min} \quad (A.6)$$

where  $p_t^2$  is the magnitude of the transverse component of  $\vec{P}_f$  measured with respect to the beam. The kinematic limit  $t_{\min}$ , which for neutron recoils is

$$t_{\min} \approx \frac{-(m_m^2 - m_\pi^2)^2}{4E_b^2} \quad (A.7)$$

with  $E_b$  the lab beam energy, is negligible at our energies for most purposes. Monte Carlo studies have found equation (A.6) to be an unbiased estimate of  $t_{pn}$  at all values except the smallest. A.2b sends a substantial number of events to positive (and unphysical)  $t_{pn}$ . Equation (A.6) depends crucially on the recoil neutron assumption. At large missing masses, far from the neutron peak, one would have to appeal to (A.2b).

Decay angle distributions in the forward  $\pi\pi$  rest frame carry a great deal of information about the produced states and their production mechanisms. Two planes are naturally defined. The production plane contains the beam, target proton and recoil neutron. The decay plane contains the forward pions and the beam. To work in the  $\pi\pi$  rest frame, we apply a Lorentz boost of magnitude and direction  $-\vec{P}_f$  to measured particles. The  $\pi\pi$  decay angles are commonly defined in terms of the  $\pi^-$  direction with respect to one of two coordinate systems. In both, the y-axis

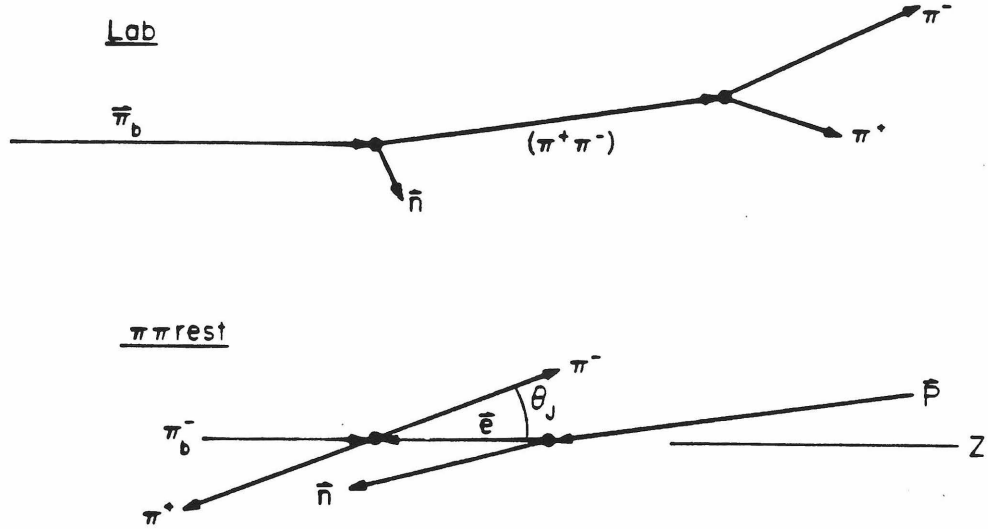


Figure A-1. Lab and Gottfried Jackson frame momentum vectors.  $\varphi_J$  is assumed zero.

is defined as normal to the production plane,

$$\hat{y} = \frac{\vec{n} \times \vec{\pi}_b}{|\vec{n} \times \vec{\pi}_b|} = \frac{\vec{p} \times \vec{\pi}_b}{|\vec{p} \times \vec{\pi}_b|} \quad (A.8)$$

where the particle name denotes its  $\pi\pi$  rest frame momentum. The choice of z-axis distinguishes the two coordinate systems. In the Gottfried - Jackson (J) frame [Ja64], the z-axis is along the  $\pi\pi$  rest frame beam vector:

$$\hat{z} = \frac{\vec{\pi}_b}{|\vec{\pi}_b|} \quad (A.9)$$

In the "s-channel helicity frame" (H), the z-axis is directed antiparallel to the  $\pi\pi$  rest frame recoil neutron,

$$\hat{z} = \frac{-\vec{n}}{|\vec{n}|}$$

This choice seems conventional. In both systems,  $\hat{x} = \hat{y} \times \hat{z}$ , and the polar angle  $\theta$  is

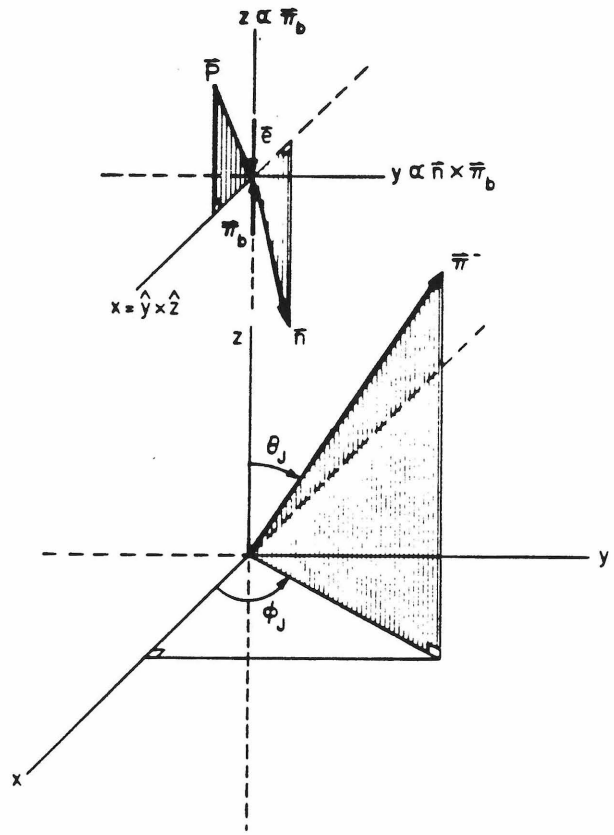


Figure A-2. Gottfried - Jackson frame momentum vectors illustrating  $\theta_J$  and  $\varphi_J$ . Production and decay planes are also shown.  $\pi^+ = \pi^-$ . The boosted proton momentum vector,  $\vec{P}$  is equal and opposite to the laboratory  $\pi^+ \pi^-$  momentum vector.

defined as the angle between the  $\pi^-$  and z-axis. The azimuthal angle,  $\varphi$ , is defined as the angle between the x-axis and the plane containing the z-axis and  $\vec{\pi}^-$ . The decay angles are then evaluated by a simple vector decomposition with respect to the axes. Our resolutions for these angles were found insensitive to the calculation method, and the choice of which forward pion (fast or slow,  $\pi^+$  or  $\pi^-$ ) we use. The transformation between the two systems is a rotation about the y-axis. In this thesis, we use only the Gottfried - Jackson frame. Figures A-1 and A-2 illustrate the Gottfried - Jackson angles,  $\theta_J$  and  $\varphi_J$ .

In rough terms, the Gottfried - Jackson frame emphasizes the spin exchanged between the beam - forward and target - recoil systems, while the H-frame emphasizes the role of the target and recoil spin. Although the transformation angle between the systems is small at small  $t_{pn}$ , amplitudes in the H-frame that are dominantly nucleon spin flip are mainly non flip in the J-frame. In the Gottfried - Jackson frame, pion (spin 0) exchange is non-flip and  $A$  meson (spin 1) exchanges are nucleon flip [Wi78].

### A.1.1 $t_{\pi\pi}$

At "high" masses,  $t_{\pi\pi}$  seems a more natural variable to use than  $\cos\theta_J$ . The form

$$t_{\pi\pi} = -2q^2(1-\cos\theta_J) \quad (\text{A.10})$$

which is exact at  $t_{pn} = m_\pi^2$  is commonly used. In the above,  $q = .5\sqrt{m_{\pi\pi}^2 - 4m_\pi^2}$  is the final state pion momentum in the  $\pi\pi$  rest frame. We note here that one can define directly observable Mandelstam variables,  $s_{\pi\pi}$ ,  $t_{\pi\pi}$ , and  $u_{\pi\pi}$ , even though  $t_{pn} \equiv P_E^2 < 0$ , where  $P_E$  is the  $p-n$  four momentum transfer. These are given by (see figure A-3)

$$s_{\pi\pi} \equiv (P_f^+ + P_f^-)^2 = (P_b + P_E)^2 \quad (\text{A.11a})$$

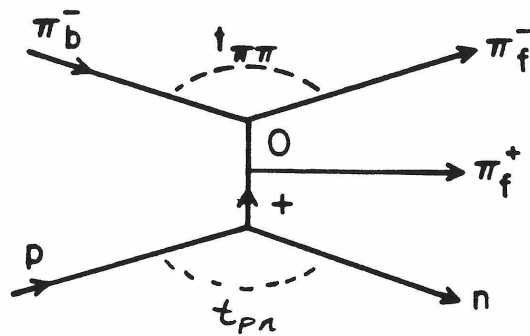
$$t_{\pi\pi} \equiv (P_b - P_f^-)^2 = (P_f^+ - P_E)^2 \quad (\text{A.11b})$$

$$u_{\pi\pi} \equiv (P_f^+ - P_b)^2 = (P_f^- - P_E)^2, \quad (\text{A.11c})$$

and satisfy

$$s_{\pi\pi} + t_{\pi\pi} + u_{\pi\pi} = 3m_\pi^2 + t_{pn}. \quad (\text{A.12})$$

The definitions (A.11) seem quite natural. Equation (A.11a) is just  $m_{\pi\pi} = \sqrt{s_{\pi\pi}}$ . The



$$t_{\pi\pi} = (P_{\pi_f^-} - P_{\pi_b^-})^2$$

$$u_{\pi\pi} = (P_{\pi_f^+} - P_{\pi_b^-})^2$$

$$s_{\pi\pi} = m_{\pi_f^+ \pi_f^-}^2$$

Figure A-3. Mandelstam variables for  $\pi\pi$  scattering.

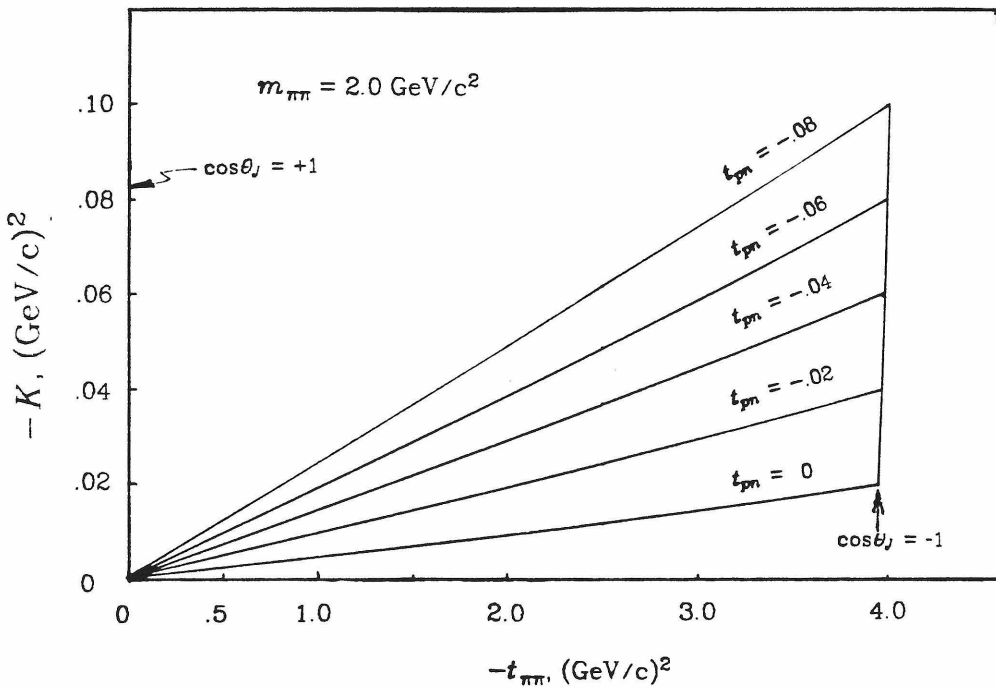


Figure A-4. Fixed  $\pi\pi$  mass dependence of  $-K$  for several  $t_{pn}$  values.

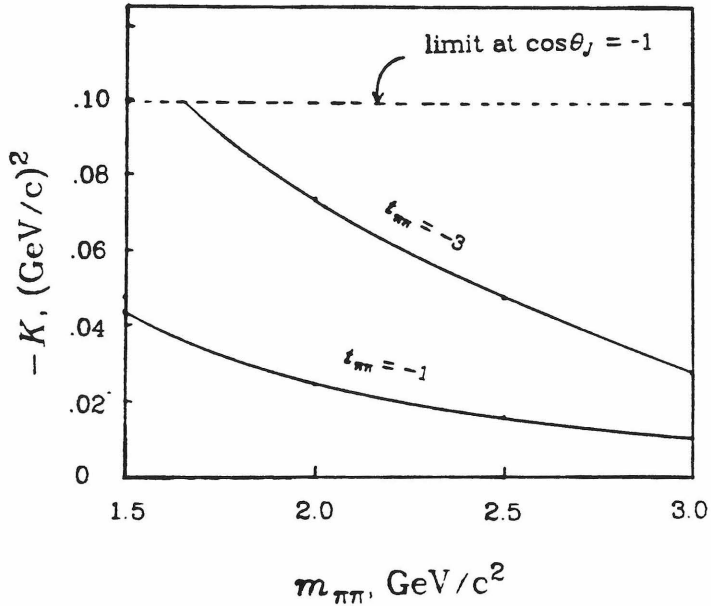


Figure A-5. Mass dependence of  $-K$  at  $t_{pn} = -0.08$  for  $t_{\pi\pi} = -1$  and  $-3$ .

values calculated through them, however, clearly apply to an off shell target of mass $^2 = t_{pn}$ . (A.12) shows that upon extrapolating to the pion pole,  $t_{pn} = m_{\pi}^2$ , not all of  $s_{\pi\pi}$ ,  $t_{\pi\pi}$ , and  $u_{\pi\pi}$  remain fixed.

An estimate of the small errors (at low  $t_{pn}$ ) in equation A.10 follows from A.11 and A.12. Assuming fixed  $s_{\pi\pi}$  and  $t_{pn}$ , we obtain

$$t_{\pi\pi} = -2q^2(1-\cos\theta_J) + K \quad (A.13)$$

where

$$K = 2\beta q^2 \cos\theta_J - m_{\pi\pi} \delta. \quad (A.14)$$

$\delta \equiv (m_{\pi}^2 - t_{pn})/(2m_{\pi\pi})$  and  $\beta \equiv \sqrt{1 + \delta(\delta + m_{\pi\pi})/q^2} - 1$ . We note  $K < 0$  for physical  $t_{pn}$ ,  $K = 0$  at  $t_{pn} = m_{\pi}^2$ , and  $K \rightarrow 0$  as  $t_{\pi\pi} \rightarrow 0$ . Figures A-4 and A-5 illustrate typical  $K$  values. In A-4 we plot  $-K$  vs  $t_{\pi\pi}$  for various  $t_{pn}$  values and  $m_{\pi\pi} = 2$  GeV/c $^2$ . In A-5 we fix  $t_{pn}$  at  $-0.08$ , and plot  $-K$  vs  $m_{\pi\pi}$  for two values of  $t_{\pi\pi}$ . Also, if we fix both  $t_{pn}$

and  $t_{\pi\pi}$  (or  $\cos\theta_J$ ), we find  $K$  is almost independent of  $m_{\pi\pi}$ .  $K$  is strictly independent of  $P_{lab}$ .

Equation A.10 is good enough for our purposes. We note that our acceptance grid is in terms of  $\cos\theta_J$ , not  $t_{\pi\pi}$ . At low  $t_{pn}$  and at low  $t_{\pi\pi}$   $K$  is negligible, and our bin sizes are relatively large. The place where  $K$  would be largest,  $\cos\theta_J \approx -1$  is affected more by the  $q^2$  factor in (A.10) changing over a mass bin than by  $K$ . In some cases (scatter plots) we have used  $t_{\pi\pi}$  from (A.11b). For our high mass fits and dip maps, we have used (A.10) to transform results obtained in terms of  $\cos\theta_J$ .

## A.2 One Pion Exchange

The one pion exchange model is among the oldest descriptions of the strong force. Indeed, its roots are the work of Yukawa [Yu35], in which the existence of the pion was postulated to explain the short range of the nuclear force. The importance of pions as the dominant quanta of soft collisions follows from their being the lightest observable strongly interacting particles. More modern origins of the model, applying it to high energy reactions, are the work of Goebel [Go58], Chew and Low [Ch59], and Drell [Dr60]. Goebel, Chew and Low also opened the related field of  $\pi\pi$  scattering. The strong force at "large" distances of order 1 fm, is such that single exchanges are not a good approximation of the force, but they remain important first order terms.

Figure A-6 is an OPE diagram for  $\pi^- p \rightarrow \rho^0 n$  with  $\rho^0 \rightarrow \pi^+ \pi^-$ . The one pion exchange differential cross section is [Ma76]

$$\frac{\partial^4 \sigma}{\partial t_{pn} \partial m_{\pi\pi} \partial \cos\theta_J \partial \varphi_J} = \frac{m_{\pi\pi}^2 q_{cm}}{8\pi^2 q_{cm}^2 s} \frac{(g^2/4\pi)(-t_{pn})}{(t_{pn} - m_\pi^2)^2} \frac{d\sigma_{\pi\pi}^{off}}{d\cos\theta_J} \theta(t_{min} - t_{pn}). \quad (A.15)$$

The  $\theta$  function expresses the  $t_{min}$  cutoff of equation A.7,  $q_{cm}$  is the center of mass momentum of the beam  $\pi^-$  proton system,  $s$  is given by equation A.2a, and  $q_{\pi\pi}$  is

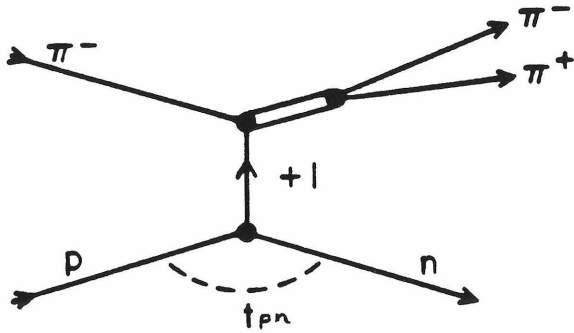


Figure A-6. OPE Feynman diagram for  $p^0$  production.

the  $\pi^+\pi^-$  breakup momentum (see equation A.10). The term  $d\sigma_{\pi\pi}^{off}/d\cos\theta_J$  includes any resonant amplitudes from the upper vertex. We observe that this form has no  $\varphi_J$  dependence on the right hand side. Following from the pion spin being zero, this gives the Treiman - Yang test for  $\pi$  exchange dominance:  $\varphi_J$  distributions are flat. The next essential point is that the  $-t_{pn}$  factor in the numerator, which comes from nucleon vertex terms, implies  $d\sigma/dt_{pn} = 0$  at  $t_{pn} = 0$ . Neither prediction is born out in  $\pi\pi n$ . Distributions in  $\varphi_J$  are not flat. The cross section does not go to zero as  $t_{pn} \rightarrow 0$ , although the observed cross section does have a forward dip in  $d\sigma/dt_{pn}$  below  $t_{pn} \approx m_\pi^2$ . Also,  $d\sigma/dt_{pn}$  has a much steeper  $t_{pn}$  dependence than implied by OPE.

These and other failings have been taken not as evidence that pion exchange doesn't occur, but that the strong force contains other significant effects. One pion exchange alone is not viable, but pion exchange must be an important factor in any situation where the strong force is present, quantum numbers allow it, and collisions are not so violent that finer scale structures (quarks) are evident.

Simply introducing form factors to collimate  $d\sigma/dt_{pn}$  doesn't do anything for the  $\varphi_J$  dependence, and neither does simple Reggeization of the  $\pi$  exchange. However, more sophisticated Regge models [Ki73, Ki77], which explicitly include  $\pi$ ,  $A_1$ ,  $A_2$  poles and cuts as exchanges are in quantitative agreement with  $\pi^-p \rightarrow \rho^0 n$  data at energies up to 63 GeV/c. The Kimel *et al.* models are quite involved and have been tested only at the  $\rho^0$ . Absorbed  $\pi$  exchange models for  $\pi\pi n$  have also had some success, although they are mainly useful in situations where other exchanges can be ignored or lumped together as part of the absorption mechanism. Since we have referred to one such model frequently, we spend some time describing it.

### 7.3 PMA

The Williams, or "Poor Man's Absorption" (PMA) model, [Wi70, Fo71a], as extended by Wagner, Ochs, and Shimada [Wa73, Oc73, Sh80] provides a useful framework for discussing our data. The simplest absorption model to remedy the gross defects of simple OPE, PMA has been rather successful at lower energies in describing  $\pi$ -exchange dominated reactions in the low  $|t_{pn}|$  region. The  $t_{pn}$  dependence in PMA is governed by a pion propagator, absorption, and by angular momentum conservation [Wi78]. Although recent results [Wi78] have shown the limitations of the model, the qualitative success of PMA is impressive.

Although PMA is usually formulated in terms of s-channel helicity frame partial wave amplitudes, it is more useful for us to use forms based on production amplitudes in the Gottfried-Jackson frame. Ochs and Wagner [Oc73] express the full PMA amplitude in the Gottfried Jackson frame as

$$F_\alpha = \frac{g}{4\pi} \left\{ \frac{\sqrt{-t_{pn}}}{t_{pn} - m_\pi^2} F_0 - \frac{C_A m_{\pi\pi}}{m_{\pi\pi}^2 - m_\pi^2} F_1 \exp(-i\alpha\varphi_J) \frac{\partial}{\partial\theta_J} \right\} T(m_{\pi\pi}^2, \theta_J), \quad (\text{A.16})$$

where we have specialized to the case of  $\pi^-p \rightarrow \pi^+\pi^-n$ .  $T$  is the  $\pi\pi$  elastic scattering amplitude, and has no explicit  $t_{pn}$  dependence. The  $\pi^+pn$  coupling constant is

$g^2/4\pi = 29.2$ .  $F_n = F_n(m_{\pi\pi}, t_{pn})$  are collimating form factors with  $F_n = 1$  at  $t_{pn} = m_\pi^2$ .  $C_A$  is an absorption parameter. Absorption is expressed by this and the form factors. The index  $\alpha = \pm 1$  gives the s-channel helicity frame nucleon spin flip, and the factor  $m_{\pi\pi}/(m_{\pi\pi}^2 - m_\pi^2) \approx 1/m_{\pi\pi}$  results from a rotation from the s-channel helicity frame to the Gottfried Jackson frame. Absorption corrections are most naturally introduced in the s-channel helicity frame, even though the Gottfried Jackson frame may be more convenient for later work. Assuming both s-channel nucleon flip dominance and small  $t_{pn}$ , Ochs and Wagner find that the  $\pi\pi n$  cross section has the form

$$\frac{d^4\sigma}{dm_{\pi\pi}dt_{pn}d\cos\theta_Jd\varphi_J} = \frac{g^2qm_{\pi\pi}^2}{4\pi m_p^2 P_{lab}^2} (I'_0 + I'_1 \cdot \cos\varphi_J) \quad (\text{A.17a})$$

where

$$I'_0 = \frac{-t_{pn}}{(m_\pi^2 - t_{pn})^2} F_0^2 |T|^2 + \frac{|C_A|^2 m_{\pi\pi}^2}{(m_{\pi\pi}^2 - m_\pi^2)^2} F_1^2 \left| \frac{\partial T}{\partial \theta_J} \right|^2, \quad (\text{A.17b})$$

$$I'_1 = \frac{\sqrt{-t_{pn}}}{(m_\pi^2 - t_{pn})} F_0 F_1 \operatorname{Re} C_A \frac{m_{\pi\pi}}{(m_{\pi\pi}^2 - m_\pi^2)} \frac{-\partial}{\partial \theta_J} |T|^2. \quad (\text{A.17c})$$

The factor  $q = .5\sqrt{m_{\pi\pi}^2 - 4m_\pi^2}$  is the final state pion momentum in the  $\pi\pi$  rest frame.

PMA does not specify the  $\pi\pi$  elastic amplitude  $T$ . That is, it is not a  $\pi\pi$  scattering model. Rather, it is a model for the  $t_{pn}$  dependence of the "target" pion and its major background. In PMA, the background is determined solely by the absorption of elementary one pion exchange and angular momentum conservation.

The original Williams model, [Wi70], effectively assumed  $C_A = 1$ . Estabrooks and Martin [Es72] showed that, at the  $\rho^0$  mass  $C_A$  has a small imaginary part. Ochs and Wagner [Oc73] then determined  $\operatorname{Re} C_A$  from the Cern Munich 17.2 GeV  $\pi\pi n$  data. They found that  $\operatorname{Re} C_A$  depends on  $m_{\pi\pi}$ , dropping from (an assumed) 1 at

$m_{\pi\pi} < 0.9 \text{ GeV}/c^2$  to  $\approx 0.4$  at  $m_{\pi\pi} = 1.9 \text{ GeV}/c^2$ . Accepting  $C_A$  as a mass dependent parameter resolved the major problem with PMA, and extended its useful region from just the  $\rho$  to all  $\pi\pi$  masses.

The low  $|t_{pn}|$  nature of PMA is emphasized by equations (A.17), which admit no moments  $\langle Y_L^m \rangle$  with  $m > 1$  [Oc73]. This is certainly not the case for  $|t_{pn}| \gtrsim 0.15 \text{ (GeV}/c)^2$ . Both this, and lower energy experiments see significant  $m = 2$  moments at larger  $|t_{pn}|$  values. Both  $A_1$  and  $A_2$  exchanges have been found necessary in  $\pi^- p \rightarrow \rho^0 n$ , largely with the help of a high statistics polarized target experiment [Be79b, Be79c, Ki73]. A Regge model [Ki77] including these exchanges as well as  $\pi$  exchange has been found in quantitative agreement with the  $t_{pn}$  dependence of  $\langle Y_L^m \rangle$  moments for the  $\rho^0$  at 63 GeV, [Al78]. At fixed  $m_{\pi\pi}$ , the  $A$ -exchanges are predicted to become more important with increasing  $P_{lab}$ , but at any given  $P_{lab}$ , less important with increasing  $m_{\pi\pi}$ . Associating  $m=2$  moments with significant  $A$  exchanges, our results imply that they are mainly important near the  $\rho$  mass, and are apparently a minor feature at  $m_{\pi\pi} \gtrsim 1.5$  (see figures 6-3 to 6-10).

In this light, we assume that PMA is an acceptable framework for describing our low  $t_{pn}$  data. PMA does successfully predict a non vanishing  $d\sigma/dt_{pn}$  as  $t_{pn} \rightarrow 0$ , and the presence of significant  $m = 1$  moments at low  $|t_{pn}|$ . At low energies, a prediction [Oc73] that the ratio

$$\frac{-m_{\pi\pi}}{\sqrt{L(L+1)}} \frac{\langle Y_L^0 \rangle}{\langle Y_L^1 \rangle} \quad (\text{A.18})$$

does not depend on  $L$  has been verified. (The ratio does depend on  $\text{Re } C_A$ .) Section 5.5.1 repeats this test.

The collimating form factors  $F_n$  are not specified by PMA, but are usually taken to be exponentials of the form  $e^{.5B_n(t_{pn} - m_\pi^2)}$ , and often the  $B_n$  are taken to be equal. The exponential form for  $F_n$  seems well established at low energies, however,

Wicklund *et al.* [Wi78] established differences in  $B_n$  for PMA amplitudes applying to specific partial waves at the  $\rho^0$ . They also observed  $P_{lab}$  dependences which extrapolate to  $\approx 9$  to 11 at our energies, depending on partial wave amplitude. Considering our relatively small data set, it seems reasonable to assume

$$F_0^2(t_{pn}) = F_1^2(t_{pn}) = e^{B(t_{pn} - m_\pi^2)} \quad (\text{A.19})$$

with  $B$  around 10 to 15.

## Appendix B

### Trigger Electronics

An overview of the trigger electronics is given in figure B-1. This system was designed by R. Gomez and J. Pine. Essential differences between E110 and E260 were the multiplicity and veto counter electronics used by E110, and deletion of the E260 calorimeter electronics. The general structure had three stages. First a pretrigger flagged an interacting beam particle. Then, if the pretrigger survived various tests for spectrometer readiness or double beam, it "strobed" the multiplicity outputs of several of the pwc's and veto counters to determine if we had a "trigger". We considered a trigger to occur at this point whether or not the spark chambers could fire. The third stage involved the spark chamber firing electronics and fast reset inhibit. If the spark chambers fired, various latches held the trigger electronics and scalers idle until the event was read into the on line computer. They would then resume normal operation, but the spark chambers would not fire until a preset recharging (dead) time had elapsed. The events actually recorded on magnetic tape are viewed as a random sample of the triggers we had.

The trigger system was built to take advantage of the 18 ns *rf*, structure of the Fermilab beam and the relatively low intensities required for this experiment. Fast logic pulses were typically about 5 to 10 ns wide. The fast electronics were NIM standard Lecroy and EG&G modules, with Latches, OR's and AND's being Lecroy 364 or 365 units set to appropriate levels. The multiplicity logic was built by our group.

Assuming the spectrometer was ready to accept a trigger, and we were within the  $\sim 1$  second long BEAMGATE (derived from beam start/stop pulses provided by the lab), the trigger sequence began with the arrival of a beam particle,

$$BEAM = Sa \cdot Sb \cdot \overline{Sc} \cdot BEAMGATE \quad (B.1)$$

which suffered a (loosely defined) interaction,

### MPS TRIGGER ELECTRONICS - OVERVIEW

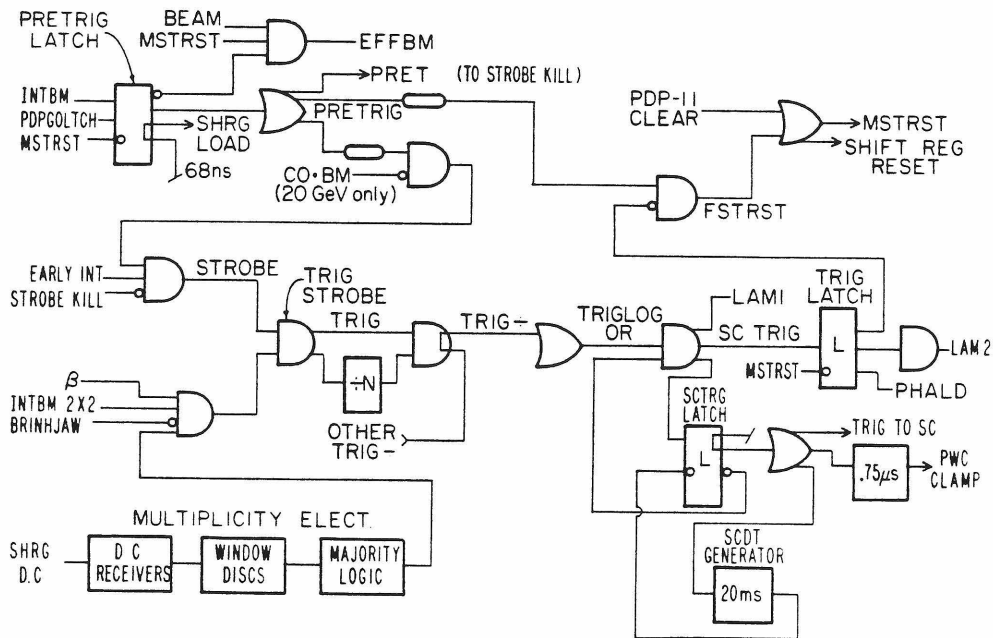


Figure B-1. E110 trigger electronics overview, see text.

$$INTBM = IB2 \times 2 + IBDEDX$$

$$= (BEAM \cdot \overline{2 \times 2}) + (BEAM \cdot DEDX \geq 2) \quad (B.2)$$

as shown in figure B-2a.

The INTBM signal set the pretrigger latch which sent a clipped line shaped signal, SHRGLOAD, to load the shift register. Setting of the PRETRIG LATCH stopped accumulation of effective beam, EFFBM, until a master reset pulse, MSTRST, reset the latch.

An output of the PRETRIG LATCH was shaped, split, and sent off to the reset logic, strobe kill generation, and trigger logic areas. Unless a spark chamber trigger occurred, the pulse sent to the reset logic created a MSTRST pulse to clear the PRETRIG LATCH. The pulse sent to the trigger logic had to survive a "STROBE KILL" to reach it. (At 20 GeV, a large electron and muon background prompted us

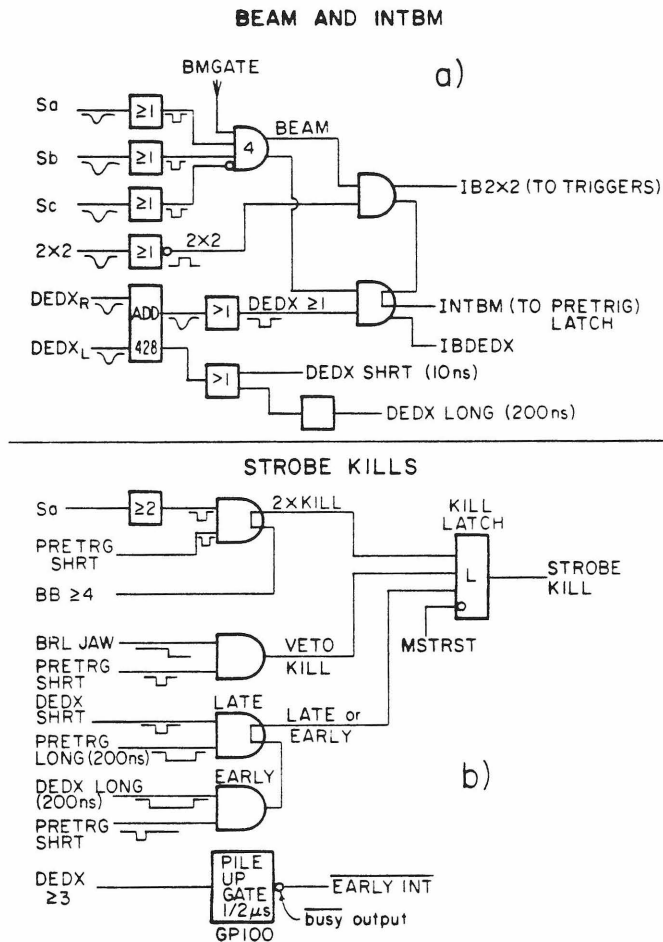


Figure B-2. Beam counter and Strobe Kill electronics.

to use  $C_0$  as an on line veto at the strobe kill. The STROBE scaler then recorded the effective beam used in cross sections.)

The strobe kill electronics, figure B-2b, were provided to insure that the spectrometer was in a relatively clean state prior to an event and to veto potential triggers by multiple beam particles. A second beam particle arriving near in time to the pretriggering particle, either before or after it but within the resolving time of the proportional chambers, could easily satisfy the two body trigger electronics. Early and late particles in a  $\pm 200$  ns window were flagged by the DEDX counter and

resulted in the EARLY and LATE kill pulses. Another test for multiple particles was to use the output of the BBX, Y and U chamber daisy chains and require  $BBX + BBY + BBU = BB \leq 3$ . That is, kill on  $BB \geq 4$ . Finally, a kill for two particles in a single rf bucket was provided by the Sa counter, with a discriminator set just below the two particle peak. In the spring '77 data, we threw away more single particles through Landau fluctuation than actual double buckets. The Sa2X kill rate was  $\sim 7\%$  while the real double beam rate was  $\gtrsim 1\%$ . (For the winter '78 run, we added an Sb2X discriminator and required Sa2X · Sb2X for the beam counter kill. The  $\gtrsim 1\%$  number was taken from the winter '78 data with the SaSb coincidence required.)

We also required that the photon vetoes, Barrel and Jaws, be below threshold at least one bucket before the pretrigger event. This was mainly important for the Barrel which could suffer large, slowly decaying pulses, from halo strikes. A failure to be below threshold before the pretrigger event caused a VETO KILL.

The timing for creating all the fast kill pulses (all the above except BB) was set so that the pretrigger pulse would not kill itself. The STROBE KILL pulse was then

$$STROBEKILL = 2XKILL \cdot EARLY\ KILL \cdot LATE\ KILL \cdot VETO\ KILL \quad (B.3)$$

where

$$2XKILL = (Sa\ 2X) \cdot (BB \geq 4) \quad (B.4)$$

In Run II, the 2XKILL also included an Sb2X signal to reduce Landau fluctuation losses. The STROBE KILL was latched until reset by a MSTRST pulse. If set, the output of this latch intercepted and vetoed the pretrigger pulse on its way to the trigger strobe of figure B-1. Surviving pretriggers were known as STROBES.

A bit over halfway through Run I (at run 281), a previous interaction kill was added to the strobe kill in response to 'old' events too often superimposed on good

events. This EARLY INTERACTION kill was generated by a pile up gate with  $1/2 \mu\text{s}$  output duration fed by a  $DEDX \geq 3$  signal. As for the other kills, the timing was such that the pretrigger event wouldn't kill itself, but any interaction within  $1/2 \mu\text{s}$  before the event would kill the strobe pulse.

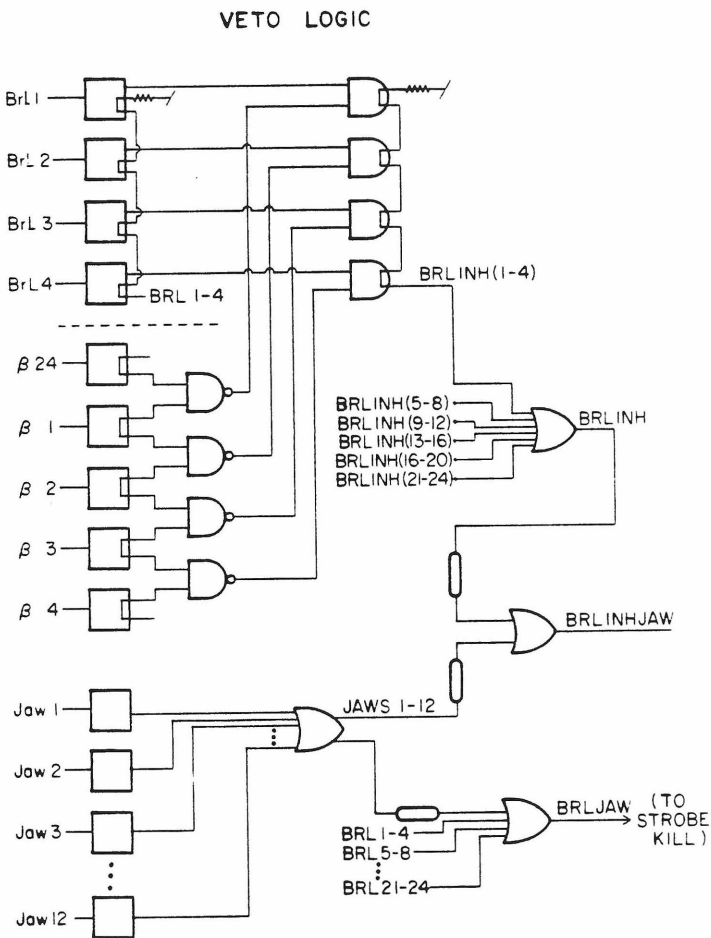


Figure B-3. Photon veto electronics. Note that the Lead Wall and other photon detectors downstream of the magnet were *not* in the trigger.

The STROBE KILL (EARLY INT kill) did not make decisions based on the forward topology of the event under consideration; it looked either upstream of the target (multiple beam) or at the readiness of the spectrometer prior to the event. Thus,

in terms of the reactions of interest, the strobe kill was an unbiased rejection of pretriggers. That, in turn, is equivalent to throwing away the effective beam accumulated in order to generate the pretrigger. Over a large number of pretriggers, this fractional loss of effective beam is proportional to the scaler ratio STROBE/PRETRIG, and we correct the EFFBM scaler by this ratio in cross section calculations.

Veto counters, depending on the trigger, were used to reject events on their own merit, and not for reasons of beam condition or spectrometer readiness. Their electronics is shown in figure B-3. The Barrel and Jaw inputs are phototube pulses, the  $\beta$  chamber signals came from special outputs of its current division amplifiers and were 8-wire groups located to cover the division between two barrel staves. The veto output BRINHJAW was an "or" of the Jaw counters and  $\beta$  inhibited Barrel counters. The  $\beta$  inhibit was included for the main proton recoil reaction,  $K^0\pi p$ , which needed veto coverage, but did not want protons penetrating the Barrel to cause vetoes. For  $\pi\pi\pi\eta$ , the  $\beta$  inhibit on the veto, in turn, required that we use  $\beta = 0$  in the trigger explicitly. This  $\beta = 0$  signal was derived from the shift register daisy chain, figure B-4b, (which had a lower effective threshold than the  $\beta$  chamber inhibit). The  $\beta$  chamber inhibit pulses, and each output of the Barrel and Jaw counters, all had tag bits.

Examples of the multiplicity logic are shown in figure B-4 for the A station and  $\beta$  chamber. The BB and  $\Gamma$  chambers followed the  $\beta$  chamber example, and the many BCD combinations were similar to the A station setup. The shift register multiplicity (daisy chain) outputs were analog signals proportional to the number of hits in a chamber (AIOUT, see figure 2-9 in section 2.3.7). The daisy chain receivers matched impedances and had output lines to the window discriminators and to our ADC's. Each window discriminator module had one input feeding four window discriminators. Each discriminator had two independent digital settings from one

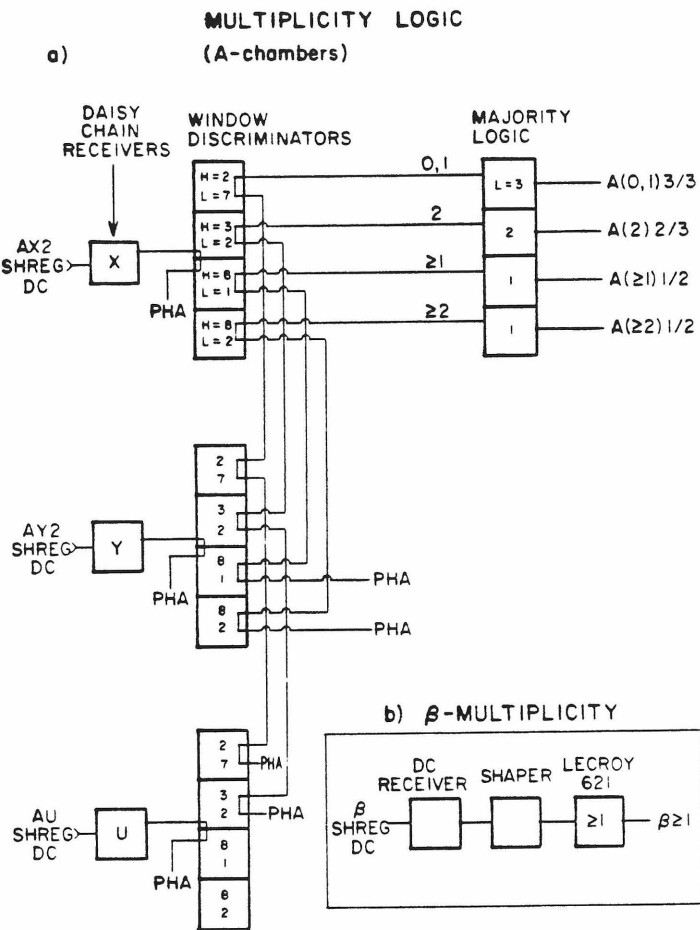


Figure B-4. Multiplicity electronics (examples).

to eight and was designed so that a low limit of eight or a high limit of seven turned off that limit. The digital outputs were high impedance and paired so that chains of discriminator outputs could be set up. The majority logic units were similar to the window discriminators except that only lower limit settings were available. Thus the majority test was based on the sum of the window discriminator outputs. The  $A(2)2/3$  pulse was then formed by at least two of the three ("2/3") A chamber window discriminators claiming two "(2)" hits in the daisy chain.

The window discriminators and majority logic units were not gated. This was a relatively slow part of the electronics, pulses were long to cover pwc rise and fall

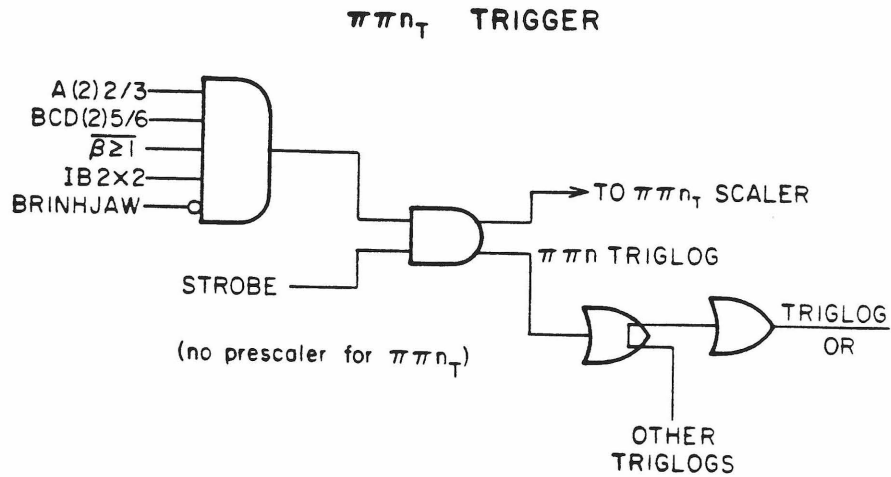


Figure B-5. Final trigger selection for  $\pi\pi n_T$ .

times, the rise time of shift register daisy chains, and timing differences resulting from particle flight times between chambers. Signals were a bit noisy, and at high multiplicities subject to late changes of mind about the hit counts by the shift registers. However, the system was fairly reliable at multiplicities  $\sim 2$  or less.

The trigger coincidence is shown in figure B-5 for the  $\pi\pi n_T$  trigger. It was formed by an "AND" of A(2)2/3 and BCD(2)5/6 from the majority logic units,  $\beta \geq 1$  (that is,  $\beta = 0$ ) from the  $\beta$  multiplicity electronics, and the IB2X2 (interacting beam 2X2) pulses. A pulse in the BRINHJAW line could veto the whole mess. If these conditions were satisfied, and the strobe pulse existed (has not been killed), then the  $\pi\pi n_T$  trigger was formed. Whether or not the spark chambers fired, we consider that the experiment has triggered at this point. The number of these triggers was scaled and used in the  $\sigma_{TRIGLOG}$  calculation for  $\pi\pi n$ .

Table B-1 lists the requirements for the Run I triggers. Some of them,  $\pi\pi X$ ,  $\pi\pi B$ ,  $3\pi P$ , and the curve through (CT) were used to develop correction factors for the  $\pi\pi n_T$  data. In the table, "W" is the range, or "window," of hits allowed for the chambers of a group, and ML is the majority level required of the group. V

TABLE 2-8 Trigger Requirements

Trigger	DEDX	$\overline{2 \times 2}$	V	$\beta$	A	BCD	BCD'	Special	D	$\Gamma$
					W	ML W	ML	W	ML W	ML
IB DEDX <sup>(a)</sup>	$\geq 3$							$\geq 2$	2	
IB $2 \times 2$ <sup>(a)</sup>		Yes								
$\pi p$		Yes		$\geq 1$			1	3		
$3\pi p$	$\geq 3$				$\geq 2$	1	3	3	2-4	5
$\pi\pi n_T$		Yes	Yes	0	2	2	2	5		
$\pi\pi n_P$	$< 2.7$	Yes	Yes	0	2	2	2	3	2	1
									1,2	2
$\pi\pi X$		Yes			2	2	2	5		1,2
$\pi\pi n_H$			Yes	0	2	2		$2^{(b)}$	3	1
$K^0 \pi p$	$\geq 1$	Yes	Yes	$\geq 1$	0,1	3	3	3	2-4	5
$K^0 \pi\pi X$	$\leq 3$			$\geq 1^{(c)}$	2	$2^{(d)}$	4	3	3-5	5
$K^0 K^0 X$	$\leq 1$	Yes			0	$2^{(d)}$			$\geq 3$	5
$\pi\pi B$		Yes	Brl=1	0	2	2	2	5		
				Jaw=0						

C.T. (Curve Through) Require only: BEAM  $\cdot 2 \times 2$

Notes: (a) IBDEDX and IB $2 \times 2$  are OR'ed to form single IB, (b) B and C chambers only,

(c)  $\beta$  or a Barrel hit required, (d) x and y planes only.

refers to BRINHJAW = 0,  $\overline{2 \times 2}$  is INTBM  $2 \times 2$ .

The various triggers were OR'ed in a daisy chain to form the TRIGLOGOR pulse which was also scaled. The prescale unit (divide by N) of figure B-1 was not in the electronics for  $\pi\pi n_T$  or the other major triggers. Its purpose was to reduce the number of spark chamber triggers for the background reactions by giving a nonzero output only every Nth input pulse, N being set by switches on the unit. The prescale units were connected as shown for all background triggers except  $\pi\pi B$ , which did not need one, IB and  $\pi p$  elastic. These last two used the spark chamber trigger pulse, SCTRIG of figure B-1, as input to the prescale unit.

Unless the spark chambers were ready to fire, the TRIGLOGOR output was inhibited by the spark chamber dead time latch, SCTRGLATCH. In this case, the PRETRIG and STROBE KILL latches were reset by a fast reset pulse derived from a suitably delayed PRETRIG pulse, and the whole multiplicity electronics started up again with the next interacting beam after the clears.

If the spark chambers were ready, the TRIGLOGOR signal initiated the spark chamber firing and dead time electronics and set the trigger latch, TRIGLATCH. The output of this latch intercepted the PRETRIG pulse and halted the fast resets. With a spark chamber trigger, all latches using the MSTRST reset remained latched, until the on line computer completed its data acquisition and sent a PDP-11 CLEAR pulse to generate a MSTRST. The PHALD pulse from the TRIG LATCH was shaped near the ADC's and used for ADC load gates.

The output of the SCTRGLATCH was clipped and fanned out to the spark chamber prepulser (to fire the chambers), the spark chamber dead time generator (a pair of EG&G - GG202 gate generators in series), and a gate generator to create a pwc "clamp". This clamp prevented electronic noise from the spark chambers from unloading the shift registers. The SCTRGLATCH was reset by a pulse from the dead time generators. Most Run I data taking on multitrigger runs was with a 20 ms spark chamber dead time, although this was 30 ms for early runs (through the 50 GeV data taking). The dead time was set to 50 ms for curve through "alignment" runs. Run II multitrigger running was mainly with a 10 ms dead time (which was comparable to the computer read in time).

A number of Camac and visual scalers provided essential normalization data as well as monitoring functions. The EFFBM, PRETRIG, STROBE, and TRIGLOG scalers were used for normalization, each trigger having its own TRIGLOG scaler. In addition, scalers for BEAM, INTBEAM, TRIGLOGOR, and SCTRGLATCH monitored the electronics. SCTRGLATCH was nominally equal to the number of events written on tape, differences

occurring only in cases of tape or computer errors. Such errors were random, and do not affect our cross section results.

Early in our data taking, an inefficiency of a few percent was noticed in some of the trigger tag bits, section 2.3.7. This resulted in events on tape whose trigger couldn't be identified. Although this did not affect our cross section analysis (see section 3.4), the loss of events traceable to a given trigger was undesirable, and a second set of tag bits was added with more liberal loading gates.

## Appendix C

### TEARS

#### C.1 Overview

TEARS [Fo75, Br79] performed our tracking and vertex analysis, tackling the time consuming pattern recognition job of track finding from chamber data. For  $\pi\pi\pi$  and other non-vee triggers, it made no judgements on events beyond setting flags for successful operations such as the vertex finding. Selection of good events from the TEARS results was left to later analysis programs. For vee triggers, such as  $K^0\pi p$ , the desired topology was an integral part of the formalism.

The tracking began downstream of the MPS magnet with independent xz and yz view fits and a view matching operation, sections C.2 and C.3. Next, a beam particle trajectory was found, section C.4, and then the front end (between the target and magnet) analysis began, sections C.5 and C.6. The immediate front end goal was to find "links" for the matches, meaning front end tracks that joined to the matched tracks at the magnet and find their momenta. The next goal was to locate main and vee (depending on the trigger) vertices. Distributed throughout these analyses were several "cleanup" operations designed to remove most spurious tracks and matches and yet remain highly efficient for real particles.

The front end analysis was performed twice on every event using the systems "Vtrig" and "Targtrk", optimized for topologies with and without secondary vertices (vees) respectively. Both sets of results were written to DST's, but for CST's and beyond we specialized to the results of the system appropriate to a given trigger. On CST's, the Vtrig results were written for the vee triggers,  $K^0\pi p$ ,  $K^0\pi\pi X$ , and  $K^0K^0X$ . Targtrk results were used for all other triggers unless Targtrk failed. In that case Vtrig results were substituted as a backup. Sections C.2 through C.6 give details for the various analysis steps.

## C.2 Straight Line Fits

Our tracking both before and after the magnet sought straight lines separately in the  $xz$  and  $yz$  views. For simplicity, we discuss this for the after magnet tracking here and note front end differences in sections C.5 and C.6. The straight line tracks were found by the routine `Onenv1`, which directed the pattern recognition, spark deletion for  $\chi^2$  minimization, and single view cleanups, and the routine "Fitlin", which did the actual  $\chi^2$  fits.

The pattern recognition began with spark searches. If there were enough sparks within a 1 cm "road" connecting a spark near the magnet (in the E1 or a D chamber) to one in or behind the F2 chamber to satisfy the minimum spark ("minspk") requirements a  $\chi^2$  fit would be attempted. At most one spark (the closest to the road center) per chamber could be included in a road, and both overall and all group minspk requirements had to be satisfied, see Table C.1. A road was rejected if the spark requirements weren't met, or if its defining sparks were already part of a track satisfying  $\bar{\chi} = \chi^2 / (\text{total sparks} - 2) \leq 2.5 = \chi_0$ .

If a road was successful, a  $\chi^2$  fit to a straight line was made on the sparks within it. If the resulting  $\bar{\chi}$  was less than  $\chi_0$ , the track was passed to the single view cleanup. If not, high  $\chi^2$  sparks were successively deleted and a refit performed until either  $\bar{\chi} < \chi_0$  or all minspk requirements were reached. In the latter case, we required  $\bar{\chi} \leq \chi_1 = 5.0$  in order to keep the track. In these fits, the spark resolution of each E chamber was taken as .7mm, and the resolution of each F spark chamber was set at 1.0mm, values consistent with residual widths observed in chamber alignment studies (see Fr82). For proportional chambers, the resolution was  $nd/\sqrt{12}$ , where  $d$  was the wire spacing,  $n$  the number of consecutive wires firing, and  $1/\sqrt{12}$  the standard error of a square, unit width distribution. To avoid biasing against crossing tracks or high multiplicities expected on some triggers, sparks were never "erased" when tracks containing them were found.

Table C.1

After Magnet Track Requirements

View	Pass	Chambers	Minspk	Group
X	1	E1,E2,E3,E4,F1,F2, F3,F4,Dx,Dx',F''x	6	x overall
X	1	Dx,E1,E2,E3,E4	3	E/Dx group
X	1	F1,F2,F3,F4	1	Fx group
X	1	F2,F3,F4,Dx',F''x	1	Z-end
Y	1	E1,E2,E3,E4,F1,F2,F3, F4,Dy,Dy',F''y,F''y	6	y-overall
Y	1	Dy,Dy',E1,E2,E3,E4	3	E/Dy group
Y	1	F1,F2,F3,F4	1	Fy group
Y	1	F2,F3,F4,F''y,F''y	1	z end
X	2	Dx,E1,E2,E3,E4	4	overall
X	2	E3,E4	1	Z-end *
X	2	Dx,E1	1	Z-beg *
Y	2	Dy',Dy,E1,E2,E3,E4	4	overall
Y	2	Dy',Dy,E1	1	Z-beg
Y	2	E3,E4	1	Z-end
X	n.a.	Dx',F''x	1	Sclean-x
Y	n.a.	F''y,F''y	1	Sclean-y

After magnet tracking requirements. Requirements

marked with a "\*" are redundant. Sclean requirements

apply only to tracks within  $\pm 5\text{cm}$  of beam.

The above procedure often found duplicate tracks, and a single view cleanup was used to identify and resolve such cases. This procedure compared a "just found" track with all previously found tracks in its view, first to detect an "identical" pair, and then to select the better one and reject the other. Given two tracks,

a count of the number of chambers in which they used different sparks was made. If that difference exceeded 5 (out of 11 x or 12 y chambers), the tracks were passed to the next test. If the difference was 5, both tracks had to have  $\bar{x} \leq x_0$  in order to be passed. Otherwise, the tracks were declared identical and the poorer one was rejected. The next test compared slopes and positions at the track midpoints, ( $z \approx 9.5m$ ). To be considered distinct, either the slopes had to differ by at least .01, or the positions had to be at least 3 cm apart. If two tracks were declared identical, the poorer one was rejected. The decision of which track of an identical pair to retain was made as follows. If one track had  $\bar{x} < x_0$  and the second had  $x_0 < \bar{x} < x_1$ , then the first track was kept. If both tracks had  $\bar{x} < x_0$ , or both had  $x_1 < \bar{x} < x_1$ , then the track using the most sparks was kept, and if the spark counts were the same, then the track with the smaller  $\bar{x}$  was kept.

We had a storage limit of 10 tracks per view. As a guard against the possibility that inferior and/or spurious tracks might fill up the storage before all good tracks were found, the tracks were ordered in quality, first by spark count, and then by  $\bar{x}$ . Whenever the limit of 10 was reached, a new track candidate would be first checked to see if it was worse than the last track in the list. If so, it was rejected immediately, and if not, it was passed to the cleanup procedure described above. If it passed, then the previous worst track was removed to make room.

For each view, the after magnet tracking was done in two passes. In pass 1, all tracks were required to have F chamber sparks. In pass 2, the F chambers were completely ignored in an effort to find tracks that missed them. (In pass 2, the road defining chambers were adjusted appropriately.) No explicit fiducial cuts were placed on either pass, except for a weak magnet aperture check, so pass 2 tracks pointing to the F station were possible, and were found. Although essential in the y view, good pass 2 x view tracks are expected to miss the F station (unless the particle was absorbed by an interaction). The single view cleanup was relied upon to

eliminate pass 2 tracks that were merely fragments of pass 1 tracks. Since almost every pass 1 track would have an analogue pass 2 track before the cleanup and extremely few x view pass 2 tracks are seen to hit the F station, the single view cleanup is seen to be quite efficient. A few such tracks survive, but the number is consistent with the expected rate of decays and interactions. We have found that if these tracks do find matches, they typically match to "old" beam tracks.

### C.3 Matching and Match Cleanups

In our only formal act of xy view matching, the slant (u,v) spark chambers were used to identify matches, or xy track pairs that specified particle paths. We shall use the term "match" to mean only xy matches after the magnet.

In searching for matches, all xy track pairs were considered. Given such a pair, projections to the slant chambers were made, and a search for sparks within 1 cm of the projections was conducted. At most one spark per chamber (the closest to the projection) was considered, and to be included in an initial match spark list, it had to have a  $\chi^2$  contribution less than 2.5. If the list of such sparks did not satisfy the match minspk requirements (Table C.2) the match was rejected. If the match survived this test,  $\chi_m = \chi^2/\text{spark}$  was calculated and minimized by removing the high  $\chi^2$  sparks until either  $\chi_m < 5$  or the minspk requirements were met. The match was rejected if minspk was reached and  $\chi_m > 5$ . Surviving matches were ranked first by the number of match sparks and then by  $\chi_m$  up to a total of 25 matches. If that total was met, a new match had to be better than previous matches in order to be kept, in which case the worst was deleted.

Next several cleanup operations were conducted. These were developed from early Monte Carlo studies and experience with E260 and E110 including event display scans. The basic cleanup compared the lists of match sparks of every pair of matches involving the same x view track. Given such a pair, the match with the

Table C.2  
XY Match Requirements

Chambers	Minspk	Group
E1,E2,E3,E4,F1,F2,F3,F4	3	overall *
E1,E3,F3,F4	1	-5.7° group
E2,E4,F1,F2	1	+5.7° group

\* Overall requirements reduced to 2 for matches involving pass 2 tracks that miss the F-station.

higher  $\chi_m$  was removed if its list of sparks was a subset of the other's.

The next cleanup, Sclean, did not literally remove matches, but only flagged them as good or bad. Also, Sclean did not operate immediately after the matching, but waited until after some of the front end processing was done. It was run separately for the Vtrig and Targtrk systems, and it only looked at matches known to link through the magnet to the front end. Sclean assumed initially that all x view tracks were real, but that only the best xy match involving a given x track was true. Here, "best" used the match ordering described above. All other matches involving the x track were flagged as redundant. Matches involving a given y track but different x tracks were allowed for several reasons. First, the uv stereo angle implied a good x resolution, but not y. Also, the y aperture was smaller and y tracks were virtually unbent by the magnet. Good tracks merging in the y view were thus considered fairly likely.

Sclean also included a beam region test, using the better pwc time resolution to remove "old" beam region tracks that might link along with good beam region tracks. Matches projecting to within a 10 cm square around the 2x2 counter were required to have at least one hit in each view in the F' pwc's in order to be judged good. (In our 20 GeV/c data, the bent beam missed one of the F'x chambers completely and went through a dead spot in the other, so this test was revised for this momentum to require two F'y hits and ignore the F'x chambers. For the winter '78 run, we added a slant BA type pwc that moved with the 2x2 and only a single BA hit

was required to pass the test. Failing that the basic  $F'xy$  test was reverted to. The slant BA chamber was also used in the track matching.)

For Vtrig, Sclean tested only matches known to link to the B and C stations, and only Sclean approved matches were admitted to the full Vtrig analysis. This was done to reduce the number of hypotheses fit by Vtrig. In the Targtrk analysis, Sclean was used only after the vertex was found, and it operated only on matches linking front end tracks found by Targtrk. In this case, Sclean was used to address a problem of multiplicity feed up that was observed in event displays, and was one of the reasons we reprocessed CST's.

The above discussion ignored differences between pass 1 and pass 2 tracks. Except for a reduction of the overall match spark requirement by one when a track missed the F station, there was none. Mixed pass matches were largely eliminated by the basic requirements, and the various cleanups. Those that survived were found to be almost always bad or associated with decays and interactions and were removed by later event structure cuts. The only valid mixed pass cases involved pass 2  $x$  view tracks that passed through the dead edges of the Fx chambers (figure 2-8) but live Fy regions. Pass 2 only matches that were aimed directly at the F station occurred at a rate consistent with decays and interactions. Ultimately, we chose our fiducial volume, decay and interaction corrections so that the analysis used only pass 1 tracks. Events with pass 2 or mixed pass matches were cut from the data.

Our cleanup philosophy was not to be completely efficient at removing spurious matches or tracks. To do so would increase inefficiencies to an unreasonable level. Rather, we sought to remove enough of them to make our final event selection cuts unambiguous and efficient. We relied on the good time resolution of the front end chambers to insure that most bad matches wouldn't link to the front end. Sclean was added to the Targtrk analysis because the bad matches that did link used the

same front end tracks as a good match, and so would increase the apparent vertex multiplicity, affecting one of our basic cuts. Event scans indicated that Sclean analysis was our best tool for selecting the best match when two used the same front end tracks.

#### C.4 Beam Processing

A good beam track was essential, both for efficient vertex finding and for a good  $t$  measurement. Having only two stations  $\sim 19.5$  m apart made track fitting useless. So we used instead a procedure [St78b] that always produced a single beam trajectory for each event, with flags and errors to indicate its quality. Multiple beam particles weren't a problem as the strobe kill suppressed them, and the  $\pi\pi\pi$  topology cuts removed whatever survived. The beam trajectory was obtained by connecting pairs of points locating the beam at the BA and BB stations with a straight line. Its error matrix was calculated formally from the errors assigned to the points.

On most events, all BA (2x and 2y) and BB (1x, 1y, and 1u) planes had single hits, making the point selection obvious. Also, the proper hits could be identified in most cases of delta rays or chamber noise by comparing the various chambers at each station. For example, if BAx2 had two hits and BAx1 had just one, the BAx2 hit closest to the single BAx1 hit was selected, and these two were used in forming the BAx point as if both planes had just one hit. If BAx2 had no hits and BAx1 had one, then the point used BAx1 only. At BB, if one plane, say BBy had two hits while the BBx and BBu had just one, we could use their data to select the proper y view hit. Indeed, if BBy had no hits at all, the other planes could be used to construct a BBy point if they each had one hit.

We attempted to "save" the data in a plane only if it had 0 or 2 hits (single hits were fine) and only if the other needed plane(s) had exactly one hit. All other cases

were considered too unreliable to save. The evaluation and saving operations were carried out independently at BAx, BAy, and BB. Use of the slant plane at BB mixed the x and y views when a plane needed saving. At BB, if the x or y view had a single hit but the other view needed saving and could not be, the view with a single hit was still considered good.

If a point was declared unreliable, we assigned a position and error obtained from the average beam spot and its width as a beam particle was a priori known to be in the beam spot. The large error minimized the impact of a poorly known beam on the reconstruction, especially the vertex. For the same reason, point errors were increased if the data used to define it were found inconsistent.

Explicit quality flags were set for the x and y views indicating whether or not the data at each station was perfect, saved, or unreliable according to the hit counting described above. The flags were originally meant to identify cases of double beam events. But for  $\pi\pi n$ , forward topology cuts completely eliminated double beam cases and we found that the flags were a measure of the chamber response to a single beam particle. To insure a good  $t_{pn}$  measurement in  $\pi\pi n$  we cut out any events that had any unreliable plane. The events lost by this cut were an unbiased fraction of the recorded events, and the large errors of the beam track in such cases prevented a loss of reconstruction efficiency, so a correction weight derived from just the ratio of cut to total events could be applied.

### C.5 Targtrk

Targtrk was our front end analysis system for non-vee topologies such as  $\pi\pi n$ , and the physics studies reported here used only events successfully analyzed by it. Targtrk sought before magnet tracks coming from our target and linking to the matches. It fit for only a main vertex, and made no judgements about the number of vertex particles. The linking requirement was absolute. Targtrk found no tracks

for particles without matches.

The number and locations of the front end chambers were not sufficient for reliable unassisted pattern recognition. Because of our  $K^0$  decay region, the BC lever arm was not long enough to provide sufficient discrimination between near A-station hits. This remained true even if information from the matches was used. We needed assistance from beam track information and a vertical focusing correction in addition to match data to provide reliable front end pattern recognition. This was done by creating "pseudo" sparks in several artificial chambers created by the program. One such chamber was near the target, using the beam to define its spark, one was at the magnet midpoint,  $z=4.47$  m and using match extrapolations to set the spark, and in the y view only, a chamber was defined at  $z = 1.60$  m, again using a match extrapolation.

Table C.3

Tracking Requirements -- Targtrk

View	Chambers	Minspk	Group
y	Ay1, Ay2	1	Ay group
y	By, Cy	1	By group
y	Ay1, Ay2, By, Cy	2	Overall
x	Ax1, Ax2, Au, Av, Bx', Bx, Cx	4	Overall
x	Ax1, Ax2, Au, Av	2	Ax group
x	Bx', Bx, Cx	1	BCx group

The pseudo sparks at the target and magnet midpoint were used to define a 1.5 cm road for (nearest) spark searches. If the number of *real* sparks did not meet or exceed the minsapk requirements of Table C.3, the road was rejected. All pseudo sparks were used in initial fits and could not be removed to reduce the track  $\bar{\chi}$  (as defined in section C.2). Real sparks could be, and if necessary were, removed to reduce  $\bar{\chi}$  below 3.0. If all minsapk requirements were reached before  $\bar{\chi}$  passed this

limit, the track was rejected. For acceptable tracks, the beam and  $z = 1.60\text{m}$  pseudo sparks were then removed and the track was refit with the remaining sparks.

The beam pseudo spark was especially important in selecting correct A station sparks. The selection was fairly sensitive; a poor beam spark choice, or a bad beam track could easily mess it up. As a result much work was invested in our beam alignment and analysis (section C.4), and Targtrk was structured as a loop over three candidate beam sparks each at a different  $z$ . To maintain good efficiency at our target, these  $z$  values were  $-.60$ ,  $-.30$ , and  $0.00\text{ m}$ , each with an error of  $\sigma_z = .25\text{m}$ . They bracketed our target and the last was near our DEDX counter. The coordinate of the beam spark was taken as the beam track extrapolation, and its error,  $\sigma_0$ , was initially the projected track error or  $1\text{mm}$ , whichever was larger. Once the slope,  $b$ , of a road was set, this error was increased to  $\sigma = \sqrt{\sigma_0^2 + (b\sigma_z)^2}$

The complete Targtrk analysis was repeated for each beam spark selection, (and all tracks and vertices found were indexed by it). This consisted of projecting matched tracks through the magnet to form pseudo sparks at  $z = 4.47\text{ m}$  (mid magnet) and  $z = 1.60$  (y view only). Y view projections used a Wind's method [Co77] calculation to account for vertical focusing effects which were found significant at low momenta ( $\gtrsim 5\text{ GeV/c}$ ). Y view pseudo spark errors were set to  $5\text{ mm}$  at mid magnet and  $5\text{ cm}$  at  $1.60\text{ m}$ . The x view projection to the magnet mid point had a curvature correction, and a  $3\text{mm}$  error added in quadrature with an estimate derived from the after magnet error matrix. Both the vertical focusing and curvature corrections used preliminary momentum estimates derived from the after magnet track and the front end road being set up.

The y view was done first with at most one front end track, or "link", being found for each match. Next, x view tracks were sought for those matches having y view links. The y link for a match was used to project the Au and Av sparks to the x

view with the y track error being combined with the chamber error. Au and Av were not explicitly required to be on a track since the Ax group minspk was only 2 for 4 chambers, but they did help to flush bad matches lucky enough to link in y. When an x view track was found, its momentum was found with a square field calculation, section 3.2.

Once the tracking for all three beam spark choices was completed, a vertex was sought for each set of tracks found with simultaneous x and y view fits to a common  $z_v$ . The beam track was required to be on all vertices, but forward tracks in either view could be deleted to reduce the vertex  $\chi^2$ . Particles were flagged as to whether or not they were in the vertex in one, both, or neither view. The successful vertices (just one per beam spark) were compared in turn, and the best one was flagged. A vertex whose tracks *missed* more A station sparks than the previous one was "rejected". That being equal, the vertex using fewer xy track pairs was "rejected". These tests being passed, the vertex with the lower  $\chi^2$  was preferred. All Targtrk results from the three beam spark choices were written to DST's (to allow for studies), but only the tracks and vertex for the best choice were written to CST's. The A station spark counting test was the most sensitive. A bad vertex usually resulted from a poor A station spark assignment. An incorrect track would usually share sparks with a good track, miss its proper sparks, and thereby increase the unused spark counts. Noise and delta ray sparks would rarely affect the count of missed sparks.

Targtrk was judged successful if any vertex was found, regardless of the number of particles in it. If no vertex was found at all, Vtrig results were written to the CST as a backup. Sclean was not used by Targtrk. Bad matches that linked to the front end in both views always shared tracks with good matches, and thereby did not distort the analysis. However, this sharing did lead up to a feed up problem for the multiplicity tests. To deal with this, Sclean was used to flag bad linking

matches after Targtrk was done.

### C.6 Vtrig

Although we did not use Vtrig results in the analysis reported here, it was used for the vee triggers and Vtrig results were written for Targtrk failures. Part of our confidence in Targtrk rests with the observation that no Targtrk "failures" succeeded in Vtrig.

Vtrig fit front end tracks and vertices to the specific topology characteristic of a given trigger. For  $\pi\pi\pi$  that was two charged particles from the main vertex. For a vee trigger, such as  $K^0\pi p$ , this was the nominal number of vees and nominal number of main vertex charged particles. Vees were made only of oppositely charged particle pairs known to link through the magnet using only the B and C stations for front end tracking. All such pairs were potential vees. Successful vees passed a z-vertex cut,  $z_V > .1m$ , and had four tracks (two for each particle) in the vertex. Having vees, main vertex hypotheses were tried. (Since no vees are needed in  $\pi\pi\pi$ , Vtrig started with the main vertex for it.) The number of main vertex hypotheses was set by the number of vee candidates, the number of charged tracks, and the desired charged main vertex multiplicity. If more than one main vertex hypothesis succeeded (and each contained a specific vee choice), the best one was selected depending mainly on the total tracks (including neutral "tracks" from the vee) from both x and y views in the main vertex, and then on the vertex  $\chi^2$  if need be. To reduce the number of hypotheses tested, Vtrig included the Sclean match cleanup. (Sclean was originally designed for Vtrig.) For Vtrig, this ran only on matches that linked to the BC stations, and only Sclean approved matches were admitted to the full Vtrig analysis.

### C.7 Kinks

Our square field momentum calculation with a  $p_t$  kick of .7510 has proven extremely good. Monte Carlo studies comparing this approximation to an integration of our field map found square field errors completely negligible compared to our momentum resolution. Unfortunately, there is a catch resulting from alignment errors. The momenta measured by TEARS have a systematic shift characteristic of a kink of  $.084 \pm .007$  milliradians between the upstream and downstream (of the MPS magnet) chamber alignments. The kink had no noticeable effect on our tracking and linking efficiencies. The above studies have shown that this kink is not an effect of the square field approximation. It is less than our angular resolutions (Table 2.8), so it could easily have been missed by the alignment runs (given their statistics), which used  $3\pi p$  data with the magnet simply turned off, and straight line fits through the full MPS from the A to F' stations. The alignment fits did not include any parameters for residual fields. The kink is qualitatively of the same order as the expected bend from residual fields ( $\sim 15$  gauss with unquoted errors) at zero current observed in our field map measurements.

Although small, the kink is a systematic effect easily seen in our missing mass spectra. Its effect is to shift measured momenta up or down depending on the bend angle which, in turn, depends on the charge of a particle and the magnet polarity. The effect of the kink is adequately parameterized as

$$P = P_m (1 + \delta\theta / \theta) \quad (C.1)$$

where  $P$  is the true momentum,  $P_m$  the measured momentum,  $\theta$  the bend angle and  $\delta\theta$  the kink. This correction was applied at the PST and CST levels on individual particles to allow for evaluation of  $\delta\theta$  with our full data sample. The effect of using uncorrected momenta on our missing mass is shown in figure C-1, which plots  $Mx^2$  at 100 GeV/c as a function of

$$x^- = (E^- - E_b/2) / (E_b/2) \quad (C.2)$$

where  $E^-$  is the  $\pi^-$  energy and  $E_b$  is the beam energy. These shifts are appreciable when compared to our missing mass resolution, figure 2-11. The data for these plots was the mean  $Mx^2$  resulting from fits to a Gaussian for the neutron missing mass peak after a  $\pi\pi X$  background subtraction (and without a kink correction). A straight line adequately follows the  $x^-$  dependence. The shift in  $Mx^2$  upon a magnet polarity change,

$$\Delta Mx^2 = \langle Mx^2 \rangle_{Imag = -180} - \langle Mx^2 \rangle_{Imag = +180} \quad (C.3)$$

shown in figure C-2a is approximately

$$\Delta Mx^2 = \left[ -4m_p E_b^2 \delta\theta / P_K \right] x^- \quad (C.4)$$

where  $P_K$  is the magnet  $p_t$  kick. Iterative fits using equation C.4 to predict  $\delta\theta$  result in our value of  $.084 mR$ . Figure C-2b shows our final  $\Delta Mx^2$  result and figure C-3 shows the individual polarity  $Mx^2$  distributions with the kink correction. The small residual slope is unexplained. It is small enough to be caused by either the approximation 3.1, our our square field assumption. In either case, it can be ignored, the shifts it represents being much smaller than our  $Mx^2$  resolution.

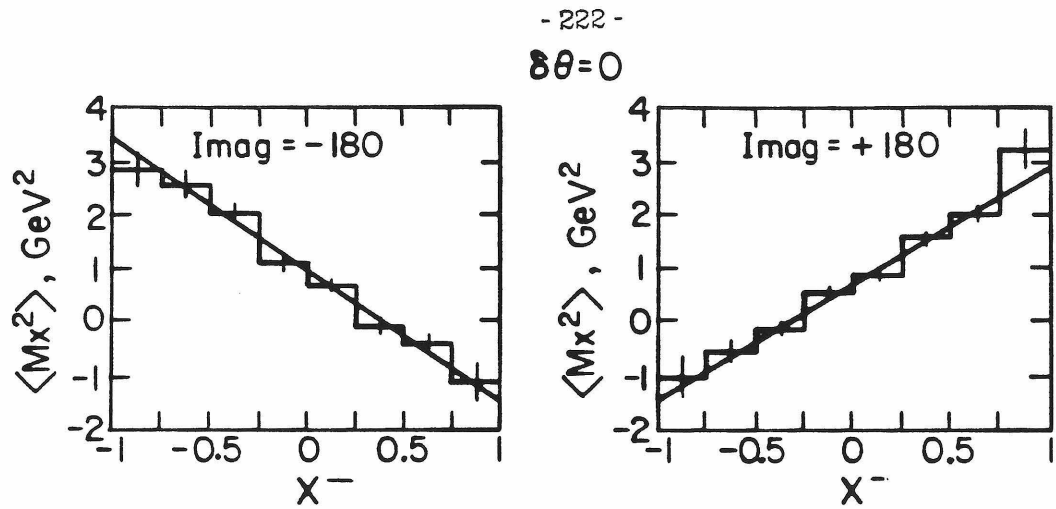


Figure C-1. Missing mass<sup>2</sup> calculated without kink correction factor.

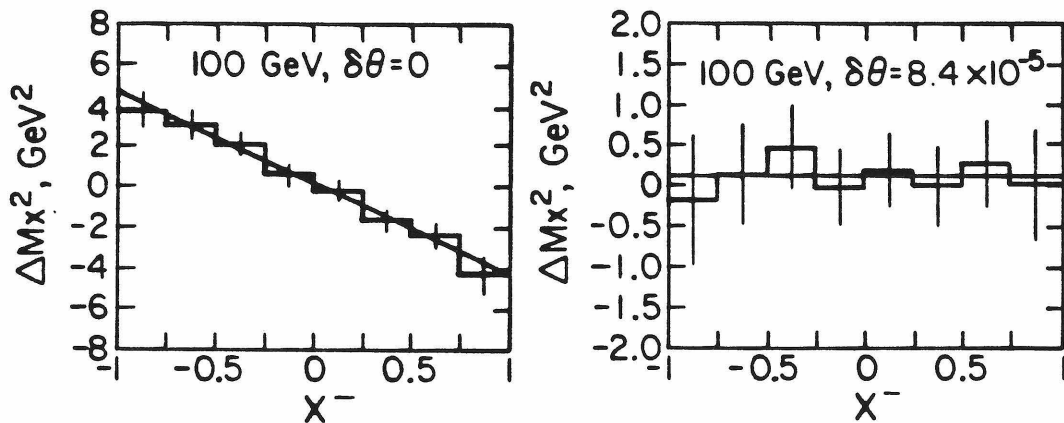


Figure C-2.  $\Delta \langle Mx^2 \rangle$  before (a) and after (b) kink correction.

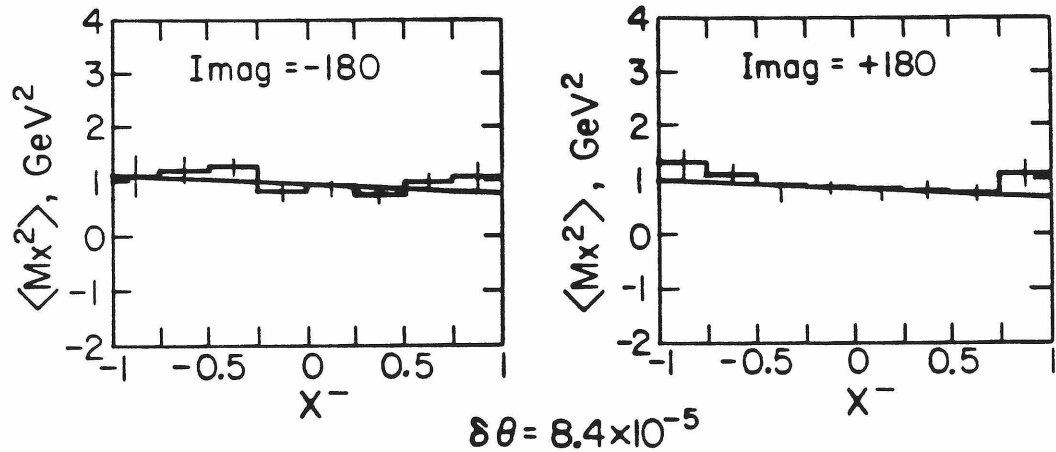


Figure C-3.  $Mx^2$  after kink correction. No correction was applied for residual slope.

## Appendix D

### Corrections

#### D.1 Introduction

In this appendix we expand on the development of some of the more significant non-acceptance corrections. In some cases, unusual methods were used and they merit a review. Since the development of our A-station [Fr82] and C1C2 [Da78] methods are given elsewhere and our discussion for them in Chapter IV was reasonably complete, they are not discussed here. Although some repetition exists, this appendix assumes corresponding sections of Chapter IV are read in parallel.

#### D.2 Veto House Correction

Because of inherent instrumental inefficiencies and one large hole (the forward magnet aperture) in the veto house, there is a considerable ( $\sim 10\%$ ) background under the neutron in a  $\pi\pi m_T$  missing mass squared ( $Mx^2$ ) plot at 100 GeV, figure 1-4. The background is smaller at 20 and 50 GeV, mainly due to better  $Mx^2$  resolutions at the lower momenta. We need the veto house ( $\beta$ ,  $V0$ ,  $V1$ ,  $V2$ ,  $V3$ ) to suppress a tremendous background, see figure 4-4, of events with extra (unseen)  $\pi^0$ 's and charged recoils. Without it, the topological trigger would take virtually only background data, and our limited  $Mx^2$  resolution would fail to isolate the relatively small fraction of  $\pi\pi n$  events.

In a one particle exchange picture, figure D-1, extra  $\pi^0$ 's can come from either vertex (or both vertices). Lower vertex  $\pi^0$ 's would be from recoiling  $N^*$  (and  $\Delta$ ) resonances, while upper vertex  $\pi^0$ 's would be decay products of mesons such as the  $\omega^0$ . Because upper vertex  $\pi^0$ 's are typically "fast" and result in large  $Mx^2$  values, most of the background under the neutron comes from lower vertex processes. Another upper vertex background characteristic is that the  $\pi^+\pi^-$  mass is shifted

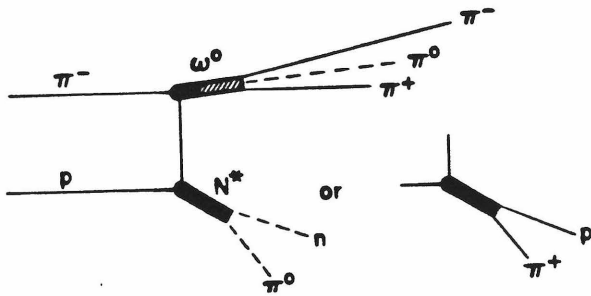


Figure D-1. One particle exchange model for  $\pi^0$  backgrounds. Resonant amplitudes at both vertices are shown for brevity. Upper vertex can be almost any nonstrange meson giving one or more  $\pi^0$ 's and a  $\pi^+\pi^-$  pair. The  $\omega^0$  is just the lightest such state.

down from the parent mass; and is concentrated at  $\pi\pi$  masses at or below the  $\rho$ , see figure 1-3. On the other hand, the  $\pi^+\pi^-$  mass spectrum for events with extra  $\pi^0$ 's associated only with the lower vertex, is quite similar to the spectrum from  $\pi^+\pi^-n$ .

The topological trigger stops most upper vertex charged particle backgrounds. Charged decays of  $N^*$ 's are vetoed by the  $\beta$  chamber, and V1 if the  $\beta$  chamber fails to fire. Hadrons routinely penetrate and are detected by V1. Indeed, of the charged particles seen by  $\beta$  and not V1, all seem to be delta rays. Charged recoil products that miss V1 and strike the A-station would violate the topological trigger.

Part of the experiment design was set by our desire to measure veto failure backgrounds and, if possible, subtract them. We had a prescaled background trigger,  $\pi\pi X$ , with no veto house requirements at all, and we kept the front end geometry fixed to facilitate measurements which combine all our momentum settings.

All veto failures were (up to prescaling) contained in the  $\pi\pi X$  trigger. The background in  $\pi\pi n_T$  is the non  $\pi\pi n$  part of  $\pi\pi X$  times the veto "failure rate", defined below. Veto failing backgrounds are assumed to have the same  $\pi^+\pi^-$

distributions as found in  $\pi\pi X$ . That is, no special configurations of the  $\pi^+\pi^-$  are selected as veto failures from among the  $\pi\pi X$  sample. Our studies indicate that this is a reasonable assumption.

The background "observed" in  $\pi\pi n$  results from the production of background states and subsequent failures to detect the extra (excluding forward  $\pi^+\pi^-$ ) decay products. The veto "failure rate",  $F$ , is defined as the fraction of the background for which the veto counters fail to detect the extra particles.  $F$  depends on the flux of extra decay products in direction and energy, the veto counter geometry and counter efficiencies. Background decay kinematics are dominated by available energies, and when discussing only the extra particles such as  $\pi^0$ 's, this is roughly half of  $Mx^2$ :

$$Mx^2 = m_p^2 + t + 2m_p(E_{beam} - E_{forward}) \quad (D.1)$$

where  $t$  is the momentum transfer to the recoil neutron or  $N^*$ . Averaging over many (background) events, the decay product flux at any direction, and hence the failure rate, depend mainly on  $Mx^2$ . This even extends to upper vertex backgrounds.

To a good approximation, no other dependence for  $F$  is needed, and the measured failure rates show little, if any,  $m_{\pi\pi}$  or  $p_t$  effects.

At any momentum setting, we can exclude all the background resolved from the neutron by a simple  $Mx^2$  cut. But unresolved background can't be measured at that momentum setting. Without reference to other momentum settings, we could only use simple extrapolations and fits which run the danger of not being able to extract a reasonably correct background shape under the neutron. (Simple extrapolations were used for a preliminary study [St78], and for the neutron veto correction in sections 4.4 and D.3.)

By keeping the front end geometry fixed, measurements of the failure rate at any  $Mx^2$  value from any beam momentum setting will apply to the other settings. Once we know the failure rates, we can use the  $Mx^2$  spectrum from  $\pi\pi X$  to estimate the background in  $\pi\pi n$ . Thus, 50 and 20 GeV/c measurements of  $F$  and the 100 GeV/c  $Mx^2$  distribution from  $\pi\pi X$  can be used to "predict" the veto failure background at 100 GeV/c. Failure rate measurements at 100 GeV/c do not directly help because we can measure  $F$  only at  $Mx^2$  values away from the neutron peak. However, the main check on this method is agreement between failure rates seen at the different beam momenta in  $Mx^2$  regions where the measurements overlap.

#### D.2.1 Failure Rate Measurement

The  $\pi\pi X$  trigger was essentially  $\pi\pi n_T$  without the veto house requirement. There was a weak "special D" requirement for  $\pi\pi X$  (1 or 2 hits in both Dx and Dy), but the only effect of this was a slight delta ray (at D) suppression and our method compensates for this by construction.

The failure rates were measured by plotting  $Mx^2$  distributions for both  $\pi\pi n_T$  and  $\pi\pi X$  data on CST's. The same trigger and topology cuts were used for both types excepting no veto cuts were made in  $\pi\pi X$  data. In each  $Mx^2$  bin (at least  $3\sigma_{Mx^2}$  from the neutron peak) the failure rate,  $F$ , was evaluated as:

$$F = \frac{(Events \text{ in } \pi\pi n_T) \cdot \delta}{(Events \text{ in } \pi\pi X) \cdot P} \quad (D.2)$$

where  $P$  is the  $\pi\pi X$  prescaling factor (= .5 at 20 GeV/c, 40 at 50 GeV/c and either 40 (early runs) or 80 (late runs) at 100 GeV/c).  $\delta$  is an average  $\beta$  chamber delta ray correction for  $\pi\pi n_T$ , leaving it out would underestimate  $F$ . The  $\pi\pi X$  trigger was not subject to  $\beta$  chamber delta ray vetos or corrections. We needed to use both types of triggers, as the number of  $\pi\pi n_T$  events in the  $\pi\pi X$  sample was too small to be useful. The prescale factor  $P$  was then necessary, as only  $1/P$  of the  $\pi\pi X$  events

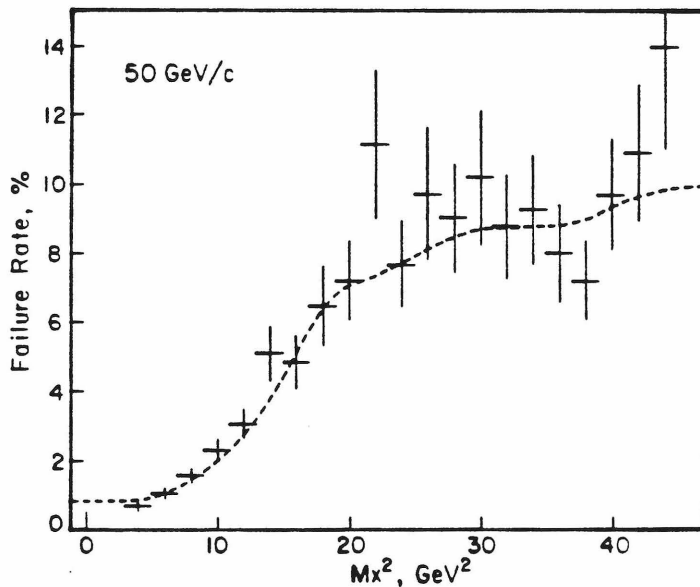
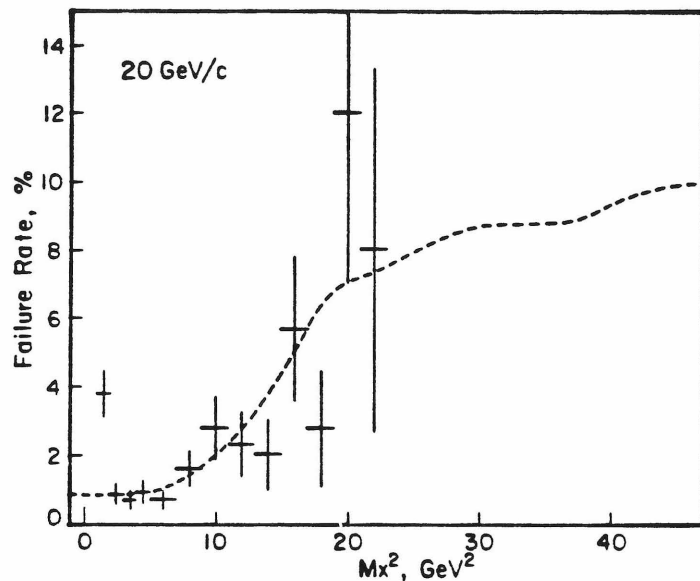


Figure D-2a. Failure rate measurements at 20 and 50 GeV/c.

allowed by the spark chamber dead time were recorded.

For the measurements, we split the data into sets distinguished by beam momentum and prescale factors. To be consistent with A-station cuts, we restricted the study to  $m_{\pi\pi}$  values  $> 500$  MeV.  $p_t$  and  $m_{\pi\pi}$  dependencies were searched for with no significant effects seen.  $Mx^2$  overlap regions between the

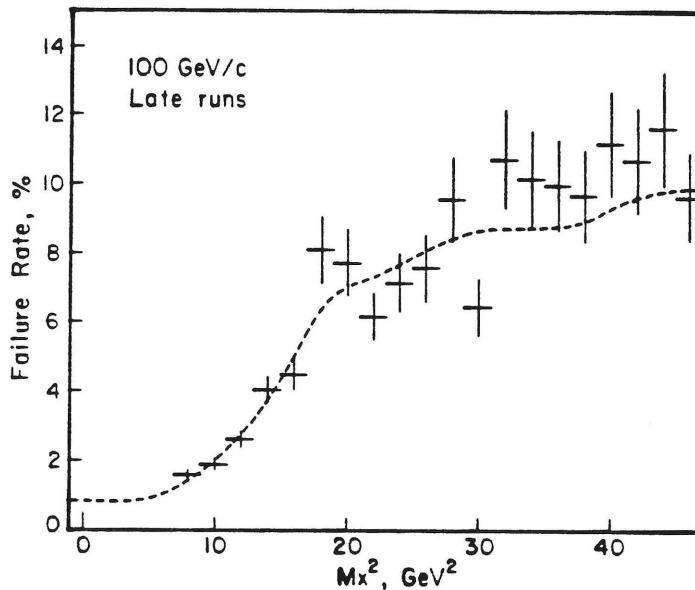
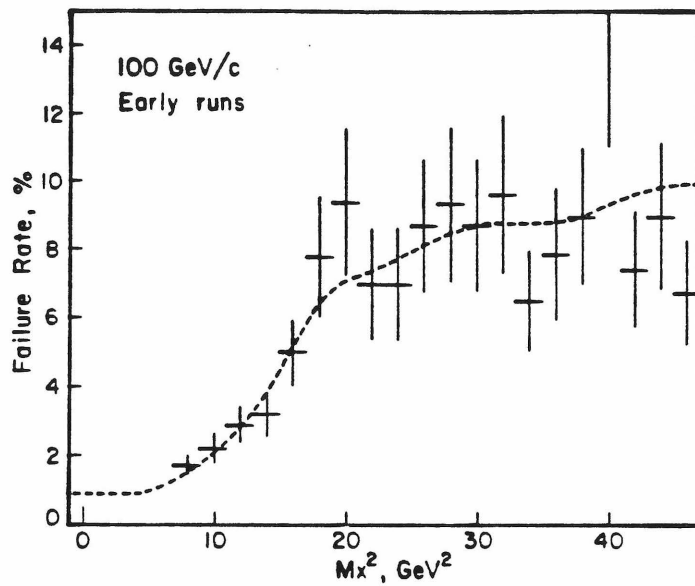


Figure D-2b. Failure rate measurements at 100 GeV/c. Early and late 100 GeV/c run sets differ in both prescale factor and B8 status (broken in late set).

various beam momenta were reviewed and found consistent. We then combined the failure rates by averaging the observed values whenever data sets overlapped. The combined result is shown in figure 4-3. Here we show individual sets in figures D-2. The lowest  $Mx^2$  value (" $\Delta^0$  bin") in the combined and 20 GeV plots represents a

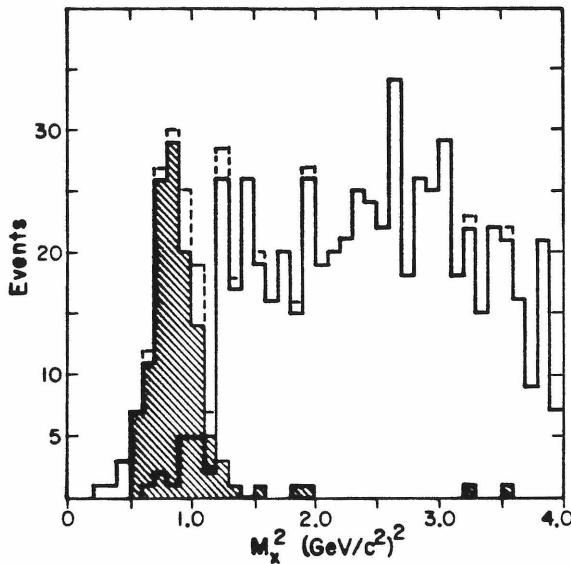


Figure D-3 20 GeV/c  $\pi\pi X$   $Mx^2$  spectrum. Hatched area satisfied  $\pi\pi n_T$  trigger requirements. Other histograms are all events (uppermost, including both dashed and solid lines) and the remaining after  $\pi\pi n_T$  tags were removed.

problem at the  $\Delta^0$  and will be discussed shortly. The smooth curves of figures 4-3 and D-2 are single pass smoothings of the combined set from the plotting program. They exclude the  $\Delta^0$  bin and are for comparison purposes only. The first two bins of the combined plot (-1 to +1 and +1 to 3 GeV $^2$ ) are actually the  $\Delta^0$  bin ( 1.20 to 2 GeV $^2$ ) and 2 to 3 GeV $^2$  bins from 20 GeV/c.

The other bins are all 2 GeV $^2$ , a size motivated by the 100 GeV/c  $Mx^2$  resolution, and carried into the 50 and 20 GeV/c analyses for lack of data at the lower momenta.

At 20 GeV/c we can just barely resolve the  $\Delta^0$  from the neutron, as in figure D-3, a plot of  $\pi\pi X$  data only, and we cannot resolve the  $\Delta^0$  from higher mass  $N^*$ 's. Although the statistics are rotten, the  $\Delta^0$  appears shifted down a bit from a nominal peak value of  $\sim 1.52$  GeV $^2$  ( $=(1.232)^2$ ). This is a predicted effect [Ja64], but it doesn't help our resolution any. For veto failure rate measurements, we define the " $\Delta^0$ " (at 20 GeV/c) as all non  $\pi\pi\pi\pi$  data between 1.2 and 2.0 GeV $^2$ . This is slightly

inside the neutron cut of .45 to  $1.35 \text{ GeV}^2$ , so we subtracted an estimate of the good neutron content in the  $\pi\pi n_T$  data for the neutron tail between 1.2 and  $1.35 \text{ GeV}^2$  in the failure rate measurement. This attempt to get into the neutron peak was only done at 20  $\text{GeV}/c$ , and only because the  $\Delta^0$  failure rate is a problem and the  $n - \Delta$  separation is poor.

On the failure rate plots, the  $\Delta^0$  bin sticks up like a sore thumb. Otherwise, the failure rate behavior is roughly as expected from early Monte Carlo studies, although at a higher value than the studies predicted. The failure rate (excepting the  $\Delta^0$ ) is fairly flat below  $\sim 8 \text{ GeV}^2$  with a rise above that value from geometric effects.  $N^*$  decay products ( $\pi^0$ ) tend to go forward as the  $N^*$  mass increases. That the failure rate flattens out at extremely high  $Mx^2$  apparently indicates most events with upper vertex  $\pi^0$ 's also have  $N^*$  recoils. The veto house is not expected to be effective for cleanly produced  $\omega^0 n$  states. Fortunately, the rise in veto failure rates occurs above the neutron  $Mx^2$  cut, even at 100  $\text{GeV}/c$ .

### D.2.2 Background Subtraction

To subtract the veto failure background from our  $\pi\pi n_T$  data, we chose to subtract weighted  $\pi\pi X$  events directly. This was done to preserve correlations between the variables  $M_{\pi\pi}$ ,  $\cos\theta_J$ ,  $\varphi_J$  and  $t$ ;  $\pi\pi X$  distributions being a bit different than those seen in  $\pi\pi n_T$ . Multivariable arrays with reasonable granularity would require more bins than data.

We first extract background events from the  $\pi\pi X$  data by removing all events that could be real  $\pi\pi n$ . Within the neutron  $Mx^2$  cut only, we remove all events that satisfied the  $\pi\pi n_T$  trigger, all neutron veto events, and all  $\beta$  chamber delta ray vetoes. This avoids double counting good events and the neutron and  $\beta$  chamber veto corrections. Delta rays in the  $\beta$  chamber were identified by hits in  $\beta$  and no hits in any other veto counter. We checked that this cut was as pure in  $\pi\pi n$  as the

$\pi\pi n_T$  trigger. Neutron veto events were identified by having a single barrel stave struck with no other veto counter firing. The struck veto counter had to be within a  $p_t$  dependent  $\Delta\phi$  (hit-recoil) cut of  $2.5\sigma$  about the average  $\Delta\phi$  peak seen in the neutron veto measurement, section 4.3. The  $\Delta\phi$  cut is  $p_t$  dependent, and no single barrel strikes were removed below  $p_t = .08$  GeV/c, the neutron veto threshold. A few background events are lost by these cuts, but that loss is extremely small.

Given these removals, we made PST's of the  $\pi\pi X$  data with a flag set to distinguish them from  $\pi\pi n_T$  PST's. The background processing was done in the same job as the  $\pi\pi n_T$  data. All corrections and cuts were done in the same manner as for  $\pi\pi n_T$  except that neutron veto and  $\beta$  chamber delta ray weights were excluded, veto counter cuts were not done, and we applied an additional term to the  $\pi\pi X$  weight. The extra weight was  $w_v = -PF$  where  $P$  was the prescale factor and  $F$  the failure rate.  $F$  is  $Mx^2$  dependent. Within the  $\pi\pi n$   $Mx^2$  cut, we must combine a smeared  $\Delta^0$  failure rate with a flat everything else. Although only a small part of  $\pi\pi X$ , the  $\Delta^0$  accounts for a significant part of the veto failures. Outside the neutron cut, we used the combined measurements directly for the  $Mx^2$  plots of section 4.2.

### D.2.3 $\Delta^0$ Smearing

To smear the  $\Delta^0$  in the failure rates, we view the background at any  $Mx^2$  value, as composed of a  $\Delta^0$  part of fraction  $f_\Delta$  and everything else, a fraction  $(1-f_\Delta)$ . Missing mass resolution is the sole reason for  $\Delta^0$  smearing. We know that  $\Delta^0$  events have a poor failure rate but cannot tell which events are actually  $\Delta^0$ 's. The net failure rate as a function of  $Mx^2$  is then

$$F(Mx^2) = F_1(1-f_\Delta) + F_2 f_\Delta \quad (D.3)$$

where  $F_1$  is the flat part of the failure rate (= average of all bins within the neutron  $Mx^2$  cut other than the  $\Delta^0$ ) and  $F_2$  is the  $\Delta^0$  failure rate. A smearing function

$S(Mx^2)$ , is applied to the  $\Delta^0$  failure rate,  $f_\Delta = f'_\Delta S(Mx^2)$ , where  $f'_\Delta$  is the number derived below.  $S(Mx^2)$  is a simple Gaussian smear of a square distribution from 1.2 to 2.0  $\text{GeV}^2$  (the 20  $\text{GeV} \Delta^0$  cut) with unit area:

$$S(Mx^2) = \frac{1}{1.6} \left[ \text{erf} \left( \frac{2-Mx^2}{\sigma\sqrt{2}} \right) - \text{erf} \left( \frac{Mx^2-1.2}{\sigma\sqrt{2}} \right) \right] \quad (\text{D.4})$$

where  $\sigma$  is the appropriate missing mass resolution. This procedure is needed only at 50 and 100  $\text{GeV}/c$ . At 20  $\text{GeV}/c$ ,  $f_\Delta = 1$ , and  $F(Mx^2) = F_2$ . Only a few  $\Delta^0$  decays penetrate the neutron peak.

We had to resort to some modeling to get  $f_\Delta$  at 50 and 100  $\text{GeV}/c$ . There are simply no measurements of  $\pi^+\pi^-\Delta^0$  or  $\rho^0\Delta^0$  at very high energies. Existing measurements, which are also not compatible with our cuts, go only up to  $\sim 20 \text{ GeV}/c$ , and one 200  $\text{GeV}/c$  bubble chamber experiment [Bi74] gives only an  $8\mu b$  upper limit to  $\rho^0\Delta^0$  (95% C.L., no events).

To get  $f_\Delta$ , we start with

$$f_\Delta \equiv \frac{\pi\pi\Delta}{\pi\pi X} = \frac{\pi\pi\Delta}{\pi\pi n} \times \frac{\pi\pi n}{\pi\pi X}. \quad (\text{D.5})$$

We can use our data to get  $\pi\pi n/\pi\pi X$ , and this provides the only  $\pi\pi$  mass dependence used in  $F(Mx^2)$ . Plots of this ratio are given in figure D-4 along with the linear fit actually used for  $f_\Delta$  ( $m_{\pi\pi}$  in  $\text{GeV}/c^2$ ):

$$\frac{\pi\pi n}{\pi\pi X} = .0457 + .0328 m_{\pi\pi} \quad (\text{D.6})$$

For  $\pi\pi\Delta/\pi\pi n$ , we note that both reactions are dominated by  $\pi$  exchange and so assume that they have the same  $\pi\pi$  mass dependence. The reactions have different  $t$  dependences and  $t_{\min}$  values. We assume that the  $P_{beam}$  dependences of  $d\sigma/dt$  are the same. Thus we are assuming that

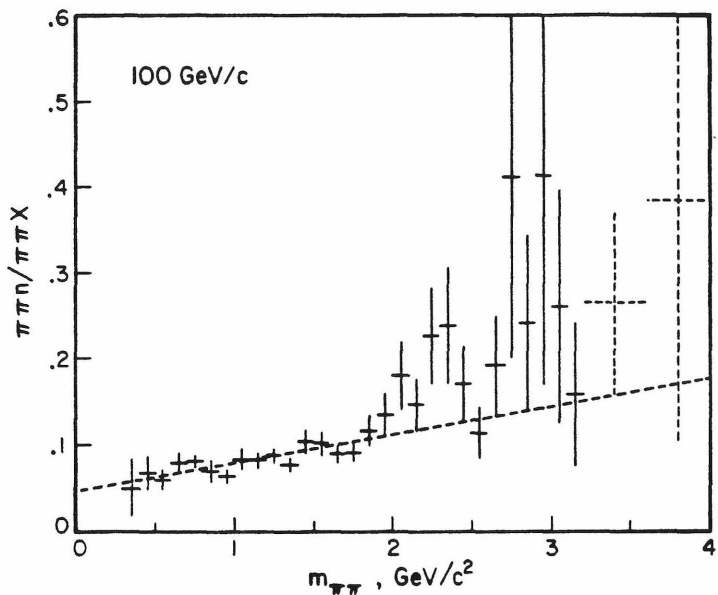


Figure D-4. Ratio of events  $\pi\pi n_T / \pi\pi X$  with neutron  $Mx^2$  cut. Data from CST's, dashed points not used in the fit.

$$\frac{\pi\pi\Delta^0}{\pi\pi n} = \frac{\rho^0\Delta^0}{\rho^0 n} = \frac{\sigma(\rho^0\Delta^0)}{\sigma(\rho^0 n)}, \quad (D.7)$$

and we can use data to get the ratio at 20  $\text{GeV}/c$  and then extrapolate it to higher  $P_{beam}$  values by integrating over the  $d\sigma/dt$  forms. Using  $\pi\pi X$  data, we find (statistical error only)

$$\frac{\rho^0\Delta^0}{\rho^0 n} = 1.70 \pm .20 \quad \text{at } 20 \text{ GeV}/c. \quad (D.8)$$

Given our arbitrary upper cut of 2.0  $\text{GeV}^2$  for the  $\Delta^0$ , this is a reasonable value. In this ratio, we included non neutron events in the  $\rho^0\Delta^0$  set even when  $Mx^2$  was below 1.2  $\text{GeV}^2$ . Events identified as  $\beta$  chamber delta rays or neutron vetoes were included in the  $\rho^0 n$  set.

For the beam momentum extrapolation of  $\sigma(\rho^0\Delta)/\sigma(\rho^0 n)$ , we take  $d\sigma/dt$  forms inspired by the poor man's absorption model for  $\pi$  exchange [Fo71b]:

$$\frac{d\sigma}{dt} \Big|_{\rho^0 \Delta^0} = \frac{k}{p^\alpha} \frac{e^{bt}}{(t - m_\pi^2)^2} \quad (D.9a)$$

$$\frac{d\sigma}{dt} \Big|_{\rho^0 n} = \frac{k}{p^\alpha} \frac{-te^{bt}}{(t - m_\pi^2)^2} \quad (D.9b)$$

where numerical constants are grouped into  $k$ ,  $p$  is the beam momentum;  $\alpha \sim 2$  and  $b = 4$  are assumed the same for both reactions. The  $b$  value was inspired by fits by Kirmel and Owens [Ki77] to the  $\rho^0 n$  reaction. Their  $\pi$  exchange terms have effectively  $\sqrt{b} \sim 2$  (the correction is insensitive to  $b$ ).

Letting

$$I_\Delta(p) = \int_{-\infty}^{t_{\min}} \frac{e^{bt}}{(t - m_\pi^2)^2} dt \quad (D.10a)$$

and

$$I_n(p) = \int_{-\infty}^{t_{\min}} \frac{-te^{bt}}{(t - m_\pi^2)^2} dt \quad (D.10b)$$

we have

$$\frac{\sigma(\rho^0 \Delta^0)}{\sigma(\rho^0 n)} = \frac{\sigma(\rho^0 \Delta^0)}{\sigma(\rho^0 n)} \Big|_{20} \frac{I_\Delta(p)}{I_\Delta(20)} \frac{I_n(20)}{I_n(p)}. \quad (D.11)$$

The  $I_\Delta$  and  $I_n$  integrals can be evaluated in terms of exponential integral functions  $E_1$  and  $E_2$ , which have been tabulated [Ab64].

$$I_\Delta(p) = \frac{e^{bm_\pi^2}}{(m_\pi^2 - t_{\min})} E_2(b(m_\pi^2 - t_{\min})) \quad (D.12a)$$

$$I_n(p) = e^{bm_\pi^2} \left[ (1 + bm_\pi^2) E_1(b(m_\pi^2 - t_{\min})) - \frac{m_\pi^2}{(m_\pi^2 - t_{\min})} e^{-b(m_\pi^2 - t_{\min})} \right]. \quad (D.12b)$$

The  $p$  dependence is in  $t_{\min}$ . We find  $I_n(20)/I_n(p) = 1.000$  at all  $p$ , the 20 GeV  $t_{\min}$

for  $\rho^0 n$  being already well below  $m_\pi^2$ , and the (-t) in  $d\sigma/dt$  suppresses low t cross sections. The  $\Delta^0$  terms contain significant effects. For the sake of simplicity, we used a single  $t_{\min}$  value, evaluated at  $m_\Delta^2 = 1.5 \text{ GeV}^2$ , and obtain the following values (statistical error only):

Table D.1			
Model Results			
$p, \text{ GeV}/c$	$t_{\min}(\rho^0 \Delta^0)$	$I_\Delta(p)/I_\Delta(20)$	$\sigma(\rho^0 \Delta^0)/\sigma(\rho^0 n)$
20	$-1.02 \times 10^{-2}$	1.000	$1.70 \pm .20$
50	$-3.93 \times 10^{-3}$	1.347	$2.29 \pm .27$
100	$-1.39 \times 10^{-3}$	1.503	$2.56 \pm .30$

Since we claim no  $\pi\pi$  mass dependence observed in  $F(Mx^2)$ , and yet use one for the  $\Delta^0$ , we should note that the  $\Delta^0$  is a relatively small fraction of  $\pi\pi X$  at 50 and 100  $\text{GeV}/c$ , and that it is unresolved from the neutron at these momenta. Thus we can't hope to see a mass dependence from the  $\Delta^0$  in the failure rates.

#### D.2.4 B8 Failure

Part way through Run I, after the 50 GeV runs but well before the 20 GeV runs, one barrel counter, B8 (figure 2-5), failed. We decided not to repair it, and instead enabled an unprescaled background trigger at 100 GeV,  $\pi\pi B$ , which was originally planned for 20 GeV neutron veto studies. Running this trigger at 100 GeV turned out to be crucial for neutron veto measurements, but it has not been mentioned yet in relation to veto failures. At 100 GeV the  $\pi\pi B$  trigger was intended to estimate the number of veto failures from the loss of one barrel counter. But, rather perversely, the best estimate of the effect of the loss comes from our 20 GeV data. The loss of a single counter does not affect the veto efficiency for cases where at least

two of the barrel staves would normally fire, or a barrel stave and a jaw counter or the  $\beta$  chamber fires. However, we expect an efficiency drop of  $\sim 4\%$  for single barrel strike vetoes, a value comparable to our  $\Delta^0$  failure rate. However, the data indicate that the missing barrel stave is not our problem. Most vetoes involve at least two veto counters firing. Further, the 20 GeV missing mass distributions of figure D-7 lead us to believe that most single barrel vetos probably involve  $\Delta^0$  decays, and they can be used to estimate the  $\Delta^0$  failure rate contribution from the loss of B8. There are about 10  $\Delta^0$  events in the neutron  $\Delta\varphi$  cut between 1.2 and 2.0  $\text{GeV}^2$ , and 62 events outside the  $\Delta\varphi$  cut below  $2.0 \text{ GeV}^2$  for a total of 72  $\Delta^0$  events with a single barrel hit. This implies  $\sim 1/23 \times 72 = 3$  events would have had a hit in the dead counter.

There were about 900  $\rho^0\Delta^0$  events in the same running (181  $\rho^0\Delta^0$  events recorded in  $\pi\pi X$  times the prescale factor of 5). Thus the  $\Delta^0$  failure rate coming from the dead counter is  $\sim 3/900 = .3\%$ , much less than the observed rate. We conclude that the high failure rate at the  $\Delta^0$  is from an inherent inefficiency for low recoil masses, which correspond to the softest photons seen by the Barrel.

### D.3 Neutron Vetos

The  $\pi\pi B$  trigger discussed in the proceeding section was most useful for measuring our neutron veto rate. As shown in figure 4-6, this trigger displays a strong neutron peak in the variable  $\Delta\varphi = \varphi_{forward} - \varphi_{Barrel}$ .  $Mx^2$  cuts are needed to cleanly extract the neutron signal from these data, but it was generally cleaner than that of the  $\pi\pi m_T$  trigger after these cuts were made.

We found the neutron veto rate (neutron detection efficiency) by parallel analyses of  $\pi\pi B$  and  $\pi\pi m_T$  data. Only runs for which the  $\pi\pi B$  trigger was active were used. The same topology,  $m_{nn} (> 600 \text{ MeV})$ , and  $Mx^2$  cuts were used for both triggers. No C1 C2 cuts were made, all forward particles being assumed pions. A

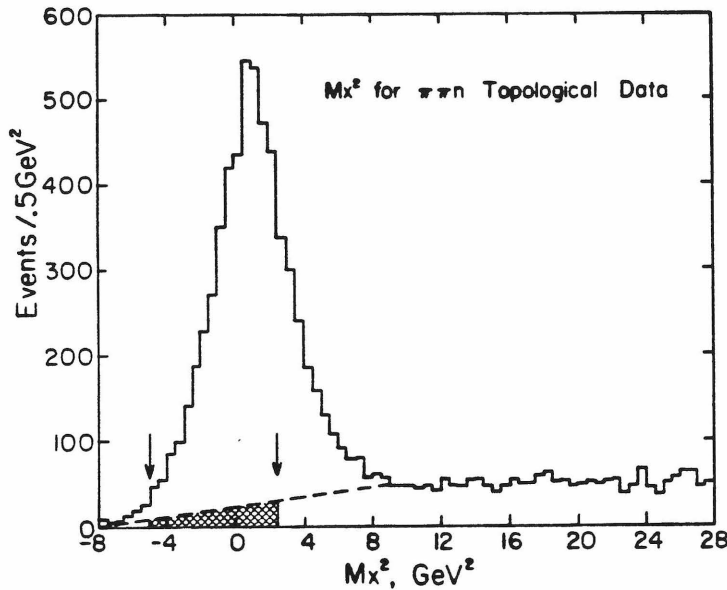


Figure D-5.  $Mx^2$  spectrum for  $\pi\pi n_T$  data used in neutron veto study. Shown are  $Mx^2$  cuts used, and the rough background estimate used.

conservative  $Mx^2$  cut of  $-5 < Mx^2 < 2.5 \text{ GeV}^2$  was used at 100 GeV, as shown in figure D-5, to reduce background subtraction burdens. Figure D-6 shows a preliminary background subtraction study for  $\pi\pi B$  with a fixed ( $\pm 22.5^\circ$ )  $\Delta\phi$  cut. A similar plot, figure D-7, made with 20 GeV data, shows that most of the large  $\Delta\phi$  background is single photon hits from  $\Delta^0$  decays.

The  $\sqrt{-t}$  (approximated as  $|p_t|$ ) dependence of the neutron veto rate was found after a study of the peak in figure 4-4 as a function of  $\sqrt{-t}$ . We found that the  $\Delta\phi$  resolution depended on  $\sqrt{-t}$  and that the neutron detection efficiency had a threshold of  $\sqrt{-t} \sim .08 \text{ GeV}/c$ . The  $\Delta\phi$  resolution at 100 GeV is shown in figure D-8, which used three different sets of large  $\sqrt{-t}$  bins in an attempt to flush out statistical fluctuations, and have enough data to allow fitting.  $\Delta\phi$  distributions (not shown) for these bins were fit to a Gaussian with a flat background. The mean, width, and height of the peak, and the background level were all free parameters. The fits break down for bins below  $\sqrt{-t}$  below  $\sim .1 \text{ GeV}^2$ , an effect that could be due to either

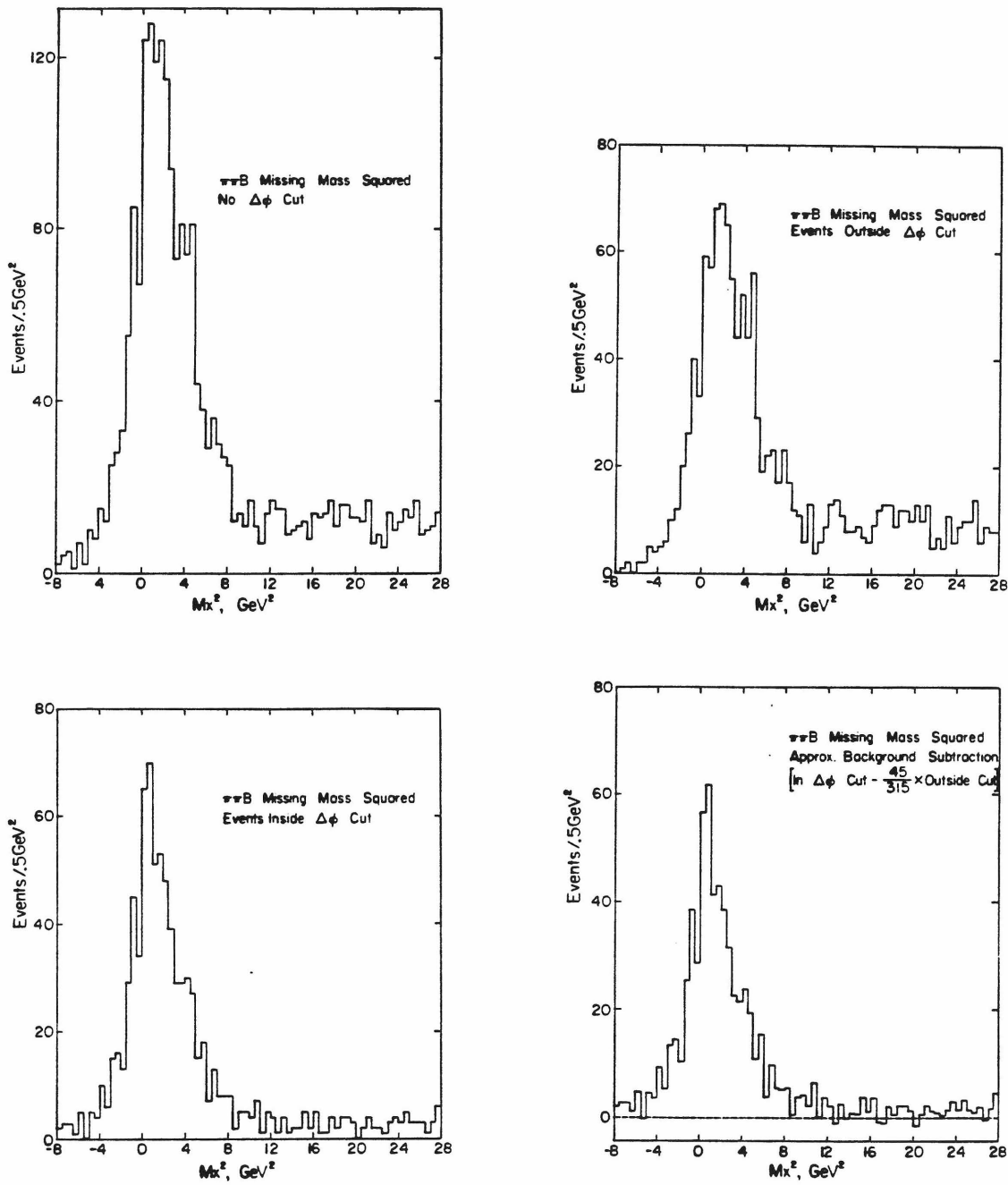


Figure D-6. Preliminary fixed  $\Delta\phi$  cut study on 100 GeV/c  $\pi\pi B$  data. Note that the uncut and cut failing distributions are shifted to higher  $Mx^2$ .

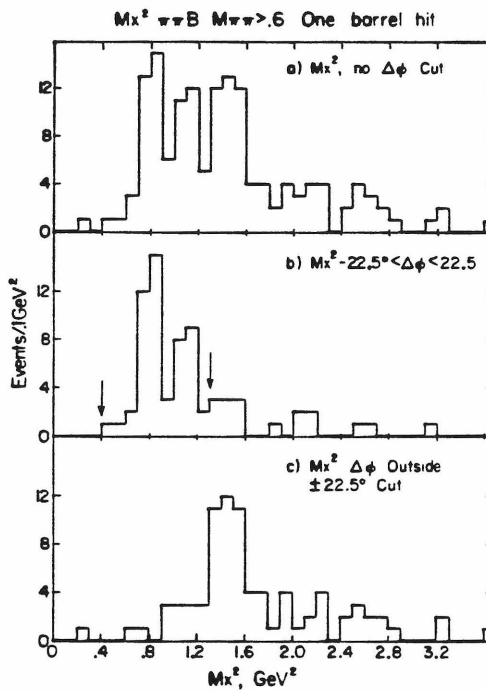


Figure D-7.  $\Delta\varphi$  study at 20 GeV/c. Events outside the  $\Delta\varphi$  cut are clearly dominated by the  $\Delta(1236)$  resonance.

resolution or a threshold. We favor a threshold because we see one in 20 GeV data, figure D-9, where the resolution is better, and the effect coincides with a predicted neutron threshold for the Barrel [Pi74].

The neutron detection efficiency was found from the ratio of  $\sqrt{-t}$  distributions in  $\pi\pi B$  and  $\pi\pi n_T$ . The smooth curve of figure D-8 was used to set  $3\sigma$  ( $\Delta\varphi$ ) cuts as a function of  $\sqrt{-t}$  in  $\pi\pi B$ . The background outside the cuts was flat, and was used to subtract the single photon background from the neutron veto signal. We also did a background subtraction for the  $\pi\pi n_T$  data. For that, we used a  $\sqrt{-t}$  distribution from the  $\pi\pi X$  trigger scaled to the event total in the hatched region of figure D-5. Both the  $\pi\pi X$  and single photon backgrounds were peaked at smaller  $\sqrt{-t}$  values than  $\pi\pi n_T$  or  $\Delta\varphi$  cut  $\pi\pi B$  distributions.

Since neither  $\pi\pi n_T$  or  $\pi\pi B$  were prescaled, the neutron detection efficiency, defined as the ratio of detected neutrons to total neutrons, is found as

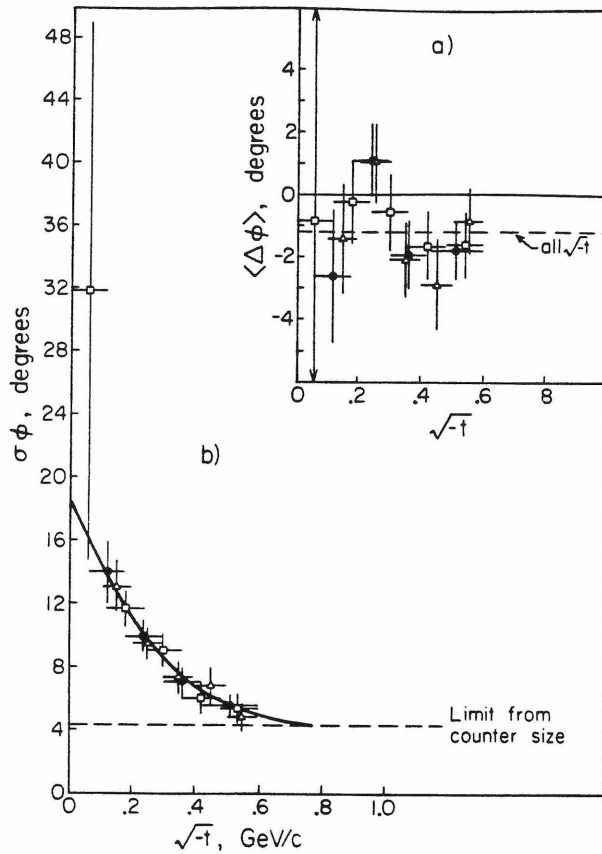


Figure D-8. Recoil neutron azimuth resolution at 100 GeV/c (b). Points were found in three sets of fits to a Gaussian plus flat background. Smooth line is the dependence used in  $E_{nn}$  measurement. This was not used for the study of figure D-6, but was used for our  $E_{nn}$  measurement. Also shown (a) is the error in surveyed counter orientation.

$$E_{nn} = \frac{B}{N+B} \quad (D.13)$$

where B is the number of detected neutrons from  $\pi\pi B$  and N is the number of  $\pi\pi n\gamma$  events. Equation D.13 assumes background subtractions have been made. The two triggers are complementary, one having a veto on neutrons and the other not. A side effect was differing backgrounds under the neutron, but having subtracted these, the other corrections are the same, and they cancel out in D.13. Thus this equation represents the fraction of  $\pi\pi n$  events that suffered neutron interactions in the barrel, and hence the loss of such events from the  $\pi\pi n\gamma$  trigger.

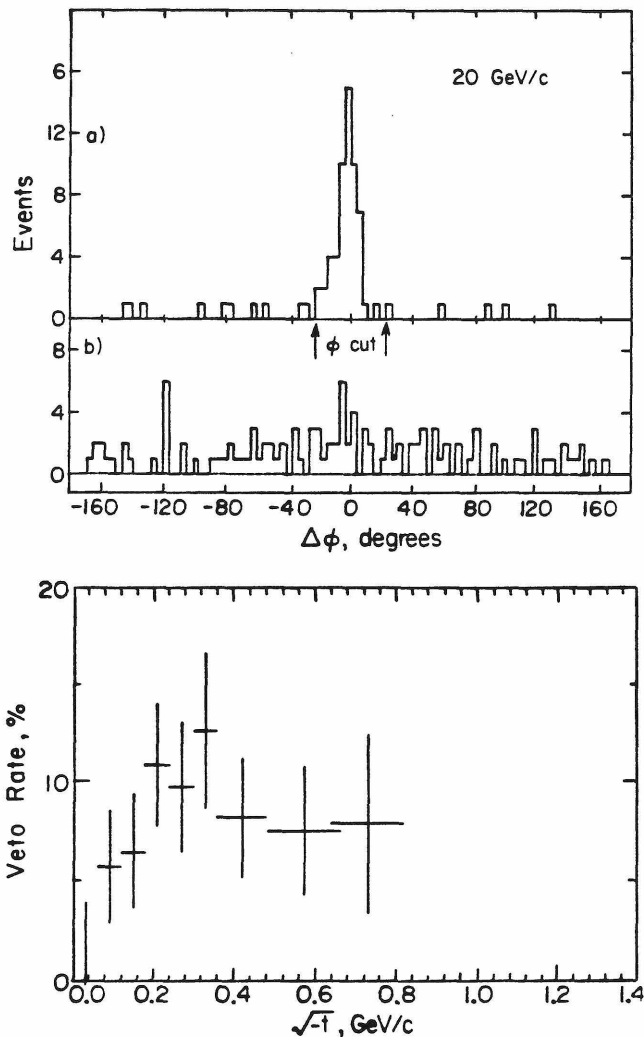


Figure D-9. 20 GeV/c  $\Delta\phi$  distributions for events inside (a) and outside (b) neutron  $Mx^2$  cut. (c) shows 20 GeV/c  $E_{nn}$  values.

Figure 4-7 shows  $E_{nn}$  at 100 GeV/c. And our results are given in section 4.3.

#### D.4 BCD Delta Rays

We now discuss the development of the BCD delta ray correction. This correction was designed to account for delta ray losses in our tight BCD trigger requirement for  $\pi\pi\eta\eta$ , and was tailored for consistency with the reconstruction efficiency correction. That correction includes effects for the chamber efficiencies in the trigger and track finding. Our BCD software trigger cuts were set to cleanly

separate the problems of the delta ray and chamber efficiency corrections. The formalism discussed below was built around a measurement of the needed parameters from curve through data, that being the only trigger free of BCD requirements and, hence, our only trigger that allowed a bias free measurement of the delta ray rates.

The BCD delta ray formalism makes use of the stiff BCD trigger requirement to deal in a simple way with correlations between chambers. We include as "correlations" chance pairs of delta rays created by one particle and seen in different chambers, as well as "true" correlations caused by penetrating single delta rays. Delta rays coming from different particles are not viewed as correlations. We need not distinguish between one delta ray seen by a chamber and several delta rays seen by that chamber. For a *single* particle, we need only use the following classes of events: a) no chamber sees any delta rays, b) exactly one chamber sees a delta ray signal, and c) delta ray signals are seen by two or more chambers. Class b) splits into six subclasses, one for each chamber.

For  $\pi\pi\pi$  events, small but finite, chamber inefficiencies in the BCD chambers require that we distinguish between cases where all chambers satisfy the (software) trigger requirement of a hit on each of the two particles (6ok), and cases where one chamber fails this requirement (5ok). Trigger cuts insure that there are only two such classes we need to deal with. In the 6ok case, we can have (any number of) delta rays detected by one of the six chambers. A veto would require delta rays to be detected by at least two chambers. In the 5ok case, a delta ray signal seen by any of the five good chambers would cause a veto as one chamber is already bad. We express the delta ray corrections for the 5ok and 6ok cases of  $\pi\pi\pi$  in terms of parameters found for the several single track cases defined above.

Consider first the 6ok case. Let  $P_{k0}$  be the chance that the k'th particle made no delta rays at all,  $P_{km}$  be the chance that this particle created delta ray signals in

Table D.2			
BCD Single Track Parameters			
$P_0 = .8212 \pm .0039$			
$P_1 = .1291 \pm .0034$			
$P_m = .0497 \pm .0022$			
chamber		$p_i$	$p_{oi}$
Bx	1	$.0280 \pm .0017$	$.1507 \pm .0036$
By	2	$.0179 \pm .0014$	$.1608 \pm .0037$
Cx	3	$.0145 \pm .0012$	$.1642 \pm .0038$
Cy	4	$.0156 \pm .0013$	$.1632 \pm .0038$
Dx	5	$.0241 \pm .0016$	$.1547 \pm .0037$
Dy	6	$.0289 \pm .0016$	$.1498 \pm .0036$
(statistical errors only)			

two or more chambers, and  $p_{ki}$  the chance that it made a delta ray signal in only the  $i$ 'th chamber. We assume that  $P_{k0}$ ,  $P_{km}$ , and  $p_{ki}$  are all independent of track location within a chamber and that these values are unaffected by the presence of other particle(s). We define  $P_{k1}$  as the chance that exactly one chamber had a delta ray signal, not worrying about which chamber it was:

$$P_{k1} = \sum_i p_{ki} \quad (D.14)$$

For a single particle we have

$$1 = P_{k0} + P_{km} + P_{k1} \quad (D.15)$$

For two particles, we have just the product of single particle expressions.

$$1 = (P_{10} + P_{1m} + P_{11}) \times (P_{20} + P_{2m} + P_{21}) \quad (D.16)$$

Only those terms in D.16 involving  $P_{km}$  or  $p_{1i}p_{2j}$   $i \neq j$  can lead to vetos. Calling  $P_{nv}$  the chance no veto occurs, we rearrange D.16 using D.14 and D.15 to get two expressions for  $P_{nv}$  :

$$P_{nv} = 1 - (P_{1m} + P_{2m} - P_{1m}P_{2m} + \sum_{i \neq j} p_{1i}p_{2i}) \quad (D.17a)$$

$$P_{nv} = P_{10}P_{20} + P_{10}P_{21} + P_{20}P_{11} + \sum_i p_{1i}p_{2i} \quad (D.17b)$$

Invoking the above assumption ( $P_{kj} = P_{ji}$  for particles j and k), these become

$$P_{nv} = 1 - (2P_m - P_m^2 + \sum_{i \neq j} p_{1i}p_{2j}) \quad (D.18a)$$

$$P_{nv} = P_0^2 + 2P_0P_1 + \sum_i p_i^2 \quad (D.18b)$$

where  $P_{10} = P_{20} = P_0$  ,  $P_{1m} = P_{2m} = P_m$  ,  $P_{11} = P_{21} = P_1$ , and  $p_{1i} = p_{2i} = p_i$ . Either of equations D.18 may be used to express  $P_{nv}$  , and their equality was a check on the measured numbers.  $P_{nv}$  is used to get an event weight:

$$w_6 = 1 / P_{nv} \quad (D.19)$$

The less frequent 5ok case is easier to express. If any chamber other than the one failing to have hits on both tracks has a delta ray, the event would be killed. Define  $p_{oi}$  to be the chance per particle of seeing delta ray(s) in any chamber other than the i'th chamber. Then, since either particle can make the offending delta ray signal, the correction weight is

$$w_{5i} = 1 / (1 - p_{oi})^2 \quad (D.20)$$

There is one such factor for each of the six BCD chambers. Delta rays seen in chamber i (the one missing its hit) do not cause vetos and do not enter into D.20.

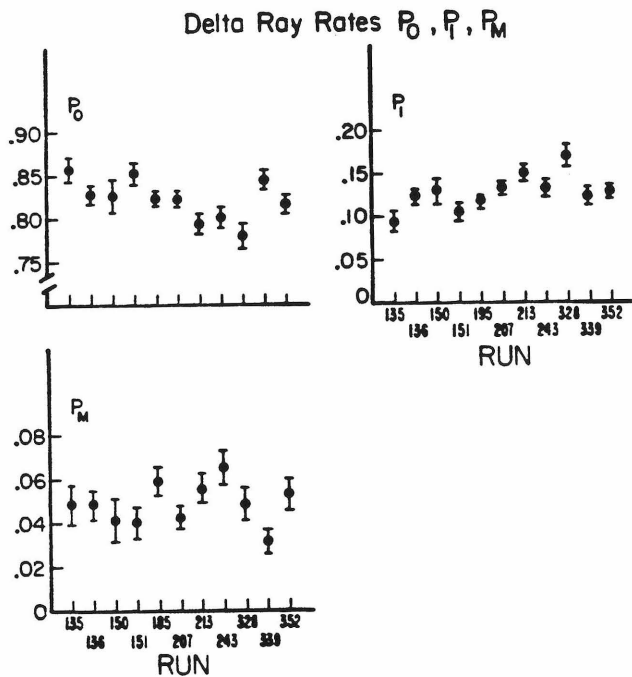


Figure D-10. BCD delta ray rate parameters  $P_0$ ,  $P_1$ , and  $P_m$  for the various curve through runs. These runs were combined for the values in Table D.2.

With the above formalism, we needed only thirteen parameters to evaluate the BCD delta ray weights. As mentioned above, we used curve through data for the parameters. This single particle trigger is the only one in E110 without BCD chamber trigger requirements and a reasonable topology; it required only BEAM-2x2 as its trigger. Of the fourteen curve through runs made in the spring '77 running, only three runs were excluded from the study. During one the Cx chamber was dead--disabled by water dripping from the magnet; and two were muon contamination runs in which a calorimeter module was placed in the beam. That compromised the track clean up procedures used.

The data were analyzed with cuts insuring that only one beam particle was present without imposing any conditions on the BCD chambers, and allowing for delta rays to reach the spark chambers and be found as tracks. Multiple beam

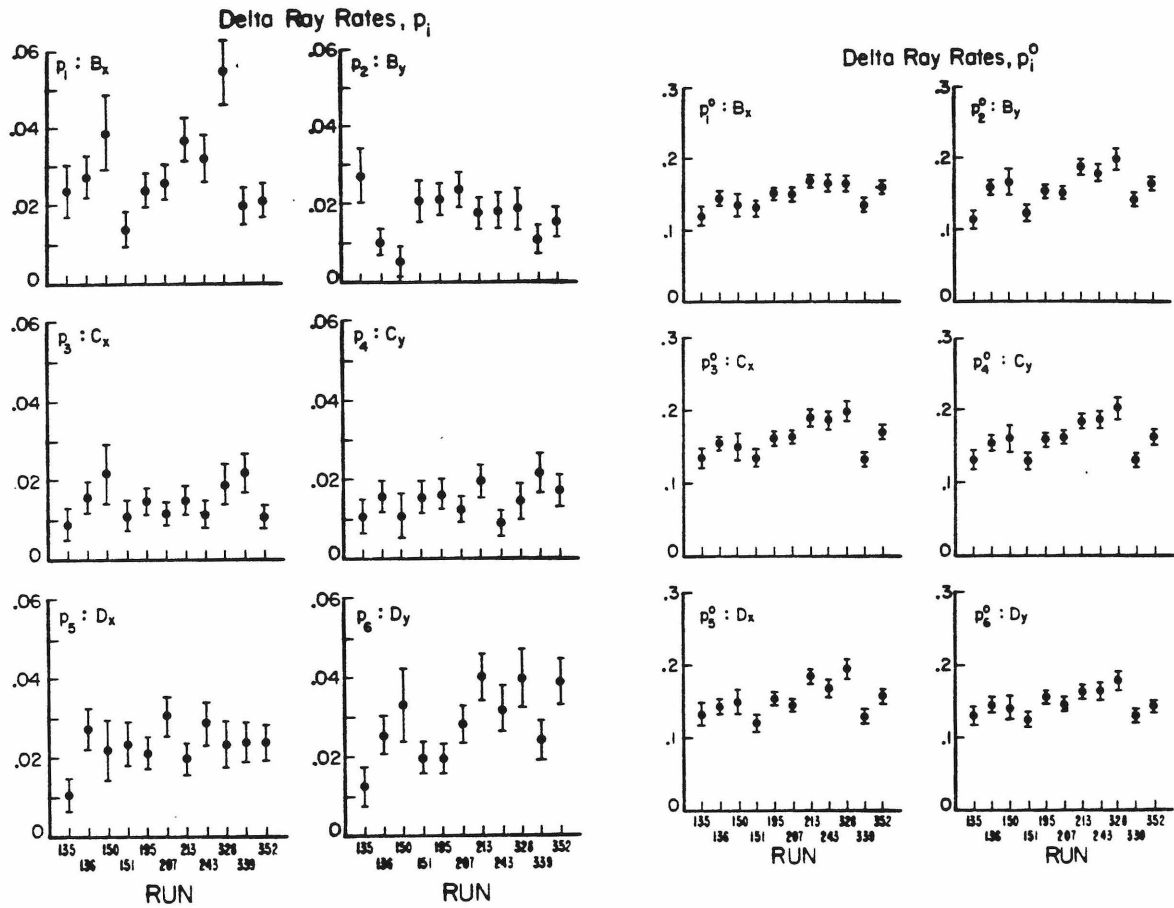


Figure D-11. BCD delta ray parameters  $p_i$  and  $p_0i$  versus curve through run and for the various chambers.

particles in the same r.f. bucket, or just within the resolving time of the proportional chambers could look like delta rays and distort the measurement, so care to eliminate them was needed. Any event that seemed to have extra particles involved was rejected. The runs were studied separately to see if any were pathological (none were), and were then combined to produce the results. All beam momenta were included as their results appear consistent and no beam momentum dependence should be expected in this delta ray effect. Chamber sagging from beam intensity could have been an effect, but no significant beam intensity effects were seen (unlike the Beta chamber correction), probably because the BCD chambers

were normal to the beam, and delta rays are a reasonable distance from tracks. Out of 22287 events in the curve through runs, 9639 passed all the cuts and were used in the analysis.

Delta rays were counted as the total hits in a chamber less the number of hits on the good track. This removed miscounts that could arise from inefficiencies. The values for the various  $P$ 's were taken from a histogram of the number of chambers having delta rays in each event. The  $p$ 's came from plots of the appropriate count of delta rays in each event. Figure D-10 gives the run dependence of the  $P$ 's, while figure D-11 gives the run dependences of each of the  $p_i$  and  $p_{oi}$ , respectively. Table D.2 gives the values of the parameters for the combined data set, and table 4.1 gives the resulting weights.

The curve through data allow us to test the validity of the assumptions made; that delta ray rates are independent of track location and are not affected by the presence of a second track. These were checked with plots of the distance,  $D$ , between a track and the delta rays it created (in the coordinate measured.) Distributions in  $D$  were taken for each chamber in 5 mm bins in the range  $-3m \leq D \leq 3m$ . The distributions had a central peak of half width about 5 centimeters, and long, substantial tails. (Special fine resolution plots verified that the delta rays were never actually on the tracks.) The peaks came mainly from single plane delta rays (the kind that made  $p_i$ ), while the tails were mainly from multi plane delta rays. To get an overestimate of the chance that a delta ray would land on top of a second track, we found the ratio of the contents of the most populated bin to the total entries in the plot, correcting for actual wire separations. The largest values were about 8% for single plane delta rays, and 5% for multi plane delta rays. These ratios are the chance that a delta ray would be masked by a track if it went through the worst bin. The chance that a track was at the wrong place at the wrong time is itself only a few percent. Thus, delta ray-track overlaps appear rare.

These distributions also gave an indication of the potential position dependence of the delta ray weights. The worst case is a track near the edge of a chamber. Then, the rates for that chamber would drop by about half on that track. Using Dx as the example, we note that Dx participates in about 48% of the multiplane delta rays. For a track near the chamber edge, this fraction would drop to 24%. For this track,  $P_m$  drops to about 76% of its curve through value. In  $\pi\pi\pi$ , tracks near a chamber edge are low momentum and accompanied by a stiff track near the beam line. Referring to equation D.17a, we see that  $P_{m\pi}$  is dominated by  $P_{1m} + P_{2m}$ . A reduction of 24% in one of these values, results in a reduction of the veto rate by about 12%, and this is a worst case. Mainly for this, we assign a systematic error of 10% of the fractional part of the weight in table 4.1.

Lastly, we have only discussed delta rays resolved from tracks. This means there was at least one "quiet" wire between the delta ray and the track. Delta rays unresolved from their creating track can cause event vetos by merging the hits from two close tracks. In a delta ray free world, one would choose a separation cut of about 1.5 wires to insure good trigger efficiency against merged tracks. Plots of the number of neighboring wires excited by a track indicated that a 1.5 wire cut was not enough, but that a three wire cut was adequate. This cut applies to x-view separations as measured at the Bx station, and affects all the BCD chambers except Dx, where bending by the magnet can cause legitimate tracks to cross. In such a case, the trigger is viewed as 50k, since the other five chambers must be perfect for the event to survive.

#### D.5 Target Region Delta Rays

As for the BCD delta ray correction, the target region, or  $\beta$ -chamber delta ray correction used curve through data to provide measurements for the veto rates. In the curve through runs, the  $\beta$  chamber recorded hits passively. A simple absorption model was then used to account for the strong z-vertex dependence of the veto rate in  $\pi\pi\eta$ . A more complicated model, described later, was also tried, but abandoned.

Curve through data give us the delta ray detection rate when a single particle passes through the entire target and the vacuum jacket end cap. All the spring '77 curve through runs were studied, as well as three of the winter '78 100 GeV runs. (The latter were used for target empty data; no target empty curve through runs were taken in the spring '77 session.) We measured the rate of  $\beta$  chamber hits after a series of fairly stiff cuts to insure a sample of events with single beam particles that had no hadronic interactions in the spectrometer. We required that the beam pwc's find a unique beam track (beam flags  $\geq 1$ ), that TEARS find just one particle after the magnet, and that this particle link to the front end with measured momentum within  $\pm 10\%$  of the beam momentum. We also required that the photon vetos (Jaws and especially the Barrel) be quiet. Delta rays do not penetrate into the Barrel, but hadrons do. The measurement was for the rate of any nonzero number of delta rays seen by the  $\beta$  chamber. Multiple delta rays were just as deadly to an event as single delta rays.

We looked for an x dependence of the delta ray rate, where x is the horizontal location of the particle at the target center. The rate was consistent with flat.

The delta ray rate does depend on the beam intensity. This reflects a change in efficiency of the chamber as delta ray production rates are independent of beam intensity. For this work, we never actually measured the absolute efficiency of the  $\beta$  chamber. All we need is the detection rate  $\approx$  efficiency  $\times$  delta ray flux at  $\beta$ . The

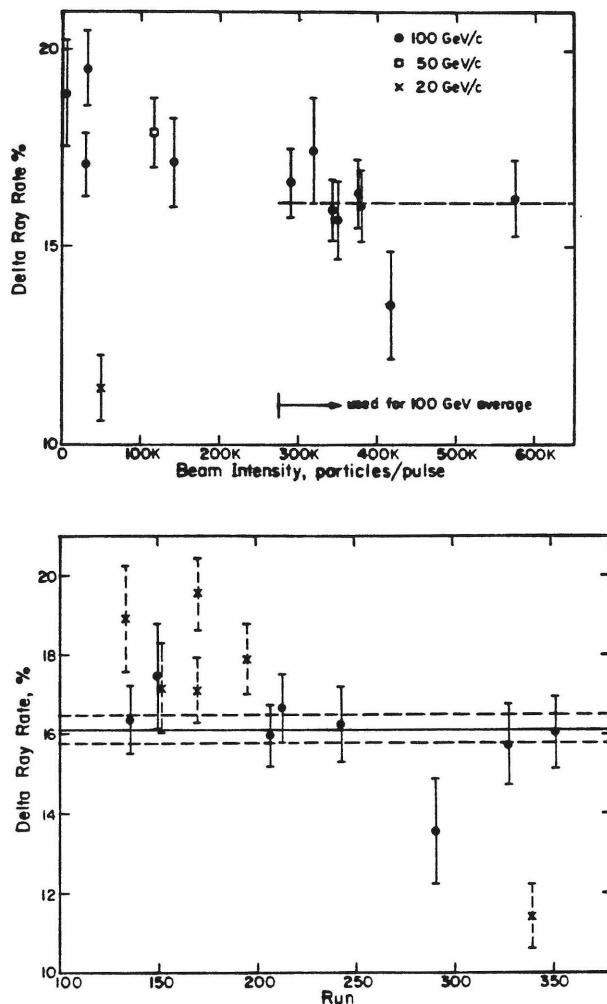


Figure D-12. Delta ray rates at the  $\beta$  chamber. Data are from curve through runs and are plotted against beam intensity (a) and run number (b).

$\beta$  chamber delta ray rate dependence with beam intensity is shown in figure D-12a, which shows a reduction of about 20 to 25% in going from essentially no beam to 600K particles per pulse. This reduction in rate (hence also efficiency) seems to be from "sagging" of the chamber high voltage during beam pulses. Such sagging is more pronounced at higher beam intensities, and is believed to come from increased levels of beam halo and other radiation about the chamber. Beam halo is particularly destructive. A particle passing through the chamber parallel to its axis will deposit much more ionization in it than a particle coming from the target

would. Furthermore, much of the halo would have interacted in the first Jaw counter,  $V_0$ , to produce showers parallel to the  $\beta$  chamber.

The 20 GeV point is an apparent exception to the intensity dependence claims. But there is evidence that we had much more halo than beam at 20 GeV. The BEAM rate was about 50K particles per pulse, while the rate into  $\text{S}\alpha\text{-Sb}$  was over five times this. A lot of particles missed the hole in  $\text{Sc}$ . The beam focus was much poorer at 20 GeV than at the other momenta, and it is reasonable to expect that there was considerable halo outside the beam counters. For these reasons, we use the measured delta ray rates at 20 GeV, rather than the value that the 100 GeV data would imply at 50K particles per pulse. The 50 GeV rate is consistent with the 100 GeV intensity dependence, and the curve through conditions at 50 GeV were comparable to the  $\pi\pi\pi$  conditions at 50 GeV. So we use the measured curve through value in the 50 GeV correction.

The 100 GeV  $\pi\pi\pi$  data were virtually all taken at beam intensities greater than 300K particles per pulse. Since the measured delta ray rate is seen to be constant above that level, we combined the data from the runs above 290K particles per pulse for the rates used here. No explicit beam intensity dependence was used in the correction weights beyond the beam momentum selection. The delta ray rate was plotted against run number, figure D-12b, to look for chamber deterioration; none was observed.

The spring '77 curve through runs were all done with a full target. We also need target empty data to separate delta rays coming from the liquid hydrogen and from the vacuum jacket end cap. For this, we used three 100 GeV curve through runs from the winter '78 data set, two with target full and one with the target empty. With these we obtained a target empty rate expressed as a fraction of the target full rate of  $6.90 \pm 1.93\%$ . The curve through delta ray rates are given in table D.3.

Table D.3					
Curve Through Delta Ray Rates and Model Parameters					
	Raw (%)	$LH_2$ (%)	End Cap (%)	$p$ (/meter)	$P^{cap}$
100 GeV	$16.12 \pm .34$	$15.01 \pm .46$	$1.11 \pm .31$	$.533 \pm .018$	$.989 \pm .003$
50 GeV	$17.91 \pm .89$	$16.67 \pm .96$	$1.24 \pm .35$	$.598 \pm .037$	$.988 \pm .035$
20 GeV	$11.42 \pm .82$	$10.63 \pm .85$	$.79 \pm .23$	$.369 \pm .031$	$.992 \pm .002$

The correction factor for a  $\pi\pi n$  event was built using a simple absorption model with its parameters derived from the curve through results. We assumed that the probability per unit length,  $p$ , for a track to create detected delta rays is constant along the length of the hydrogen target. We discuss how reasonable this is later. The probability  $P_L^h$  that a particle survives its passage through the entire target without making delta ray hits is :

$$P_L^h = e^{-pL} = 1 - R^h \quad (D.21)$$

where  $L = .3048m$  is the target length, and  $R^h$  is the measured delta ray rate from curve through data, as given in the  $LH_2$  column of table D.3. The chance that a particle passes through the end cap without making delta ray hits is

$$P^{cap} = 1 - R^c \quad (D.22)$$

where the  $R^c$  values are given in table D.3 which also gives the  $p$  and  $P^{cap}$  values.

For a  $\pi\pi n$  event, the probabilities of survival for each particle in the hydrogen depend on its path length in the liquid:

$$P_{beam}^h = e^{-p(z_v - z_u)} \quad (D.23)$$

$$P_{\pi^+}^h = P_{\pi^-}^h = e^{-p(z_d - z_v)} \quad (D.24)$$

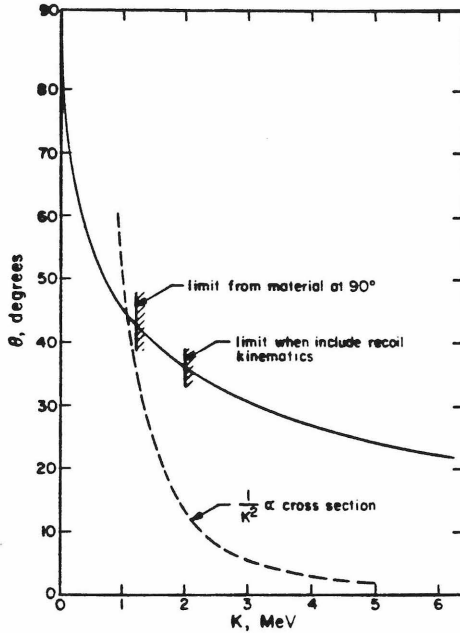


Figure D-12. Delta ray kinematics. Smooth curve is the recoil angle - energy dependence. Dashed curve is proportional to the cross section, vertical scale for it is arbitrary. Hatched limits show effects of target region material. Detected delta rays would be produced with energies  $\gtrsim 2$  MeV.

where  $z_v$  is the vertex,  $z_u$  and  $z_d$  are the upstream and downstream ends of the hydrogen flask,  $L = z_d - z_u$ . Using this, and including a  $P^{cap}$  factor for each of the two forward particles the chance that an event survives a delta ray veto is,

$$\begin{aligned}
 P_s &= P^{h_{beam}} P^{h_{\pi^+}} P^{h_{\pi^-}} (P^{cap})^2 \\
 &= P^{h_L} (P^{cap})^2 e^{-p(z_d - z_v)} \\
 &= .8313 e^{-.539(z_d - z_v)} \quad \text{at } 100 \text{ GeV/c.}
 \end{aligned} \tag{D.25}$$

Each observed event is then given the weight  $w_s = 1/P_s$ .

Delta ray production is simply  $\pi e$  elastic scattering. An estimate of the veto rate can therefore be calculated from general principles using formulae for the  $\pi e$  cross section, simple recoil kinematics, the range-energy relation for electrons, and

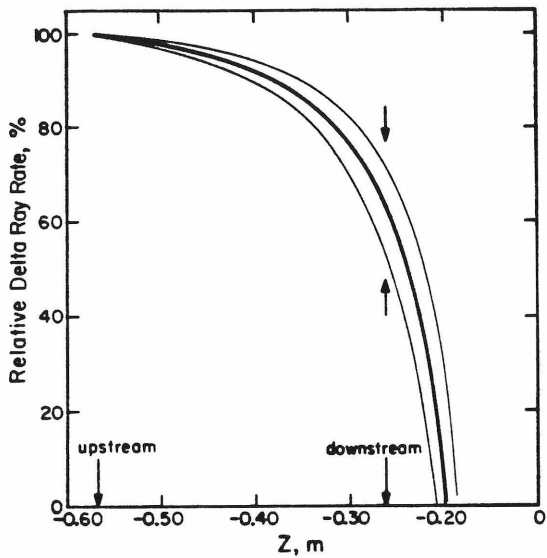


Figure D-14. Position dependence of the veto chance  $1-p$ . Heavy curve uses our estimate of the target region material.

values for the  $\beta$  chamber efficiency and the amount of material through which a delta ray must pass. This calculation has been made using our best estimate of the material in the target area and an efficiency value found during test run measurements of the  $3\pi p$  reaction. The asymptotic efficiency value was  $\varepsilon \approx .94$ , a value we expect is higher than the true value for 100 GeV running. The calculation ignored electron straggling, assumed a pencil beam through the target center (so no azimuthal integration was needed), and considered that any electron getting into the  $\beta$  chamber had chance  $\varepsilon$  of being detected.

Figure D-13 illustrates the recoil electron kinematics. The solid curve is the recoil angle with respect to the beam. The calculated lower limit  $T_{\min}$  of the electron energy imposed by the kinematics and range-energy relation is shown. This model does show that the probability  $p$  in equation D.21 is  $z$  dependent, an effect not in the simple model, because of a "high" momentum, low recoil angle cutoff

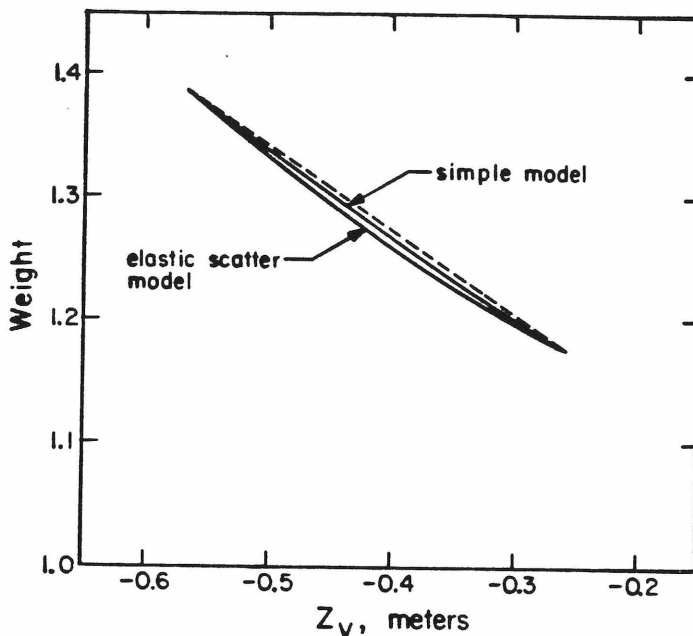


Figure D-15. Comparison between simple model (used for corrections) and the elastic scatter model. Both corrections are constrained by the measured curve through delta ray rate. For all practical purposes, they are equivalent.

imposed on delta rays by the target and  $\beta$  chamber geometry. Figure D-14 shows the  $z$  dependence, normalized to 1 at  $z_u$ . (the figure assumes an infinitely long flask). Using an efficiency of .94 and an estimated  $T_{\min}$  of 1.85 MeV the calculation predicted a 13.4% delta ray rate for the hydrogen flask, about 1.5% below the 100 GeV measurement.

Fortunately, we don't need to pursue the elastic scatter calculation beyond this qualitative level. Such work would require using the  $3\pi p$  trigger to find beam intensity dependent efficiencies, a probable relaxing of the simplifying assumptions, and adjusting  $T_{\min}$  to agree with the curve through measurements, (with possible changes in it for beam intensity related threshold changes). We are saved because the simple absorption model with a constant  $p$  is good enough. Numerically, it is within 1% of the elastic scatter results when we set  $T_{\min}$  to conform to a crucial

constraint. *The delta ray corrections for  $z = z_u$  and  $z = z_d$  are fixed by the curve through measurements regardless of the model we choose.* The results of this are shown in figure D-15 for 100 GeV weights.

The curve through based numbers can be checked with a small sample of real delta ray vetos contained in the  $\pi\pi X$  data, although there are too few such events to get a decent  $z_v$  measurement with  $\pi\pi X$ . The rate agrees with the results of this section.

#### D.6 Chamber Efficiency Measurements

Position dependent chamber efficiencies were central to our tracking efficiency correction, section 4.9. Most chambers sag by varying amounts in the beam region. In the x-and some u-spark planes, the efficiencies fall off near the chamber edge. Also, the x-spark chambers have a geometric cutoff at there edges from the u-spark chambers (x and u share a common gap.) Finally the proportional chambers had a number of "dead" wires, from amplifier problems and/or discontinuous wires through their epoxy wire supports.

In determining chamber efficiencies, one must know that a real track passed through a chamber in order to give it a valid reason to respond. It seems evident, therefore, that using found and reliable tracks is essential to the process. But this implies that the tracks used have already introduced a bias, both from the trigger and tracking requirements. A simple ratio of sparks (or pwc hits) on tracks to total tracks overestimates the chamber efficiency and a method to remove the biases must be developed. One (approximate) option would be to find tracks with reduced requirements, somehow remove new spurious tracks, and do the simple ratio, knowing that the biases are reduced. As a function of the "looseness" of the new requirements, one might be able to determine efficiencies as the limit at no requirements at all. We chose, instead, to remove our biases directly with the method described

below, which did not need any second or third rounds of tracking with reduced requirements.

Our efficiencies were found by analyzing tracks from the  $3\pi p$  trigger. This trigger was chosen because although it was heavily divided, it was quite clean and had a reasonably large amount of good track data, and a loose, more easily unbiased trigger than the other reactions. Indeed, there were more good  $3\pi p$  events than  $\pi\pi n$  events.

One expects that chamber efficiencies depend only where a track went, not on the trigger or reaction. Our efficiency results were verified by also studying  $\pi p$  elastic data. The  $3\pi p$  CST's for the same runs used in  $\pi\pi n$  analysis, were analyzed by first requiring a good three body event. A three particle vertex in the hydrogen target, total charge -1, and no particles striking the 2x2 were all required. All tracks considered were SCLEAN approved and TARGTRK analysis was required. We required that the total energy be less than 105 GeV, but permitted off energy (missing neutral particles) events to enhance the slow particle flux. A software trigger cut was made.

Assured of using good tracks, the crucial step is removing the trigger and tracking biases. A chamber's response is taken as unbiased if that chamber is *not* needed to form the trigger or find the track. That is, if other chambers involved in a requirement provide enough hits to satisfy it, then a track will be found regardless of the response of the chamber in question. This is equivalent to the claim that if a track has exactly the minimum number of hits needed to satisfy a requirement, then the chambers with the hits are all biased and only the chambers with no hits are unbiased. Further, if the minimum hit requirement is exceeded, even by just one hit, then all chambers are unbiased. This applies to each and every one of our requirements.

It is clear why we need to remove the biases. All observed tracks have met at least the minimum requirements. We wouldn't see a track if it didn't. Ignoring them would artificially inflate the efficiencies. By making topology cuts, we deal only with tracks we can reliably associate with real particles. Since the loose TEARS requirements allow many phony or "ghost" tracks to be found, even after cleanups, including them would cause efficiencies to be underestimated.

We examined the satisfaction of trigger and tracking requirements by an event looking for chambers which must be thrown out because of requirements met only minimally. As most chambers are involved in more than one requirement, usually a small group or two and overall view, a chamber is removed only in the sense of using its hit (if present) for its own efficiency calculation. It is still available for satisfying requirements when other chambers are considered. A final criterion for eliminating a chamber is shared hits, from close tracks. Because the ionization in a chamber is doubled when two tracks pass the same location, the inefficiency is roughly squared. The shared hit test was only available for pwc's.

Next, after a chamber fiducial check, the response of acceptable chambers is output in a series of scatter plots, half of which record the track position, and the other half recording the track location when a hit is present. Ratios of appropriate scatter plot slices were then used to make position dependent efficiency arrays. The bin size in the arrays is itself position dependent, giving fine binning near the beam and large bins away from the beam where statistics become marginal. The small bin size is .5 cm for spark chambers, and one wire spacing (rounded to the nearest millimeter) for the pwc's. One and two bin holes in the pwc's were checked to be sure they were from bad channels and not the binning. Two bin holes in a pwc reflect a poor wire at or near a bin edge. Plots of the efficiency arrays for positive magnet are shown in figures D-16 and D-17. The coordinates are in the lab, and the scale reflects the double bin size, being expanded in the beam region. Points

outside a chamber's fiducial volume are assigned zero efficiency, and average values, denoted by "A" with no error bar, are assigned in cases of zero or extremely few events within the chamber itself. A local average was used near the x spark chamber edges because of their construction method, figure 2-8.

The efficiency arrays were indexed only by the coordinate measured for storage reasons, (they have about ten thousand bins as it is). We thus assume that the efficiency is constant along a wire. This assumption works well when we make beam region (2x2) cuts. Beam region problems in the proportional chambers seem concentrated in the two dimensional beam spot. Wires passing through the beam spot behave "normally" away from the spot. This constant efficiency assumption runs into a problem at the edge of the x-spark chambers because the x wires share their gap with the u (slant) wires. Special procedures were developed to deal with this, but we later decided to exclude this region from the spectrometer fiducial volume.

Separate arrays were created for each beam momentum and magnet polarity. Otherwise, the efficiencies are whole run averages. We checked that the reconstruction efficiencies are consistent over the run by doing the analysis initially on smaller sets of runs. A failure of an F spark chamber for a few late runs didn't even affect the results, attesting to the loose requirements of TEARS. We see poor reconstruction efficiencies only when most or all chambers in a requirement have rotten efficiencies where a track passes.

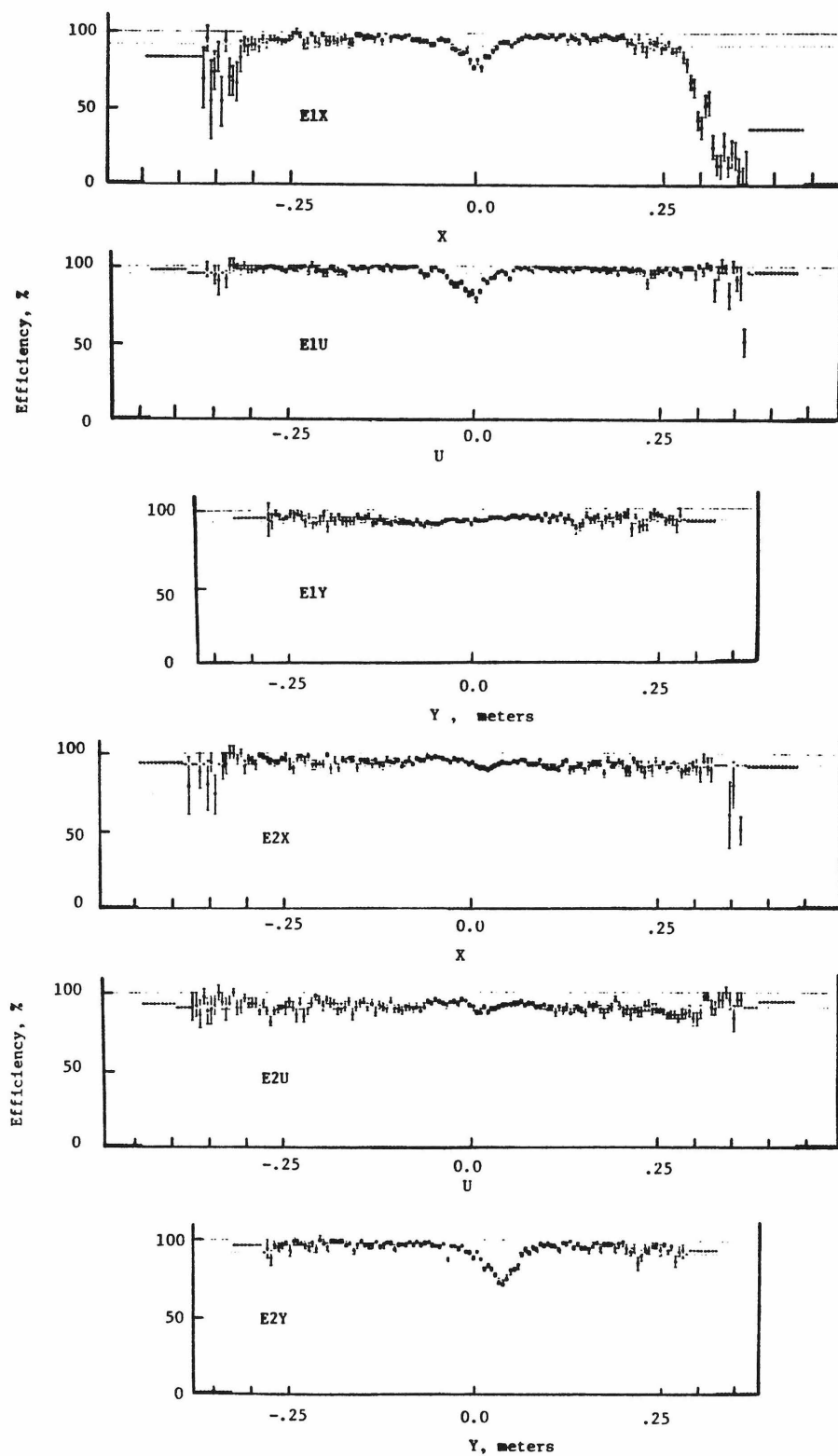


Figure D-16a. E-1 and E-2 Spark chamber efficiencies, 100 GeV/c,  $I_{mag} = +180$ . Note: Beam regions are expanded in *all* chamber efficiency plots. Divisions along horizontal axes are equally spaced at indicated scale.

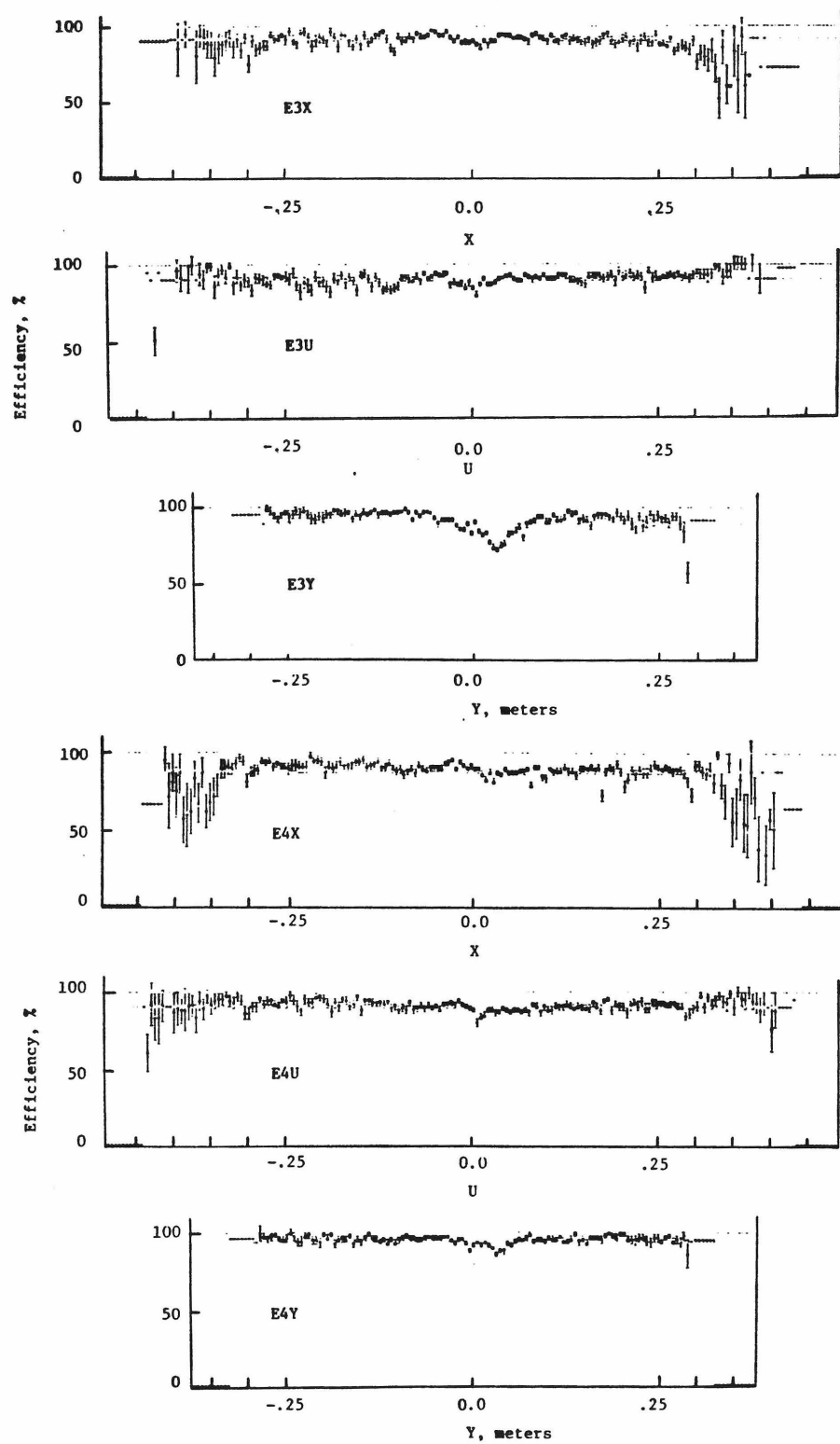


Figure D-16b. E-3 and E4 Spark chamber efficiencies, 100 GeV/c,  $I_{mag} = +180$ .

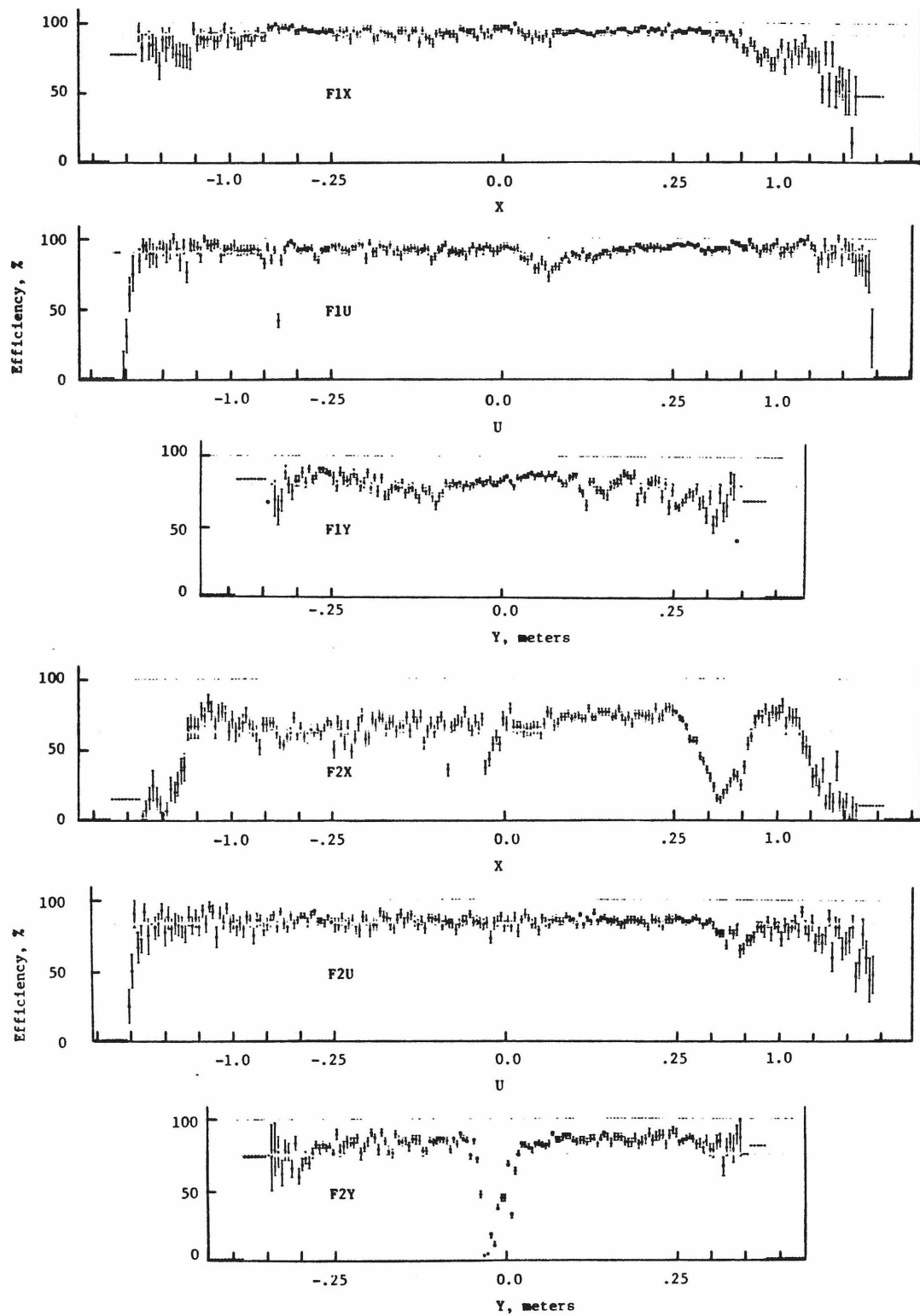


Figure D-16c. F-1 and F-2 Spark chamber efficiencies, 100 GeV/c,  $I_{mag} = +180$ .

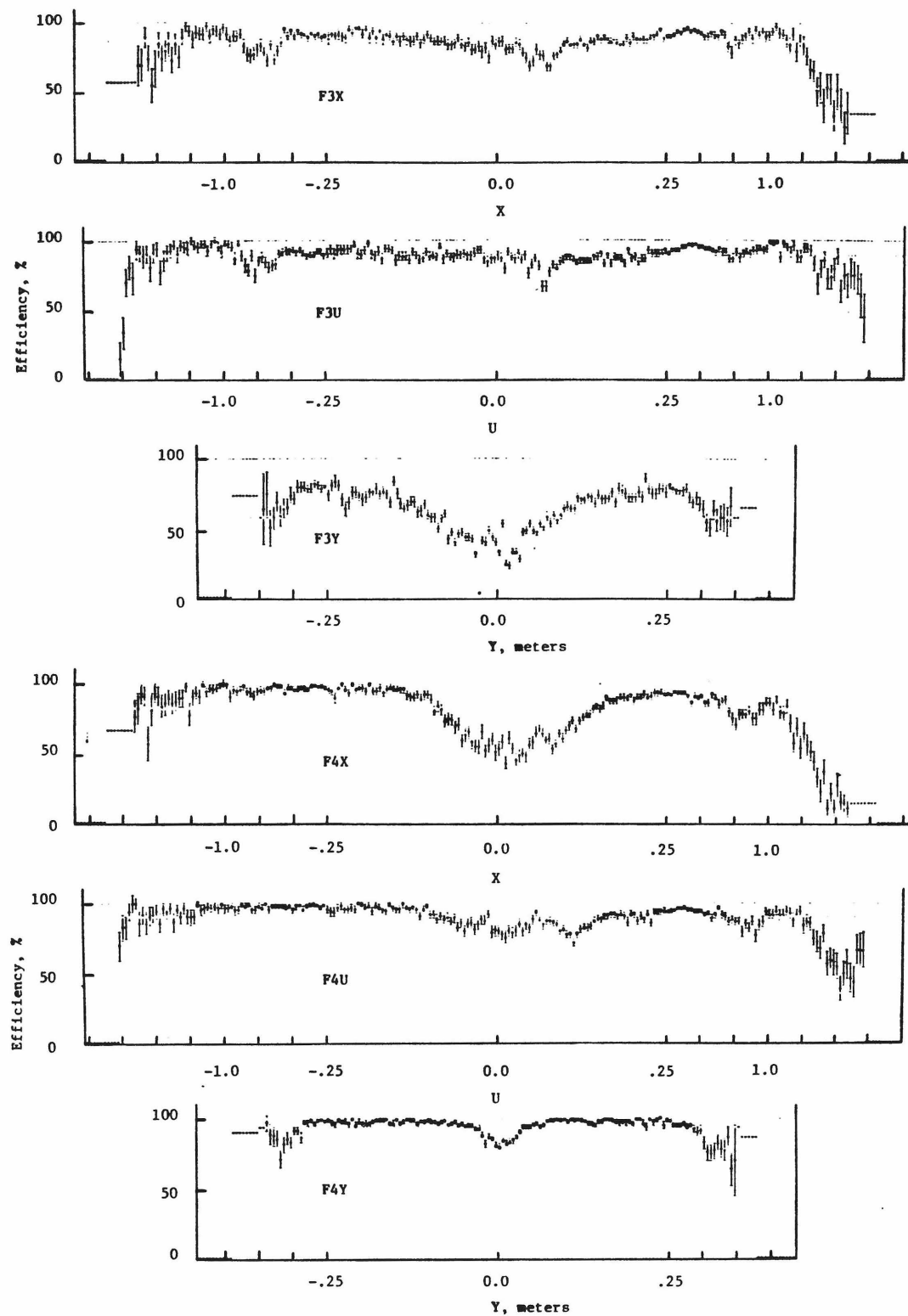


Figure D-16d. F-3 and F-4 Spark chamber efficiencies, 100 GeV/c,  $I_{mag} = +180$ .

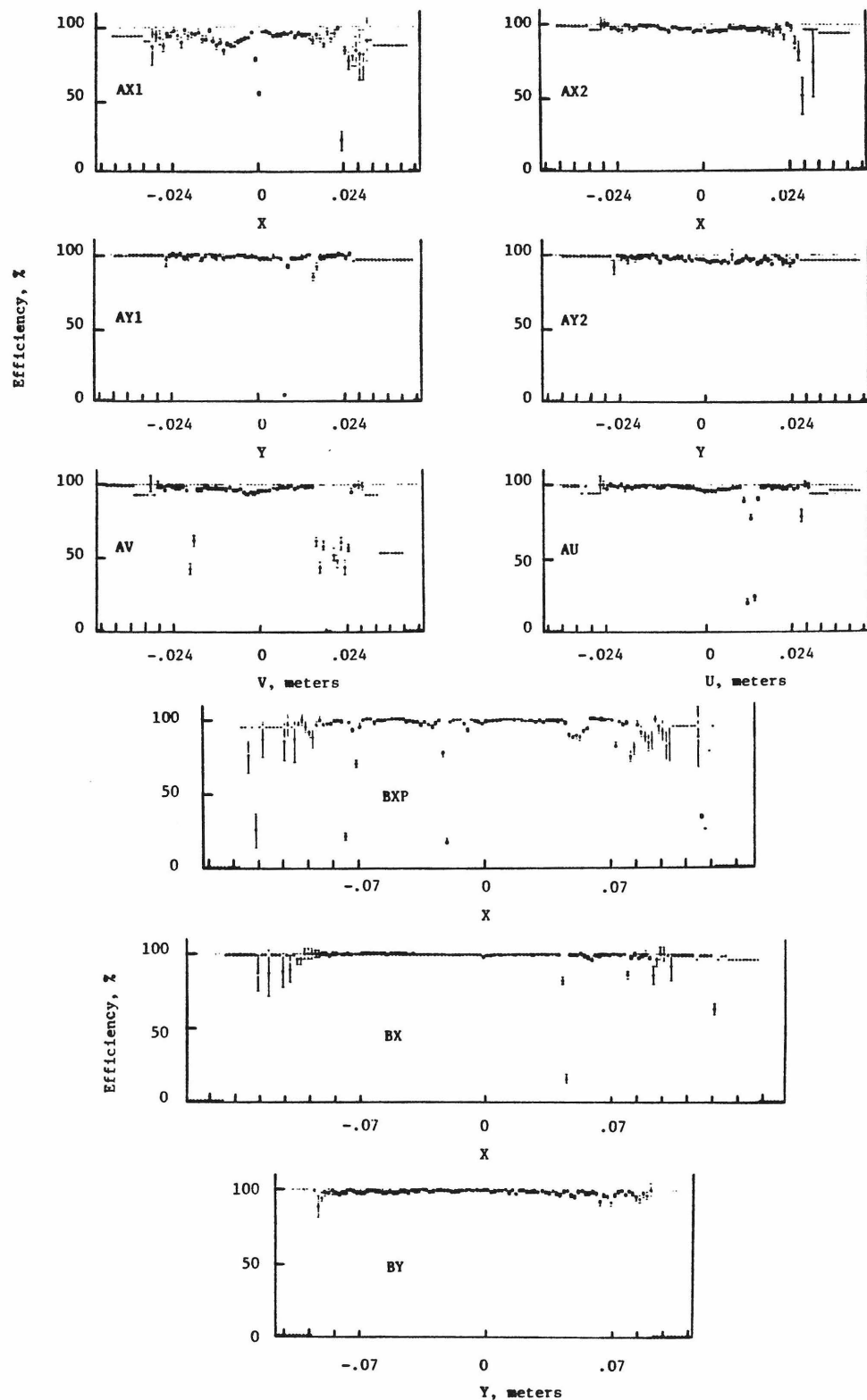


Figure D-17a. A and B station proportional chamber efficiencies, 100 GeV/c,  $I_{mag} = +180$ . Note: Beam regions are expanded in *all* chamber efficiency plots. Divisions along horizontal axes are equally spaced at indicated scale.

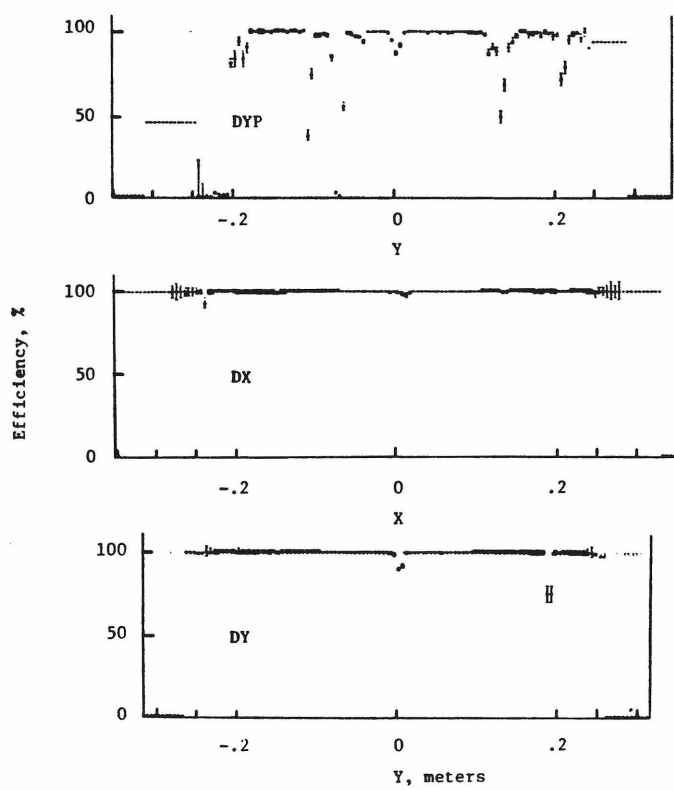
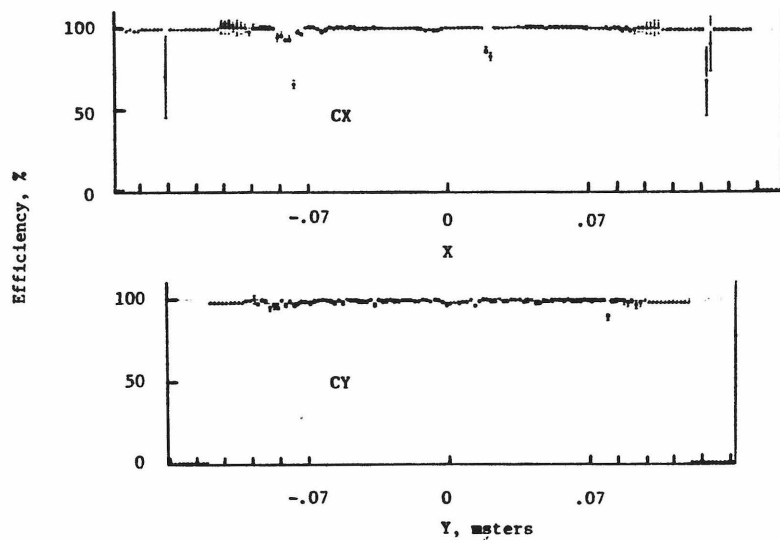


Figure D-17b. C and D station proportional chamber efficiencies, 100 GeV/c,  $I_{mag} = +180$ .

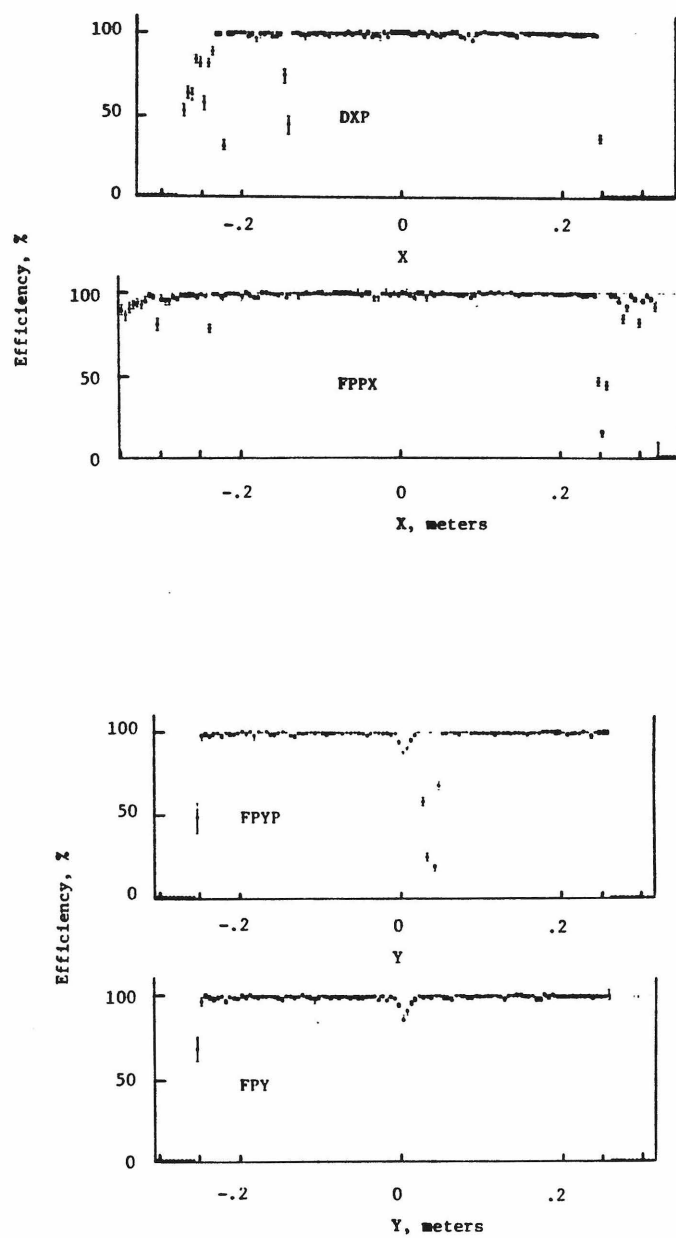


Figure D-17c. F-station proportional chamber efficiencies, 100 GeV/c,  $I_{mag} = +180$ .

References

Ab64 M. Abramowitz and I. Stegun, "Handbook of Mathematical Functions", National Bureau of Standards #55, 1964, (Dover 1965).

Al78 B. Alper *et al.*, Rho Production at 63 GeV/c, submitted to 19th International Conference on High Energy Physics, Tokyo 1978.

An76 R. Anderson and J. Grant, Nucl. Instrum. Methods **135** 267 (1976).

Ay74 D. Ayres, ANL Report, 1974, unpublished.

Ay77 D. S. Ayres, *et al.*, Phys. Rev. **D15** 3105 (1977).

Ba80 A. Barnes, Measurements of Pion Charge Exchange and Other Things at Fermilab Energies, Cal Tech PhD Thesis, (1980), unpublished.

Be72a M. Benot, J. Litt, and R. Meunier, Nucl. Instrum. Methods **105** 431 (1972).

Be72b B. Bertolucci, Camac Magnetostrictive Readout System Using Schottky Memories, SLAC-PUB-1177, presented at the IEEE 1972 Nuclear Science Symposium, Miami, Florida, December 6-8, 1972.

Be79a G. Ray Beausoleil, E260 Beam Cerenkov Analysis, unpublished E260 memo, CIT-64-79 (1979).

Be79b H. Becker, *et al.*, Nucl. Phys. **B150** (1979) 301.

Be79c H. Becker, *et al.*, Nucl. Phys. **B151** (1979) 46.

Bi74 H. H. Bingham, *et al.*, Phys. Lett. **51B** 397 (1974).

Bo64 L. Bondar *et al.*, Il Nuovo Cimento, **31** 4 (1964).

Br72 E. Bracci, *et al.*, Compilation of Cross Sections I -  $\pi^-$  and  $\pi^+$  Induced Reactions, CERN/HERA 72-1, CERN Scientific Information Service (1972).

Br79 C. Bromberg, "Recent Software Modifications", unpublished E110 internal memo, Cal Tech CIT-59-79 (1979).

Br80 C. Bromberg *et al.*, Phys. Rev. **D22** 1513 (1980).

Ch59 G. F. Chew and F. E. Low, Phys. Rev. **113** 1640 (1959).

Co71a E. Colton, *et al.*, Phys. Rev. **D3** 2028 (1971).

Co71b E. Colton and E. Malamud, Phys. Rev. **D3** 2033 (1971).

Co77 C. Cole, "Wind's Method", unpublished E110 internal memo, Cal Tech, CIT-50-78, (1977).

Co78 M. J. Corden *et al.*, Nucl. Phys. **B137** (1978) 221.

Co79 M. J. Corden *et al.*, Nucl. Phys. **B157** (1979) 250.

Da78 W. Danchi, C.I.T. Bachelor of Science Thesis, unpublished (1978), and E110 internal memo CIT-56-79, unpublished.

Da79 C. Daum, *et al.*, Elastic and Total  $\pi^+\pi^-$  Cross Sections from a High Statistics Measurement on the Reaction  $\pi^-p \rightarrow \pi^+\pi^-n$  at 63 GeV/c", presented by P. Weilhammer, Proceedings of the 20th International Conference on High Energy Physics, Geneva, 1979.

De80 R. Delzenero, "Vertex Finding Algorithms", and "Main Vertex Errors", unpublished E110 internal notes, UICC (1980).

De82 R. Delzenero, University of Illinois Chicago Circle PhD. Thesis, unpublished (1980).

Di80 J. Dickey *et al.*, D and E Mesons and Possible KKK Enhancements, Presented at the VI International Conference on Experimental Meson Spectroscopy, Brookhaven National Laboratory (1980).

Dr58 S. D. Drell, Proceedings 1958 Annual International Conference on High Energy Physics at CERN (CERN, Geneva, 1958), pp. 20-24,27-33.

Dr60 S. D. Drell, Phys. Rev. Lett. **5** 342 (1960)

Dz76a A. Dzierba, NAL Proposal 523, A Proposal to Study Multiparticle Peripheral Hadron Reactions Yielding Forward  $\pi^0$  and  $\eta^0$  Mesons, A. Dzierba, spokesman (1976), unpublished.

Dz76b A. Dzierba, E260 Online Software note, E110/E260 Multi User's Guide, July 1976, unpublished. Multi was originally created by F.J. Bartlett, and is now supported by the FNAL computing department.

Dz77 A. Dzierba, E. Malamud, and D. Mcleod, "Multiparticle Spectrometer at Fermilab", prepared for the MPS workshop at Fermilab (1977), unpublished.

Ea71 W. T. Eadie, *et al.* "Statistical Methods in Experimental Physics" (North Holland, 1971).

Eg74 T. Eguchi, T. Shimada, and M. Fukugita, Nucl. Phys. **B74** (1974) 102.

Er61 A. R. Erwin, Phys. Rev. Lett., **6** 628 (1961).

Es72 P. Estabrooks and A. D. Martin, Phys. Lett. **41B** (1972) 350.

Fi78 R. D. Field, "Dynamics of High Energy Reactions", Proceedings of the 19th International Conference on High Energy Physics, Tokyo (1978) 743.

Fo71a G. C. Fox, "On the Importance of Being an Amplitude", in Phenomenology in Particle Physics, California Institute of Technology, Pasadena, Calif. (1971).

Fo71b G. C. Fox,  $\pi$  Exchange, Invited talk at Argonne Workshop on Meson Spectroscopy, ANL HEP - 7208, Vol. II, 1971.

Fo75 G. C. Fox, many unpublished Cal Tech E110 memos including CIT-10B-74, CIT-25-76, CIT-14-75, CIT-16-75, and CIT-24-76.

Fr59 W. R. Frazier and J. R. Fulco, Phys. Rev. Lett. **2** 365 (1959).

Fr82 F. Frederickson, Indiana University PhD. Dissertation, unpublished (1982).

Gi72 G. Giacomelli, in Proceedings of the 16th International Conference on High Energy Physics, 1972, National Accelerator Laboratory, Batavia, Ill. 1973.

Gi76 G. Giacomelli, Phys. Lett. **23C** (1976) 123.

Go58 C. Goebel, Phys. Rev. Lett. **1** 337 (1958).

Gr74 G. Grayer, *et al.*, Nucl. Phys. **B75** (1974) 189.

Ha75 H. Haggerty *et al.* "Magnetic Field Measurements on M.P. Spectrometer Magnet", unpublished Fermilab memo, (1975).

Ha75b H. Haggerty, "Multiparticle Spectrometer Calorimeters", in Proceedings of the Calorimeter Workshop, Fermilab, May 1975.

He81 R. Heinz "E110 Corrections", E110 internal memo, Indiana University, (1981).

Hy68 B. D. Hyams, *et al.*, Nucl. Phys. **B7** (1968) 1.

Ja64 J. D. Jackson, Il Nuovo Cimento, **34** (1964) 1645.

Ja65 J. D. Jackson, "Peripheral Interactions", Lecture delivered at Les Houches, NATO Summer School of Theoretical Physics (1965).

Ja65a J. D. Jackson, "Particle and Polarization Angular Distributions for Two and Three Body Decays", Lecture delivered at Les Houches, NATO Summer School of Theoretical Physics (1965).

Ki73 J. D. Kimmel and E. Reya, Nucl. Phys. **B58** (1973) 513.

Ki77 J. D. Kimmel and J. F. Owens, Nucl. Phys. **B122** (1977) 464.

Li65 D. B. Lichtenberg, "Meson and Baryon Spectroscopy", (Springer - Verlag, 1965).

Ma70 J. Mathews and R. L. Walker, "Mathematical Methods of Physics", (W. A. Benjamin, Inc. 1970).

Ma76 B. R. Martin, D. Morgan, and G. Shaw, "Pion - Pion Interactions in Particle Physics", (Academic Press, 1976).

Ma78a H. J. Martin, unpublished E110 internal memos, "Single Particle Acceptance", April 1978, and "Status of the Acceptance Programs for the 2X2 and Geometry", IU-19-78, September 1978.

Ma78b H. J. Martin, unpublished E110 internal memos, "Review of the Magnetic Field Data", IND-6-78, and "More on the Magnetic Field Data", IND-8-78 (1978).

Me80 M. Medinnis, "Charged Particle Production at High Transverse Momentum in 200 GeV/c  $p\bar{p}$ ,  $\pi^+p$ , and  $\pi^-p$  Collisions", UCLA Doctoral Dissertation, UCLA-3001 (1980), unpublished.

Oc73 W. Ochs and F. Wagner, Phys. Lett. **44B** (1973) 271.

Od71 R. Odorico, Phys. Lett. **34B** 65 (1971).

Od72a R. Odorico, Phys. Lett. **38B** 37 (1972).

Od72b R. Odorico, Phys. Lett. **38B** 411 (1972).

PDG80 Particle Data Group, Review of Particle Properties, Rev. Mod. Phys. **52** No. 2 (1980), and references therein.

Pe73 M. R. Pennington, "Zeros in  $\pi\pi$  Scattering". AIP Conference Proceedings, Number 13,  $\pi-\pi$  Scattering - 1973, (Tallahassee Conference), AIP (1973).

Pe74 M. L. Perl, "High Energy Hadron Physics", (John Wiley & Sons, 1974).

Pe78 D. Petersen, "A Study of A Station Trigger Efficiencies Using  $3\pi$  Trigger Events", unpublished E110 internal memo, IND-15-78 (1978).

Pe80a D. Petersen, "Kaon Pair Background in PIPIN Data", unpublished E110 internal memo, Indiana University, (1980).

Pe80b D. Petersen, "A-Station Trigger Efficiency Studies", unpublished E110 internal memo, Indiana University (1980).

Pi61 E. Pickup, Phys. Rev. Lett., **7** 192 (1961).

Pi71 J. Pine (correspondent), Experiment 110, Proposal to Study Multiparticle Peripheral Hadron Physics at NAL, unpublished (1971), The date is approximate.

Pi72 J. Pine (spokesman) Proposal 110A, Proposal to Study Multiparticle Peripheral Physics at NAL, (1972), and addendum dated 5-5-74, unpublished.

Pi73 J. Pine (spokesman), A Proposal to Study High  $P_T$  Physics With a Multiparticle Spectrometer, Fermilab proposal 260, unpublished (1973).

Pi74 J. Pine, "Neutron Interactions in Experiment 110 Veto House", unpublished E110 internal memo, Cal Tech, (1974).

Ro73 W. J. Robertson, *et al.* Phys. Rev. **D7** 2554 (1973).

Sh80 T. Shimada and F. Wagner, Preprint MPI-PAE/Pth 54/79, 1980, unpublished.

St61 D. Stonehill, Phys. Rev. Lett., **6** 624 (1961).

St78 S. Stampke, "A Veto House Study", CIT-53-78 (1978), unpublished E110 internal memo.

St78b S. Stampke, "The Great Beam Routine Memo", CIT-51-78 (1978), unpublished E110 internal memo.

St82 S. Stampke, "The Indiana Event Rotation (Details)", unpublished E110 internal memo, Cal Tech, (1982).

Tr62 S. B. Treiman and C. N. Yang, Phys. Rev. Lett. **8** (1962) 140.

Ve68 G. Veneziano, Il Nuovo Cimento, **57** (1968) 190.

Wa72 R. L. Walker, "Attenuation of Light in Long Scintillation Counters, Some Causes and Cures", unpublished Cal Tech High Energy Physics Report, Internal Report #60, CALT-68-348 (1972).

Wa73 F. Wagner, Nucl. Phys. **B58** (1973) 494.

Wi70 P. K. Williams, Phys. Rev. **D1** (1970) 1312.

Wi78 A. B. Wicklund, *et al.*, Phys. Rev. **D17** 1197 (1978).

Yu35 H. Yukawa, Proc. Phys. Math. Soc. Japan **B17**, 48 (1935).

Yu80 K. W. Yung, "Study of Hadronic Jets Produced by Charged Pion and Proton Beams Incident on Hydrogen and Aluminum Targets", Cal Tech PhD Thesis (1980), unpublished.